

## REPORT DOCUMENTATION PAGE

Form Approved  
OMB No. 0704-0188

The public reporting burden for this collection of information is estimated to average 1 hour per response, including the time for reviewing instructions, searching existing data sources, gathering and maintaining the data needed, and completing and reviewing the collection of information. Send comments regarding this burden estimate or any other aspect of this collection of information, including suggestions for reducing the burden, to Department of Defense, Washington Headquarters Services, Directorate for Information Operations and Reports (0704-0188), 1215 Jefferson Davis Highway, Suite 1204, Arlington, VA 22202-4302. Respondents should be aware that notwithstanding any other provision of law, no person shall be subject to any penalty for failing to comply with a collection of information if it does not display a currently valid OMB control number.

**PLEASE DO NOT RETURN YOUR FORM TO THE ABOVE ADDRESS.**

1. REPORT DATE (DD-MM-YYYY) 9/Oct/2001	2. REPORT TYPE DISSERTATION	3. DATES COVERED (From - To)		
<b>4. TITLE AND SUBTITLE</b> ISSUES IN THE DESIGN, MODELING, AND MANUFACTURE OF MULTIPLE JOINT SOLKDER SELF ASSEMBLED MICRO-ELECTRO-MECHANICAL SYSTEM (MEMS)		5a. CONTRACT NUMBER		
		5b. GRANT NUMBER		
		5c. PROGRAM ELEMENT NUMBER		
<b>6. AUTHOR(S)</b> CAPT KLAUDITIS PAUL E		5d. PROJECT NUMBER		
		5e. TASK NUMBER		
		5f. WORK UNIT NUMBER		
<b>7. PERFORMING ORGANIZATION NAME(S) AND ADDRESS(ES)</b> UNIVERSITY OF COLORADO AT BOULDER			<b>8. PERFORMING ORGANIZATION REPORT NUMBER</b> CI01-261	
<b>9. SPONSORING/MONITORING AGENCY NAME(S) AND ADDRESS(ES)</b> THE DEPARTMENT OF THE AIR FORCE AFIT/CIA, BLDG 125 2950 P STREET WPAFB OH 45433			<b>10. SPONSOR/MONITOR'S ACRONYM(S)</b>	
			<b>11. SPONSOR/MONITOR'S REPORT NUMBER(S)</b>	
<b>12. DISTRIBUTION/AVAILABILITY STATEMENT</b> Unlimited distribution In Accordance With AFI 35-205/AFIT Sup 1				
<b>13. SUPPLEMENTARY NOTES</b>				
<b>14. ABSTRACT</b>				
<b>DISTRIBUTION STATEMENT A</b> Approved for Public Release Distribution Unlimited			20011016 179	
<b>15. SUBJECT TERMS</b>				
<b>16. SECURITY CLASSIFICATION OF:</b> a. REPORT   b. ABSTRACT   c. THIS PAGE		<b>17. LIMITATION OF ABSTRACT</b>	<b>18. NUMBER OF PAGES</b> 331	<b>19a. NAME OF RESPONSIBLE PERSON</b>
				<b>19b. TELEPHONE NUMBER (Include area code)</b>

**Issues in the Design, Modeling, and Manufacture of  
Multiple Joint Solder Self-Assembled  
Micro-Electro-Mechanical Systems (MEMS)**

by

Paul Emmanuel Kladitis

B.S., Wright State University, 1996

M.S., Air Force Institute of Technology, 1997

A thesis submitted to the  
Faculty of the Graduate School of the  
University of Colorado in partial fulfillment  
of the requirement for the degree of  
Doctor of Philosophy  
Department of Mechanical Engineering  
2001

The views expressed in this article are those of the author and do not reflect the official policy or position of the United States Air Force, Department of Defense, or the U. S. Government

This dissertation entitled:

**Issues in the Design, Modeling, and Manufacture of  
Multiple Joint Solder Self-Assembled  
Micro-Electro-Mechanical Systems (MEMS)**

written by  
Paul Emmanuel Kladitis

has been approved for the Department of Mechanical Engineering

Victor M. Bright  
Victor M. Bright, Ph.D., Committee Chairman

Y. C. Lee  
Y. C. Lee, Ph.D., Committee Member

6 Aug, 2001  
Date

The final copy of this dissertation has been examined by the signators,  
and we find that both the content and the form  
meet acceptable presentation standards of scholarly work  
in the above mentioned discipline.

## ABSTRACT

Kladitis, Paul Emmanuel (Ph.D., Mechanical Engineering)

**Issues in the Design, Modeling, and Manufacture of  
Multiple Joint Solder Self-Assembled  
Micro-Electro-Mechanical Systems (MEMS)**

Thesis directed by Professor Victor M. Bright

Using the surface tension of molten solder to assemble micro-sized structures or micro-electro-mechanical systems (MEMS), otherwise known as "solder self-assembly" is a recent development. Complex three-dimensional assemblies, previously not realizable, can now be realized using surface micromachined MEMS and solder assembly. Not only can complex or non-complex assemblies be realized using solder self-assembly, but realized by adopting means already established commercially for mass production.

This work is the first in the world to quantify or address the known entirety of major issues that go into realizing multiple joint solder self-assembled polysilicon surface micromachined MEMS. An assembly process for multiple joint solder self-assembled MEMS is developed with a yield of 94.3%. Chemical, temperature, and timing issues are detailed for the assembly process. Guidelines on the proper design of hinges, solder pads, and connecting structures for multiple joint solder self-assembled MEMS are developed. 259 two joint test structures were designed, assembled, and measured. An assembly model of series connected n-solder joint, microstructures is developed. The experimental results are compared to the model predictions.

Worst-case and statistical tolerance analysis techniques are used to predict and quantify the probabilistic nature of the variation of assembly position of multiple joint solder self-assembled MEMS. It is found that the impact in variation of assembly position, from greatest to least, comes from solder volume variation, scavenging and overwetting, residual stress in bilayer structures, temperature, structure dimension, solder pad warpage, hinge play, and polysilicon residual stress. Guidelines on increasing the precision of assemblies are given.

Several novel examples of multiple joint solder self-assembled MEMS devices and accessories are developed. These novel examples, each projects in their own right, are solder self-assembled microrobot legs, resistive point heaters, an axial flow fan, fiber optic cable gripper, electrostatic switches, and micro containers.

This work will serve as a template or starting point in the design and manufacture of future complex solder self-assembled MEMS. This work is essential for product control and design feasibility determination in current MEMS research and the future commercialization of complex solder self-assembled MEMS.

"This most elegant system of the sun, planets, and comets could not have arisen without the design and dominion of an intelligent and powerful being. And if the fixed stars are the centers of similar systems, they will all be constructed according to a similar design and subject to the dominion of *One*, ..." †

... To *Him*

† Sir Isaac Newton, *Philosophiae Naturalis Principia Mathematica*, 3<sup>rd</sup> ed., Will. & Jno. Innys, Printers to the Royal Society, 1726. (Translation provided by I. Bernard Cohen)

## **ACKNOWLEDGEMENTS**

I would like to thank the Defense Advanced Research Projects Agency (DARPA) and Air Force Research Laboratory, Air Force Materiel Command, USAF, under agreement number F30602-98-1-0219 for sponsoring this work. I would also like to thank my advisor Dr. Victor M. Bright for his mentorship again. Victor's trust, kindness, and respect for me did not go unappreciated. It is my hope that my future actions, as his colleague, make him proud. Many thanks to my dissertation committee members Drs. Y. C. Lee, Martin L. Dunn, Ganesh Subbarayan, and John A. Neff for their extremely valuable and much welcomed constructive criticism of this work. I would like to also acknowledge my "partner in solder", Kevin Harsh, for the wonderful working relationship we had.

Most of all I would like to thank my virtuous wife is [REDACTED]. The degree of support from her can only be described by one word – love. Her love for God is like a beautiful field of flowers hidden in a mountain meadow. The Lord blessed us with twin girls, [REDACTED] and [REDACTED], on May 25, 2001, during the writing of this dissertation. [REDACTED] disregard for her own life, in the care of these blessings, must be noted here – especially in this capacity has she supported me.

## TABLE OF CONTENTS

1	Introduction.....	1-1
1.1	Definition Of A Multiple Joint Solder Self-Assembled MEMS.....	1-2
1.2	The Issues, Achievements, And Organization Of This Work .....	1-4
1.3	Publications Related To This Work.....	1-7
1.4	Summary .....	1-8
2	Background.....	2-1
2.1	Background Of Micro-Electro-Mechanical Systems (MEMS) .....	2-1
2.2	Background Of Surface Micromachining .....	2-2
2.2.1	Commercial Surface Micromachining Processes (MUMPs) .....	2-4
2.3	Solder Self-Assembly .....	2-11
2.3.1	Motivation For Solder Self-Assembly.....	2-11
2.3.2	Theoretical Background Of Solder Self-Assembly .....	2-14
2.3.3	History Of Solder Self-Assembly .....	2-22
2.4	Tolerance Analysis.....	2-25
2.4.1	Motivation For Tolerance Analysis .....	2-25
2.4.2	Theoretical Background Of Tolerance Analysis.....	2-26
2.4.2.1	Worst-Case Analysis.....	2-26
2.4.2.2	Statistical Analysis.....	2-27
2.4.2.3	Monte-Carlo Analysis.....	2-28
2.4.3	History of Tolerance Analysis .....	2-29
2.5	References.....	2-31

3	Issues In Design .....	3-1
3.1	The Two-Solder-Joint Test Structure.....	3-1
3.2	CAD Tool.....	3-7
3.3	Hinge Design .....	3-9
3.3.1	Substrate Hinge Design .....	3-11
3.3.2	Scissor Hinge Design.....	3-13
3.4	Solder Pad Design.....	3-15
3.4.1	Test Structure Solder Pad Dimensions .....	3-15
3.4.2	General Joint Level Pad Design.....	3-16
3.4.3	General Chip Level Pad Design.....	3-17
3.5	Assembly Structure Design .....	3-18
3.6	Linkage Design.....	3-19
3.7	Summary.....	3-20
3.8	References.....	3-21
4	Issues In Manufacture And Processing.....	4-1
4.1	Solder And Solder Pad Material Issues .....	4-1
4.1.1	Indium Solder On Gold Pads.....	4-2
4.1.2	60In/40Pb Solder On Gold Pads .....	4-3
4.1.3	63Sn/37Pb Solder On Au Pads .....	4-4
4.2	Deposition Techniques and Processes .....	4-5
4.3	High Yield Assembly Process .....	4-8
4.3.1	Pre-Release .....	4-8
4.3.2	Preflow .....	4-8
4.3.3	Release .....	4-13
4.3.4	Reflow.....	4-13

4.4	Chemical And Temperature Issues .....	4-16
4.5	Failure Issues .....	4-19
4.5.1	Scavenging & Overwetting.....	4-19
4.5.2	Preflux Wetting .....	4-27
4.5.3	Roll-Off.....	4-27
4.5.4	Unreleased Solder Joints.....	4-29
4.6	Summary.....	4-30
4.7	References.....	4-31
5	Issues in Modeling .....	5-1
5.1	Solder Angle Modeling .....	5-1
5.2	Modeling Deformation .....	5-20
5.2.1	Deformation Of A Bilayer Structure Due To Internal Residual Stress And Stress Due To Misfit Strain .....	5-22
5.2.2	Deformation Of A Single Layer Structure Due To Internal Residual Stress Only.....	5-24
5.2.3	Deformation Of Polysilicon Due To Solder .....	5-25
5.3	N-hinge Model .....	5-26
5.3.1	General Overview Of The Assembly Function Algorithm.....	5-27
5.3.2	Specific Description Of The Assembly Function Algorithm.....	5-30
5.4	Summary.....	5-35
5.5	References.....	5-35
6	Issues In Assembly Precision .....	6-1
6.1	The Precision Issues That Are Not Being Considered .....	6-1
6.2	The Precision Issues That Are Being Considered.....	6-2
6.2.1	Solder Volume Variation .....	6-2

6.2.2	Solder Pad Size Variation By Scavenging And Overwetting .....	6-6
6.2.3	Variation Of Structure Deformation Due To Residual Stresses.....	6-6
6.2.3.1	Residual Stress Of A Bilayer Structure: Gold On Poly2 .....	6-7
6.2.3.2	Residual Stress Of A Single Layer Structure.....	6-8
6.2.3.3	Deformation Of Poly2 Due To Solder.....	6-9
6.2.4	Hinge Location Variation .....	6-9
6.2.5	Variation Of Structure Dimensions .....	6-10
6.2.6	Temperature Variation.....	6-10
6.3	Comparison Of Model Predictions With Experimental Measurements .....	6-11
6.3.1	8 Mil Test Structures.....	6-13
6.3.2	8 Mil Warp Test Structures.....	6-16
6.3.3	4 Mil Warp Test Structures.....	6-19
6.3.4	Tabular Comparison Of Experimental Data With Model Predictions .....	6-21
6.4	Hierarchy And Impact Of Contributors To The Precision Of An Assembly .....	6-22
6.5	Summary .....	6-28
6.6	References.....	6-31
7	Issues In The Realization Of Specific Complex Solder Self-Assembled MEMS .....	7-1
7.1	Solder Assembled Arrays Of Microrobot Legs Using Photolithographically Patterned Indium On Gold .....	7-1
7.2	Normally Open And Closed, Electrostatically Actuated, Solder Assembled Switches.....	7-4
7.3	Resistive Point Heaters For MEMS Remote Solder Self-Assembly .....	7-7

7.4	Solder Self-Assembled Micro Axial Flow Fan Driven By A Scratch-Drive-Actuator Rotary-Motor.....	7-8
7.5	Solder Assembled Fiber Optic Cable Gripper .....	7-8
7.6	Micro Channels & Packages.....	7-10
7.7	References.....	7-13
8	Conclusions.....	8-1
8.1	Limitations .....	8-2
8.2	Future Paths And Improvements .....	8-3
	<b>Appendix A Equipment and Procedures.....</b>	<b>A-1</b>
A.1	Dicing Saw.....	A-1
A.2	Scanning Electron Microscope .....	A-3
A.3	Computing .....	A-5
A.4	Image Recording And Photography.....	A-5
A.5	MEMS Manipulation And Electrical Characterization.....	A-6
A.6	Reflow Station .....	A-7
A.7	Plasma Cleaner .....	A-9
A.8	Thermal Evaporator .....	A-10
A.9	Sacrificial Oxide Etching (Also Known As "Release") And Drying .....	A-12
	A.9.1 Pre-Release And Release Procedures .....	A-12
	A.9.2 Drying Procedures .....	A-14
A.10	Wirebonding .....	A-16
A.11	Optical Measurement.....	A-16
A.12	Interferometric Microscope .....	A-19
A.13	Photolithography.....	A-21
	A.13.1 Mask Making .....	A-22

A.13.2 Photoresist Processing .....	A-23
A.14 Photoresist Assembly Of MEMS .....	A-26
Appendix B Model Code .....	B-1
B.1 assybuild.m .....	B-1
B.2 angsolv.m.....	B-3
B.3 geoequations.m .....	B-4
B.4 getshape.m .....	B-5
B.5 assyio_2h8.m .....	B-6
B.6 assyio_2h8warp.m.....	B-9
B.7 assyio_2h4warp.m.....	B-12
Appendix C Selected Published Papers .....	C-1
C.1 Solder Angle Modeling .....	C-1
C.2 Solder Self-Assembled Microrobot Legs .....	C-14
C.3 Resistive Point Heater For MEMS Remote Solder Self-Assembly .....	C-20
C.4 Micro Fan.....	C-32
Appendix D Experimental Results .....	D-1
D.1 8 Mil Test Structures .....	D-2
D.2 8 Mil Warp Test Structures.....	D-7
D.3 4 Mil Warp Test Structures.....	D-12
Appendix E CAD Design Summaries .....	E-1
E.1 MUMPs 27.....	E-1
E.2 MUMPs 29.....	E-2
E.3 MUMPs 32.....	E-3
E.4 MUMPs 33.....	E-4
E.5 MUMPs 34.....	E-5

E.6	MUMPs 35.....	E-7
E.7	MUMPs 36.....	E-12
E.8	MUMPs 38.....	E-17
E.9	MUMPs 39.....	E-20
E.10	MUMPs 40.....	E-22
E.11	MUMPs 42.....	E-24

## LIST OF TABLES

Table 2-1:	Comparison between the type of microstructure and manner of solder self-assembly used by the Imperial College group and this work.....	2-24
Table 3-1:	Important mask file parameters for the MUMPs process .....	3-7
Table 4-1:	Comparison of solder material, solder pad, and flux combinations tried during this research.....	4-2
Table 4-2:	Estimate of degree of scavenging and overwetting. A minus sign indicates overwetting.....	4-26
Table 6-1:	Tabulation of measured solder sphere diameter parameters.....	6-3
Table 6-2:	Tabulated comparison of estimated mean and standard deviation of experimental measurements with model predictions in the x and y directions.....	6-21
Table 6-3:	Tabulation of average impacts ranked from greatest to least for the 8 mil test structure. The number "1" is being the greatest. ....	6-23
Table 6-4:	Tabulation of average impacts ranked from greatest to least for the 8 mil warp test structure.....	6-23
Table 6-5:	Tabulation of average impacts ranked from greatest to least for the 4 mil warp test structure.....	6-24
Table 6-6:	Tabulation of average sensitivities and diminishing statistical tolerance of the 8 mil warp test structure.....	6-25

## LIST OF FIGURES

- Figure 1-1: A scanning electron micrograph of the world's first man-made micro-sized axial flow fan..... 1-3
- Figure 1-2: A SEM and captured video image of a fiber optic cable gripper..... 1-3
- Figure 2-1: Nathanson et al.'s resonant gate transistor [2]..... 2-3
- Figure 2-2: Depiction of a side profile of one of Howe et al.'s suspended beams..... 2-4
- Figure 2-3: Captured video images of (left) a section of a microelectronics chip containing transistor circuits and wiring; and (middle/right) sections of a MEMS chip showing gears, motors comprised of electro-thermal actuators, hinged mirror, and microtweezers alongside a human hair for size perspective [5]..... 2-5
- Figure 2-4: Depiction of the available layers and features in the MUMPs surface micromachining process..... 2-7
- Figure 2-5: Depiction of the available layers and features in the SUMMiT surface micromachining process..... 2-10
- Figure 2-6: Scanning electron micrograph of a microrobot. Inset shows a closer view of one surface micromachined leg that was assembled into position by hand..... 2-12
- Figure 2-7: SEM of micromirror system [15]..... 2-13
- Figure 2-8: Depiction of solder self-assembly during reflow of solder and the basic elements of solder self-assembly, after Harsh et al. [38]..... 2-14
- Figure 2-9: Depiction of a central cross section of a molten body of solder whose volume has been reduced to the point that the body takes on an almost spherical shape. ..... 2-16
- Figure 2-10: SEM of the side view of a solidified solder joint wetted between two gold-coated polysilicon plates, a close view of a hinge, and a not to scale drawing of a gold on polysilicon solder-wettable plate pair without solder..... 2-19
- Figure 2-11: Captured sequence of video images of an actual 63Sn/37Pb solder self-assembled polysilicon plate pair

during reflow of the solder: (a) unmelted solder already prewetted across a set of two 96 $\mu\text{m}$ by 96 $\mu\text{m}$ gold wettable pads, (b-e) sequence showing free plate (left plate) rotating toward its equilibrium position, (f) molten solder joint resting at an equilibrium angle, $\alpha \approx 55^\circ$ .....	2-20
Figure 2-12: Depiction of the possible assembly angle extremes. ....	2-22
Figure 2-13: Actual images showing examples of achievable assembly angle extremes.....	2-22
Figure 3-1: CAD layout (top) and SEM (bottom) of seven variants of the 8 mil version of the test structure. ....	3-2
Figure 3-2: Different SEM views of seven variants of the 8 mil version of the test structure shown in Figure 3-1.....	3-3
Figure 3-3: Depiction of the ideal side profiles of the different variations of the non-warping test structures.....	3-4
Figure 3-4: CAD layout (top) and SEM (bottom) of seven variants of the 8 mil warped plate version of the test structure. Three of the variants shown are not assembled properly due to unreleased 45° solder pads. This figure is used as an illustration in Chapter 4. ....	3-5
Figure 3-5: CAD layout (top) and SEM (bottom) of seven variants of the 4 mil warped plate version of the test structure.....	3-6
Figure 3-6: Depiction of the different MUMPs layer combinations as viewed from L-edit. This figure is best viewed in color. ....	3-8
Figure 3-7: Comparison of CAD drawing of a substrate hinge with a SEM of same fabricated structure. This figure is best viewed in color.....	3-9
Figure 3-8: CAD drawing of a solder pad pair. ....	3-10
Figure 3-9: Depiction of a side profile of a substrate hinge arrangement at the desired assembly angle.....	3-12
Figure 3-10: CAD of properly designed substrate hinge (left) and SEM of the actual fabricated and assembled design (right). ....	3-13

Figure 3-11:	Depiction of a side profile of a scissor hinge arrangement at the desired assembly angle.....	3-14
Figure 3-12:	CAD of properly designed scissor hinge (left) and SEM of the actual fabricated and assembled design (right).....	3-15
Figure 3-13:	Captured video image of solder deposition in the form of evaporated and patterned patches of indium. ....	3-17
Figure 3-14:	SEMs of solder self-assembled MEMS demonstrating the various methods of linkages developed in this research. ....	3-20
Figure 4-1:	SEM showing whisker-like growth from the 60In/40Pb solder - gold solder pad interface.....	4-3
Figure 4-2:	Depiction of different methods of commercial solder deposition.....	4-6
Figure 4-3:	Example of flattened 8 mil diameter manufactured solder sphere disk placement. Three solder pad sizes are indicated 217 $\mu\text{m}$ x 217 $\mu\text{m}$ , 131 $\mu\text{m}$ x 131 $\mu\text{m}$ , and 70 $\mu\text{m}$ x 70 $\mu\text{m}$ .....	4-7
Figure 4-4:	Captured video image of an unreleased preflowed chip containing an array of 8 mil version test structures. ....	4-10
Figure 4-5:	SEMs of an unreleased, preflowed chip containing an array of 8 mil version test structures, showing close views of individual solder joints, and solder pad dimensions. ....	4-11
Figure 4-6:	Captured video image of an unreleased, preflowed chip containing an array of 4 mil warp version test structures. SEMs show close views of individual solder joints, and solder pad dimensions. ....	4-12
Figure 4-7:	SEM of an unreleased, preflowed chip containing an array of 8 mil warp version test structures.....	4-13
Figure 4-8:	Sequence of captured video images showing reflow of a chip containing an array of seven 8 mil version test structures. The total time of assembly, from (a) to equilibrium (h), is 45 seconds. The time duration of images (a) – (f) is 28 seconds. ....	4-15
Figure 4-9:	Legend for the following figures describing the chemical and temperature history during the processing	

of a multiple joint solder self-assembled MEMS. This figure is best viewed in color.....	4-16
Figure 4-10: Chemical and temperature history during the prerelease (30 s) / release (4 m) and drying of a multiple joint solder self-assembled MEMS. This figure is best viewed in color.....	4-17
Figure 4-11: Chemical and temperature history during the preflow of a multiple joint solder self-assembled MEMS. This figure is best viewed in color.....	4-18
Figure 4-12: Chemical and temperature history during the reflow of a multiple joint solder self-assembled MEMS. This figure is best viewed in color.....	4-18
Figure 4-13: Depiction of competing surface tension forces at the perimeter of a solder joint (not to scale). .....	4-20
Figure 4-14: SEMs showing a mild example of scavenging by an 8 mil diameter equivalent volume of solder, after preflow, and before final release and reflow.....	4-22
Figure 4-15: SEM showing an aggressive case of scavenging by a 4 mil diameter equivalent volume of solder after reflow. This view is from behind the solder pads where the dark area, outlined in white, is where the solder is still attached to the pad. ....	4-23
Figure 4-16: SEM showing overwetting of 135° 8 mil solder pads (left) and a 90° 8 mil solder pads (right).....	4-23
Figure 4-17: SEM showing overwetting of a 135° 8 mil solder pad that occurred during preflow.....	4-25
Figure 4-18: SEM showing a catastrophic example of overwetting on 8 mil warp version test structures. ....	4-26
Figure 4-19: SEM showing an extreme example of roll-off due to contamination.....	4-29
Figure 5-1: SEM of the side view (left) and front view (right) of a solidified solder joint showing important parameters that will be referred to throughout the rest of this work. ....	5-1
Figure 5-2: Geometric equilibrium angle prediction model used by Syms, where $\gamma$ is the surface tension coefficient, $\beta$ is the angle of curvature, $\alpha$ is the angle between the solder	

pads of length  $l$ ,  $P$  is the internal pressure of the liquid,  
 $h$  is the height of the initial electroplated solder volume,  
and  $T_{NET}$  is the net torque per unit length (into the page)  
between the internal pressure and surface tension..... 5-4

- Figure 5-3: Comparison of Surface Evolver equilibrium angle predictions to Syms's model (top), and a plot of Syms's radius of curvature ..... 5-5
- Figure 5-4: Depiction of important parameters in the development of the three-dimensional geometric solder model. This figure is best viewed in color..... 5-7
- Figure 5-5: Captured video images showing two-dimensional depictions of missing spherical sections from spheres superimposed on solder joints..... 5-10
- Figure 5-6: Pictorial equation showing the modeling of a solder joint shape by the volume of a sphere – 2 x the volume of a section of sphere ..... 5-10
- Figure 5-7: Plot comparing geometric model equilibrium angle predictions to *Surface Evolver* (\*) predictions for different square solder pad lengths while keeping a fixed volume of solder equivalent to an 8 mil diameter sphere ..... 5-12
- Figure 5-8: Plot of error between geometric model equilibrium angle predictions and *Surface Evolver* predictions for different square solder pad lengths while keeping a fixed volume of solder equivalent to an 8 mil diameter sphere ..... 5-12
- Figure 5-9: Plot showing the behavior of the radius of curvature,  $R_w$ , of the geometric model for different square solder pad lengths while keeping a fixed volume of solder equivalent to an 8 mil diameter sphere. The radius of an 8 mil sphere is also plotted as a straight line..... 5-13
- Figure 5-10: Plot comparing geometric model equilibrium angle predictions to *Surface Evolver* (\*) predictions for different square solder pad lengths while keeping a fixed volume of solder equivalent to a 4 mil diameter sphere ..... 5-14
- Figure 5-11: Plot showing the behavior of the radius of curvature,  $R_w$ , of the geometric model for different square solder pad lengths while keeping a fixed volume of solder

equivalent to a 4 mil diameter sphere. The radius of a 4 mil sphere is also plotted as a straight line. ....	5-14
Figure 5-12: Plot comparing corrected geometric model equilibrium angle predictions to <i>Surface Evolver</i> (*) predictions for different square solder pad lengths while keeping a fixed volume of solder equivalent to an 8 mil diameter sphere. ....	5-17
Figure 5-13: Plot of error between corrected geometric model equilibrium angle predictions and <i>Surface Evolver</i> predictions for different square solder pad lengths while keeping a fixed volume of solder equivalent to an 8 mil diameter sphere. ....	5-18
Figure 5-14: Plot comparing corrected geometric model equilibrium angle predictions to <i>Surface Evolver</i> (*) predictions for different square solder pad lengths while keeping a fixed volume of solder equivalent to a 4 mil diameter sphere. ....	5-18
Figure 5-15: Plot of error between corrected geometric model equilibrium angle predictions and <i>Surface Evolver</i> predictions for different square solder pad lengths while keeping a fixed volume of solder equivalent to a 4 mil diameter sphere. ....	5-19
Figure 5-16: Graph of the two-dimensional solution space when the corrected geometric model equations are posed as a least squares minimization problem. The crossing of the red lines locates the minimum, in this case at an equilibrium angle of 90°, while $R_w$ is kept constant at the value that it would have at the solution. Furthermore, the volume of solder is equivalent to an 8 mil diameter sphere. ....	5-19
Figure 5-17: Closer view of the location of the minimum of Figure 5-16. ....	5-20
Figure 5-18: Depiction of nomenclature and conventions used in the derivation of the deformation models in the following sections. ....	5-21
Figure 5-19: Depiction of the nature of the assembly function. ....	5-26
Figure 5-20: A block diagram of the assembly function organization. ....	5-28

Figure 5-21:	An example of a plate matrix defining a warp version of the test structure.....	5-30
Figure 5-22:	The Assembly Builder algorithm.....	5-34
Figure 6-1:	Captured video images used to measure the actual diameters of the manufactured solder spheres.....	6-3
Figure 6-2:	Histogram of 4 mil ball measurements.....	6-4
Figure 6-3:	Histogram of 8 mil ball measurements.....	6-4
Figure 6-4:	Plot of equilibrium angle while varying square solder pad dimensions and varying the solder ball diameter by $4.3878 \pm 0.4491$ mil.....	6-5
Figure 6-5:	Plot of equilibrium angle while varying square solder pad dimensions and varying the solder ball diameter by $8.4547 \pm 1.0217$ mil.....	6-5
Figure 6-6:	Output of the Zygo interferometric microscope showing the measurement of radius of curvature of gold on poly2 bilayer structure.....	6-8
Figure 6-7:	Output of the Zygo interferometric microscope showing the measurement of radius of curvature of solder on poly2.....	6-9
Figure 6-8:	Legend for the result figures.....	6-11
Figure 6-9:	90/45 8 mil variant.....	6-14
Figure 6-10:	90/90 8 mil variant.....	6-15
Figure 6-11:	90/45 8 mil warp variant.....	6-17
Figure 6-12:	45/135 8 mil warp variant.....	6-18
Figure 6-13:	90/45 4 mil warp variant.....	6-20
Figure 6-14:	Depiction of the end position ( $P$ ) of a two-joint structure.....	6-27
Figure 7-1:	SEM of an array of microrobot legs assembled using the surface tension of molten solder.....	7-2
Figure 7-2:	A close view of one of the robot leg assemblies.....	7-2

Figure 7-3:	A SEM of a different design of solder self-assembled microrobot leg.....	7-3
Figure 7-4:	Captured video images of the patterned indium before release of the microrobot legs.....	7-4
Figure 7-5:	(a) SEM of a normally closed (N.C.) and two normally open (N.O.) electrostatically actuated switches and (b) a top view of the same switches. ....	7-5
Figure 7-6:	Depiction of a normally closed (N.C.) and a normally open (N.O.) electrostatically actuated switches.....	7-6
Figure 7-7:	SEM of a normally closed electrostatically actuated switches.....	7-6
Figure 7-8:	SEM of a fiber optic cable gripper assembled with 8 mil 63Sn/37Pb manufactured solder spheres. ....	7-9
Figure 7-9:	SEM of another fiber optic cable gripper assembled with 8 mil 63Sn/37Pb manufactured solder spheres.....	7-9
Figure 7-10:	Captured video images of a preflowed micro package.....	7-11
Figure 7-11:	SEM of reflowed micro packages.....	7-12
Figure 7-12:	Close views of reflowed micro packages.....	7-12
Figure 7-13:	SEM of a proposed section of a micro channel assembled with two 63Sn/37Pb 8 mil manufactured solder spheres.....	7-13
Figure A-1:	Dicing Saw.....	A-1
Figure A-2:	R. J. Lee Scanning Electron Microscope.....	A-3
Figure A-3:	Comparison between SEMs: SED (left) and quad-backscatter (right). .....	A-4
Figure A-4:	ISI scanning electron microscope.....	A-5
Figure A-5:	Probe Station.....	A-6
Figure A-6:	Reflow Station. ....	A-8
Figure A-7:	Reflow Station close views of: manufactured solder sphere storage (left) and heating stage (right).....	A-8
Figure A-8:	Plasma Cleaner. ....	A-10

Figure A-9: Thermal Evaporator.....	A-11
Figure A-10: Release station in chemical hood (top) and critical point dryer (below).....	A-15
Figure A-11: Wirebonder. ....	A-16
Figure A-12: Optical Measurement System. ....	A-17
Figure A-13: Captured video image of optical calibration slide. ....	A-18
Figure A-14: Captured video image of a 135°/135° two-solder-joint structure exemplifying the measurement of x-y position of the end of the last plate with respect to the first solder joint hinges.....	A-19
Figure A-15: Zygo Interferometric Microscope. ....	A-21
Figure A-16: UV Flood Exposure Machine. ....	A-23
Figure A-17: Photoresist spinner, chemicals, hotplate, chemical hood.....	A-23
Figure A-18: Mask Aligner. ....	A-24
Figure A-19: Depiction of chip arrangement on a 2 inch silicon wafer for photolithography on 2 mm x 2 mm chips. ....	A-25
Figure A-20: SEM of photoresist assembled MEMS plate. ....	A-27
Figure D-1: Legend for the following plots.....	D-1
Figure D-2: 90/135 8 mil variant.....	D-2
Figure D-3: 135/135 8 mil variant.....	D-3
Figure D-4: 135/90 8 mil variant.....	D-4
Figure D-5: 135/45 8 mil variant.....	D-5
Figure D-6: 45/135 8 mil variant.....	D-6
Figure D-7: 90/90 8 mil warp variant.....	D-7
Figure D-8: 90/135 8 mil warp variant.....	D-8
Figure D-9: 135/135 8 mil warp variant.....	D-9
Figure D-10: 135/90 8 mil warp variant.....	D-10

Figure D-11:	135/45 8 mil warp variant.....	D-11
Figure D-12:	90/90 4 mil warp variant.....	D-12
Figure D-13:	90/135 4 mil warp variant.....	D-13
Figure D-14:	135/135 4 mil warp variant. (No Data).....	D-14
Figure D-15:	135/90 4 mil warp variant.....	D-15
Figure D-16:	135/45 4 mil warp variant.....	D-16
Figure D-17:	45/135 4 mil warp variant.....	D-17
Figure E-1:	MUMPs 27; 2 mm × 2 mm; microrobot leg array for thermally evaporated indium solder self-assembly.....	E-1
Figure E-2:	MUMPs 29 Die 1; 2 mm × 2 mm; microrobot leg array for thermally evaporated indium solder self-assembly, more compliant locking tabs, and metallization only on the solder pads. ....	E-2
Figure E-3:	MUMPs 29 Die 2; 2 mm × 2 mm; microrobot leg array for gold on polysilicon bilayer self-assembly.....	E-2
Figure E-4:	MUMPs 32 Die 1; 2 mm × 2 mm; microrobot leg array for gold on polysilicon bilayer and scratch drive self-assembly, corrugated gold on polysilicon thermally actuated bilayer cantilevers, and array of simple plates for thermally evaporated indium solder self-assembly.....	E-3
Figure E-5:	MUMPs 32 Die 2; 2 mm × 2 mm; polysilicon and PSG casts for electrostatically actuated SiCN cantilevers and corrugated gold on polysilicon thermally actuated bilayer cantilevers. ....	E-3
Figure E-6:	MUMPs 32 Die 3; 2 mm × 2 mm; polysilicon and PSG casts for electrostatically actuated SiCN cantilevers and corrugated gold on polysilicon thermally actuated bilayer cantilevers. The polysilicon cast has breakaway tethers.....	E-4
Figure E-7:	MUMPs 33 Die 1; 2 mm × 2 mm; normally open electrostatically actuated switches for 8 mil solder self-assembly.....	E-4

Figure E-8:	MUMPs 33 Die 2; 2 mm × 2 mm; polysilicon and PSG casts for electrostatically actuated SiCN supported membranes.....	E-5
Figure E-9:	MUMPs 34 Die 1; 2 mm × 2 mm; point heaters.....	E-5
Figure E-10:	MUMPs 34 Die 2; 2 mm × 2 mm; push-up, pull-up, and tandem linkage demonstrations for 8 mil solder self-assembly.....	E-6
Figure E-11:	MUMPs 34 Die 3; 2 mm × 2 mm; fiber optic cable grippers. ....	E-6
Figure E-12:	MUMPs 34 Die 4; 2 mm × 2 mm; microrobot leg array for scratch drive self-assembly. ....	E-7
Figure E-13:	MUMPs 35 Die 1; 2 mm × 2 mm; solder self-assembled micro axial flow fan. Solder pad and hinge area design – Kladitis. Rotary scratch drive motor and wing design – Linderman. ....	E-7
Figure E-14:	MUMPs 35 Die 2; 2 mm × 2 mm; simple mirrors for vertically deflecting electro-thermal actuator assembly – top half. Bottom half belongs to Kevin Harsh. ....	E-8
Figure E-15:	MUMPs 35 Die 3; 2 mm × 2 mm; 8 mil two-solder-joint test structure.....	E-8
Figure E-16:	MUMPs 35 Die 4; 2 mm × 2 mm; 8 mil warp two-solder-joint test structure.....	E-9
Figure E-17:	MUMPs 35 Die 5; 2 mm × 2 mm; 4 mil warp two-solder-joint test structure.....	E-9
Figure E-18:	MUMPs 35 Die 6; 2 mm × 2 mm; 4 mil two-solder-joint test structure.....	E-10
Figure E-19:	MUMPs 35 Die 7; 2 mm × 2 mm; normally open and normally closed electrostatically actuated switches for 8 mil solder self-assembly. ....	E-10
Figure E-20:	MUMPs 35 Die 8; 2 mm × 2 mm; mechanical NAND gates, NOR gates, XOR circuit, and 4 mil and 8 mil solder self-assembled thermostats.....	E-11

- Figure E-21: MUMPs 36 Die 1; 4 mm × 2 mm; 2-D micro conveyer with gold on polysilicon thermally actuated bilayer cantilevers as conveyer arms. ....E-12
- Figure E-22: MUMPs 36 Die 2; 2 mm × 2 mm; jumping robot powered by gold on polysilicon bifurcating plates. ....E-13
- Figure E-23: MUMPs 36 Die 3; 2 mm × 2 mm; point heaters with power optimized heaters and larger attached structure. ....E-13
- Figure E-24: MUMPs 36 Die 4; 2 mm × 2 mm; array of microrobot legs for chain and stiff beam tethered scratch drive actuator self-assembly. Bushings stuck to nitride. ....E-14
- Figure E-25: MUMPs 36 Die 5; 2 mm × 2 mm; 8 mil solder self-assembling box and simple plates where solder self-assembly is performed on the back side after flip chipping this chip to another substrate. ....E-14
- Figure E-26: MUMPs 36 Die 6; 2 mm × 2 mm; point heaters with power optimized heaters and larger linkage attached structures. ....E-15
- Figure E-27: MUMPs 36 Die 7; 2 mm × 2 mm;  $\mu$ packages. ....E-15
- Figure E-28: MUMPs 36 Die 8; 2 mm × 2 mm; 4 mil solder self-assembled electro-thermally actuated gold on polysilicon bilayer grippers. ....E-16
- Figure E-29: MUMPs 38 Die 1; 4 mm × 4 mm; solder self-assembled microrobot where the solder is deposited on the leg solder pads using mask-less electroplated solder. In the unreleased state, the whole robot is covered in PSG except for the solder pads and bond pads. ....E-17
- Figure E-30: MUMPs 38 Die 2; 4 mm × 2 mm; 8 mil two-solder-joint test structure with solder pads that span the whole width of the plate structures. ....E-18
- Figure E-31: MUMPs 38 Die 3; 2 mm × 2 mm; solder self-assembled simple plates where the solder is deposited on the solder pads using mask-less electroplated solder. In the unreleased state, the whole die is covered in PSG except for the solder pads and bond pads. ....E-19
- Figure E-32: MUMPs 38 Die 4; 2 mm × 2 mm; solder self-assembled simple plates where the solder is deposited on the

solder pads using electroplated solder. Unlike the previous version, these solder pads are not connected to the substrate.....	E-19
Figure E-33: MUMPs 38 Die 5; 2 mm × 2 mm; mechanical NAND gates, NOR gates, and XOR circuit where the gate spring compliance is varied by number of coils. ....	E-20
Figure E-34: MUMPs 39 Die 1; 2 mm × 2 mm; 8 and 4 mil solder self-assembled thermostats. ....	E-20
Figure E-35: MUMPs 39 Die 2; 2 mm × 2 mm; mechanical NAND gates, NOR gates, and XOR circuit where the gate spring compliance is varied by polysilicon layer.....	E-21
Figure E-36: MUMPs 39 Die 3; 2 mm × 2 mm; normally open and normally closed electrostatically actuated switches, for 8 mil solder self-assembly, with improved mechanical stops and modified wiring.....	E-21
Figure E-37: MUMPs 39 Die 4; 2 mm × 2 mm; 8 mil two-solder-joint test structure.....	E-22
Figure E-38: MUMPs 40 Dice 1-4; 2 mm × 2 mm; 4 mil and 8 mil warp/non warped two-solder-joint test structures.....	E-22
Figure E-39: MUMPs 40 Die 5; 2 mm × 2 mm; point heaters with inductive angular position sensors and circular mirrors. ....	E-23
Figure E-40: MUMPs 40 Die 6; 2 mm × 2 mm; array of bifurcating beams with ratcheted pre-tensioner. ....	E-23
Figure E-41: MUMPs 40 Die 7; 2 mm × 2 mm; normally open and normally closed electrostatically actuated switches, for 8 mil solder self-assembly, with less stiff flexures. ....	E-24
Figure E-42: MUMPs 42 Die 1; 2 mm × 2 mm; array of microrobot legs for chain and stiff beam tethered scratch drive actuator self-assembly. Bushings not stuck to nitride.....	E-24

## 1 Introduction

Using the surface tension of molten solder to assemble micro-sized structures or micro-electro-mechanical systems (MEMS), otherwise known as "solder self-assembly" is a recent development. Complex three-dimensional assemblies, previously not realizable, can now be realized using surface micromachined MEMS and solder assembly. Not only can complex or non-complex assemblies be realized using solder self-assembly, but realized by adopting means already established commercially for mass production.

Previous work by Syms demonstrates single joint solder self-assembled bulk micromachined structures. Syms's bulk micromachined structures consist of one releaseable layer, therefore, limiting achievable complexity, relative to surface micromachined structures. Furthermore, the low yield of Syms's process may be due to the lack of hinges and defined solder pads. More details and references concerning the work of Syms is given in Chapter 2. Prior work done by Harsh concentrated on single joint solder self-assembled surface micromachined structures. Furthermore, Harsh's assembly process is also low yield. More details and references concerning the work of Harsh is given in Chapters 2 and 6.

This work is the first in the world to quantify or address the known entirety of major issues that go into realizing multiple joint solder self-assembled MEMS. The MEMS are fabricated using polysilicon surface micromachining and the soldering is done with eutectic Sn/Pb solder on gold solder pads. Next, I will define what the descriptor, "multiple joint", means. After the definitions, I will specifically list the "issues" and achievements addressed in this work.

## **1.1 Definition Of A Multiple Joint Solder Self-Assembled MEMS**

This work defines a "multiple joint solder self-assembled MEMS" as a microstructure or system of microstructures requiring more than one solder joint for proper assembly and function. The multiple solder joints may be arranged in parallel, series, or both. A system consisting of more than one microstructure assembled into proper position by one solder joint, through linkages, will also be defined as a multiple joint solder self-assembled MEMS. The issues involved in realizing the single solder joint linkage connected system will only be briefly addressed in this work.

The following are two examples of multiple joint solder self-assembled MEMS which typify the two general categories of parallel and series assemblies. Figure 1-1 is a scanning electron micrograph (SEM) of the world's first man-made micro-sized axial flow fan -- a multiple joint solder self-assembled MEMS requiring eight solder joints, arranged in a parallel fashion, to assemble for proper fan blade positioning and flow function. Figure 1-2 is a SEM and captured video image of a fiber optic cable gripper. Each gripper finger is a multiple joint solder self-assembled MEMS requiring three solder joint, arranged in a series fashion, to assemble for proper gripper finger positioning.

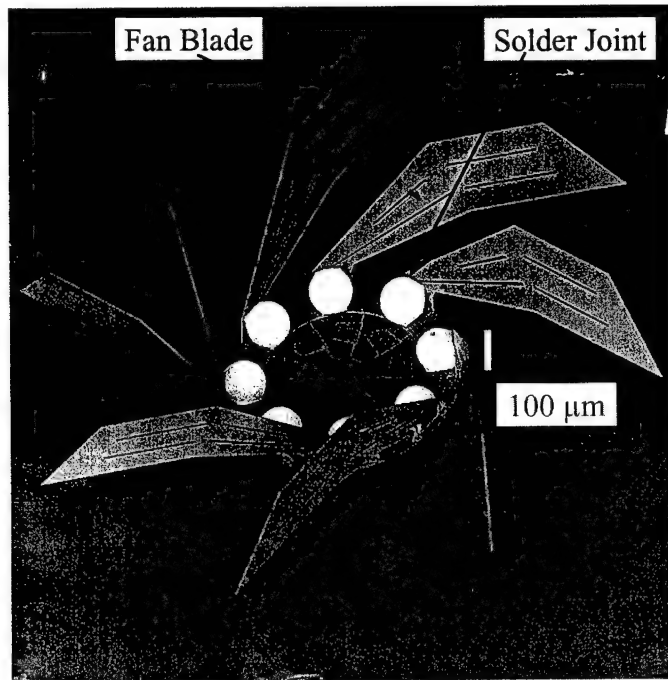


**Figure 1-1:** A scanning electron micrograph of the world's first man-made micro-sized axial flow fan.

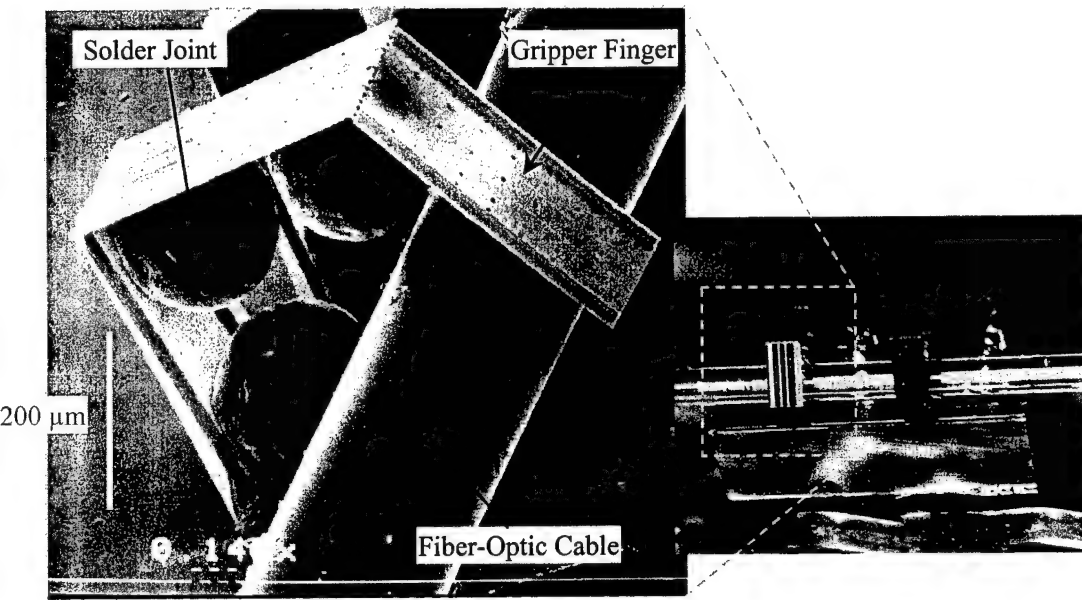


**Figure 1-2:** A SEM and captured video image of a fiber optic cable gripper.

## **1.2 The Issues, Achievements, And Organization Of This Work**

Overall, this work is based on the results of over 866, by hand, pick and place solder joints. The complexity of the issues concerning series solder joint systems, as exemplified in Figure 1-2, are usually more complex than those concerning parallel solder joint systems. Furthermore, the issues involved with the other aforementioned types of multiple joint solder self-assembled MEMS are either the same or a subset of the issues involved with series solder joint systems. Thus, this work features experiments on series connected, two-solder-joint microstructures. 259 two joint test structures were designed, assembled, and measured for the purpose of revealing the design and processing requirements of multiple joint solder self-assembled MEMS. Another purpose for the two joint test structures is to validate an assembly model of series connected n-solder joint, microstructures. The model is used to make general predictions regarding the assembly precision of multiple joint solder self-assembled MEMS and used as a modeling tool for specific multiple joint solder self-assembled MEMS designs.

Next, I will present the specific issues and achievements addressed in this work, by chapter, in outline form. The following outline will also serve as a description of the organization of this work.

### **I. Chapter 2 – Background**

- a) Overview of MEMS
- b) Comprehensive overview of surface micromachining – the method used to fabricate the microstructures in this work

- c) Comprehensive overview of solder self-assembly – the method used to assemble the structures in this work
- d) Comprehensive overview of tolerance analysis -- a set of mathematical techniques used to estimate the amount of variability in an assembly due to individual component variations.

## **II. Chapter 3 – Issues In Design**

- a) The issues encountered when designing a multiple joint solder self-assembled MEMS
- b) The design of the two joint test structure
- c) Guidelines for successful solder-joint substrate and scissor hinge designs
- d) Guidelines for successful solder pad, structure, and linkage design and placement

## **III. Chapter 4 – Issues In Manufacture And Processing**

- a) The issues in manufacture and processing, where essentially, the "how to" of making a multiple joint solder self-assembled MEMS is described
- b) Development of a high yield (94.3%) pre-release, solder preflow, release, and solder reflow sequence suitable for multiple joint solder self-assembled, commercially fabricated surface micromachined MEMS

- c) Quantification and qualification of issues that cause solder joint failures such as: scavenging, overwetting, preflux wetting, roll-off, and unreleased solder pads

#### **IV. Chapter 5 – Issues in Modeling**

- a) The issues involved in modeling a multiple joint solder self-assembled MEMS
- b) Development of simple three-dimensional analytical models for predicting the angle of assembled solder joints
- c) Development of a general model for series connected, multiple joint, solder self-assembled structures – model verified by the assembly and measurement of 259, two joint, solder self-assembled test structures

#### **V. Chapter 6 – Issues In Assembly Precision**

- a) First application of classical tolerance analysis techniques to solder self-assembled structures
- b) Quantification of the affects of solder volume variation, scavenging and overwetting, residual stress in a bilayer structure, temperature, structure dimension, solder pad warpage, hinge play, and polysilicon residual stress on the precision of a multiple joint solder self-assembled structure

#### **VI. Chapter 7 – Issues In The Realization of Specific Complex Solder Self-Assembled MEMS**

- a) Examples of the manufacture of specific, novel, solder self-assembled devices such as solder self-assembled microrobot legs, resistive point

heaters, axial flow fan, fiber optic cable gripper, electrostatic switches, and micro containers

The remainder of this work includes conclusions in Chapter 8. Equipment and procedures used in this research are detailed in Appendix A. Hardcopies of all the code, used to implement model algorithms for this work, are provided in Appendix B. As a convenience to the reader and myself, Appendix C provides copies of some of my published papers that are related to this work. Appendix D contains experimental results and tabulated model predictions for the two joint test structures used in this research. And finally, I have included summaries of all the CAD designs submitted for fabrication during this research, in Appendix E, which, include some novel inventions not specifically related to this work.

### **1.3 Publications Related To This Work**

The following list contains all of my published works relating to this research. This list is included here for the convenience of the reader and to stress the importance of this work and to provide an up front comprehensive picture of this work. [2], [4], [6], and [7] are provided in Appendix C.

- [1] P. E. Kladitis, V. M. Bright, K. F. Harsh, and Y. C. Lee, "Prototype microrobots for micro positioning in a manufacturing process and micro unmanned vehicles," *Technical Digest of 12th IEEE International Conference on MicroElectroMechanical Systems – MEMS '99*, pp. 570-575, Orlando, FL, Jan. 17-21, 1999.
- [2] P. E. Kladitis, K. F. Harsh, V. M. Bright, and Y. C. Lee, "Three-Dimensional Modeling of Solder Shape for the Design of Solder Self-Assembled Micro-electro-mechanical Systems," *Proc. 1999 ASME*

- International Mechanical Engineering Congress and Exposition MEMS Symposium*, Nashville, TN, MEMS-Vol. 1, pp. 11-18, Nov. 1999.
- [3] K. F. Harsh, P. E. Kladitis, M. A. Michalicek, J. L. Zhang, W. Zhang, A. Tuantranont, V. M. Bright, Y. C. Lee, "Solder self-alignment for optical MEMS," *Proceedings of the 1999 Lasers and Electro-Optics Society Annual Meeting – LEOS*, pp. 860-861, Nov. 8-11, 1999.
  - [4] P. E. Kladitis and V. M. Bright, "Prototype microrobots for micro positioning and micro unmanned vehicles," *Sensors and Actuators A.*, vol. 80, pp. 132-137, 2000.
  - [5] K. F. Harsh, P. E. Kladitis, Y. H. Zhang, M. L. Dunn, V. M. Bright, and Y. C. Lee, "Tolerance and Precision Study for Solder Self-Assembled MEMS," *Proceedings of the 2000 Micro-Opto-Electro-Mechanical Systems Conference – MOEMS 2000*, vol. 4075, pp. 173-184, Glasgow, Scotland, May 22-25, 2000.
  - [6] P. E. Kladitis and V. M. Bright, "Novel Resistive Point Heater for MEMS Remote Solder Self-Assembly," *2000 ASME International Mechanical Engineering Congress and Exposition*, MEMS-Vol. 2, pp. 161-167, Orlando, Florida, Nov. 5-10, 2000.
  - [7] P. E. Kladitis, R. J. Linderman, and V. M. Bright, "Solder Self-Assembled Micro Axial Flow Fan Driven by a Scratch Drive Actuator Rotary Motor," *Proceedings of the Fourteenth IEEE International Micro Electro Mechanical Systems Conference (MEMS 2001)*, pp. 598-601, Interlaken, Switzerland, 21-25 Jan. 2001.
  - [8] Ryan J. Linderman, Paul Kladitis, Victor M. Bright, "Development of the Micro Fan," *To be published in Sensors and Actuators A.*

#### 1.4 Summary

This work will serve as a template or starting point in the design and manufacture of future multiple joint solder self-assembled MEMS. This work is essential for product control and design feasibility determination in current MEMS research and the future commercialization of complex solder self-assembled MEMS. Furthermore, this work is directly applicable to single joint solder self-assembled MEMS.

For the person experienced in micro-electronics packaging, this work will be a guide on how to incorporate their already established know-how on solder bumping

into the design, modeling, and manufacture of multiple joint solder self-assembled MEMS. For the person experienced in MEMS, this work will serve as a guide on how to incorporate their already established know-how on MEMS design and fabrication into the modeling and manufacture of multiple joint solder self-assembled MEMS.

## **2 Background**

Besides a brief introduction into MEMS, this chapter gives a comprehensive overview of the key elements used in this work: surface micromachining, solder self-assembly, and tolerance analysis. Surface micromachining and solder self-assembly are the two basic ingredients used to realize the structures presented in this work. Tolerance analysis is a set of mathematical techniques used to estimate the amount of variability in an assembly due to individual component variations.

### **2.1 Background Of Micro-Electro-Mechanical Systems (MEMS)**

Micro-Electro-Mechanical Systems (MEMS) are micrometer-sized machines. The fabrication process used to create MEMS is an adaptation of similar processes used to create microelectronics -- the fabrication of transistors, computer chips, and other non-mechanical microelectronic devices or systems. Since the MEMS fabrication process is adopted from the microelectronics fabrication process, the same materials are generally used to make these tiny machines: silicon, oxides of silicon, aluminum, gold, and etc.

MEMS fabrication can be generally categorized into three different techniques: bulk micromachining, micromolding, and surface micromachining. The bulk micromachining technique typically involves etching cavities into a crystalline silicon wafer using any number of techniques including:

- 1) Isotropic wet etching by  $\text{HNO}_3$  (nitric acid) or  $\text{CH}_3\text{COOH}$  (acetic acid)
- 2) Anisotropic wet etching by  $\text{KOH}$  (potassium hydroxide and water), EDP (ethylenediamine, pyrocatechol, and water), hydrazine, TMAH (tetramethylammonium hydroxide), or  $\text{CsOH}$  (cesium hydroxide and water)
- 3) Isotropic dry etching by  $\text{XeF}_2$

- 4) Anisotropic ion assisted dry etching by RIE (reactive ion etching) or DRIE (deep reactive ion etching)

Petersen describes the early history of bulk micromachining for MEMS in his extensive and most cited paper in the MEMS field [1]. I also prefer to include microstructure formation by laser milling of a bulk material as a bulk micromachining technique.

Micromolding, in general, involves making a mold from a bulk micromachined wafer or some high aspect ratio resist/polymer, filling the mold with a material, and removing the resulting cast from the mold. The filler may be any material such as an electro/electroless-plated metal, polymer, or chemically deposited element such as polycrystalline silicon (polysilicon). Furthermore, the direct creation of a microstructure in a polymeric bath, through stereo-lithography, can be considered as a micromolding method. Surface micromachining is the technique that most closely resembles the fabrication of microelectronic components, and is discussed next.

## **2.2 Background Of Surface Micromachining**

In the mid 1960s, Nathanson et al. from the Westinghouse Research Laboratories in Pittsburgh, Pa, supported by the U. S. Air Force Avionics Laboratory at Wright-Patterson AFB, developed the resonant gate transistor. Nathanson's work was published in March 1967 [2]. The resonant gate transistor is composed of typical source and drain diffusion areas. However, instead of a typical junction field effect transistor (JFET) design where a metal gate is in direct contact with the channel

region, a novel metal gate suspended over and separated only by an air gap from the channel region, is used. This suspended gate, made from gold, is perhaps the very first surface micromachined device. The suspended gate could also be actuated electrostatically by the attraction between the suspended gate and underlying attraction plates located on the substrate.

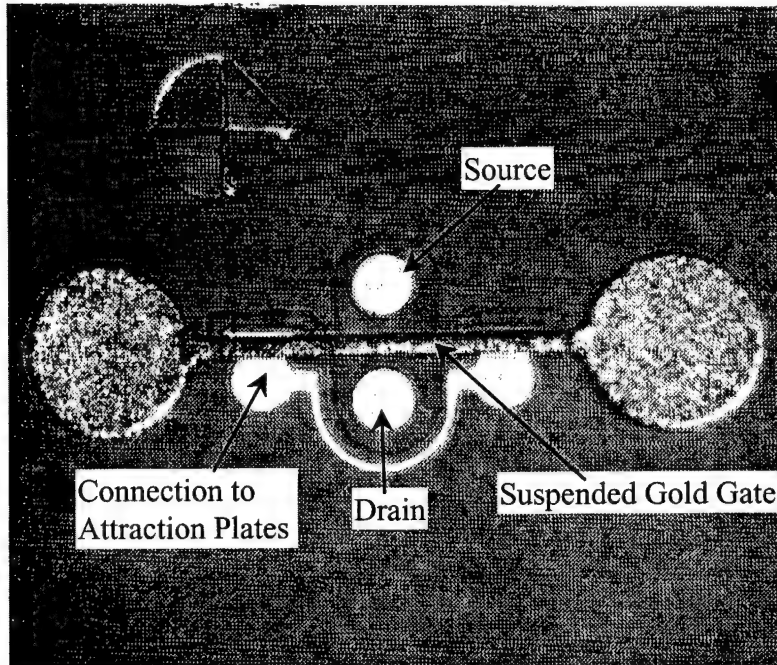


**Figure 2-1:** Nathanson et al.'s resonant gate transistor [2].

Later in 1982, Howe et al., from the group in the Department of Electrical Engineering and Computer Sciences, University of California at Berkeley, presented the first,  $2.3\text{ }\mu\text{m}$  thick, micro-electro-mechanical beams, made from polysilicon, and suspended  $3.5\text{ }\mu\text{m}$  from the substrate [3]. Howe et al.'s beams were fabricated by first depositing a  $3.5\text{ }\mu\text{m}$  thick layer of  $\text{SiO}_2$  (the sacrificial layer), on the surface of a crystalline Si wafer, using mostly chemical vapor deposition (CVD). Then, windows

were etched into the  $\text{SiO}_2$ . Next, a  $2.3\ \mu\text{m}$  thick layer of polysilicon was deposited, by pyrolysis of silane, and patterned into beams. Finally, the  $\text{SiO}_2$  was completely removed by immersion in a buffered HF (hydrofluoric acid) solution -- this step is typically called "release". For a depiction of the resulting structure before release, see Figure 2-2. Howe provides a more detailed history of surface micromachining up to 1995 in [4].

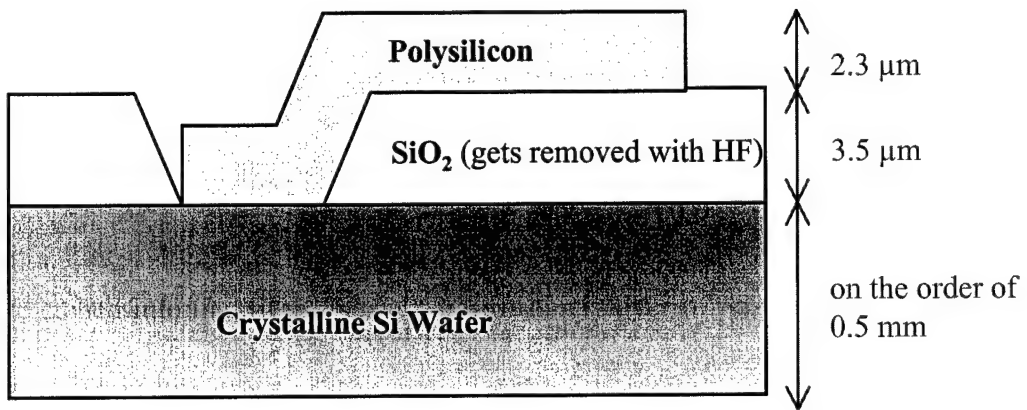


**Figure 2-2:** Depiction of a side profile of one of Howe et al.'s suspended beams.

### 2.2.1 Commercial Surface Micromachining Processes (MUMPs)

Today's method of making polysilicon surface micromachined structures is not unlike the method Howe et al. developed in 1982. In general, surface micromachined structures are realized, by a succession of CVD deposited and patterned polysilicon layers (typically less than  $3\ \mu\text{m}$  thick). The successions of polysilicon layers, which will comprise the final structure, are interspersed with patterned layers of some form of  $\text{SiO}_2$ . Before the polysilicon structures can be freestanding or moving parts, they must be released from the  $\text{SiO}_2$  layers that encase them by a bath in 49% HF or a buffered HF solution. Figure 2-3 shows captured video images

comparing a portion of a microelectronics chip and portions of a chip containing released surface micromachined MEMS. The MEMS chip shows examples of micromachined components alongside a human hair (70 - 100  $\mu\text{m}$  in diameter) for perspective of size.

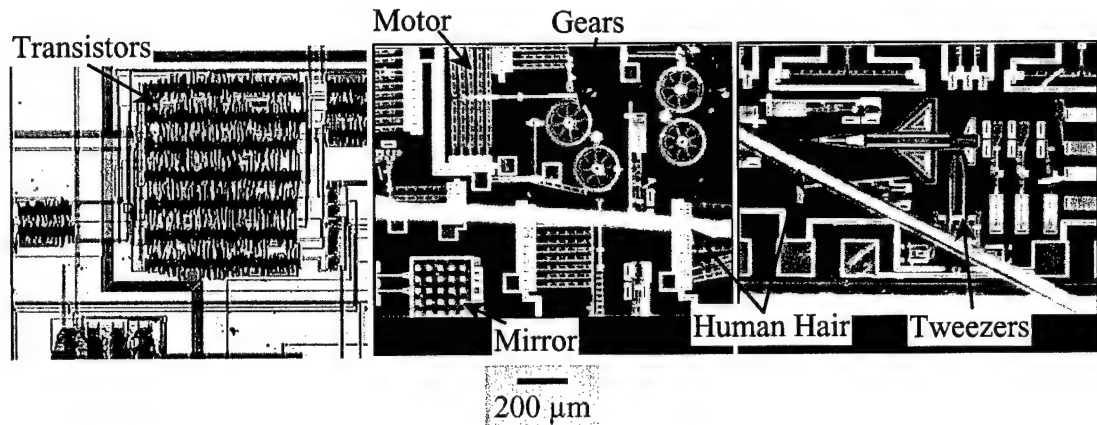


**Figure 2-3:** Captured video images of (left) a section of a microelectronics chip containing transistor circuits and wiring; and (middle/right) sections of a MEMS chip showing gears, motors comprised of electro-thermal actuators, hinged mirror, and microtweezers alongside a human hair for size perspective [5].

All of the MEMS presented in this work have been fabricated through a commercial polysilicon surface micromachining process called the Multi-User MEMS Process (MUMPs) [6]. The MUMPs process features three polysilicon layers available as structural layers poly0, poly1, and poly2. However, only poly1 and poly2 are releasable, and poly0 is always patterned on the  $\text{Si}_3\text{N}_4$  passivation layer on the (100) Si substrate. Also, gold is available as a metalization coating on poly2 only. MUMPs leaves the finished polysilicon microstructures encased in phosphosilicate glass (PSG) layers, also known as sacrificial layers. The sacrificial layers can be removed which “releases” the polysilicon microstructures, leaving them free to move

on the face of the die, if so designed. The process sequence used to fabricate microstructures, in the MUMPs process, is described next.

Figure 2-4 is a depiction of the different layers used in the MUMPs process -- please refer to it for the following discussion. The drawing shows the relative thicknesses and layer names. Note, the names used to describe the different MUMPs layers and etch masks will be used again throughout this document when describing the microstructures used in this research. The MUMPS process begins with 100 mm diameter, 500-550  $\mu\text{m}$  thick, n-type, (100) oriented silicon wafers. The wafers are heavily doped with phosphorus (POC13), in a standard diffusion furnace, to a resistivity of 1-2 ohm-cm. The sequence used to deposit and pattern the remaining layers is as follows:

- 1) Deposition of a 0.6  $\mu\text{m}$  thick layer of silicon nitride (nitride) on the surface of the wafer using low pressure chemical vapor deposition (LPCVD). The silicon nitride layer is used to electrically isolate the surface of the wafer.
- 2) Deposition of a 0.5  $\mu\text{m}$  thick layer of polysilicon (poly0) using LPCVD.
- 3) Patterning of the poly0 using photolithography. The photolithography process entails coating the wafer with positive photoresist, exposing the wafer with UV-light through the appropriate mask, developing the resist which removes the exposed resist, reactive ion etching (RIE) of the exposed polysilicon, and removal of the remaining resist.
- 4) Deposition of a 2.0  $\mu\text{m}$  thick layer of PSG (oxide1) using LPCVD.
- 5) Patterning of the oxide1 layer, by photolithography, using the “dimples” mask. The RIE, for this step, etches 0.75  $\mu\text{m}$  into the oxide1 layer.

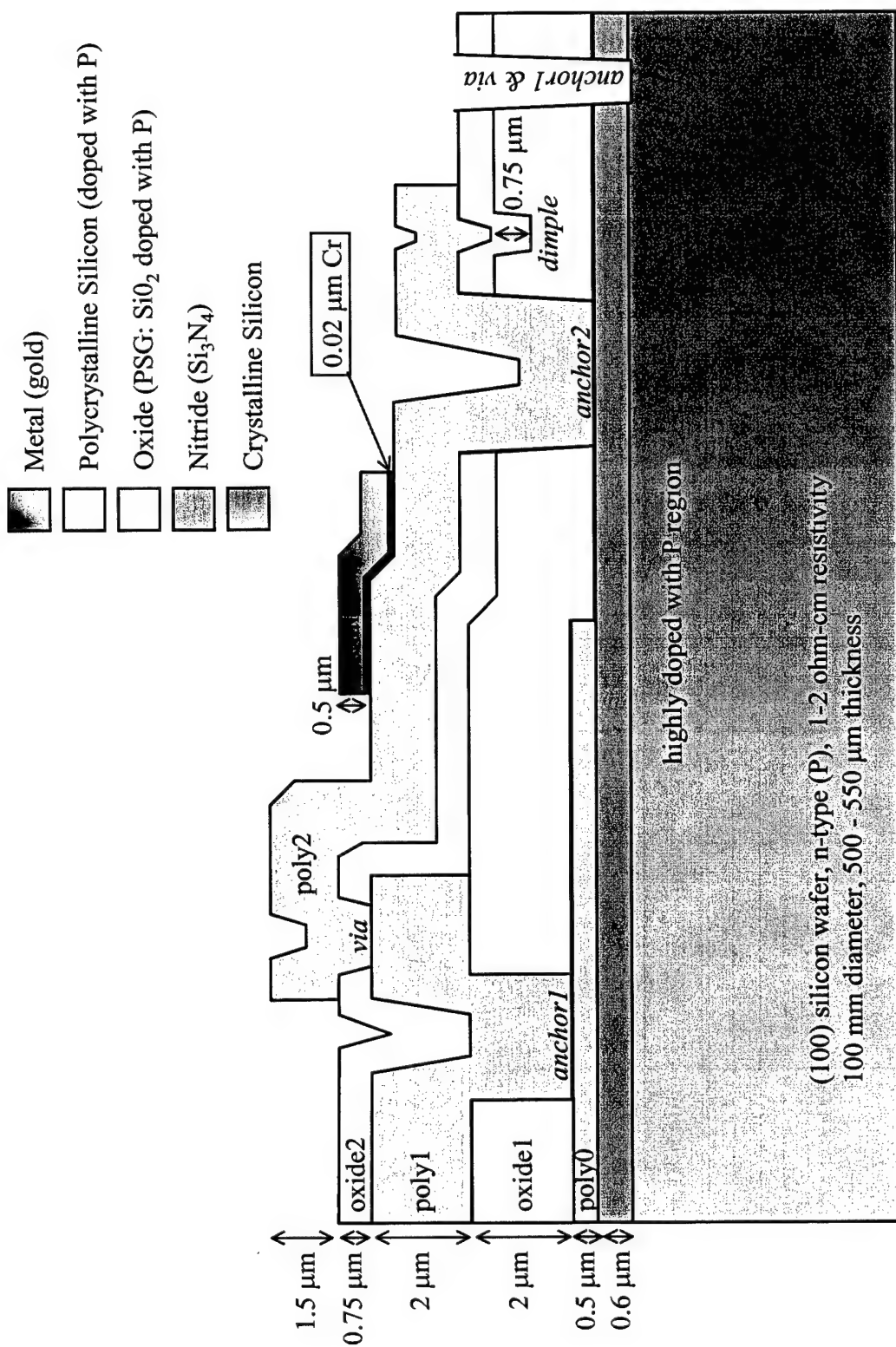


Figure 2-4: Depiction of the available layers and features in the MUMPs surface micromachining process.

- 6) Patterning of the oxide1 layer, by photolithography, using the “anchor1” mask. The RIE, for this step, etches through the oxide1 layer and stops at poly0 or nitride. The anchor1 patterns allow the “poly1” layer to be deposited or anchored onto the substrate.
- 7) Deposition of the second layer of polysilicon (poly1), 2.0  $\mu\text{m}$  thick, using LPCVD.
- 8) Deposition of a 0.2  $\mu\text{m}$  layer of PSG using LPCVD, and a 1 hour anneal at 1050° C to dope the polysilicon layers with phosphorous. The PSG acts as the dopant source.
- 9) Patterning of the PSG using photolithography. The patterned PSG becomes a mask for poly1, which is etched using RIE. The remaining PSG mask is then removed by RIE.
- 10) Deposition of a 0.75  $\mu\text{m}$  thick PSG layer (oxide2) using LPCVD.
- 11) Patterning of the oxide2 layer, by photolithography, using the “poly1poly2via” mask. The poly1poly2via patterns are etched only through oxide2, which, are meant to provide mechanical and electrical connections between poly1 and the third polysilicon layer.
- 12) Patterning of the oxide2 layer, by photolithography, using the “anchor2” mask. The anchor2 patterns are etched through oxide1 and oxide2, and are meant to provide mechanical and electrical connections between the third polysilicon layer and poly0 or nitride. As a side note, the nitride layer can be removed by combining an anchor1 and poly1poly2via etch, or an anchor1 and anchor2 etch directly over top of each other. The conductive substrate can be

utilized as an electrical contact to the poly2 layer after removal of the nitride layer.

- 13) Deposition of the third, 1.5  $\mu\text{m}$  thick, polysilicon layer (poly2) using LPCVD.
- 14) Deposition of a 0.2  $\mu\text{m}$  layer of PSG using LPCVD, and a 1 hour anneal at 1050° C to dope the polysilicon layers with phosphorous.
- 15) Patterning of the PSG using photolithography. The patterned PSG becomes a mask for poly2, which is etched using RIE. The remaining PSG mask is then removed by RIE.
- 16) Deposition of a 0.02  $\mu\text{m}$  thick chromium adhesion layer and a 0.5  $\mu\text{m}$  thick gold layer, both patterned using the lift-off method.

The MUMPs process guarantees a minimum feature widths and feature spacings of 2  $\mu\text{m}$ . Smaller feature widths and feature spacings can be achieved, but may not be reliable from one fabrication run to another.

Other surface micromachining processes, not utilized in this work, but worth mention, are the SUMMiT four-layer polysilicon process and the SUMMiT V five-layer polysilicon process, both offered by Sandia National Laboratory [7 - 11]. Figure 2-5 is a depiction of the available layers and features in the SUMMiT, four-layer, surface micromachining process. The SUMMiT V process is essentially similar with one major exception being a fifth, additional planarized layer of polysilicon.

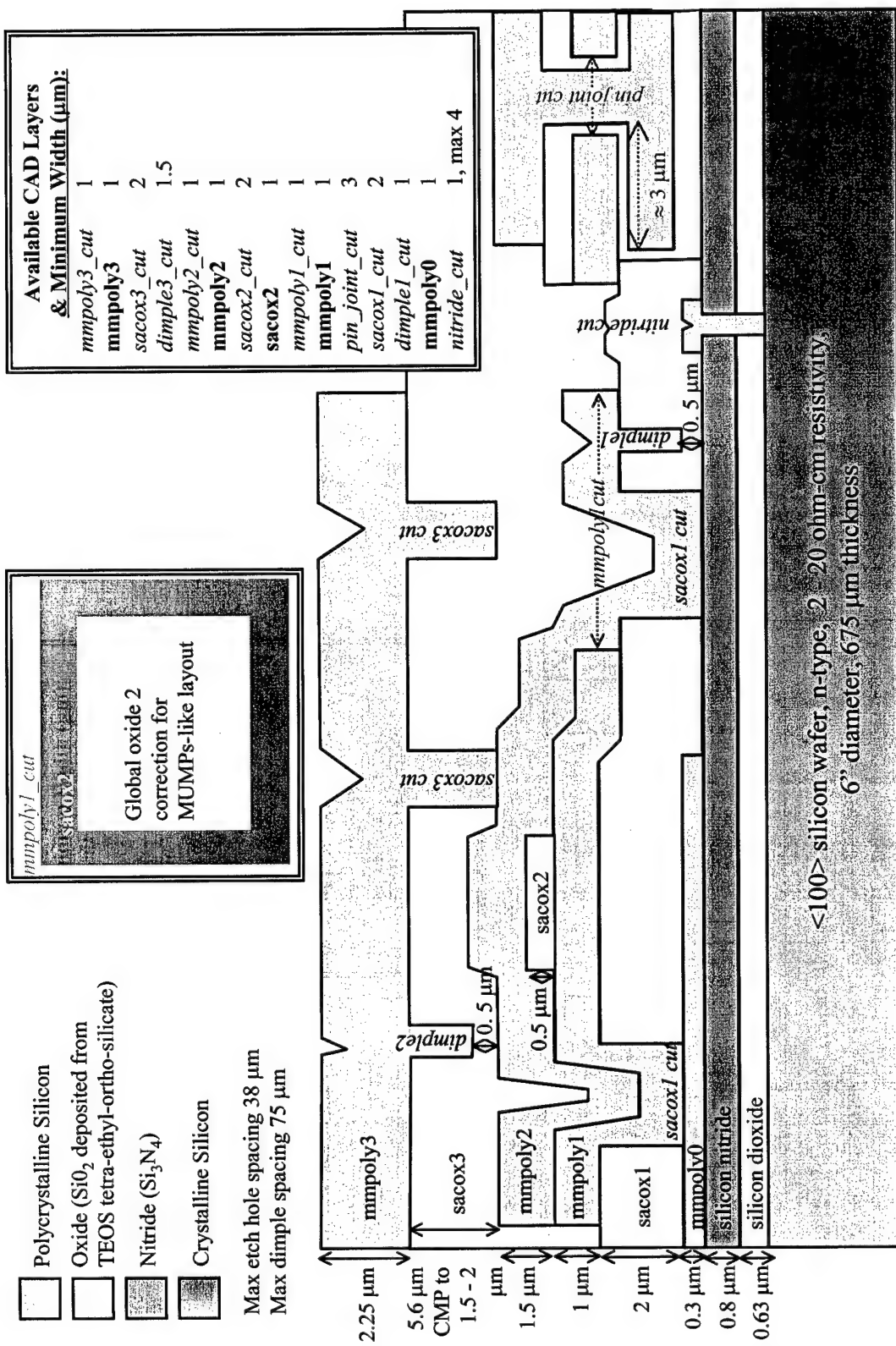


**Figure 2-5:** Depiction of the available layers and features in the SUMMiT surface micromachining process.

## **2.3 Solder Self-Assembly**

### **2.3.1 Motivation For Solder Self-Assembly**

MEMS are unique in that they are tiny machines that can be fabricated with microelectronics using microelectronic fabrication techniques such as surface micromachining discussed in the previous section. Due to the nature of the surface micromachining process, the fabricated microstructures are planar in nature -- resembling paper cut outs lying on a table. For appreciable three-dimensional function, surface micromachined structures must be assembled out of the plane of the substrate. Consequently, most surface micromachined MEMS's usefulness is limited because they require further post processing assembly. At the present, the post processing assembly can only be done by hand or by elaborate and impractical methods not compatible with a commercial manufacturing process.

Figure 2-6 shows a scanning electron micrograph (SEM) of a microrobot that has 96 legs [12 - 14]. The microrobot is actually a 1 cm by 1 cm by 0.5 mm silicon chip with 96, 270  $\mu\text{m}$  long, surface micromachined legs (electro-thermal actuators) sticking up out of the plane of the chip. Each leg was assembled into position by hand. The entire microrobot took three hours to assemble. Approximately 10% of the legs were usually damaged during, and by, the assembly process.

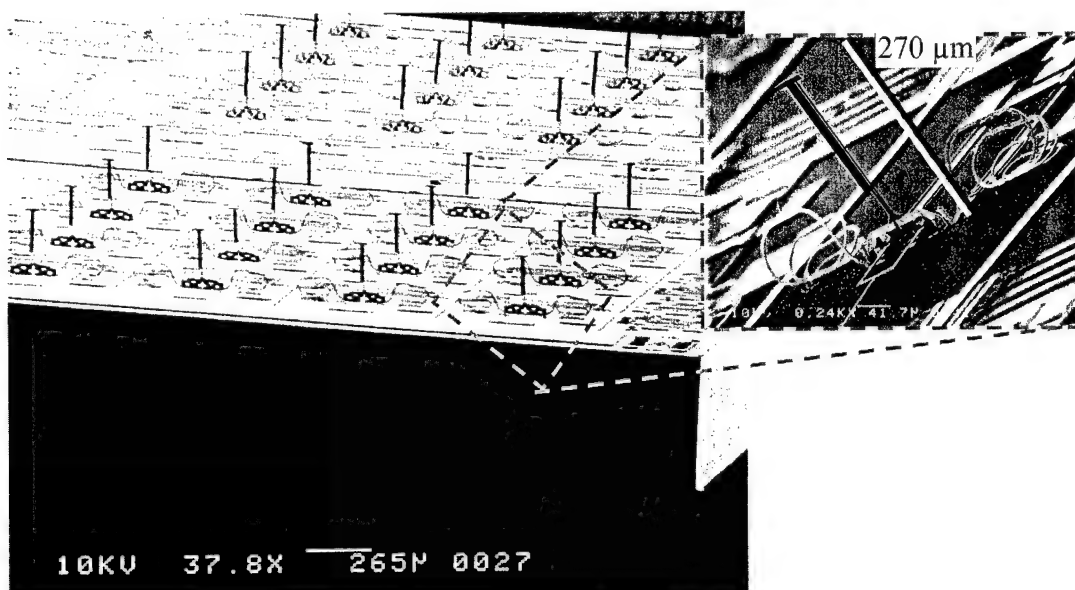


**Figure 2-6:** Scanning electron micrograph of a microrobot. Inset shows a closer view of one surface micromachined leg that was assembled into position by hand.

Figure 2-7 shows a scanning electron micrograph of micromirror system that can be assembled to a normal with the substrate position by actuating an array of actuators [15]. Hand assembly of MEMS, as exemplified in the microrobot, is impractical for mass production. The drawbacks of the assembly method of the micromirror system are that the actuator arrays take up more space than the mirror needing assembly, can be unreliable due to stiction and slop between linkages, require relatively complex control, and are relatively weak.

Solder self-assembly is where the surface tension of molten solder is harnessed to lift microstructures into place. Imagine eliminating the actuator arrays, in Figure 2-7, and lifting the micromirror using a liquid solder ball a fraction of the size of the micromirror. Solder self-assembly can also be used to mass assemble the robot legs, from Figure 2-6, in one quick reflow step [14].

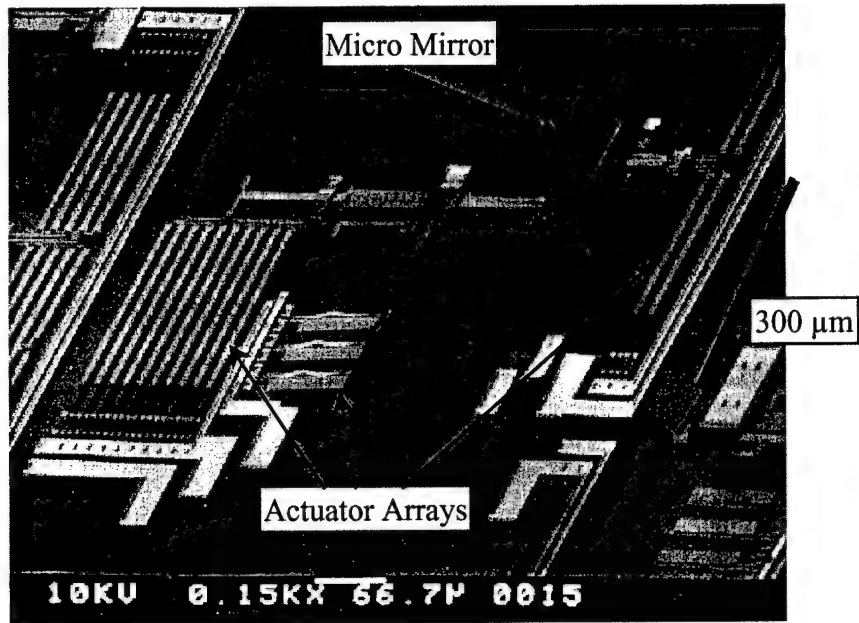


**Figure 2-7:** SEM of micromirror system [15].

Solder self-assembly is a reliable, powerful, and compact method for providing actuation, eliminating the need for thermal or electrostatic assembly schemes that usually take up more chip real-estate than the assembled device. Solder assembly requires no external electrical control lines that also take up chip real-estate, nor does solder assembly require impractical actuation voltages. The resulting solder joints in solder assembly also serve as robust low resistance electrical and mechanically rigid connections.

Solder can be strategically deposited on MEMS as part of the fabrication process. Subsequently, the MEMS can be mass assembled in one quick solder reflow step. Furthermore, solder deposition is an already existing commercial process. Finally, keep in mind that solder self-assembly is a specific method of surface tension self-assembly. Surface tension self-assembly harnesses the surface tension of any suitable liquid to perform work.

### 2.3.2 Theoretical Background Of Solder Self-Assembly

The principle of solder assembly is a simple one – use the surface tension of a molten volume of solder to lift or move structures or parts of structures. The final shape of the molten solder, which can be modeled, determines the final position of the structures. Figure 2-8 depicts solder self-assembly during reflow of solder and the basic components needed for solder self-assembly. Please refer to Figure 2-8 for the following discussion. Furthermore, assume that we are dealing with polysilicon surface micromachined structures. Although, this does not have to be the case since any appropriate material combinations will perform in the same manner and require essentially the same basic elements.

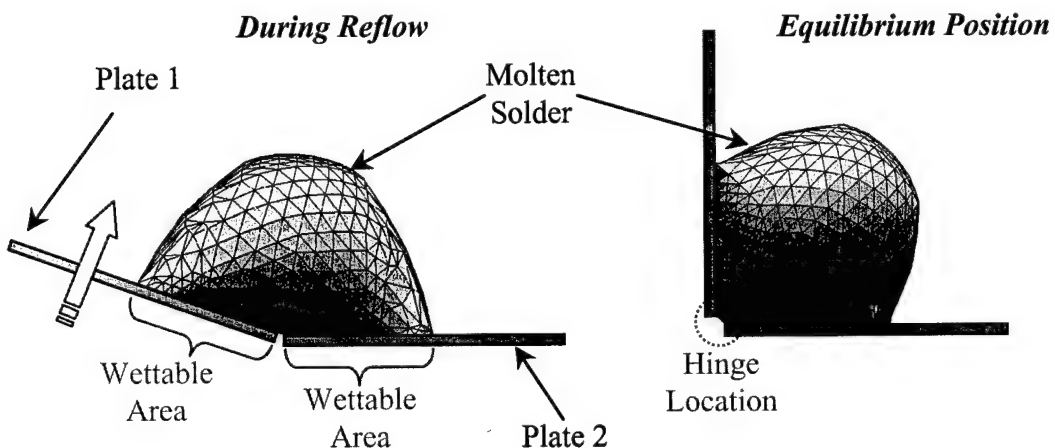


**Figure 2-8:** Depiction of solder self-assembly during reflow of solder and the basic elements of solder self-assembly, after Harsh et al. [38].

Initially, surface micromachined structures, represented by plate 1 and plate 2, are lying in the plane of the substrate in their fabricated state. Plate 1 and plate 2

have been designed such that they are connected together by some manner of hinges. The hinge connection dictates a pivot point for the subsequent solder self-assembly. Plates 1 and 2 have also been designed with solder wettable areas (since solder will not wet to the polysilicon plates) adjacent to the hinge location. Next, a volume of solder is deposited, in some manner, continuously spanning over both wettable areas. After the structures are released from the oxide, the whole system, represented in Figure 2-8, is heated to or above the melting point of the solder. The solder will wet to the wettable areas while simultaneously trying to reform itself into a shape of minimum surface energy. Either plate 1, plate 2, or both plates are designed to be free to pivot about the hinges. The solder shape reformation provides the driving force for pulling the plates together. Once the molten solder reaches a shape of minimum surface energy, the plates will rest at some equilibrium position or angle relative to each other. Figure 2-8 depicts an equilibrium angle of 90°.

In this case the structures, as well as the volume of solder, are micron sized. Any fluid will assume a shape of minimum surface energy for the given pressure, gravitational, and contact constraints. However, at this small size, gravitational constraints become negligible and the tendency for molten solder is to assume as close to a spherical shape as possible except where constrained to a contact. In other words, the problem reduces to one of just finding the minimum surface area shape. An approximate upper limit for this small regime is shown next.

Consider a molten body of solder, of density  $\rho$ , whose volume has just been reduced to the point that the body *almost* assumes a spherical shape. The body has almost a spherical radius  $r$ , while sitting on a practically non-wetting horizontal

surface in a gaseous atmosphere of negligible density, in a gravitational field of acceleration  $g$ , as in Figure 2-9. Here it is assumed a-priori that a solder droplet can be reduced in size such that gravitational effects will become negligible allowing the droplet to take on a spherical shape.

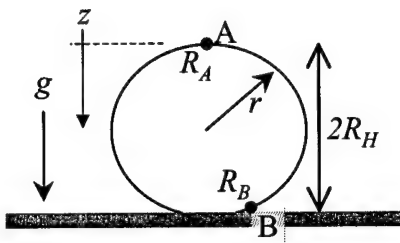


**Figure 2-9:** Depiction of a central cross section of a molten body of solder whose volume has been reduced to the point that the body takes on an almost spherical shape.

At any point on the solder-gaseous interface, the following equation holds

[16]:

$$\rho g z - \gamma(1/R_1 + 1/R_2) = \text{constant} , \quad (2-1)$$

where  $\gamma$  is the surface tension coefficient for the solder-gaseous interface, and  $R_1$  and  $R_2$  are the principle radii of curvature with respect to the surface normal at the point on the interface. The first term in Equation (2-1) represents the pressure change with respect to the distance  $z$ . The second term in Equation (2-1) is the Laplace-Young equation that describes a pressure difference between two non-mixing fluids based on the curvature of the separating interface. Referring to Figure 2-1, at point A,  $z = 0$ , and the constant in Equation (2-1) is found and Equation (2-2) follows:

$$\rho g z - \gamma(1/R_1 + 1/R_2) = -2\gamma/R_A , \quad (2-2)$$

where  $R_A$  is the radius of curvature, at point A, in all directions. While moving to point B on the interface, where the radius of curvature is approximately  $R_B$  in all directions, we descend a height of  $2R_H$ , and Equation (2-2) becomes:

$$\rho g 2R_H - 2\gamma/R_B = -2\gamma/R_A . \quad (2-3)$$

Rearranging (2-3) and expanding the left hand side as a binomial series, yields:

$$\frac{R_B R_H}{1 - \frac{R_B}{R_A}} = R_B R_H \left( 1 + \frac{R_B}{R_A} + \left( \frac{R_B}{R_A} \right)^2 + \dots + \text{higher order terms} \right) = \frac{\gamma}{\rho g} . \quad (2-4)$$

Experimentally verifiable and also demanded by Equation (2-2),  $R_A$  is larger than  $R_B$ , and the series in Equation (2-4) is convergent. If the first order and higher terms are ignored, an approximation to Equation (2-4) is:

$$R_B R_H \approx \frac{\gamma}{\rho g} . \quad (2-5)$$

Finally, since the body of solder is almost spherical,  $R_B \approx R_H \approx r$ , and Equation (2-5) yields the order of solder sphere radius where the effects of gravity can be ignored:

$$r \approx \sqrt{\frac{\gamma}{\rho g}} . \quad (2-6)$$

For pure indium, which is used as a solder and whose density and liquid surface tension is representative of other solders,  $\rho = 7310 \text{ kg/m}^3$ ,  $\gamma = 0.559 \text{ N/m}$  at  $157^\circ\text{C}$ ,  $g = 9.8 \text{ m/s}^2$ . For indium, Equation (2-6) yields  $r \approx 2.79 \text{ mm}$ . The size of solder sphere used in this research is  $r = 0.1 \text{ mm}$  and smaller.

Figure 2-10 shows a SEM of the basic element of solder self-assembly used in this work: the side view of a solidified solder joint wetted between two gold coated polysilicon plates. In this case, one plate is fixed to the substrate, while another plate of equal size is free to rotate about hinges adjacent to the fixed plate. Figure 2-10 also shows a close up of the type of hinge used to allow the free plate to rotate, and a not to scale drawing of a polysilicon solder-wettable plate pair without the solder.

The free plate, of the simple solder self-assembled structure shown in Figure 2-10, was initially lying parallel to the substrate, with a fixed volume of 63Sn/37Pb solder, placed on top of, and across both plates. The upper surface of the 300 by 300  $\mu\text{m}$  polysilicon plates were patterned with a 285  $\mu\text{m}$  by 285  $\mu\text{m}$  by 0.5  $\mu\text{m}$  thick pad of gold as part of the plate fabrication process. The substrate was subsequently heated to the melting temperature of the solder, the solder wetted to the gold coating of the plates, and the surface tension forces of the solder raised the free plate into the position shown in the figure. Finally, the substrate was allowed to cool, solidifying the solder.

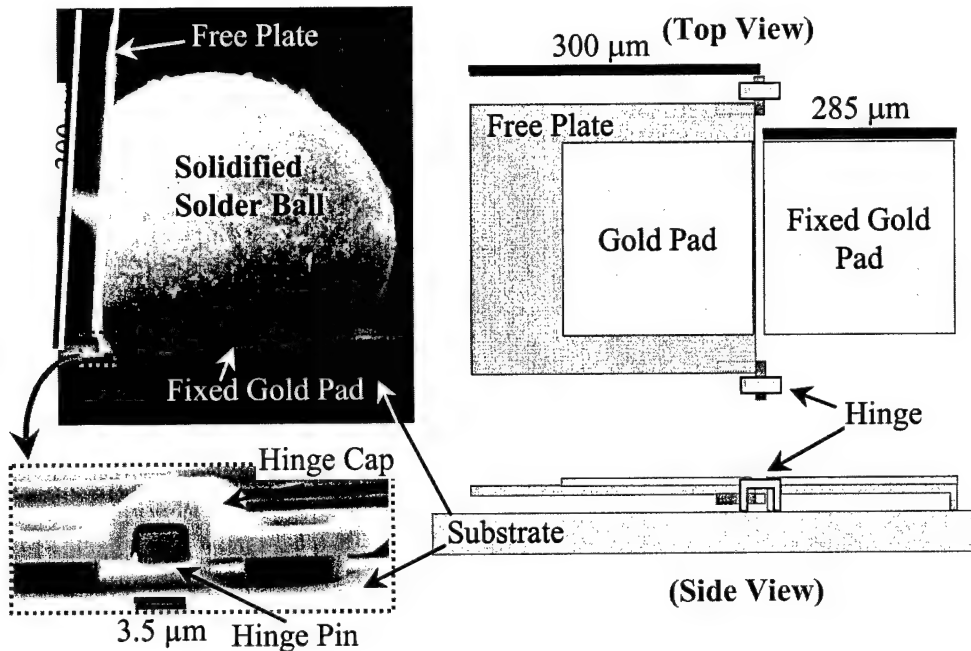


**Figure 2-10:** SEM of the side view of a solidified solder joint wetted between two gold-coated polysilicon plates, a close view of a hinge, and a not to scale drawing of a gold on polysilicon solder-wettable plate pair without solder.

Figure 2-11 shows a captured sequence of video images of an actual 63Sn/37Pb solder self-assembled polysilicon plate pair assembling during reflow of the solder. Figure 2-11 (a) shows unmelted solder already prewetted across a set of two 96  $\mu\text{m}$  by 96  $\mu\text{m}$  gold wettable pads, (b-e) sequence showing free plate (left plate) rotating toward its equilibrium position, (f) molten solder joint resting at an equilibrium angle,  $\alpha \approx 55^\circ$ . The assembly time from frame (a) to (f) is approximately 19 seconds. The volume of solder and gold wettable pad geometry determines the final equilibrium angle between the two plates. The modeling methods used to predict this equilibrium angle are discussed in Chapter 5. The solder wettable plates can be attached to or be part of larger structures and be used to rotate, or assemble, the larger structures.

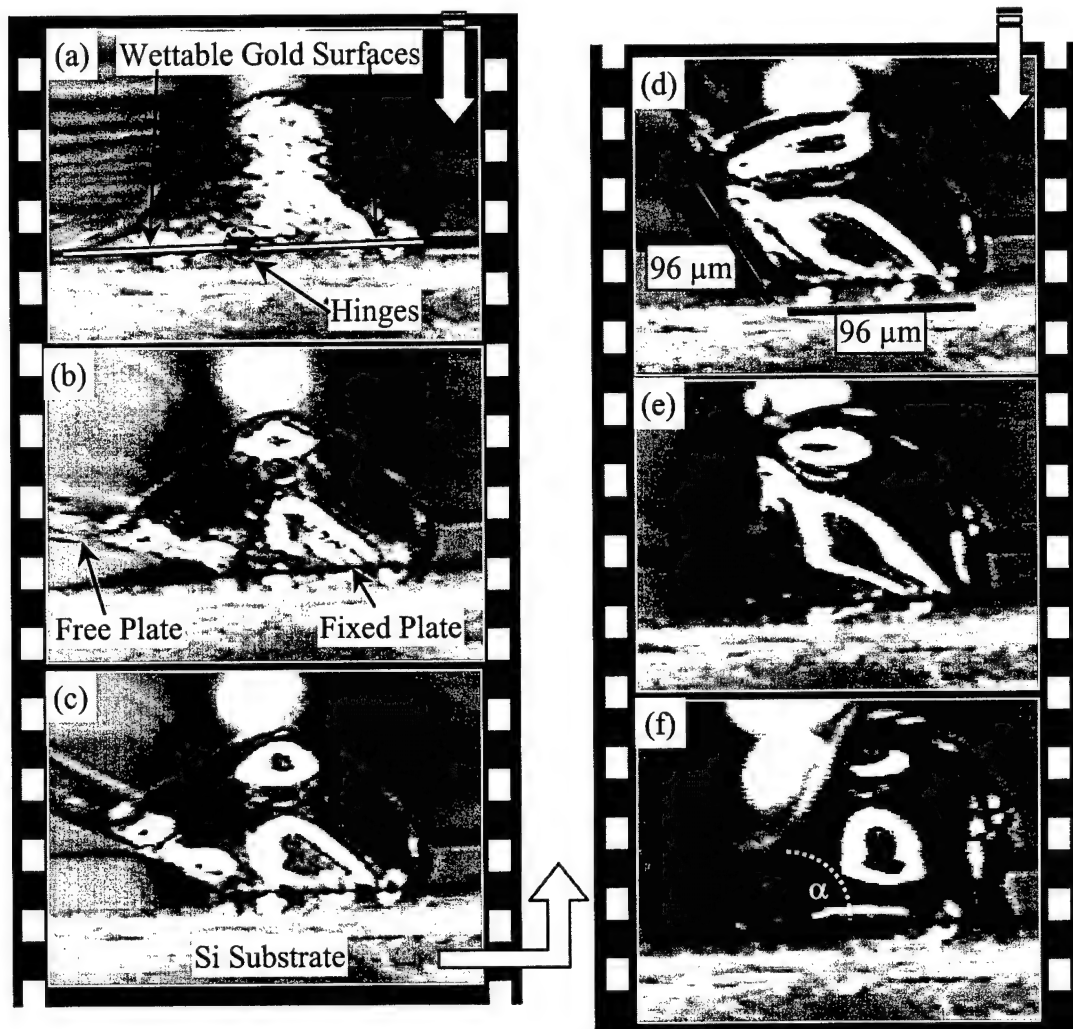


**Figure 2-11:** Captured sequence of video images of an actual 63Sn/37Pb solder self-assembled polysilicon plate pair during reflow of the solder: (a) unmelted solder already prewetted across a set of two 96  $\mu\text{m}$  by 96  $\mu\text{m}$  gold wettable pads, (b-e) sequence showing free plate (left plate) rotating toward its equilibrium position, (f) molten solder joint resting at an equilibrium angle,  $\alpha \approx 55^\circ$ .

The equilibrium angle, also referred to as the "solder angle" or "assembly angle", is defined as the angle between the two solder assembly plates, contained inside the solder. Possible solder assembly angles ( $\alpha$ ) are  $180^\circ < \alpha < 0^\circ$ , as depicted in Figure 2-12. Figure 2-13 shows actual examples of achieved assembly angle extremes. Although the extreme assembly angles of  $180^\circ$  and  $0^\circ$  are theoretically

achievable, they are impractical. In general, for a given volume of solder, the larger the solder pad area, the smaller the assembly angle. Similarly, for a given solder pad area, the larger the solder volume, the larger the assembly angle.

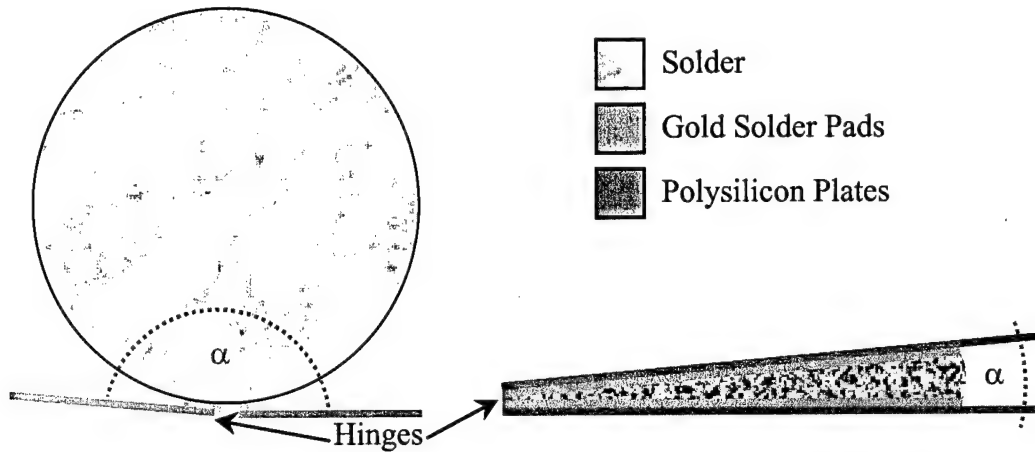


**Figure 2-12:** Depiction of the possible assembly angle extremes.

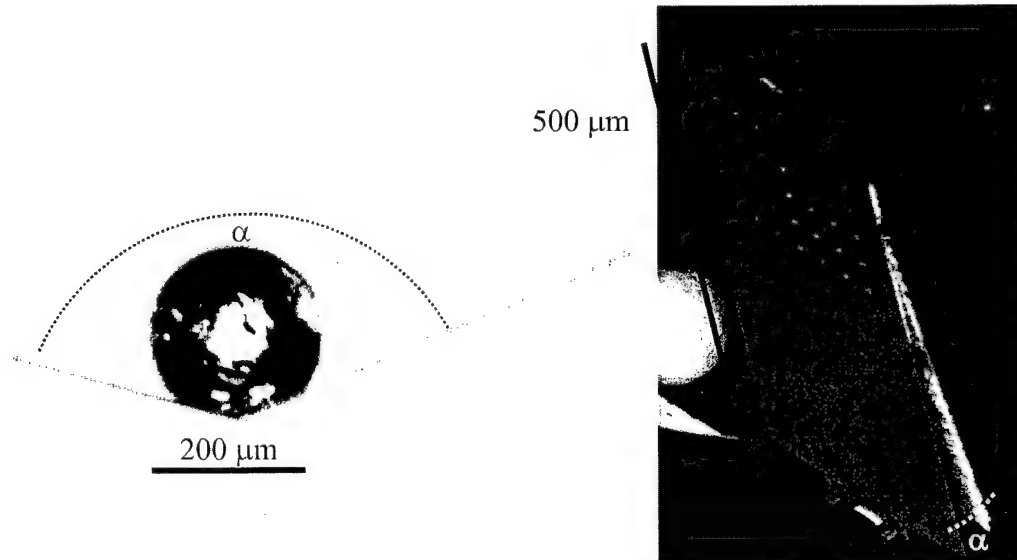


**Figure 2-13:** Actual images showing examples of achievable assembly angle extremes.

### 2.3.3 History Of Solder Self-Assembly

The undesirable effect of solder surface tension lifting small lead-less electronic components has been known in the electronic packaging community as tombstoning. Wu et al. predicts tombstoning [17]. The desirable effect of solder

surface tension moving small electronic components has also been used in the electronic packaging community to self align flip chip electronic modules. Lin et al. provides an overview of the history of solder self-alignment [18].

Syms et al., at the Imperial College of Science, London, England [19], was the first group to publish the idea of using solder surface tension to assemble microstructures in 1993 [20]. Subsequently, in 1995, Syms's group demonstrated the assembly of microstructures in a major MEMS journal [21, 22]. The Imperial College group has published several other works on this topic and related topics [23 - 33].

At the same time and independently, Y. C. Lee's group, at the University of Colorado at Boulder (CU), U.S.A. [34], was investigating the assembly of MEMS using solder surface tension. The University of Colorado group has published several other works on this topic [13, 14, 35 - 47] besides this work.

Table 2-1 is a comparison between the type of microstructure and manner of solder self-assembly used by the Imperial College group and this work. The first column lists the different characteristic categories being compared. The second column lists the characteristics of the Imperial College group's solder self-assembly process with the roman numerals distinguishing between different methods. For example, "I.", in the Imperial College column, indicates one method used to make solder self-assembled structures that includes Ni structures, electroformed in a photoresist mold, released by bulk etching the underlying Si, etc. The third column lists the characteristics of the solder self-assembly process of this work. The differences are important, and motivate the issues that will be addressed in this work.

Characteristic	Imperial College	This Work
<i>Micro Structure Material</i>	I. Ni II. B doped bulk Si III. Cu	Polycrystalline Si
<i>Structure Fabrication Method</i>	I. Electroplated in resist mold II. Undercut using EDP bulk etch III. Electroplated in resist mold	Surface Micromachining
<i>Sacrificial Layer Material</i>	I. Bulk Si II. Bulk Si III. Photo resist	Phosphosilicate Glass (PSG)
<i>Class of Fabrication Method</i>	I. Custom II. Custom III. Custom	Commercial Process, MUMPs [6]
<i>Releaseable Layers</i>	One	Two
<i>Thickness of Structural Layers</i>	I. 10 $\mu\text{m}$ II. 7 $\mu\text{m}$ III. Unknown	2 $\mu\text{m}$ and 1.5 $\mu\text{m}$
<i>Hinge Type</i>	I. None II. None III. None	Staple and scissor hinges for substrate and structure to structure constraint, respectively
<i>Solder Material</i>	I. Pb II. Pb III. SnPb (ratio unknown)	Commercially available 63Sn/37Pb and 60In/40Pb BGA solder spheres and In
<i>Solder Deposition Method</i>	I. Electroplating II. Electroplating III. Electroplating	Manual pick-and-place and thermal evaporation
<i>Solder Pad Material</i>	I. Ni II. Cr/Cu III. Cu	Au pad with Cr adhesion layer
<i>Solder Volume Range</i>	10 $\mu\text{m}$ thick $\times$ 31 $\mu\text{m}$ wide $\times$ $\approx$ 1 mm long. Volume equivalent to a 90 $\mu\text{m}$ diameter sphere. [48]	Volumes equivalent to 15 $\mu\text{m}$ to 200 $\mu\text{m}$ diameter spheres
<i>Pad Size</i>	31 $\mu\text{m}$ wide $\times$ $\approx$ 1 mm long	Ranges from $(8 \mu\text{m})^2$ to $(217 \mu\text{m})^2$
<i>Joint Shape</i>	Long and cylindrical	compact and spherical
<i>Flux Atmosphere</i>	I. N <sub>2</sub> II. N <sub>2</sub> III. Unknown	Vapor from bubbling N <sub>2</sub> through formic acid
<i>Heating Method</i>	I. Tube Furnace II. Tube Furnace III. Unknown	Standard hot plate or micro point heaters
<i>Reflow Temperature</i>	I. 350 - 540 °C II. 350 - 540 °C III. $\leq$ 200 °C	180 - 200 °C depending on process
<i>Reflow Time</i>	I. 5 minutes II. 5 minutes III. Unknown	< 2 minutes
<i>Complexity of Structure</i>	Non-Complex and single joint	Complex and multiple joint
<i>Solder Joint Yield</i>	Unknown -- probably low	94.3 %

**Table 2-1:** Comparison between the type of microstructure and manner of solder self-assembly used by the Imperial College group and this work.

Although the Imperial College group's work is novel, foundational, and also about solder self-assembled MEMS, my work stands in sharp contrast to theirs for several reasons. Simply put, the issues concerning the design, manufacture, processing, modeling, and assembly precision of multiple joint solder self-assembled surface micromachined MEMS have not been addressed in their work. Furthermore, their single releaseable layer limits the complexity of their demonstrated structures, furthermore limiting the issues that they can address. On the other hand my work harnesses the availability of a multiple layer, commercially available surface micromachining process. The availability of multiple structural layers opens up a universe of complexity not possible with the Imperial College technology. Furthermore, since little time is spent on the problem of structure fabrication in this work (the polysilicon structures are fabricated commercially), more time can be spent on the issues specific to solder self-assembled MEMS.

## 2.4 Tolerance Analysis

### 2.4.1 Motivation For Tolerance Analysis

The final position of a solder assembled structure (assembly) is actually a function of the different components that the structure is composed of. Each component can vary in some way, causing the final position of the assembly to vary about some nominal position. Tolerance analysis is the field of study dedicated to the methods used to predict the magnitude of this variation about the nominal, in other words, to predict the final position of the assembly. The magnitude of the variation about a nominal is called the tolerance. Furthermore, tolerance analysis methods are

used to investigate the effect of component variations on the assembly's final position -- providing a way of being able to make predictions about the precision of the assembly's final position.

### 2.4.2 Theoretical Background Of Tolerance Analysis

Another way to pose the mission of tolerance analysis is given by Gerth in Zhang's book [49] as follows: "Given a set of individual component tolerances, what is the resulting assembly tolerance?"

The first step in a tolerance analysis is to find the "assembly function" ( $f_{assy}$ ). The assembly function relates component dimensions ( $x_i$ ) to the dimension of interest on the assembly, as expressed in Equation (2-7):

$$f_{assy} = f(x_1, x_2, x_3, \dots, x_n) = f(x_i) . \quad (2-7)$$

Furthermore, in this work, it will be assumed that the component dimensions are normally distributed random variables. The assembly function may be found by any means. Once the assembly function is found, there are several ways of performing the tolerance analysis. This research will be based on three classical methods of tolerance analysis: Worst-Case or Stack-Up, Statistical, and Monte-Carlo analysis.

#### 2.4.2.1 Worst-Case Analysis

The worst case analysis involves considering a linearized assembly function where the assembly function is represented by a multivariate Taylor series expansion

truncated to the first order. In general, the assembly function may or may not be linear. If the assembly function is linear, it may be used as is. If the assembly function is non-linear, as in our case, the first partial derivatives must be calculated or estimated about a nominal position. Assuming bilateral component tolerances ( $tol_i$ ), the worst-case assembly tolerance ( $T_{WC}$ ) is calculated as follows:

$$T_{WC} = \sum_{i=1}^n \left| \frac{\partial f_{assy}}{\partial x_i} \right| tol_i \quad (2-8)$$

#### 2.4.2.2 Statistical Analysis

The statistical analysis involves analyzing the assembly function as a function of random variables and finding the mean and variance of the assembly function. In this research, if a component dimension is not already described by a mean and variance, the following assumptions about the components will be made: they are independent (uncorrelated) random variables ( $x_i$ ), their Process Capability Index ( $CP_i$ ) = 1, their nominal dimension is their mean ( $\mu_i$ ), and their upper ( $UL_i$ ) and lower ( $LL_i$ ) limit tolerances are bilateral and set at  $3\sigma_i$ . Therefore, given the upper and lower limit tolerances for each component dimension, the standard deviation for each component is calculated as follows:

$$\sigma_i = \frac{UL_i - LL_i}{6CP_i} = \frac{UL_i - LL_i}{6} . \quad (2-9)$$

The assembly mean ( $\mu_{assy}$ ) and variance ( $\sigma_{assy}^2$ ) can be estimated by finding the appropriate joint moments of the assembly function modeled by a multivariate Taylor series expansion truncated to the first order:

$$\mu_{assy} = E\{f_{assy}(x_i)\} \cong f_{assy}(x_i) \Big|_{x_i=\mu_i} \quad (2-10)$$

$$\sigma_{assy} = \sqrt{E\{(f_{assy}(x_i) - \mu_{assy})^2\}} \cong \sqrt{\sum_{i=1}^n \left( \frac{\partial f_{assy}(x_i)}{\partial x_i} \right)^2 \sigma_i^2} \Big|_{x_i=\mu_i} \quad (2-11a)$$

$$\sigma_{assy} \cong \sqrt{\nabla f_{assy}^T [COV] \nabla f_{assy}}, \quad (2-11b)$$

where Equation 2-11a and 2-11b is in series form and matrix form, respectively. Also,  $[COV]$  is a diagonal matrix. If we let  $CP_{assy} = 1$ , we can determine the  $3\sigma$  statistical tolerance of the assembly ( $T_S$ ) by:

$$T_S = \pm 3CP_{assy}\sigma_{assy} = \pm 3\sigma_{assy}. \quad (2-12)$$

#### 2.4.2.3 Monte-Carlo Analysis

Both the worst-case analysis and the statistical analysis neglect the true non-linear behavior of the assembly function, if indeed, the assembly function is non-linear. To get the true behavior of the assembly function, a Monte-Carlo analysis can be performed. A Monte-Carlo analysis consists of varying each component dimension and evaluating the assembly function for some set of possible combinations of component dimension variation. The Monte-Carlo analysis gives the

true worst-case behavior, however, can be computationally expensive, especially if one evaluation of the assembly function requires considerable computation. The number of assembly function calls required to perform  $m$  variations of each of  $n$  components is  $m^n$ . Another shortfall of the Monte-Carlo analysis is that it does not take into consideration the probabilistic nature of the components, meaning, the probability of the assembly being at its extreme positions is low.

#### 2.4.3 History of Tolerance Analysis

The tolerancing problem has been around for a good while. Shewhart [50] presents statistical tolerance analysis, as though it were in practice, in 1931. Shewhart also references older works. A compilation of the state of the art including the aforementioned classical tolerance analysis methods can be found in Evans famous three-part paper [51 - 53]. Other methods exist for performing a tolerance analysis, but are just variations of the three aforementioned methods or combinations thereof, such as the modified statistical model presented by Bender in 1962 [54]. Zhang's book [49] is a modern exposition of the state of the art in tolerance analysis. Most new research deals with automating the compilation of the assembly function; or the problem of automating/optimizing the proportioning of component tolerances given a desired assembly tolerance.

Sacks is the only one to come close to applying tolerance analysis to MEMS by presenting a functional analysis of MEMS gears using the configuration space approach [55, 56]. Sacks algorithm could be used as an assembly function, however, his algorithm is not meant to accommodate deformed structures and solder assembly

solder joints. Sacks algorithm models the interaction between moving parts by parameterized curve pairs and would be a suitable tolerance analysis tool for a MEMS assembly that has interactions between moving parts.

This work will be the first to apply tolerance analysis to solder self-assembled MEMS assemblies, and possibly to MEMS in general. The final assembly of a solder self-assembled MEMS is a function of several components including: the geometry of the assembly parts, volumes of solder, residual stress in surface micromachined mono-layers, misfit strain in multi-layer structures, temperature, solder pad geometry, play in hinges and linkages, and solder behavior (inter-metallic effects). In Chapter 6, the methods of classical tolerance analysis are used to make general predictions of the assembly precision of multiple joint solder self-assembled MEMS, given variations in the components of the assembly. A worst-case and statistical tolerance analysis will be performed on series connected, two-solder-joint, solder self-assembled MEMS structures. The different tolerance analyses will be compared to experimental measurements. Although the assembly function and tolerance analysis procedures can easily be used for n-solder-joints, the two-solder-joint structure is chosen as a realistic test vehicle.

## 2.5 References

- [1] K. E. Petersen, "Silicon as a mechanical material," *Proceedings of the IEEE*, vol. 70, no. 5, pp. 420-457, 5 May 1982.
- [2] H. C. Nathanson, W. E. Newell, R. A. Wickstrom, and J. R. Davis (Jr.), "The resonant gate transistor," *IEEE Transactions on Electron Devices*, vol. ED-14, pp. 117-133, March 1967.
- [3] R. T. Howe and R. S. Muller, "Polycrystalline silicon micromechanical beams," Proceedings of the Electrochemical Society Spring Meeting, pp. 184-185, Montreal, Quebec, Canada, May 1982.
- [4] R. T. Howe, "Recent advances in surface micromachining," *Technical Digest of the 13<sup>th</sup> Sensor Symposium ("Invited" Paper)*, pp. 1-8, Shigaku Kaikan, Tokyo, Japan, June 8-9, 1995.
- [5] The MEMS in the captured video images were designed by William D. Cowan at the Air Force Institute of Technology, 1996.
- [6] D. A. Koester, R. Mahadevan, A. Shishkoff, and K. W. Markus, *MUMPs Design Handbook*, Revision 4.0, Cronos Integrated Microsystems, 3021 Cornwallis Road, Research Triangle Park, NC 27709, May 1999.
- [7] J. J. Sniegowski, "Multi-level polysilicon surface-micromachining technology: applications and issues," *Proceedings of the 1996 ASME International Mechanical Engineering Congress and Exposition*, AD-Vol. 52, pp. 751-759, Atlanta, GA, November 17-22, 1996.
- [8] F. R. Davies, M. S. Rodgers, and S. Montague, "Design tools and issues of silicon micromachined (MEMS) devices," *Proceedings of the 2nd International Conference on Engineering Design and Automation*, Maui, Hawaii, August 9-12, 1998.
- [9] S. Rodgers and J. J. Sniegowski, "Designing microelectromechanical systems-on-a-chip in a 5-level surface micromachine technology," *Proceedings of the 2nd International Conference on Engineering Design and Automation*, Maui, Hawaii, August 9-12, 1998.
- [10] J. J. Sniegowski and M. S. Rodgers, "Manufacturing micro-systems-on-a-chip with a 5-level surface micromachining technology," *Proceedings of the 2nd International Conference on Engineering Design and Automation*, Maui, Hawaii, August 9-12, 1998.
- [11] H. Schriner, B. Davies, J. Sniegowski, M. S. Rodgers, J. Allen, and C. Shepard, "Sandia agile MEMS prototyping, layout tools, education and services program," *Proceedings of the 2nd International Conference on Engineering Design and Automation*, Maui, Hawaii, August 9-12, 1998.
- [12] P. E. Kladitis, *Self Assembly of Microstructures*, Master's Thesis, Air Force Institute of Technology, Wright-Patterson Air Force Base, Dayton, Ohio, 1997.
- [13] P. E. Kladitis, V. M. Bright, K. F. Harsh, and Y. C. Lee, "Prototype microrobots for micro positioning in a manufacturing process and micro unmanned vehicles," *Technical Digest of 12th IEEE International Conference*

*on MicroElectroMechanical Systems – MEMS '99*, pp. 570-575, Orlando, FL, Jan. 17-21, 1999.

- [14] P. E. Kladitis and V. M. Bright, "Prototype microrobots for micro positioning and micro unmanned vehicles," *Sensors and Actuators A.*, vol. 80, pp. 132-137, 2000.
- [15] J. R. Reid, V. M. Bright, and J. T. Butler, "Automated assembly of flip-up micromirrors," *Sensors and Actuators A*, vol. 66, pp. 292-298, 1998.
- [16] G. K. Batchelor, *An Introduction to Fluid Dynamics*, Cambridge U. P., pp. 63-65, 1967.
- [17] X. Wu, X. Dou, C.-P. Yeh, and K. Waytt, "Solder joint formation simulation and component tombstoning prediction during reflow," *Journal of Electronic Packaging*, vol. 120, pp. 141-144, June 1998.
- [18] Wei Lin, Susan K. Patra, and Y. C. Lee, "Design of solder joints for self-aligned optoelectronic assemblies," *IEEE Transactions on Components, Packaging, and Manufacturing Technology – Part B*, vol. 18, no. 3, pp. 543-551, August 1995.
- [19] Optical and Semiconductor Devices Group, Dept. of Electrical and Electronic Engineering, Imperial College, Exhibition Road, London SW7 2BT, UK.
- [20] R. R. A. Syms and E. M. Yeatman, "Self-assembly of three-dimensional microstructures using rotation by surface tension forces," *Electronics Letters*, vol. 29, no. 9, pp. 662-664, April 1993.
- [21] P. W. Green, R. R. A. Syms, and E. M. Yeatman, "Demonstration of three-dimensional microstructure self-assembly," *Journal of Microelectromechanical Systems*, vol. 4, no. 4, pp. 170-176, December 1995.
- [22] R. R. A. Syms, "Equilibrium of hinged and hingeless structures rotated using surface tension forces," *Journal of Microelectromechanical Systems*, vol. 4, no. 4, pp. 177-184, December 1995.
- [23] R. R. A. Syms, "Rotational self-assembly of complex microstructures by the surface tension of glass" *Sensors and Actuators A.*, vol. 65, pp. 238-243, 1998.
- [24] R. R. A. Syms, "Operation of a surface-tension self-assembled 3-D micro-optomechanical torsion mirror scanner," *Electronics Letters*, vol. 35, pp. 1157-1158, 1999.
- [25] R. R. A. Syms, "Surface tension powered self-assembly of 3-D micro-optomechanical structures" *Journal of Microelectromechanical Systems*, vol. 8, no. 4, pp. 448-455, 1999.
- [26] R. R. A. Syms and S. Blackstone, "3-D self-assembly of optomechanical structures using bonded SOI," *1999 Annual Meeting of the Electrochemical Society*, paper 1026, Honolulu, Hawaii, Oct. 17-22, 1999.
- [27] G. W. Dahlmann and E. M. Yeatman, High Q microwave inductors on silicon by surface tension self-assembly," *Electronics Letters*, vol. 36, no. 20, pp. 1707-1708, September 2000.
- [28] R. R. A. Syms, "Refractive collimating microlens arrays by surface tension self-assembly," *IEEE Photonics Technology Letters*, vol. 12, no. 11, pp. 1507-1509, 2000.

- [29] R. R. A. Syms, "Self-assembled 3D silicon microscanners with self-assembled electrostatic drives," *IEEE Photonics Technology Letters*, vol. 12, no. 11, pp. 1519-1521, 2000.
- [30] R. R. A. Syms, C. Gormley, and S. Blackstone, "Improving yield, accuracy and complexity in surface tension self-assembled MOEMS," *Sensors and Actuators A*, vol. 88, no. 3, pp. 273-283, 2001.
- [31] G. W. Dahlmann, E. M. Yeatman, P. Young, I. D. Robertson, and S. Lucyszyn, "MEMS high Q microwave inductors using solder surface-tension self-assembly," *2001 IEEE MTT-S International Microwave Symposium Digest*, vol. 1, pp. 329-332, Phoenix, Arizona, May 20-25, 2001.
- [32] G. W. Dahlmann, E. M. Yeatman, P. Young, I. D. Robertson, and S. Lucyszyn, "High Q achieved in microwave inductors fabricated by parallel self-assembly," *Proceedings of the 11<sup>th</sup> International Conference on Solid-State Sensors and Actuators – Transducers '01, Eurosensors XV*, Munich, Germany, June 10-14, vol. 2, pp. 1098-1101, 2001.
- [33] R. R. A. Syms, "Measurement of starting torque in surface tension self-assembly of microstructures," *Accepted for publication in Electronics Letters*.
- [34] Department of Mechanical Engineering, University of Colorado at Boulder, Engineering Center, Campus Box 427, Boulder, Colorado, 80309-0427.
- [35] Q.Tan and Y.C. Lee. "Soldering for optoelectronic packaging", *IEEE transactions on Components, Packaging and Manufacturing Technology, Part C*, pp. 28-30, May 1996.
- [36] K.F. Harsh and Y.C. Lee, "Modeling for solder self-assembled MEMS," *Proceedings of SPIE*, San Jose, CA, vol. 3289, pp. 177-184, Jan. 1998.
- [37] K. F. Harsh, R. S. Irwin, and Y.C. Lee, "Solder self-assembly for MEMS," *Proceedings of the 44th International Instrumentation Symposium*, Reno, NV, vol. 44, pp. 249-255, May 1998.
- [38] K. F. Harsh, V. M. Bright, and Y. C. Lee, "Solder self-assembly for three-dimensional microelectromechanical systems," *Sensors and Actuators A*, vol. 77, no. 3, pp. 237-244, Nov. 1999.
- [39] P. E. Kladitis, K. F. Harsh, V. M. Bright, and Y. C. Lee, "Three-dimensional modeling of solder shape for the design of solder self-assembled micro-electro-mechanical systems," *Proc. 1999 ASME IMECE MEMS Symposium*, Nashville, TN, MEMS-Vol. 1, pp. 11-18, November 1999.
- [40] K. F. Harsh, V. M. Bright and Y. C. Lee, "Study of micro-scale limits of solder self-assembly for MEMS", *Proc. of the Electronics and Components Technology Conference*, Las Vegas, Nevada, pp. 1690-1695, May 2000.
- [41] K. F. Harsh, P. E. Kladitis, Y. H. Zhang, M. L. Dunn, V. M. Bright, and Y. C. Lee, "Tolerance and precision study for solder self-assembled MEMS," *Proceedings of the 2000 Micro-Opto-Electro-Mechanical Systems Conference – MOEMS 2000*, vol. 4075, pp. 173-184, Glasgow, Scotland, May 22-25, 2000.
- [42] P. E. Kladitis and V. M. Bright, "Novel resistive point heater for MEMS remote solder self-assembly," *2000 ASME International Mechanical*

*Engineering Congress and Exposition*, MEMS-Vol. 2, pp. 161-167, Orlando, Florida, Nov. 5-10, 2000.

- [43] P. E. Kladitis, R. J. Linderman, and V. M. Bright, "Solder self-assembled micro axial flow fan driven by a scratch drive actuator rotary motor," *Proceedings of the Fourteenth IEEE International Micro Electro Mechanical Systems Conference (MEMS 2001)*, pp. 598-601, Interlaken, Switzerland, 21-25 Jan. 2001.
- [44] Ryan J. Linderman, Paul Kladitis, Victor M. Bright, "Development of the micro fan," *To be published in Sensors and Actuators A*.
- [45] K. F. Harsh, V. M. Bright, and Y. C. Lee, "Micro-scale limits of solder self-assembly for MEMS" *Accepted for publication in the International Journal of Microelectronics Packaging*, 2001.
- [46] K. F. Harsh, V. M. Bright, and Y. C. Lee, "Design optimization of surface micro-machined self-assembled MEMS structures" *Accepted for Publication in the Proceedings of the Pacific Rim/ASME International Electronic Packaging Technical Conference and Exhibition, IPACK'01*, Kauai, Hawaii, July 8-13, 2001.
- [47] K. F. Harsh, *Design Optimization For MEMS Solder Self-Assembly*, Ph.D. Dissertation, Department of Mechanical Engineering, University of Colorado at Boulder, Engineering Center, Campus Box 427, Boulder, Colorado, 80309-0427, Summer 2001.
- [48] The Imperial College group does not provide explicit dimensions for their solder pads or their structures in the literature. The length of 1 mm was estimated from the scanning electron micrographs included in their papers.
- [49] H. C. Zhang, *Advanced Tolerancing Techniques*, John Wiley & Sons, Inc., 1997.
- [50] W. A. Shewhart, *Economic Control of Quality of Manufactured Product*, D. Van Nostrand Company, Inc., New York, 1931.
- [51] David H. Evans, "Statistical Tolerancing: The State of the Art Part I. Background," *Journal of Quality Technology*, vol. 6, no. 4, pp. 188-195, October 1974.
- [52] David H. Evans, "Statistical Tolerancing: The State of the Art Part II. Methods for Estimating Moments," *Journal of Quality Technology*, vol. 7, no. 1, pp. 1-12, January 1975.
- [53] David H. Evans, "Statistical Tolerancing: The State of the Art Part III. Shifts and Drifts," *Journal of Quality Technology*, vol. 7, no. 2, pp. 72-76, April 1975.
- [54] Arthur Bender, "Benerizing Tolerances – a Simple Practical Probability Method of Handling Tolerances for Limit-Stack-Ups," *Graphic Science*, pp. 17-21, December 1962.
- [55] E. Sacks and J. Allen, "Computer-Aided Micro-Mechanism Design," *Micro-Electro-Mechanical Systems (MEMS)*, *Proceedings of the 1998 ASME International Mechanical Engineering Congress and Exposition*, Anaheim, CA, vol. 66, pp. 313-316, November 1998.

- [56] E. Sacks and J. Allen, ‘MEMS Functional Validation Using the Configuration Space Approach to Simulation and Analysis,’ *Proceedings of the Second International Conference on modeling and Simulation of Microsystems, Semiconductors, Sensors and Actuators*, pp. 136-138, 1999.

### **3 Issues In Design**

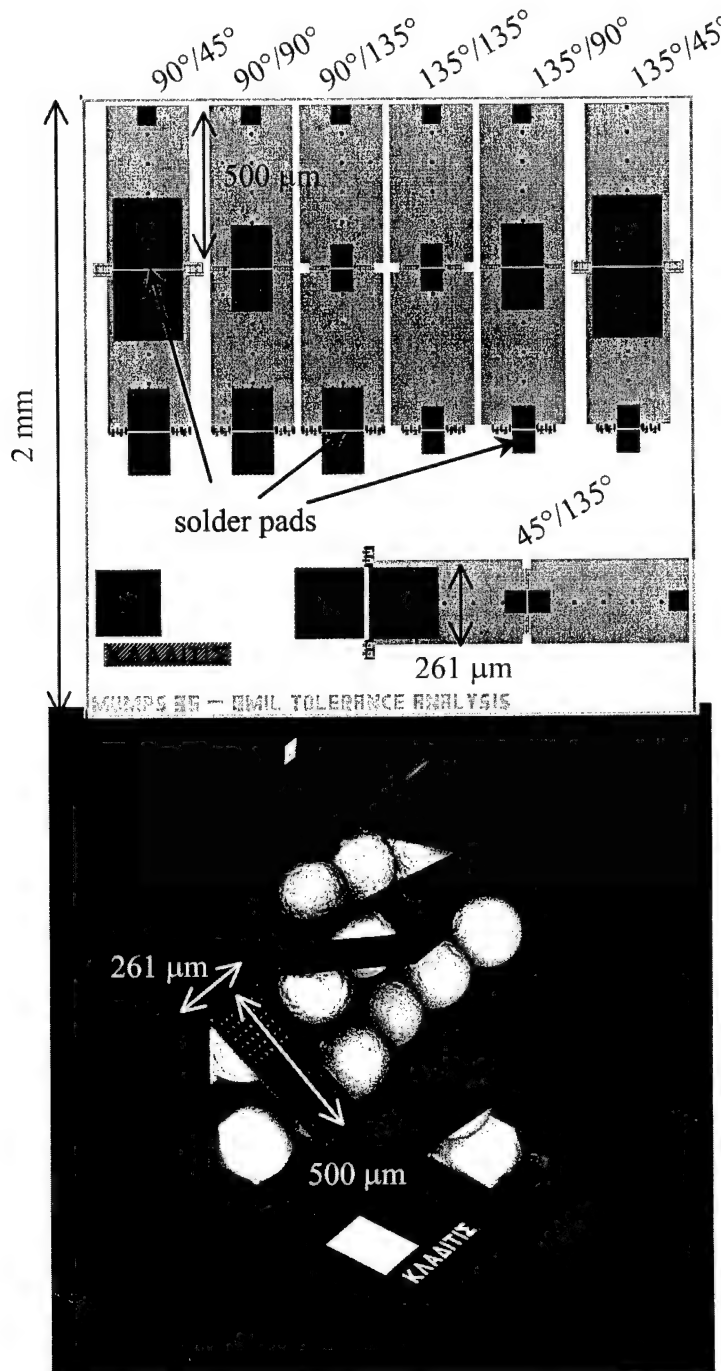
This chapter begins the journey through the processing of a multiple joint solder self-assembled MEMS. The two-solder-joint test structure, studied for this research is introduced first. The following sections will address the major issues relevant to the design of a multiple joint solder self-assembled MEMS, such as: computer aided drawing (CAD) tool, hinge design, general structure design, solder pad design, and linkage design. Although experience in MEMS design can not be replaced by reading a chapter of a dissertation, I have included the issues that I believe may not be obvious to new or experienced MEMS designers.

#### **3.1 The Two-Solder-Joint Test Structure**

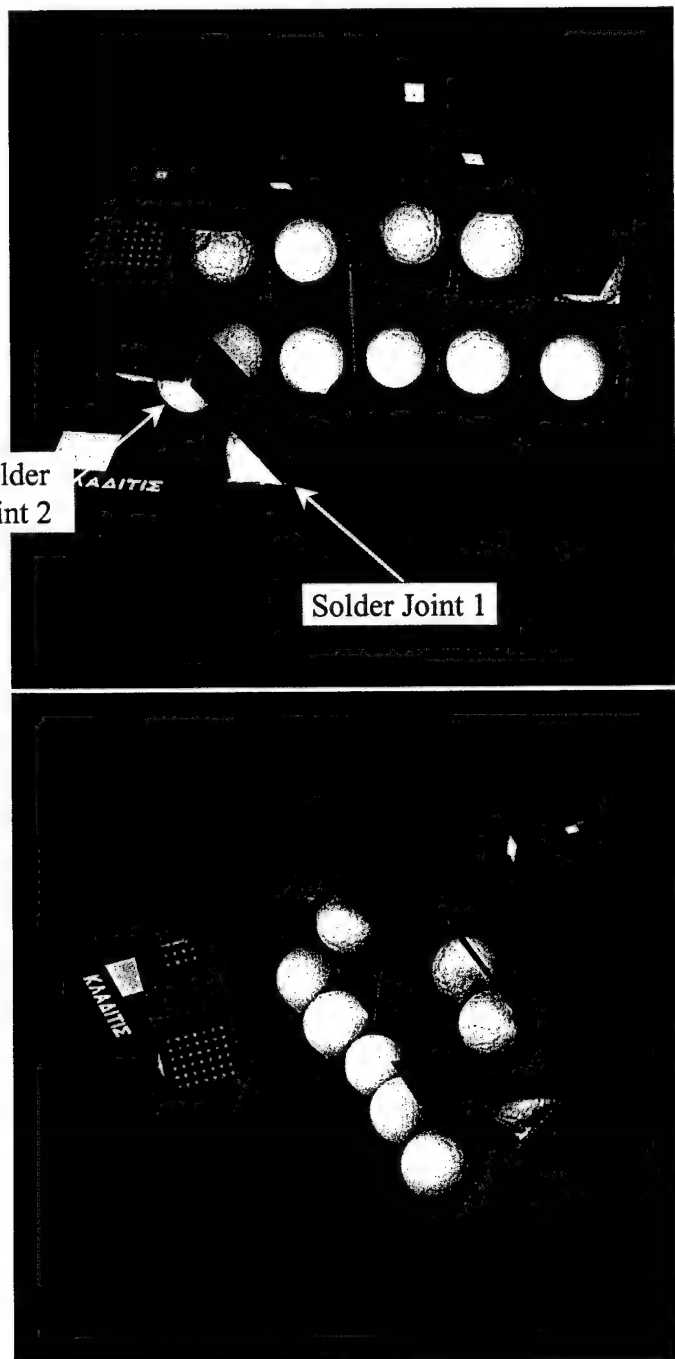
For this work, a test structure was devised that forces the investigator to explore all of the design and processing limits that any multiple joint solder self-assembled MEMS may reach. Twenty-one variants of this test structure were designed, assembled, and measured. All of the structures in this work were batch fabricated in the CRONOS MUMPs process described in Chapter 2. Designs received from CRONOS were subdiced into  $2\text{ mm} \times 2\text{ mm}$  chips using the dicing saw described in Appendix A, Section A.1, however, the subdicing was eventually subcontracted out. There are three versions of groups of seven test structures on each  $2\text{ mm} \times 2\text{ mm}$  chip.

Figure 3-1 shows the CAD layout (top) and scanning electron micrograph (SEM) (bottom) of seven variants of the "8 mil" version of the test structure. 8 mil diameter manufactured solder spheres were used to assemble each joint of this

version. Each test structure requires two solder joints to assemble in series for proper assembly. Figure 3-2 shows different views of this same version. The SEMs were captured with the scanning electron microscope described in Appendix A.



**Figure 3-1:** CAD layout (top) and SEM (bottom) of seven variants of the 8 mil version of the test structure.



**Figure 3-2:** Different SEM views of seven variants of the 8 mil version of the test structure shown in Figure 3-1.

Two solder joints were prudently chosen as to introduce just enough complexity to reveal processing requirements necessary for a general n-joint

structure. Furthermore, I desired to keep the number of solder joints per structure to a minimum to ensure a satisfactory yield for academic experiments. With reference to the CAD layout in Figure 3-1, each structure was designed to assemble at all possible combinations of roughly  $45^\circ$ ,  $90^\circ$ , and  $180^\circ$  -- the angle combination for a particular structure is labeled. The angle combinations were also prudently chosen to help reveal processing requirements necessary for a general n-joint structure. Figure 3-3 is a depiction of the ideal side profiles of the different variations of the non-warping test structures.

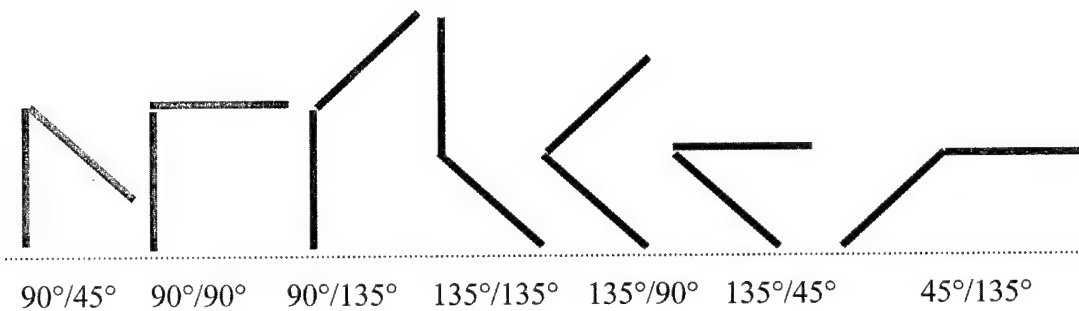


**Figure 3-3:** Depiction of the ideal side profiles of the different variations of the non-warping test structures.

Figure 3-4 shows the CAD layout (top) and SEM (bottom) of seven variants of the "8 mil" version of the test structure with warped plates. Gold covered regions have been added between the solder joints, causing a warpage of the polysilicon plates due to the misfit strain between the polysilicon plate and the gold coating. The purpose of adding the gold regions was to investigate the effects and possible drawbacks of such a combination with multiple joint solder self-assembled structures. 8 mil diameter manufactured solder spheres were also used to assemble each joint of

this version. Each test structure also requires two solder joints to assemble in series for proper assembly.

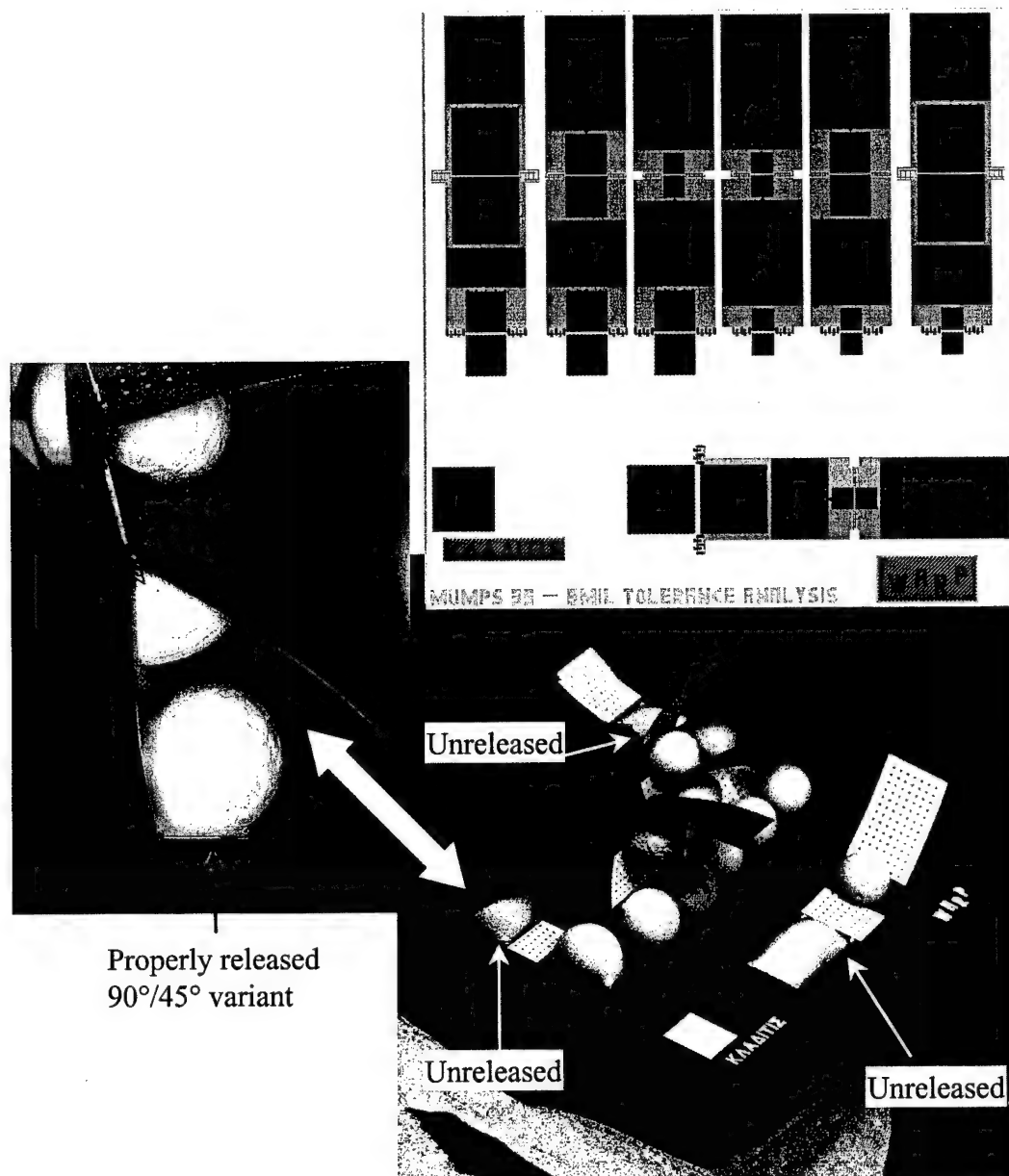


**Figure 3-4:** CAD layout (top) and SEM (bottom) of seven variants of the 8 mil warped plate version of the test structure. Three of the variants shown are not assembled properly due to unreleased  $45^\circ$  solder pads. This figure is used as an illustration in Chapter 4.

Figure 3-5 shows the third version -- the "4 mil" version of the seven variants of the test structure. Gold covered regions have also been added between the solder joints, causing a warpage of the polysilicon plates due to the misfit strain between the polysilicon plate and the gold coating. The difference here with the previous two versions is that 4 mil diameter manufactured solder spheres were used to assemble each joint of this version. Each test structure also requires two solder joints to assemble in series for proper assembly. The smaller solder volumes were chosen to investigate the effect of solder volume on the multiple joint solder self-assembled MEMS process. Hereafter, the two-solder-joint test structure will be referred to as "the test structure".

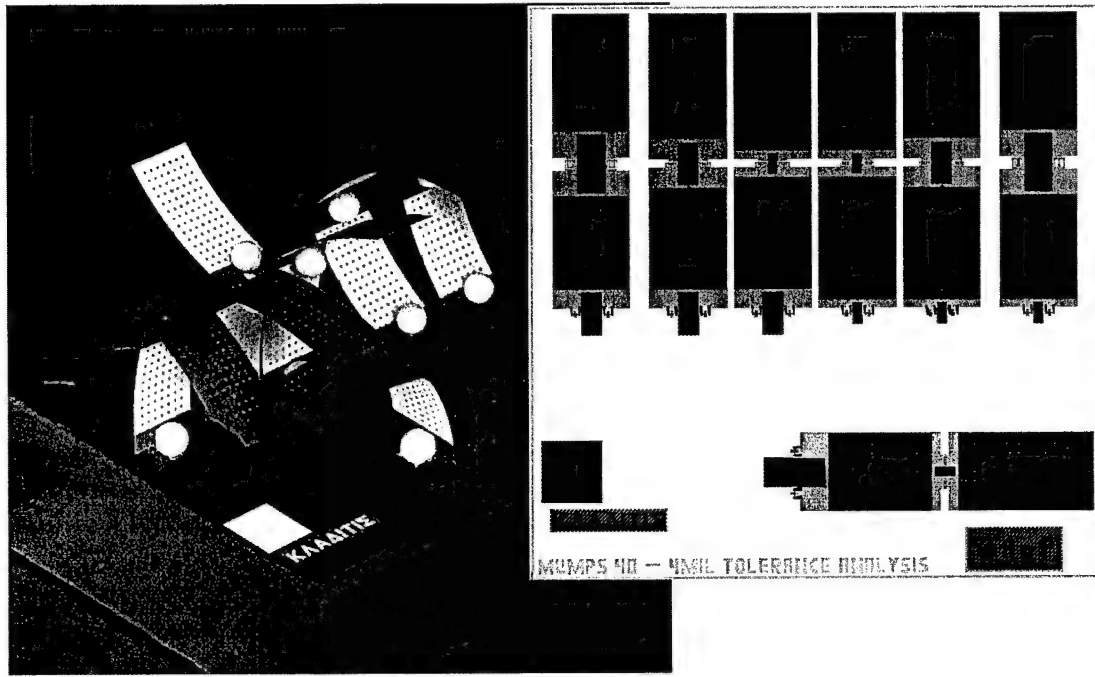


**Figure 3-5:** CAD layout (top) and SEM (bottom) of seven variants of the 4 mil warped plate version of the test structure.

### 3.2 CAD Tool

The CAD tool used for all the designs presented in this work is the L-Edit v8.03 layout editor [1]. The layout editor simply allows the user to create a two-dimensional, layered, representation of surface micromachined structures. The two-dimensional image is then converted from the layout editor's native file storage to a file used to make the masks for the fabrication process. The layout editor must have information on the specific fabrication process to be used. The information is used to describe what color and style each drawing layer should have, how those layers interact with each other, and how the layers are translated to and from the mask file formats: CIF (Caltech Intermediate Format) and/or GDS II (Stream Format) [2]. Important parameters used for the masks in the MUMPs process, described in Chapter 2, are shown in Table 3-1.

MUMPs Process		
Level	CIF Level Name	GDS Level Number
POLY0	CPZ	13
ANCHOR1	COF	43
DIMPLE	COS	50
POLY1	CPS	45
POLY1_POLY2_VIA	COT	47
ANCHOR2	COL	52
POLY2	CPT	49
METAL	CCM	51
HOLE0	CHZ	41
HOLE1	CHO	0
HOLE2	CHT	1
HOLEM	CHM	48

**Table 3-1:** Important mask file parameters for the MUMPs process.

Since the design of the multiple joint structures is discussed, and CAD images are used to illustrate, a bit of CAD legend is now presented to help the reader understand the figures to come. Figure 3-6 depicts the different MUMPs layer combinations as viewed from L-edit. For example, the structural layers Poly0, Poly1, Poly2, and Gold are drawn as pink-orange, red, gray, and blue lines, respectively. Connections between the layers are represented by the black patterned squares. Figure 3-7 shows a comparison between a CAD drawing of a hinge connected to the substrate and the actual fabricated hinge.

- (a) Poly2 connected to Poly0 using Anchor 2
- (b) Poly1 connected to Poly0 using Anchor1
- (c) Poly2 connected to Poly1 using P1P2via
- (d) Poly1 connected to Nitride using Anchor1
- (e) Poly2 connected to Nitride using Anchor2
- (f) Poly2 connected to substrate using Anchor1 and P1P2via.

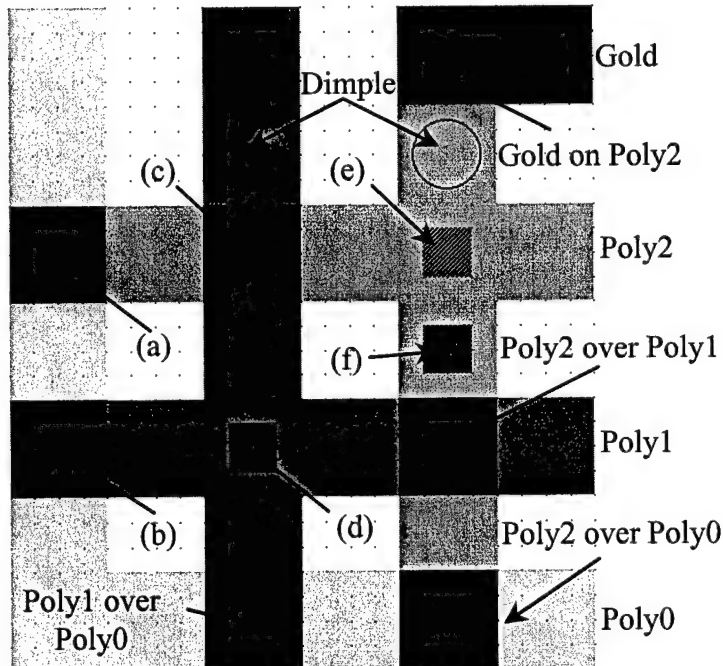


**Figure 3-6:** Depiction of the different MUMPs layer combinations as viewed from L-edit. This figure is best viewed in color.

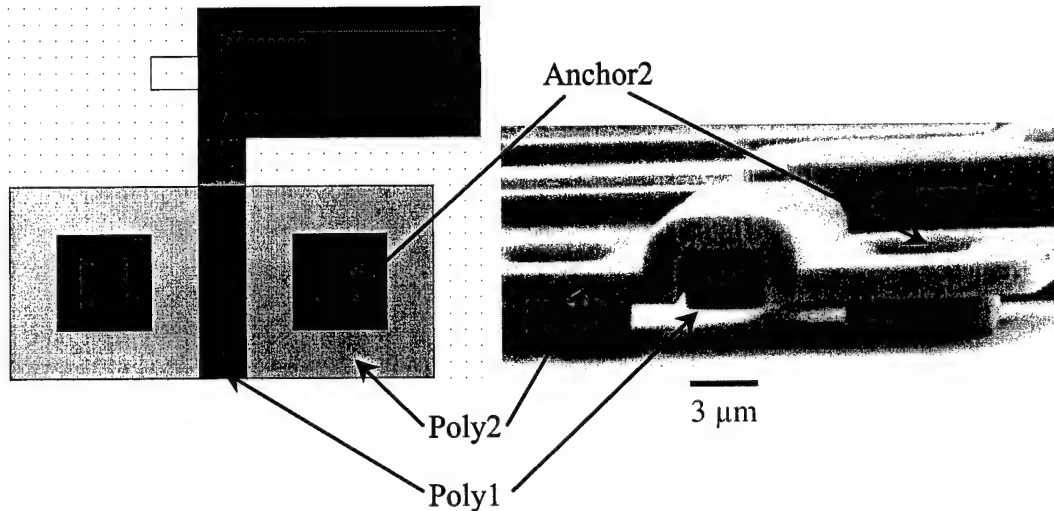


**Figure 3-7:** Comparison of CAD drawing of a substrate hinge with a SEM of same fabricated structure. This figure is best viewed in color.

### 3.3 Hinge Design

As discussed in the background, each solder joint is composed of a pair of solder pads connected to each other or near each other by hinges, as shown in the CAD of Figure 3-8. For a solder joint that has one pad fixed to the substrate, such as solder joint 1 in Figure 3-2, "substrate hinges" are used. For a solder joint that has both pads as part of free standing structures, such as solder joint 2 in Figure 3-2, "scissor hinges" are used. Pister et al. has the privilege of the first publication on these obvious and useful surface micromachined components [3].

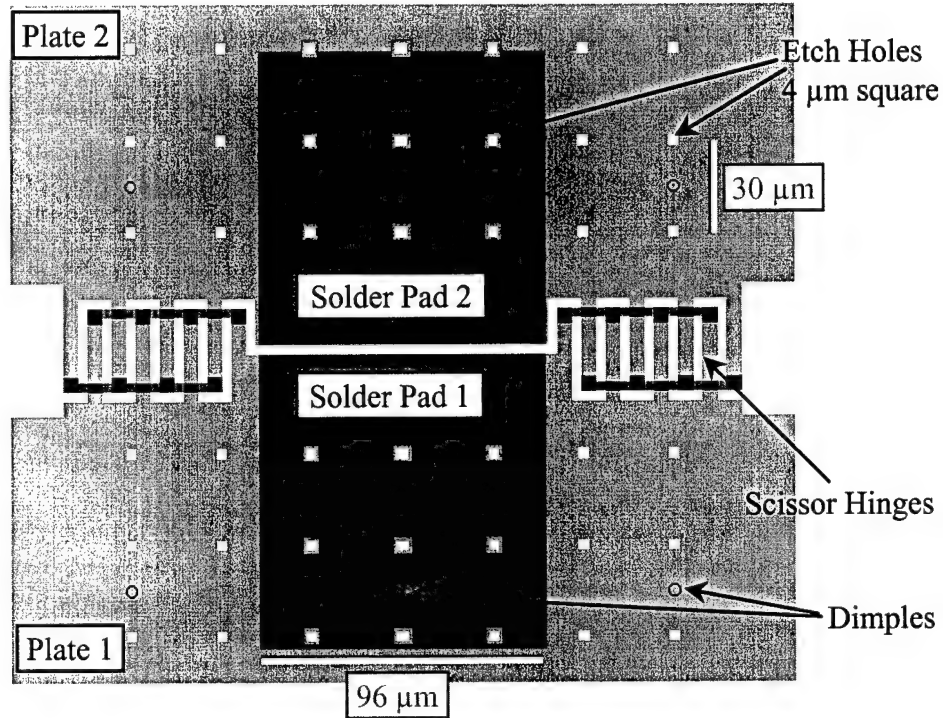


**Figure 3-8:** CAD drawing of a solder pad pair.

The sole purpose of hinges in a solder self-assembled structure is to provide some manner of loose definition of the pivot point of the solder self-assembly during reflow. The hinges do not provide structural support. The solidified solder joint provides structural support. In general, the more the hinges used at a single joint, the more the solder assembly pivot point will be defined at that joint.

Multiple joint solder self-assembled MEMS may have several solder joints assembled at different angles. Unfortunately one substrate hinge design and one scissor hinge design cannot be used for all angles. If a hinge is not specifically designed for a specific assembly angle, the hinge may cause the solder joint to bind during reflow, not allowing the joint to reach the desired equilibrium angle.

### 3.3.1 Substrate Hinge Design

The following discussion is with reference to Figure 3-9. Substrate hinges should be designed according to the following restrictions:

$$l_{h1} \geq \frac{t_{p1} \cos(\alpha) + t_{p2}}{\sin(\alpha)} , \quad (3-1)$$

$$l_{h2} \geq \frac{t_{p1} + t_{p2} \cos(\alpha)}{\sin(\alpha)} , \quad (3-2)$$

and

$$l_{h1} + l_{h2} \geq \text{minimum fabrication spacing}, \quad (3-3)$$

where  $l_{h1}$  is the distance from the edge of solder pad 1 to the point where the hinge is contacting the substrate,  $l_{h2}$  is the distance from the edge of the hinge to the edge of solder pad 2,  $t_{p1}$  is the height from the substrate to the top of solder pad 1 with the thickness of the gold not included,  $t_{p2}$  is the distance from the edge of the hinge touching the substrate to the surface of solder pad 2 with the thickness of the gold not included, and  $\alpha$  is the desired assembly angle. With respect to the local axis references labeled in Figure 3-9,  $l_{h1}$  and  $t_{p2}$  can be greater than or less than zero.

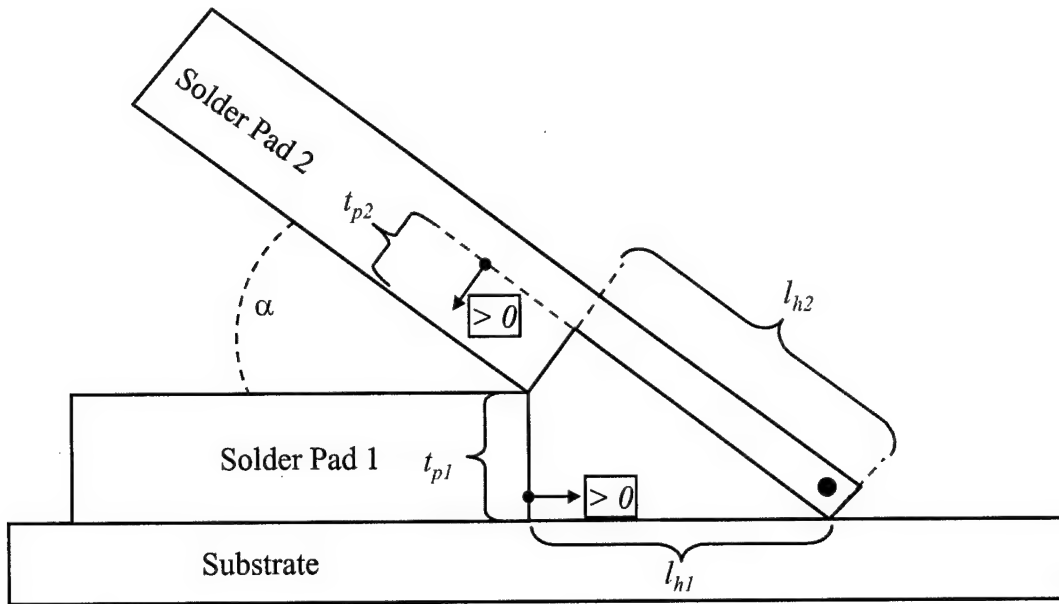


**Figure 3-9:** Depiction of a side profile of a substrate hinge arrangement at the desired assembly angle.

Abiding by these restrictions will ensure that the solder plate pair does not bind during assembly for assembly angles  $< 90^\circ$  and the edges at the joint of the solder pads meet at the desired assembly angle. Equation 3-3 ensures that the design rules of the fabrication process are not violated. Furthermore, Equation 3-3 is never violated for  $\alpha < 90^\circ$ . The thickness of the gold layer is not included in  $t_{p1}$  or  $t_{p2}$  because the gold pad will be diffused into the molten solder.

Figure 3-10 shows a CAD of a properly designed substrate hinge (left) and SEM of the actual fabricated and assembled design (right). In this case the design parameters are  $\alpha = 45^\circ$ ,  $t_{p1} = 4.25 \mu\text{m}$ , and  $t_{p2} = -2 \mu\text{m}$  (the surface of solder pad 2 is actually lower than the corner of the hinge that touches the substrate), requiring  $l_{h1} \geq 1.42 \mu\text{m}$  and  $l_{h2} \geq 4.01 \mu\text{m}$ . For the specific solder joint shown in Figure 3-10, the deposited volume of solder and solder pad dimensions turned out to be such that the

actual achieved  $\alpha$  is greater than  $45^\circ$  -- this explains why the edges of the solder pads are not quite touching each other.

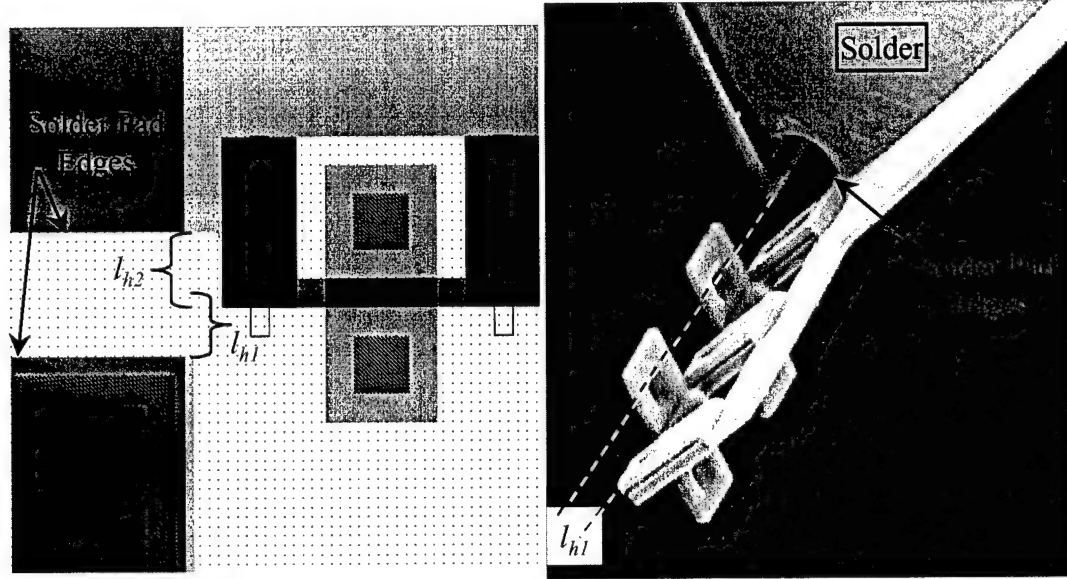


**Figure 3-10:** CAD of properly designed substrate hinge (left) and SEM of the actual fabricated and assembled design (right).

### 3.3.2 Scissor Hinge Design

The following discussion is with reference to Figure 3-11. Scissor hinges should be designed according to the following restrictions:

$$l_h \geq t_p \cot\left(\frac{\alpha}{2}\right), \quad (3-4)$$

and

$$l_h \geq \text{minimum fabrication spacing}, \quad (3-5)$$

where  $l_h$  is the distance from the edge of a solder pad to the closest edge of the scissor hinge cross member,  $t_p$  is the distance from the lowest edge of the scissor hinge cross member to the surface of the solder pad with the thickness of the gold not included,

and  $\alpha$  is the desired assembly angle. With respect to the local axis reference labeled in Figure 3-11,  $t_{p2}$  can be greater than or less than zero.

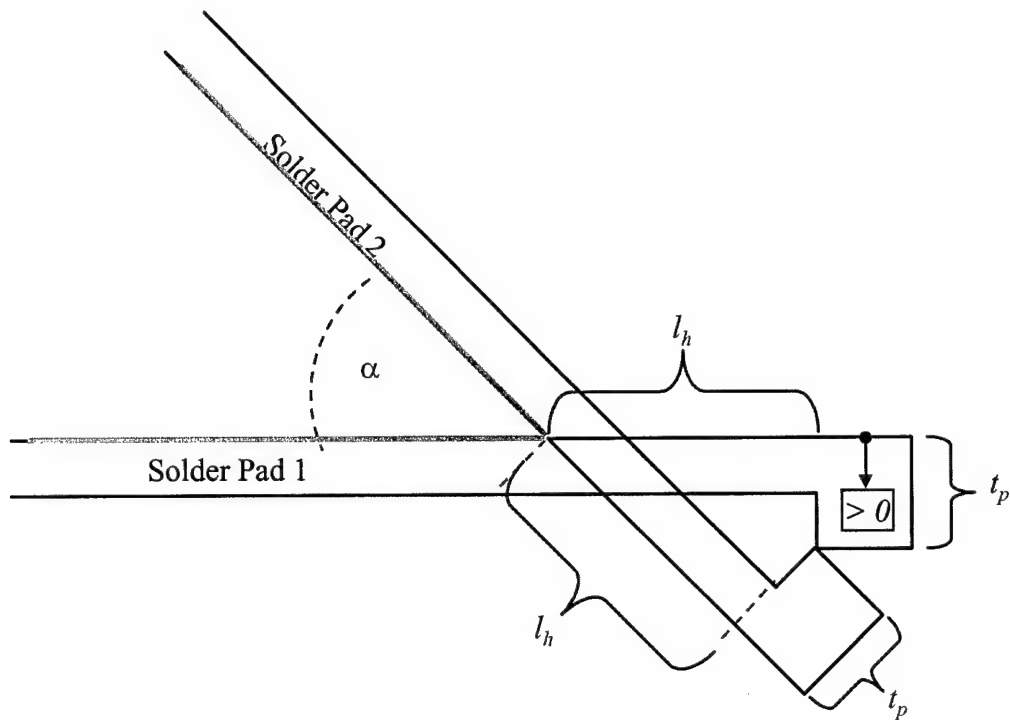


**Figure 3-11:** Depiction of a side profile of a scissor hinge arrangement at the desired assembly angle.

Abiding by these restrictions will ensure that the solder plate pair does not bind during assembly for assembly angles  $< 90^\circ$ . Equation 3-5 ensures that the design rules of the fabrication process are not violated. Furthermore, Equation 3-5 is never violated for  $\alpha < 90^\circ$ . The thickness of the gold layer is not included in  $t_p$  because the gold pad will be diffused into the molten solder.

Figure 3-12 shows a CAD of a properly designed scissor hinge (left) and SEM of the actual fabricated and assembled design (right). In this case the design parameters are  $\alpha = 45^\circ$  and  $t_p = 2.25 \mu\text{m}$  requiring  $l_h \geq 5.43 \mu\text{m}$ . For scissor hinges

the solder pads can always be designed next to each other at the minimum fabrication spacing -- see Figure 3-12. For MUMPs, a safe minimum distance is 3  $\mu\text{m}$ , but 2  $\mu\text{m}$  is possible.

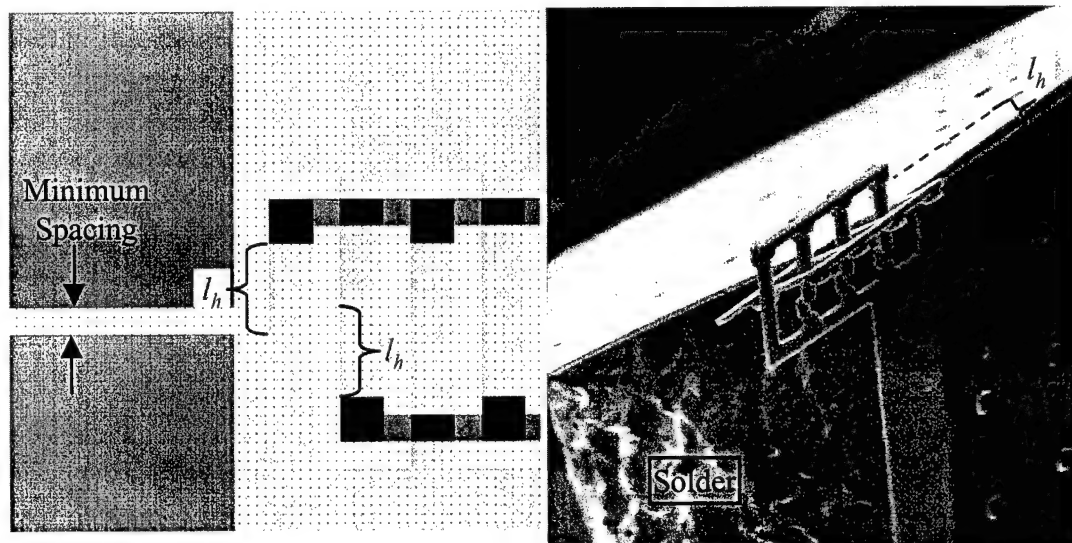


**Figure 3-12:** CAD of properly designed scissor hinge (left) and SEM of the actual fabricated and assembled design (right).

### 3.4 Solder Pad Design

#### 3.4.1 Test Structure Solder Pad Dimensions

The following solder pad dimensions were used in the test structure designs:

- a) 8 mil versions
  - 70  $\mu\text{m} \times 70 \mu\text{m}$  pads for roughly 135°
  - 131  $\mu\text{m} \times 131 \mu\text{m}$  pads for roughly 90°
  - 217  $\mu\text{m} \times 217 \mu\text{m}$  pads for roughly 45°
- b) 4 mil versions

- 33  $\mu\text{m}$  x 33  $\mu\text{m}$  pads for roughly 135°
- 69  $\mu\text{m}$  x 69  $\mu\text{m}$  pads for roughly 90°
- 96  $\mu\text{m}$  x 96  $\mu\text{m}$  pads for roughly 45°

### 3.4.2 General Joint Level Pad Design

There are as many solder pad designs as there are currently solder pad designers. However, the following general rules apply. A solder pad pair associated with substrate hinges should be designed with a spacing between them dictated by Equations (3-1) - (3-3). A solder pad pair associated with scissor hinges should be designed with a minimum fabrication spacing between them, as illustrated in Figure 3-12. Depending on the method of solder deposition, the height of the solder pads should approximately the same, thereby, increasing the probability of the solder wetting to both pads simultaneously during the preflow.

Solder pads located on free plates must have appropriately spaced etch holes. The etch holes designed on the structures used in this work are 4  $\mu\text{m}$  square, and are placed every 30  $\mu\text{m}$  center to center, as shown in Figure 3-8. One may wonder why the need for etch holes on the solder pads if the pads will be covered with solder. The reason, to be discussed in more detail in the next chapter, is because a pre-release is required in the assembly process before solder is applied. The availability of etch holes allows the sacrificial layer to be etched faster.

### 3.4.3 General Chip Level Pad Design

When laying out entire designs of multiple joint solder self-assembled structures, the method of solder deposition and location of neighboring metallized areas must be kept in mind. Solder pad pairs must be separated with enough distance as to avoid contact between deposited solder volumes or between deposited solder volumes and deposition equipment. If manufactured solder spheres are to be automatically pick-and-placed, the diameter of the solder sphere and pick-and-place capillary head must be taken into account as not to hit against already deposited spheres. Figure 3-13 is a captured video image of an array of solder assembled microrobot legs (solder deposited, but not reflowed). Volumes of solder have been deposited by thermal evaporation resulting in a  $2 \mu\text{m}$  thick layer of indium.

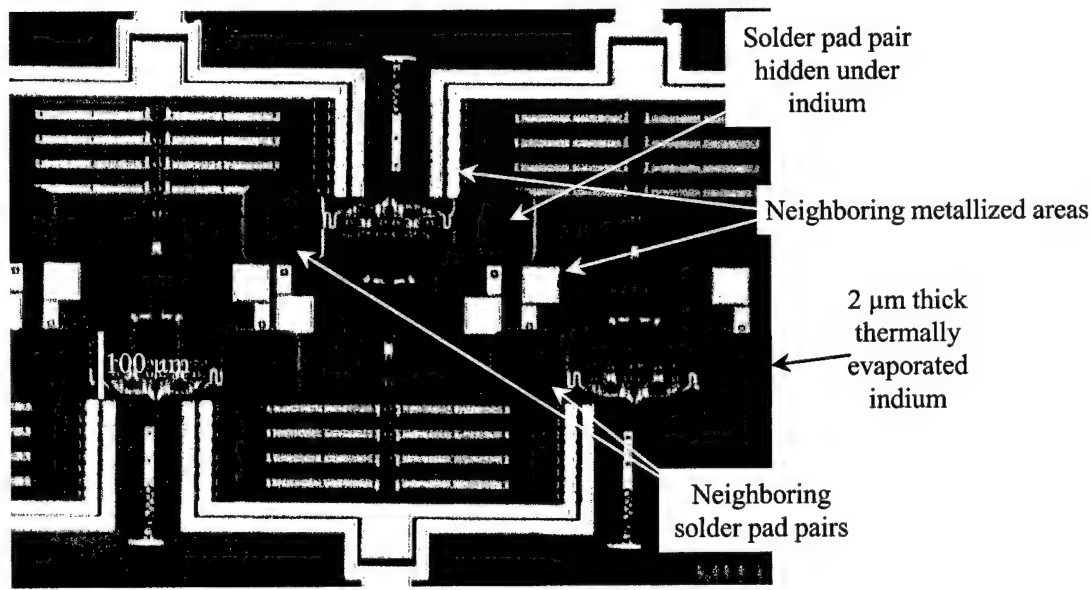


**Figure 3-13:** Captured video image of solder deposition in the form of evaporated and patterned patches of indium.

A square patch of 100  $\mu\text{m}$  was needed to get the required volume of indium for proper assembly angle. As can be seen in the figure, the designer had to be aware of the necessary width of the solder patches as to avoid contact between neighboring solder pad pairs and metallized areas. For such situations, a solder angle modeling tool, with short computation times, that can be used real-time during MEMS designs is necessary. This tool is presented in Chapter 5.

Finally, the final assembly shape must be kept in mind when designing multiple joint solder self-assembled MEMS. The solder joints must be placed such that reflowing solder joints do not assemble into each other, thereby unintentionally merging joints. Furthermore solder joints should not assemble into a metallized area of the structure, thereby unintentionally merging with another part of the structure.

### 3.5 Assembly Structure Design

Other than what has been mentioned in the preceding sections and ensuring properly spaced etch holes where necessary, solder self assembly is compatible with all aspects of MEMS design. Since the solder requires reflow at temperatures up to 200 °C any possible temperature incompatibilities with structure materials should be considered.

This work has shown that all major forms of MEMS actuation: electrostatic, electrothermal, and multilayer prestressed cantilevers are unaffected by the presence of solder joints in a structure and the necessary assembly processes. However, in general, multilayer prestressed cantilevers may not be able to be utilized during the

reflow of the solder since the misfit strain between the multilayers may be relaxed at the elevated temperature.

### 3.6 Linkage Design

To enable complex designs using a single solder joint, several methods of connection between a solder joint and other structures have been developed. The connections also serve as a means of mechanical and electrical insulation from the assembling solder joint. Figure 3-14 shows SEMs of solder self-assembled MEMS demonstrating the various methods. These three different methods are the most basic forms of linkage. Other linkage designs would just be variants of the same concept.

The pull-up method involves a solder joint on one plate assembling while simultaneously pulling up another structure connected by a linkage of any sort. The tandem method involves a solder joint on one plate assembling while simultaneously rotating up another structure connected in a side by side fashion by a linkage of any sort. And finally the push up method involves a solder joint on one plate assembling while simultaneously pushing and lifting up another structure with a linkage of appropriate design.

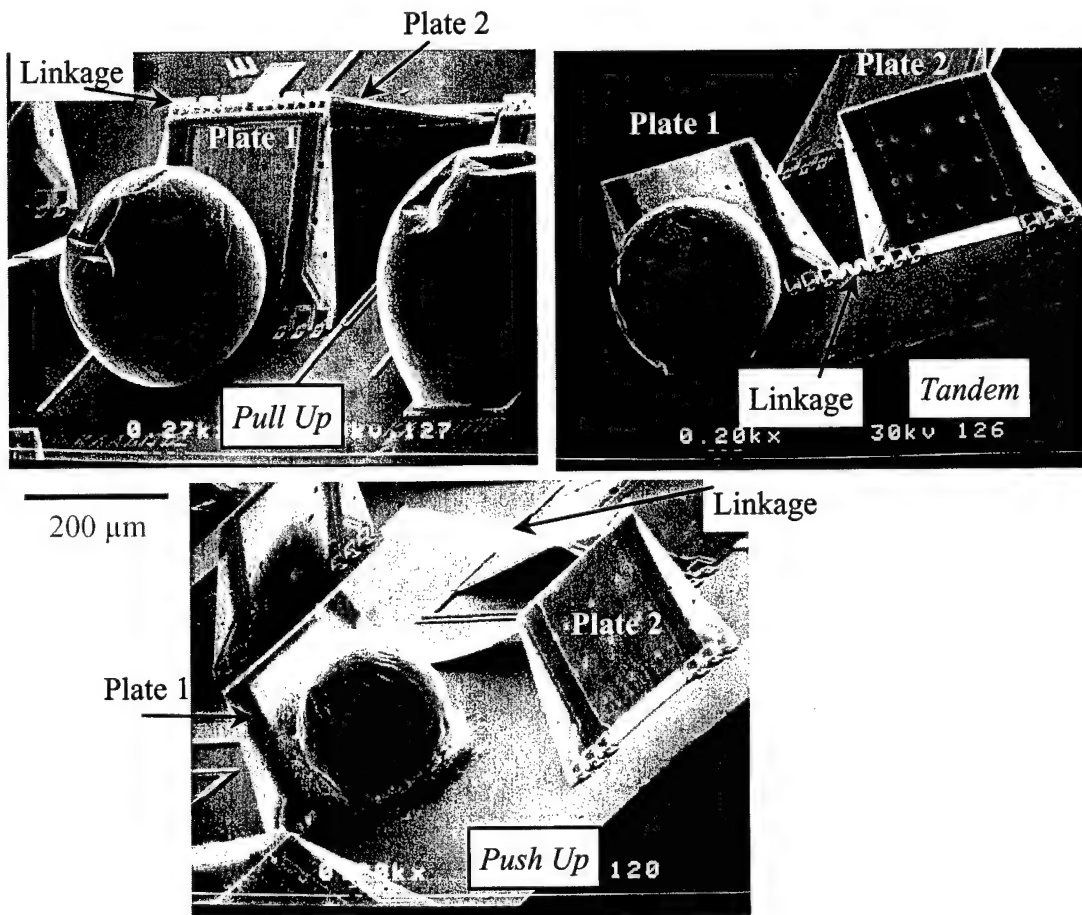


**Figure 3-14:** SEMs of solder self-assembled MEMS demonstrating the various methods of linkages developed in this research.

### 3.7 Summary

This chapter provides general guidelines for the successful design of multiple joint solder self-assembled surface micromachined MEMS. First, the design of the two-solder-joint test structures, used in this work's experiments, was described. Then, guidelines on the proper design and placement of solder joint hinges, solder pads, assembly structure, and linkages were given.

For structure fabrication processes other than surface micromachining, the guidelines may or may not need to be modified depending on the number of available

structure layers and the nature of attachment between structural layers. For bulk micro machined structures, the single structural layer, eliminates the availability of hinges. Furthermore, the nature of the sacrificial etch is different from surface micromachined structure's sacrificial etch, therefore, etch holes should be designed according to the specific bulk micromachining process.

Finally, the experiments in this work use 0.5  $\mu\text{m}$  thick gold solder pads with a 200 Å chromium adhesion layer and eutectic 63Sn/37Pb solder. In this case the gold solder pads, and possibly the adhesion layer, diffuse completely into the solder. For a different process, using a different solder and solder pad combination, the solder pad may not diffuse completely into the solder. Therefore, the thickness of the solder pad must be accounted for in Equations (3-1), (3-2), and (3-4).

### 3.8 References

- [1] Tanner EDA, A Division of Tanner Research, Inc., 2650 East Foothill Blvd. Pasadena, CA 91107, Tel: (626) 792-3000, U.S.A.
- [2] GDS II - Design interchange format developed by, and trademark of, Calma Company, a wholly owned subsidiary of General Electric Company, U.S.A.
- [3] K. S. J. Pister, M. W. Judy, S. R. Burgett, and R. S. Fearing, "Microfabricated hinges," *Sensors and Actuators A*, vol. 33, pp. 249-256, 1992.

## **4 Issues In Manufacture And Processing**

This chapter presents the "how to" of multiple joint solder self-assembled MEMS. The previous chapter described the design and fabrication of a multiple joint solder self-assembled MEMS and ends with fabricated and unreleased MEMS. This chapter conceptually begins with fabricated and unreleased MEMS and basically describes the issues concerning how solder is applied, melted, and made to assemble the MEMS. This chapter ends by addressing the different issues that cause solder joint failures and deviations from ideal assembly.

### **4.1 Solder And Solder Pad Material Issues**

Solder self-assembly requires three basic elements:

- a) Solder,
- b) Metallized solder pads for the solder to be wetted to, and
- c) A means of removing and inhibiting oxidation of the solder and solder pads during reflow (flux).

Three types of solder were used for this research: pure thermally evaporated indium (In), 8 mil diameter 60In/40Pb (Pb = lead) manufactured solder spheres, and 4 & 8 mil diameter 63Sn/37Pb (Sn = tin) manufactured solder spheres. This research was restricted to using the commercial surface micromachining process MUMPs. The available metal layer in this process is gold (Au). Since this research is dealing with the soldering of MEMS, a gaseous flux is required, because the surface tension of liquid flux would destroy assembled microstructures. I tried two types of gaseous flux schemes: reflow in nitrogen gas ( $N_2$ ) bubbled through formic acid and reflow in

pure N<sub>2</sub>. Table 4-1 gives a comparison of the results for different combinations of solder material, solder pad, and flux combinations. All reflow and preflow of solder was performed using the reflow station described in Appendix A, Section A.6. The indium thermal evaporation procedures are also described in Appendix A, Section A.8 and A.13.

Solder	Solder Pad	Flux	Results
In	Au	N <sub>2</sub>	<b>Drawbacks:</b> Solder surface remains oxidized, no reflow
In	Au	N <sub>2</sub> & Formic Acid	<b>Benefits:</b> Good successful reflow of solder <b>Drawbacks:</b> Slight film of condensed In coats all surfaces surrounding solder joint.
60In/40Pb	Au	N <sub>2</sub>	<b>Drawbacks:</b> Solder surface remains oxidized, no reflow
60In/40Pb	Au	N <sub>2</sub> & Formic Acid	<b>Benefits:</b> Successful reflow of solder <b>Drawbacks:</b> Slight film of condensed In coats all surfaces surrounding solder joint, heavy growth of In whiskers from solder - solder pad interface, and significant reduction of solder joint volume during reflow.
63Sn/37Pb	Au	N <sub>2</sub>	<b>Drawbacks:</b> Solder surface remains oxidized, no reflow
63Sn/37Pb	Au	N <sub>2</sub> & Formic Acid	<b>Benefits:</b> Excellent successful reflow of solder, excellent wetting to Au pads <b>Drawbacks:</b> Scavenging of Au pads

**Table 4-1:** Comparison of solder material, solder pad, and flux combinations tried during this research.

#### 4.1.1 Indium Solder On Gold Pads

The drawbacks of the pure indium reflow do not make that process unusable.

The indium film gives the gold surfaces a rough and dark appearance, ruining their reflectivity for ambient light. I have not determined if the film coating the substrate causes undesired electrostatic pathways that would interfere with electrostatic

actuation schemes. I have determined that the indium film does not interfere with DC operation of actuators. Furthermore, since the indium film only forms in the presence of the formic acid vapor, it is my hypothesis that a change in flux would resolve this problem.

#### 4.1.2 60In/40Pb Solder On Gold Pads

Figure 4-1 shows the results for 60In/40Pb reflow -- note the presence of the whisker-like fur growing out from the solder - solder pad interface. Through X-ray fluorescence, it was determined that the elemental constitution of the whiskers is at least pure indium. The presence of oxygen (whisker may be an oxide of indium) was not confirmed since X-ray fluorescence can not resolve, the relatively weaker, energy spectra of oxygen.

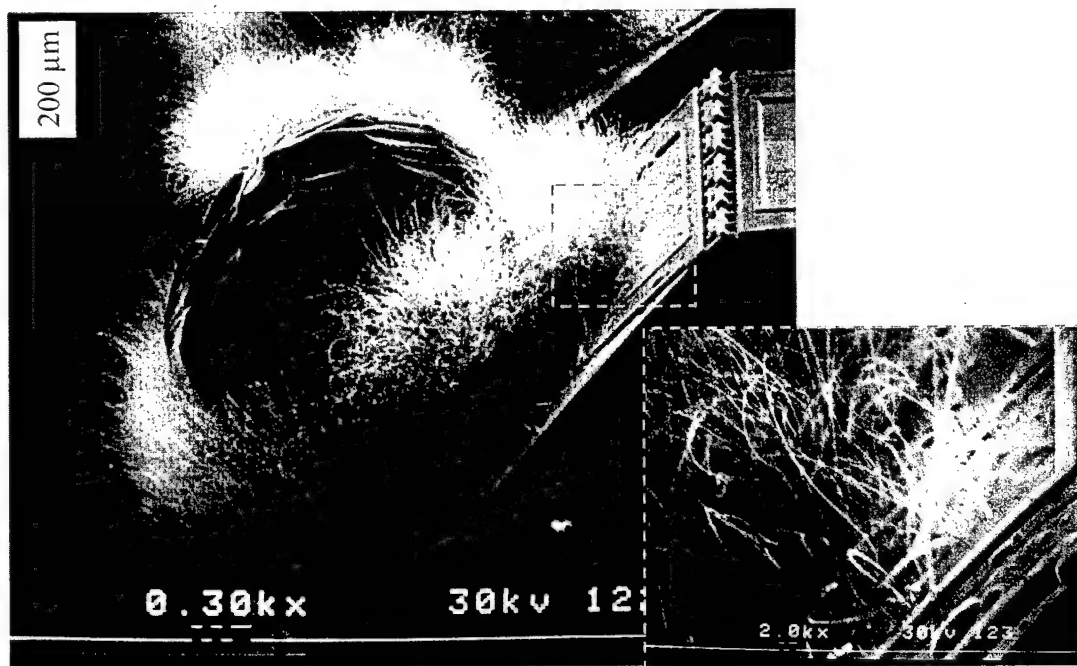


**Figure 4-1:** SEM showing whisker-like growth from the 60In/40Pb solder - gold solder pad interface.

The whiskers are most likely acicular crystal growth, which, is a possible crystal formation of elements with a tetragonal structure, such as In. Furthermore, the whiskers are similar to the tin whisker problem common on tin plated finishes of electronic components. The general consensus is that the tin whisker growth is initiated from surface sites of high stress [1]. Brusse provides a clear and succinct overview of the tin whisker problem [2]. During reflow, the solder - solder pad interface would be a sight of relatively high stress, since the surface tension of the solder surface is applying a traction at the interface.

#### **4.1.3 63Sn/37Pb Solder On Au Pads**

The best solder in combination with the gold solder pad and formic acid vapor flux was 63Sn/37Pb. This solder was chosen as the solder of choice for all of the test structure experiments. From henceforward it should be assumed that all solder joints referred to, in the following sections and chapters, are made from 63Sn/37Pb, unless specifically stated otherwise. 63Sn/37Pb solder exhibited an oxide free surface during formic acid vapor reflow – important for the solder joint to reach the modeled equilibrium angle. 63Sn/37Pb solder also wets extremely well to the gold pads. The excellent wetting of the 63Sn/37Pb solder has also presented a drawback – scavenging or consumption of the gold pads. In other words, scavenging is the separation of the solder from the original location of the solder pad, leaving behind, possibly, only the 200 Å Chromium (Cr) adhesion layer. Scavenging is addressed later in this chapter.

## **4.2 Deposition Techniques and Processes**

Several methods exist commercially for defining a volume of solder onto solder pads. Currently, these methods are only applied to microelectronics packaging commercially. Figure 4-2 is a simplified depiction of different methods of commercial solder deposition:

- a) Pick and Place – where manufactured solder spheres are picked up in some manner and placed, with flux, onto the solder pads.
- b) Lift-Off – where solder is evaporated or sputtered onto areas defined by a photoresist pattern that will later be stripped from the chip.
- c) Electroplating – where solder is electrochemically deposited onto solder pad areas defined by photoresist.
- d) Screen Printing – where solder paste is wiped through a hard stencil of some sort of the solder pads.
- e) Paste Ejection – where solder paste is dispensed onto solder pads.
- f) Jet Printing – similar to inkjet printing, a drop of molten solder is squirted out onto solder pads.
- g) Wave Soldering – where solderable areas are brought into contact with a layer of molten solder.

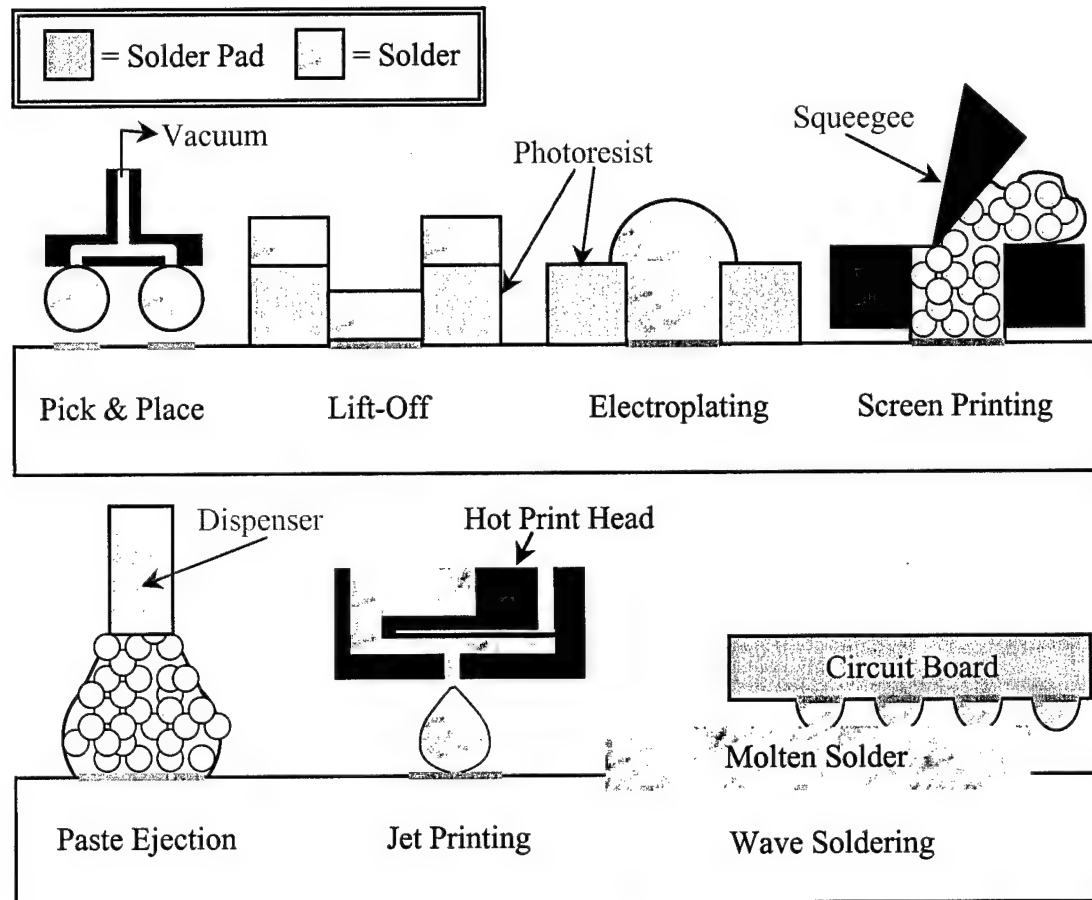


**Figure 4-2:** Depiction of different methods of commercial solder deposition.

The Lift-Off method is used to define extremely small volumes of solder for the solder self-assembly of microrobot legs, discussed in Chapter 7. For the assembly of the two-solder-joint test structure, this work takes advantage of the pick and place method. The pick and place method, used in this work, is performed manually, by hand, while working under a microscope. The procedure is as follows:

- Place manufactured solder spheres on a microscope slide, using ultra-sharp tweezers. Place another microscope slide over the top of these solder spheres – making a microscope slide sandwich with solder balls in the middle.

- b) Press on the top slide, smashing solder balls slightly, until a disk shape is achieved, with a flat spot diameter roughly the same width of one solder pad.
- c) Carefully place solder disks, using micromanipulation probes, in a position centered between solder pads, as exemplified in Figure 4-3. Solder disks may be impaled slightly with one probe to pick them up, and then wiped off, using a second probe, onto the desired location.

Steps a) – c), above, are necessary to increase the likelihood of the solder wetting to both solder pads and prevent the solder ball from rolling away from the joint.

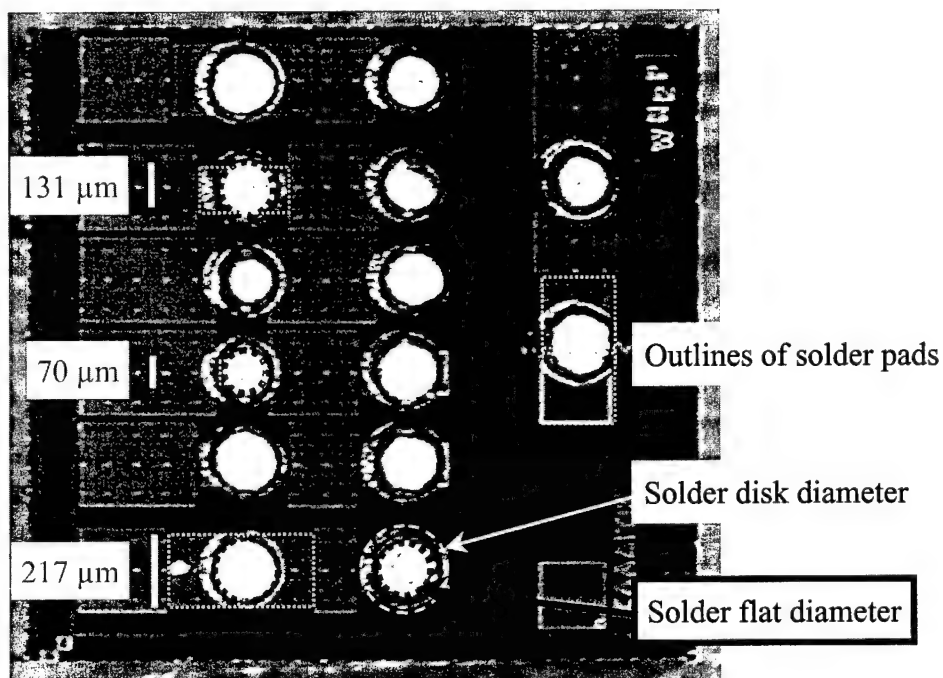


**Figure 4-3:** Example of flattened 8 mil diameter manufactured solder sphere disk placement. Three solder pad sizes are indicated 217  $\mu\text{m}$  x 217  $\mu\text{m}$ , 131  $\mu\text{m}$  x 131  $\mu\text{m}$ , and 70  $\mu\text{m}$  x 70  $\mu\text{m}$ .

### **4.3 High Yield Assembly Process**

While developing the high yield process necessary for multiple joint solder self-assembled MEMS, more than 866, by hand, pick and placed solder joints were processed. I have classified 49 solder joints as failures – a failure being defined as a solder joint that did not assemble. Therefore, the yield for this process is  $100 \times (866 - 49)/866 = 94.3\%$ . A high yield compared to existing solder self-assembly processes. The following steps outline the high yield process.

#### **4.3.1 Pre-Release**

A pre-release is necessary for the successful assembly of the test structures. Perform a pre-release and dry as outlined in Appendix A, Section A.9 with an etch time of 30 seconds.

#### **4.3.2 Preflow**

- a) This process assumes that it is beginning with an unreleased MUMPs chip, stripped of photoresist, ultra clean, and uncontaminated with any foreign matter (see Release procedures in Appendix A, Section A.9).
- b) For 8 mil solder sphere volume assembly only: plasma clean chip for 1 minute (see procedures in Appendix A, Section A.7). Do not plasma clean chip for 4 mil solder sphere assembly.
- c) Place chip in the center of the heating stage of the reflow station (see Reflow Station in Appendix A, Section A.6).

- d) Place solder disks on solder pads according to the procedures listed in Section 4.2.
- e) Cover heating stage with chamber, flow N<sub>2</sub> at 20 mm (1 liter/minute), and activate heater set at 180 °C.
- f) When controller indicates a stage temperature of 180 °C, wait 3 minutes.
- g) Increase controller to 183 °C, and immediately begin a 3 minute wait.
- h) Increase controller 1 °C per minute to 185 °C. Begin one minute wait immediately after increasing the controller.
- i) Increase controller to 186 °C. When the temperature controller indicates that the stage has reached 186 °C, you should observe slight shape changes and crumpling motions in the solder disk.
- j) Approximately 30 seconds after the stage has reached 186 °C, the slight shape changes should have ceased occurring (the solder should still have a disk shape with a crumpled foil appearance), immediately flow N<sub>2</sub>/formic acid vapor at 30 mm (2 liter/minute) while observing through microscope.
- k) While observing all solder pads across chip, as soon as you see solder begin to wet across some of the pads:
  - stop N<sub>2</sub>/formic acid vapor flow
  - increase N<sub>2</sub> flow to 50 mm (3.8 liter/minute)
  - turn off heating stage power

An average N<sub>2</sub>/formic acid vapor duration, from all preflows, is approximately 22 seconds.

- 1) Solder will continue to wet across pads. Let cool until solder solidifies. Turn off N<sub>2</sub>. Keep covered to finish cooling or carefully remove chip from stage.

Properly preflowed chips should look as shown in the following figures.

Figure 4-4 is captured video image of an unreleased preflowed chip containing an array of 8 mil version test structures. Figure 4-5 shows SEMs of an unreleased, preflowed chip containing an array of 8 mil version test structures, showing close views of individual solder joints, and solder pad dimensions. Figure 4-6 is a captured video image of an unreleased, preflowed chip containing an array of 4 mil warp version test structures. Also shown in Figure 4-6 are SEMs that show close views of individual solder joints, and solder pad dimensions. Figure 4-7 is a SEM of an unreleased, preflowed chip containing an array of 8 mil warp version test structures.

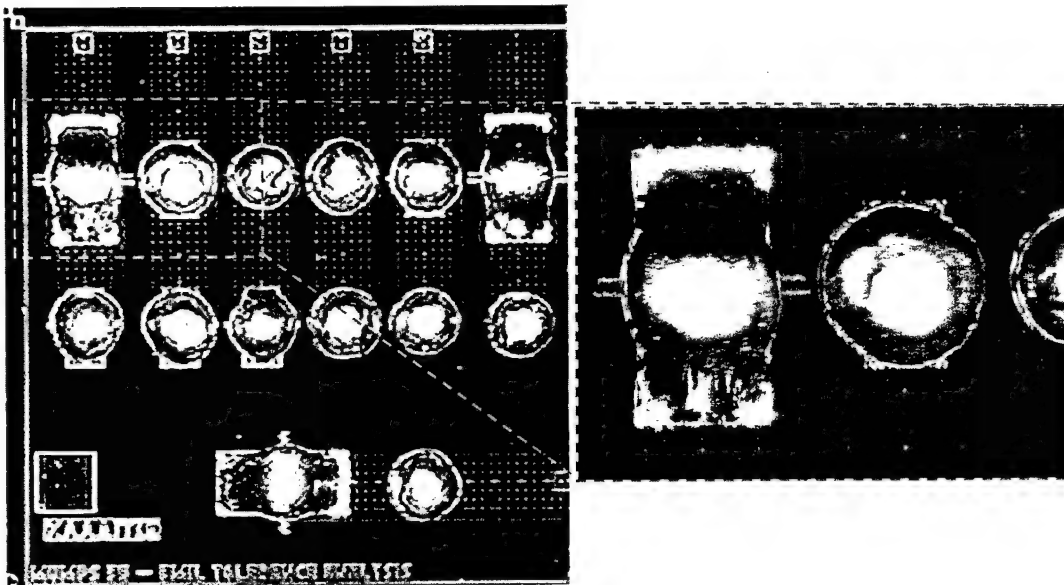


**Figure 4-4:** Captured video image of an unreleased preflowed chip containing an array of 8 mil version test structures.

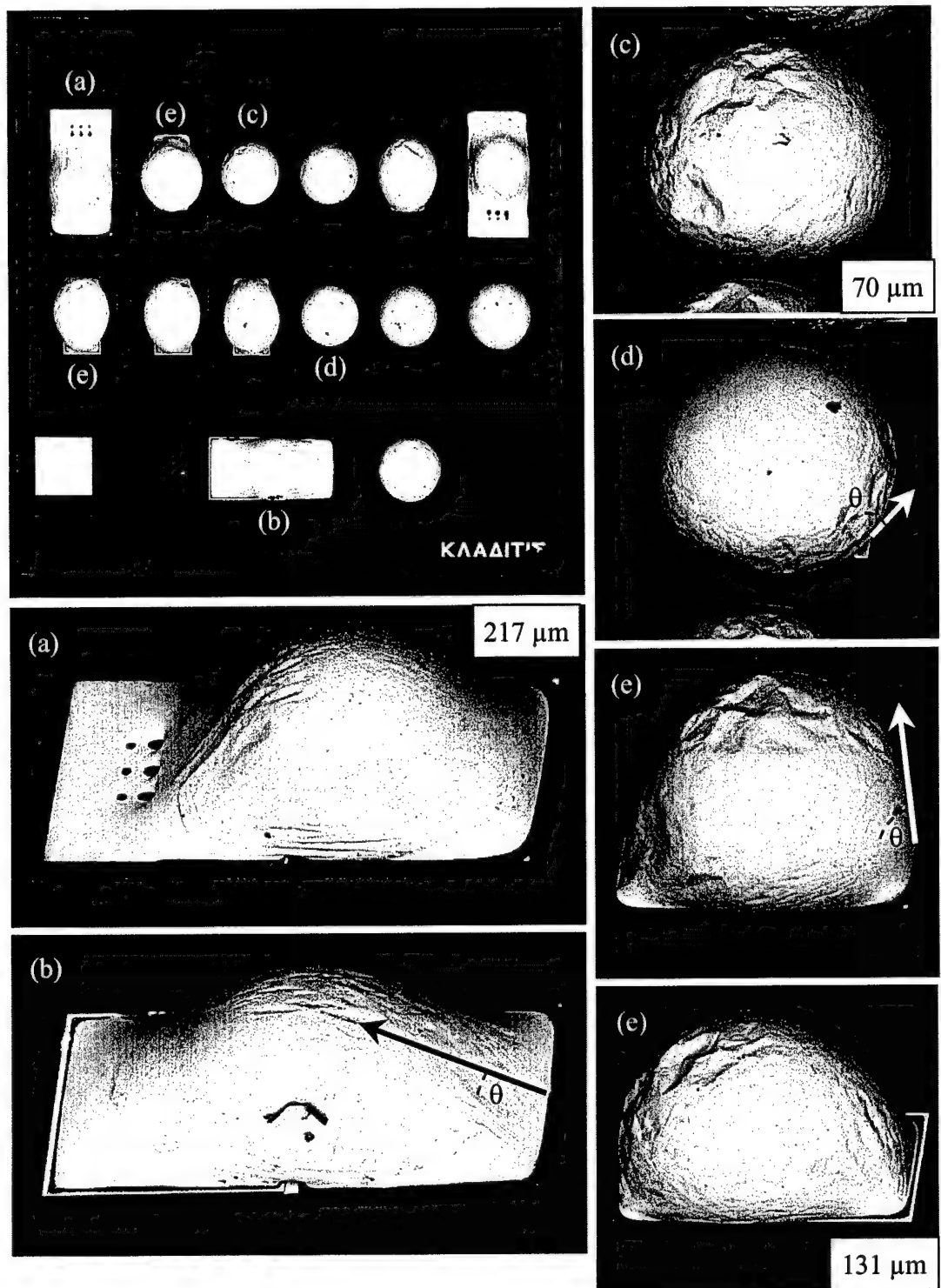


**Figure 4-5:** SEMs of an unreleased, preflowed chip containing an array of 8 mil version test structures, showing close views of individual solder joints, and solder pad dimensions.

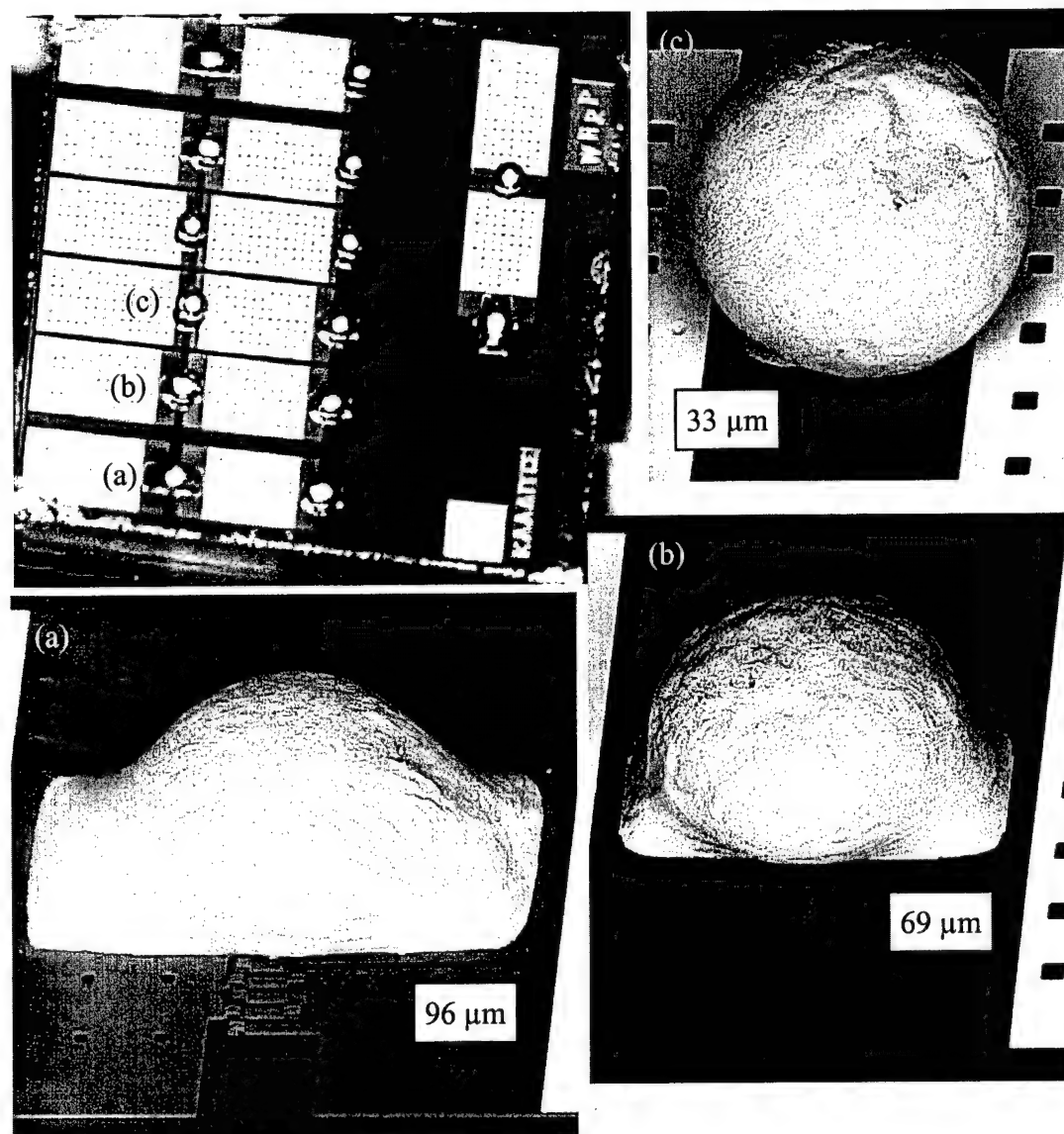


**Figure 4-6:** Captured video image of an unreleased, preflowed chip containing an array of 4 mil warp version test structures. SEMs show close views of individual solder joints, and solder pad dimensions.

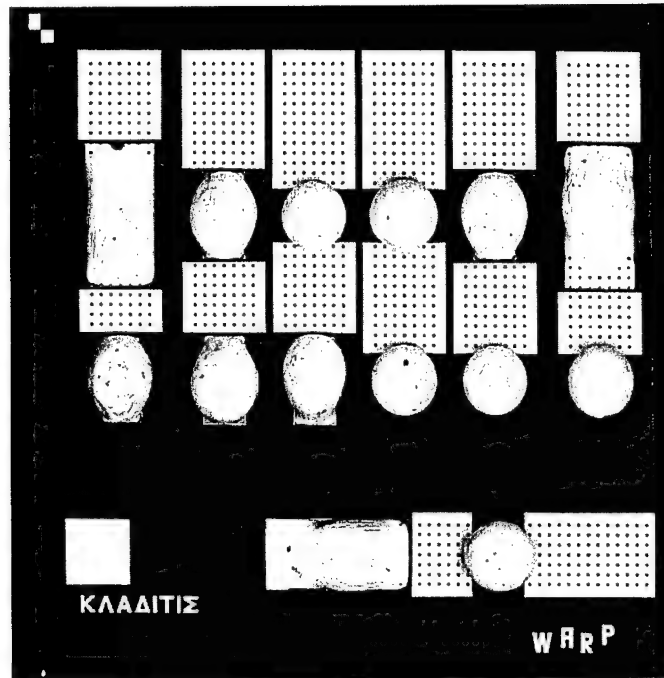


**Figure 4-7:** SEM of an unreleased, preflowed chip containing an array of 8 mil warp version test structures.

#### 4.3.3 Release

Next, the structures must be released so that they can assemble when reflowed. The release procedures are as described in Appendix A, Section A.9, starting at the HF step, with an etch time of 4 minutes. The reflow step must be performed immediately after the release. At least within an hour after release. Solder joints that are allowed to sit, for say a day, before being reflowed, take a longer time to reach and/or never fully reach their equilibrium position, during reflow. The reason for this is unknown.

#### 4.3.4 Reflow

- a) Place released chip in center of heating stage.

- b) Cover heating stage with chamber, flow N<sub>2</sub> at 20 mm (1 liter/minute), and activate heater set at 200 °C.
- c) Flow N<sub>2</sub>/formic acid vapor at 30 mm (2 liter/minute) when controller indicates a stage temperature of 170 °C.
- d) Structures should begin assembling around 180 °C and be finished assembling by the time the controller is reading 198 °C. An average from all reflows gives a total N<sub>2</sub>/formic acid vapor time of 1 minute 47 seconds. As soon as assembly is finished:
  - stop N<sub>2</sub>/formic acid vapor flow
  - increase N<sub>2</sub> flow to 50 mm (3.8 liter/minute)
  - turn off heating power

Figure 4-8 is a sequence of captured video images showing reflow of a chip containing an array of seven 8 mil version test structures. The total time of assembly, from (a) to equilibrium (h), is 45 seconds. The time duration of images (a) – (f) is 28 seconds. Image (f) is captured at the point when the second solder joints begin to melt.

- e) Let cool until solder solidifies. All solder joints are usually solidified around 150 °C. Decrease N<sub>2</sub> flow to 20 mm (1 liter/minute). Keep covered to finish cooling or carefully remove chip from stage.

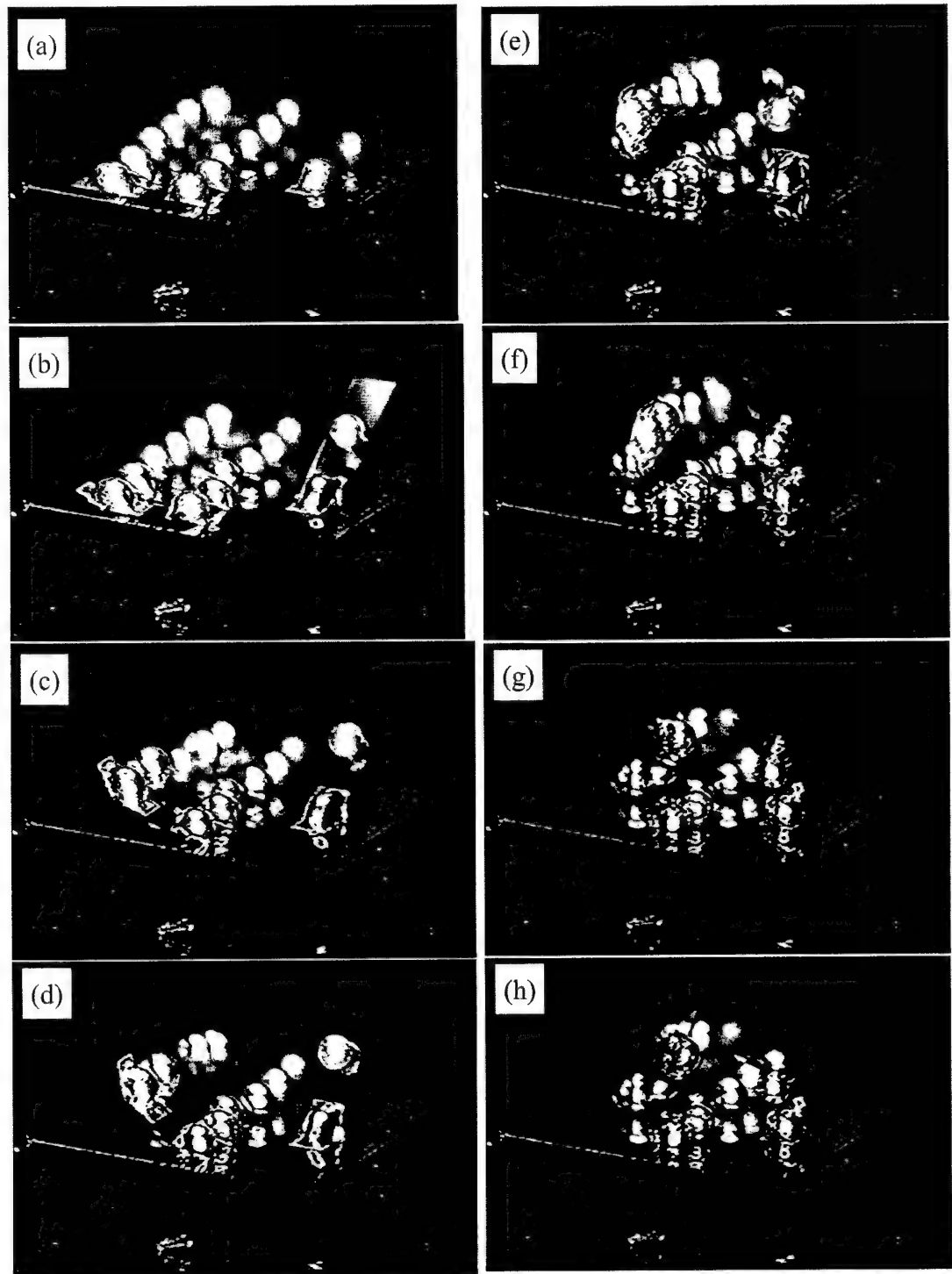


**Figure 4-8:** Sequence of captured video images showing reflow of a chip containing an array of seven 8 mil version test structures. The total time of assembly, from (a) to equilibrium (h), is 45 seconds. The time duration of images (a) – (f) is 28 seconds.

#### 4.4 Chemical And Temperature Issues

The assembly process for multiple joint solder self-assembled MEMS requires several chemical steps at varying temperatures. When developing a multiple joint solder self-assembled application, compatibility with the chemical and temperature processing should be considered. The following figures are a graphical representation of the chemical and temperature history during the processing steps of multiple joint solder self-assembled MEMS. Figure 4-9 is the legend for the subsequent figures.

#### Legend

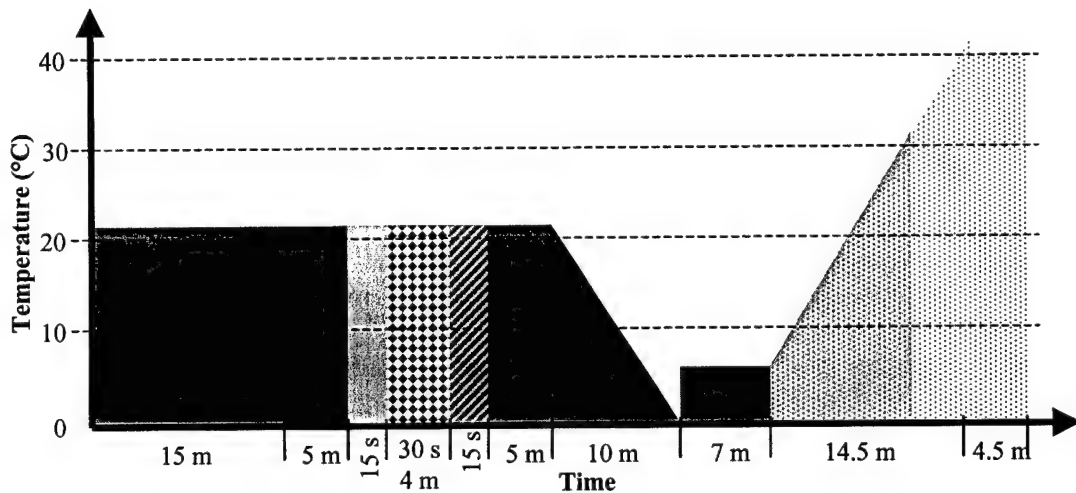
-  = Acetone (Dimethyl Ketone)  $\text{CH}_3\text{COCH}_3$
-  = 2-Propanol (Isopropyl Alcohol)  $\text{CH}_3\text{CHOHCH}_3$
-  = Deionized Water
-  = 48% Hydrofluoric Acid HF
-  = Methanol  $\text{CH}_3\text{OH}$
-  = Methanol:DIW 3:1
-  = Carbon Dioxide  $\text{CO}_2$  gas
-  =  $\text{CO}_2$  liquid
-  = Methanol mixed with liquid  $\text{CO}_2$
-  = Nitrogen  $\text{N}_2$
-  =  $\text{N}_2$  -- 88% Formic Acid HCOOH Vapor
-  = Argon plasma Ar+

m = minute  
s = seconds

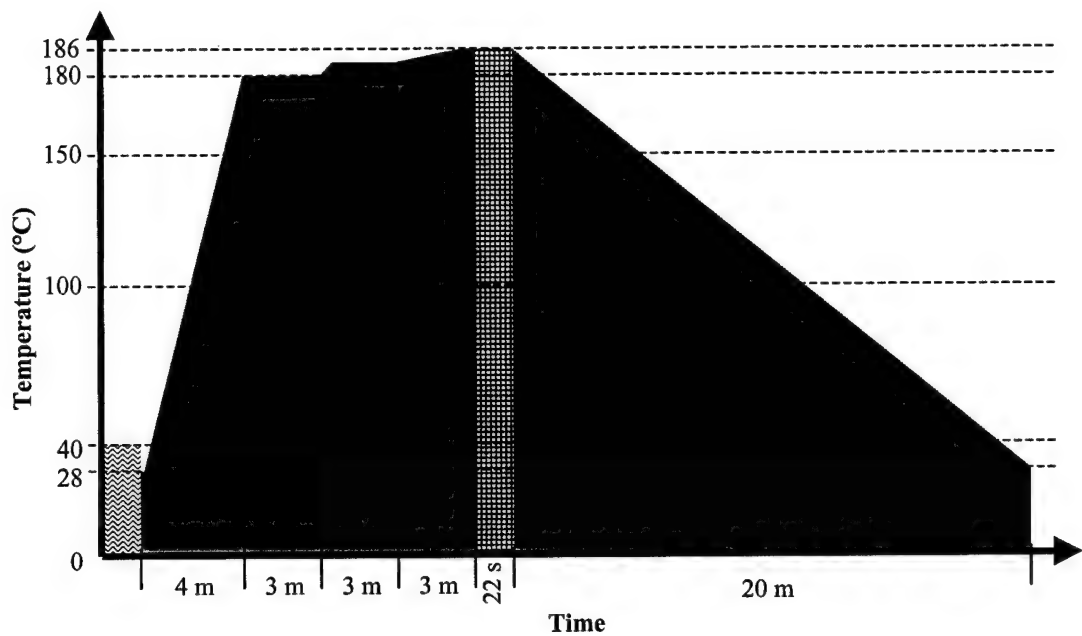
**Figure 4-9:** Legend for the following figures describing the chemical and temperature history during the processing of a multiple joint solder self-assembled MEMS. This figure is best viewed in color.

Figure 4-10 is the chemical and temperature history for either the prerelease (30 seconds in HF) and drying, or the release (4 minutes in HF) and drying of a multiple joint solder self-assembled MEMS. Figure 4-11 is the chemical and temperature history during the preflow of a multiple joint solder self-assembled MEMS. Figure 4-12 is the chemical and temperature history during the reflow of a multiple joint solder self-assembled MEMS. Note, the time intervals, representing step times in seconds, are not to scale. Furthermore, heating and cooling are represented as linear functions of time for simplicity.

Please note, that although the melting temperature for the eutectic Sn/Pb solder balls is  $\approx 183$  °C, the reflow temperature must go as high as 198 °C to ensure that the solder joints, that are raised off of the substrate, become fully molten. The heat transfer to the upper solder joints comes from convection from the substrate, and possibly mainly conduction through the polysilicon structure between joints.



**Figure 4-10:** Chemical and temperature history during the prerelease (30 s) / release (4 m) and drying of a multiple joint solder self-assembled MEMS. This figure is best viewed in color.



**Figure 4-11:** Chemical and temperature history during the preflow of a multiple joint solder self-assembled MEMS. This figure is best viewed in color.

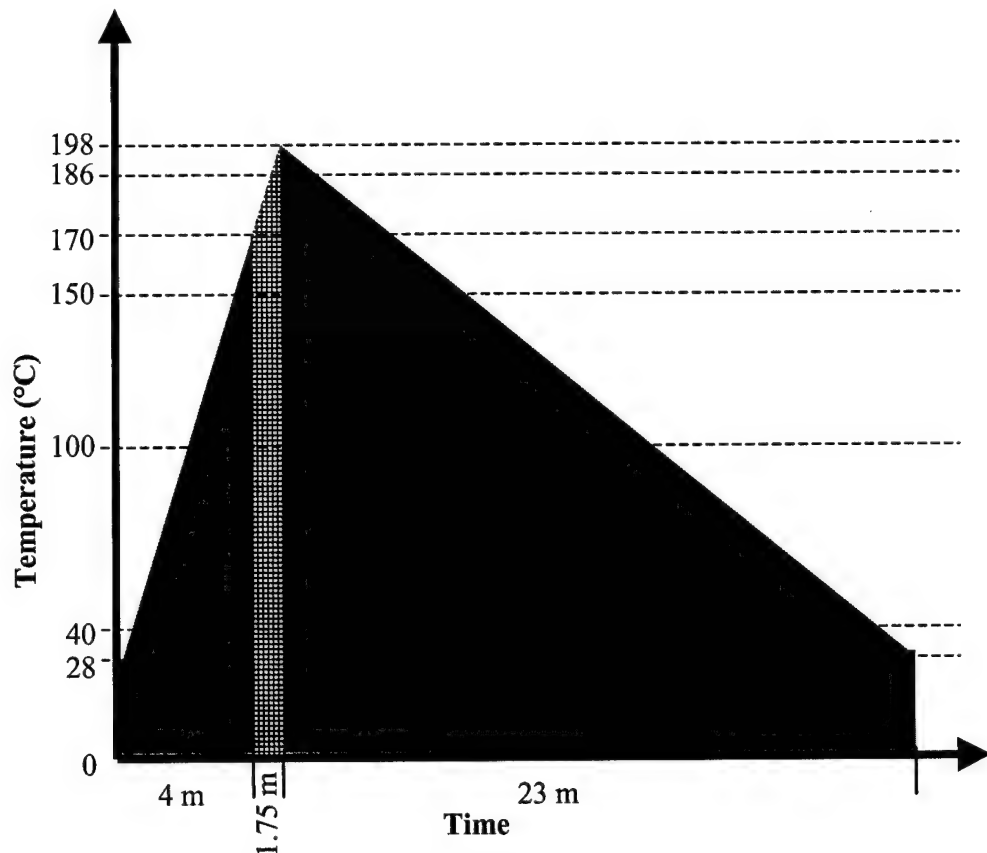


**Figure 4-12:** Chemical and temperature history during the reflow of a multiple joint solder self-assembled MEMS. This figure is best viewed in color.

## 4.5 Failure Issues

### 4.5.1 Scavenging & Overwetting

Although scavenging did not cause failure often, it can. The gold pads will completely diffuse into the solder. I have performed experiments where 4 mil and 8 mil 63Sn/37Pb manufactured solder spheres were wetted to gold pads on MUMPs chip, then immersed in 37 % hydrochloric acid (HCl) for 5 minutes. The results were that all of the solder was dissolved, including the Au where the solder pad used to be. All unsoldered Au coated regions were un-dissolved. Furthermore, during reflow and especially during preflow, de-wetting from the pad area begins occurring once the solder wetting reaches the boundary of the Au pad. The thin coating like residue, in the shape of the original gold solder pad, is also left behind in this case, and is visible by optical or scanning electron microscope observations. This thin coating may be the 200 Å Cr adhesion layer or a compound formed from some combination of Au, Cr, Sn, Pb, and/or Si.

Complete removal of the solder from the original solder pad locations was not uncommon in some of my experiments. This phenomenon, called scavenging, was tolerated for all of my experiments. The processing sequence that I developed kept the scavenging to a minimum, however. Significant scavenging was found to occur only in the presence of the formic acid vapor flux. Thus, a cornerstone of my developed process is keeping the time that the solder joints are in the formic acid flux vapor, to a minimum. I was able to qualitatively characterize the behavior of and quantify the magnitude, to some degree, of the scavenging by observation of several

hundred solder preflows and reflows, and by making random measurements of the amount of scavenging found on assembled test structure's solder joints.

Figure 4-13 is a depiction of competing surface tension forces at the perimeter of a solder joint (not to scale). The following discussion is with reference to Figure 4-13. The force vectors  $\gamma_{F-S}$ ,  $\gamma_{P-F}$ , and  $\gamma_{S-P}$  represent the solder-flux vapor, pad-flux vapor, and solder-pad surface tension forces, respectively and at the triple point. Since the gold diffuses into the solder, the pad, as discussed earlier, may be the Cr adhesion layer or something else.

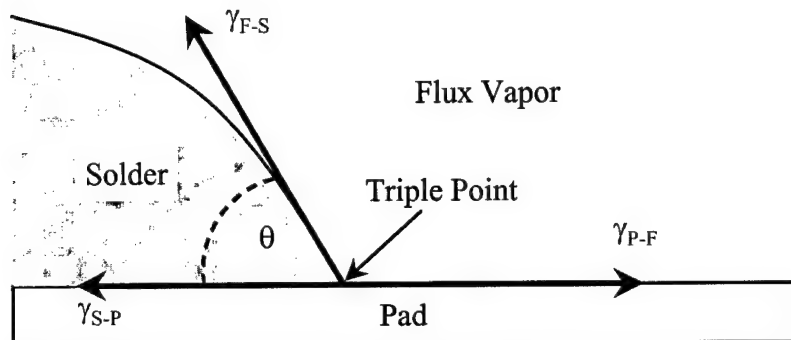


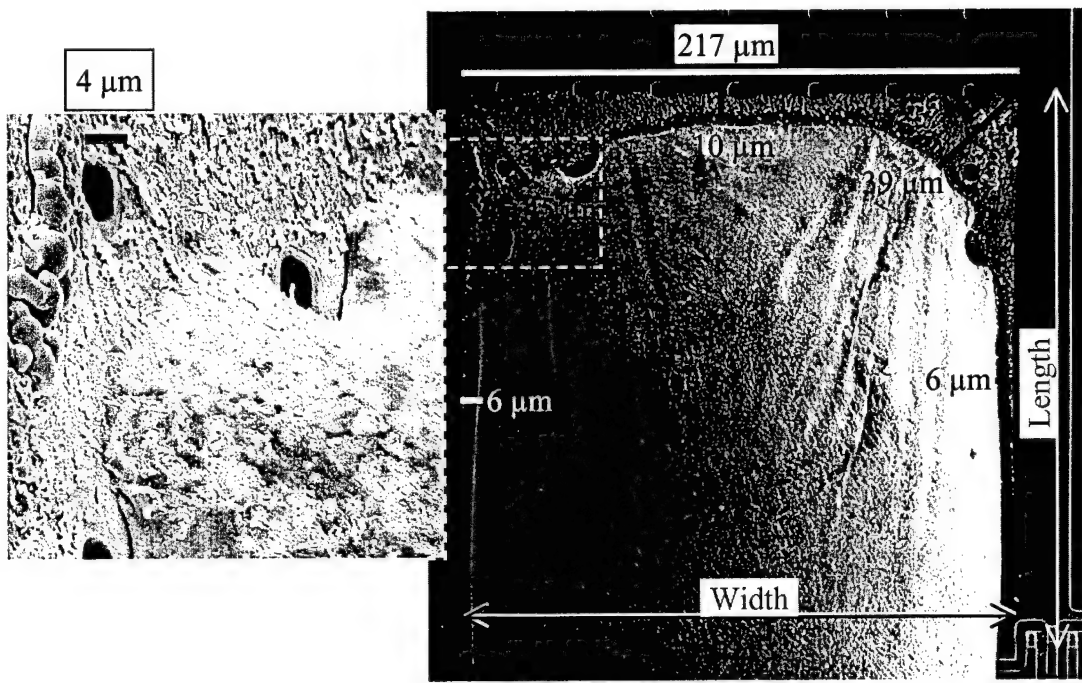
**Figure 4-13:** Depiction of competing surface tension forces at the perimeter of a solder joint (not to scale).

Initially, when the solder wets to the perimeter of the Au pad, the angle  $\theta$  is purely a function of the volume of solder and the shape of the constraining solder pad. However, if this constraint is removed by the gold completely diffusing into the solder, and the solder is allowed to stay in a fully molten state, the triple point will move to the left or right until  $\theta$  becomes the contact angle. If the weight of the solder is negligible, for fully molten solder, the contact angle is purely a function of the

solder, flux, and pad materials. Equivalently, from an energy point of view, for a given combination of solder, flux, and pad material, the solder will re-shape itself into a minimum surface energy shape.

Most of the scavenging seemed to occur during preflow. During preflow, the degree of scavenging was largest when the solder pad area was large relative to the solder volume, or equivalently, when  $\theta$ , at the solder pad perimeter constraint, is small (see Figure 4-5). By keeping the solder in a partially molten state, and minimizing the time the solder is exposed to flux vapor, the change in  $\theta$  was minimized during preflow. It is my hypothesis that the degree of scavenging is relieved somewhat, during reflow, because the solder is allowed to pull the plates together thereby, allowing  $\theta$  to approach the value of the contact angle without having to scavenge.

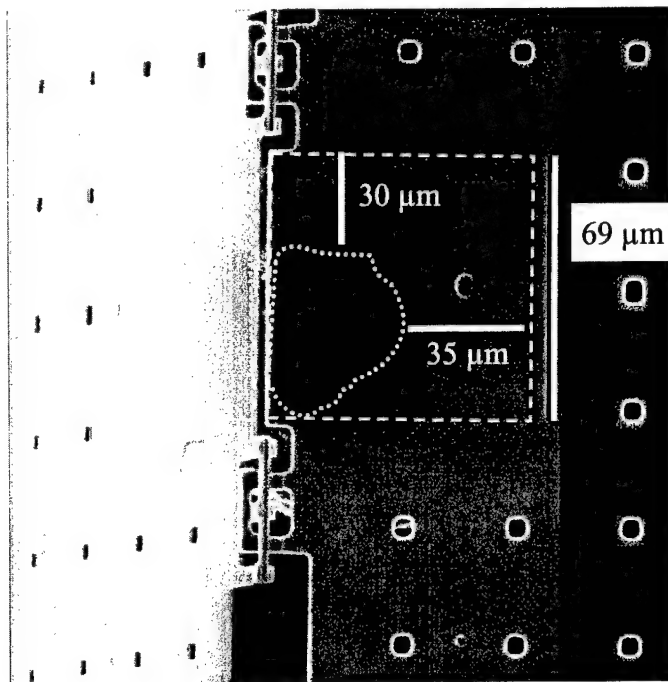
Figure 4-14 shows a SEM of a mild example of scavenging, by an 8 mil diameter equivalent volume of solder, of a preflowed solder joint. The outline of the original 217  $\mu\text{m}$  solder pad can still be seen. The degree of scavenging was found to be greater in the length of a solder pad than the width. This makes sense since the initially constrained  $\theta$  is smaller lengthwise than widthwise, and further from the value of the contact angle. The width of a solder pad is defined as the pad dimension in parallel with the axis of rotation of the solder joint. The length is perpendicular to the width, see Figure 4-14. Again, casting the explanation in terms of energy, the easiest way for the solder's surface energy (surface area) to be minimized (become more spherical), is for the triple point perimeter to first move away from the edge of the solder pad lengthwise.



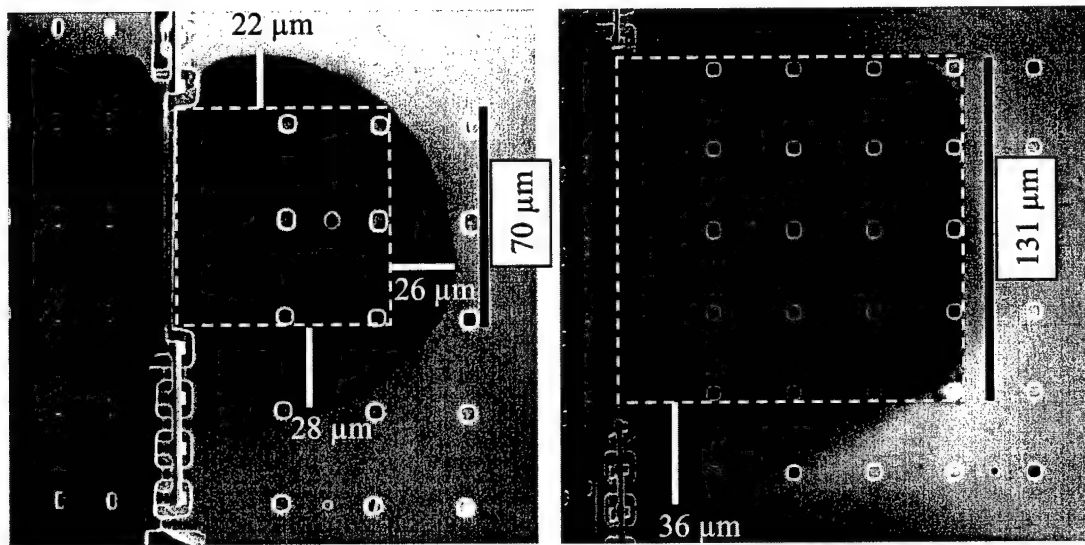
**Figure 4-14:** SEMs showing a mild example of scavenging by an 8 mil diameter equivalent volume of solder, after preflow, and before final release and reflow.

Figure 4-15 is SEM of an aggressive case of scavenging by a 4 mil diameter equivalent volume of solder after reflow. This view is from behind the solder pads where the dark area, outlined in white, is where the solder is still attached to the pad. The outlined square is the original perimeter of the solder pad.

This research discovered an unexpected behavior of the solder. For the smaller solder pads of the 4 mil ( $33 \mu\text{m}$  pads) and 8 mil ( $70 \mu\text{m}$  pads) assemblies, designed to assemble to  $135^\circ$ , it was found that the solder would actually wet out further than the solder pads. I have named this phenomenon overwetting. Figure 4-16 is a SEM showing overwetting of  $135^\circ$  8 mil solder pads (left). One uncommon example of overwetting was found on a set of  $90^\circ$  8 mil solder pads, Figure 4-16 (right).



**Figure 4-15:** SEM showing an aggressive case of scavenging by a 4 mil diameter equivalent volume of solder after reflow. This view is from behind the solder pads where the dark area, outlined in white, is where the solder is still attached to the pad.



**Figure 4-16:** SEM showing overwetting of 135° 8 mil solder pads (left) and a 90° 8 mil solder pads (right).

Observations of random samples, showed that overwetting occurred to some degree in most of the smaller 4 mil and 8 mil 135° solder pads. For the smaller solder pads, the initially constrained  $\theta$  is probably larger than the contact angle. Thus, after the Au is totally diffused into the solder, the unconstrained triple point is allowed to move until  $\theta$  reaches the contact angle or equivalently the surface energy is minimized – the same reasoning used to explain scavenging. It was also observed that the degree overwetting is greater in the width than the length. This makes sense since the initially constrained  $\theta$  is larger widthwise – or equivalently, the easiest way for the surface energy (surface area) to be minimized, is for the triple point to move away from the pads widthwise.

For the non-warp versions of the test structures, overwetting was not catastrophic – only caused smaller assembly angles than expected. However, for the warp versions of the test structure, overwetting allowed the solder to bridge the 10  $\mu\text{m}$  gap between the solder pad and the adjacent gold layer on the plate. Once the gap is bridged, giant solder pads are created causing those solder joints to rotate towards a zero degree assembly angle. Overwetting did not usually occur until reflow, however, an uncommon case of preflow overwetting is shown in Figure 4-17.

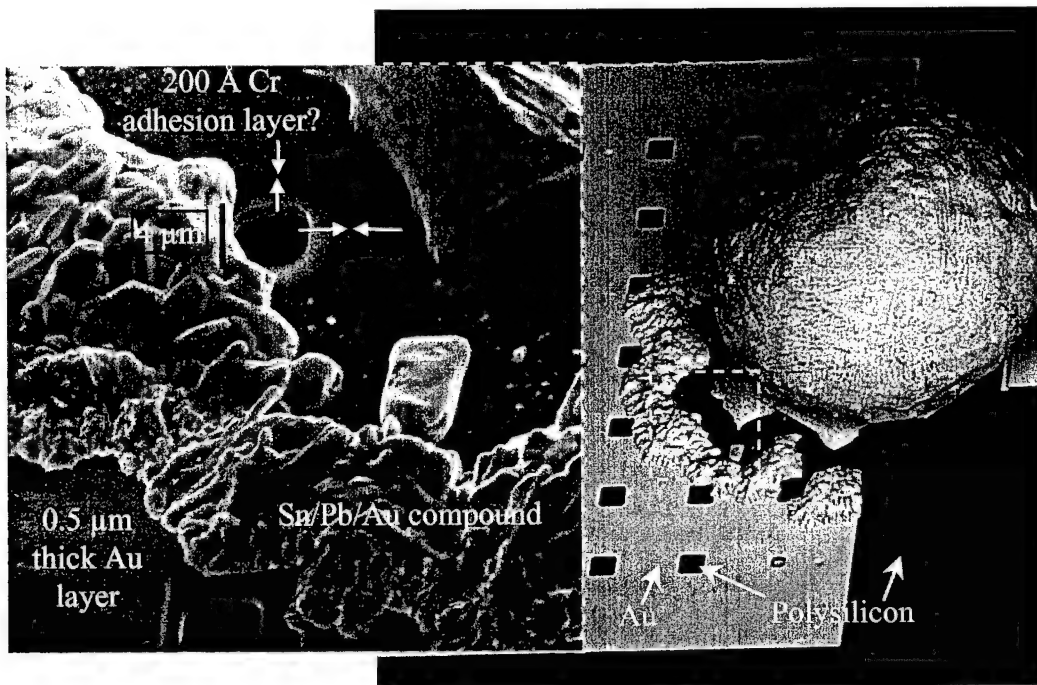


**Figure 4-17:** SEM showing overwetting of a 135° 8 mil solder pad that occurred during preflow.

Table 4-2 is an estimate of degree of scavenging and overwetting. These figures come from the largest values of a random sample of assembled test structures observed in the scanning electron microscope. Since all of the samples did not have a maximum amount of scavenging or overwetting, the largest value of scavenging or overwetting was halved. The half amount of scavenging is then considered the mean amount ( $\mu_{scav}$ ). A minus sign on the mean amount of scavenging indicates overwetting. "Early process" indicates earlier experiments where the formic acid times were not as precisely monitored. Also, please keep in mind that the width scavenging value includes the degree of scavenging from both sides of the solder pad combined. Figure 4-18 shows a particularly disturbing example where several 8 mil warp version test structures' solder joints have overwet.

Solder Pads	Amount of Scavenging in Length $\mu_{scav} \pm tol_{scav}$ ( $\mu\text{m}$ )	Amount of Scavenging in Width $\mu_{scav} \pm tol_{scav}$ ( $\mu\text{m}$ )
217 $\mu\text{m}$ (8 mil) (early process)	22 $\pm$ 22	7 $\pm$ 7
131 $\mu\text{m}$ (8 mil) (early process)	6 $\pm$ 6	6 $\pm$ 6
70 $\mu\text{m}$ (8 mil) (early process)	-9 $\pm$ 9	-18 $\pm$ 18
217 $\mu\text{m}$ (8 mil)	15 $\pm$ 15	7 $\pm$ 7
131 $\mu\text{m}$ (8 mil)	6 $\pm$ 6	6 $\pm$ 6
70 $\mu\text{m}$ (8 mil)	-5 $\pm$ 5	-18 $\pm$ 18
96 $\mu\text{m}$ (4 mil)	8 $\pm$ 8	13 $\pm$ 13
69 $\mu\text{m}$ (4 mil)	0 $\pm$ 2	0 $\pm$ 8
33 $\mu\text{m}$ (4 mil)	-2 $\pm$ 2	-6 $\pm$ 6

**Table 4-2:** Estimate of degree of scavenging and overwetting. A minus sign indicates overwetting.

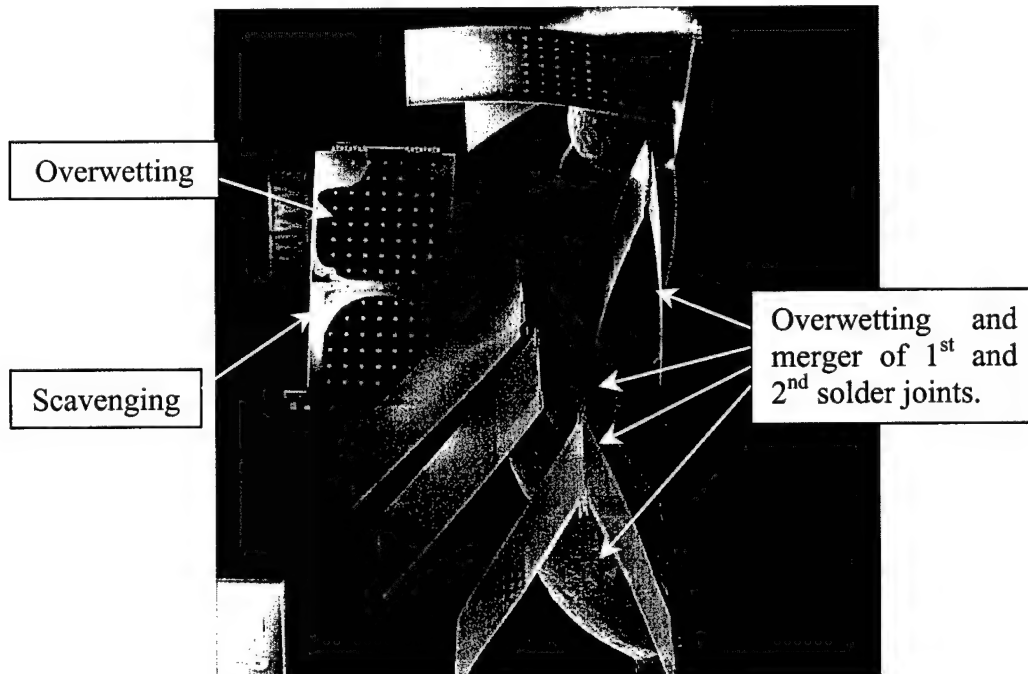


**Figure 4-18:** SEM showing a catastrophic example of overwetting on 8 mil warp version test structures.

#### **4.5.2 Preflux Wetting**

The major effect of solder size was discovered during the preflow process. It was discovered that a small percentage of the 4 mill solder balls would begin wetting to the solder pads before the flux vapor was applied at temperatures from 183 °C to 185 °C. Once 186 °C was reached and the flux vapor turned on, the solder balls that had wet early would completely scavenge and de-wet from the original solder pad locations, causing those joints to fail. To discourage the early wetting, the plasma cleaning step was eliminated from the preflow procedures for 4 mil balls. This change in process virtually eliminated the early wetting. My working hypothesis of the causes of the early wetting is that, relative to the 8 mil solder ball, the smaller volume of solder allows less heat loss and less of a temperature gradient – i.e. a hotter ball. Furthermore the small size may have a greater inconsistency in elemental proportions of Sn to Pb causing variation in melting temperature among the balls. The reasons why preflux wetted solder joints tend to totally scavenge the gold pads, once the flux vapor is applied, is unknown.

#### **4.5.3 Roll-Off**

Another mode of failure is when a solder ball only wets to one side of a pair of solder pads. This failure is called roll off. Roll off has been found to occur for several reasons:

- a) When skipping the preflow step and placing solder disks on released MEMS, then reflowing, the pad fixed to the substrate has less thermal resistance than the released side plate. The fixed plate is therefore hotter, causes the solder to

wet to it first, and pulls it away from the released side plate. Remedy – perform preflow on an unreleased or pre-released chip.

- b) The problem in a) is further compounded by a multi-joint structure such as the test structure in this research. If solder joint 1 successfully wets and begins assembly, solder joint 2 will be lifted in the air before it has time to wet and completely roll off of the structure. Remedy – perform preflow on an unreleased or pre-released chip.
- c) In some cases the nearby hinges are higher than the solder pad surface. If a solder disk that has been flattened wider than the solder pads is setting on the hinge, the solder disk will teeter to one pad or the other, and wetting may initiate at the touched pad first, thereby pulling the whole solder volume to that side. Remedy – flatten solder balls as described in the solder placement procedures.
- d) Finally, the solder pads and or solder balls may be contaminated with foreign matter such as photoresist residue. The solder just may not be able to wet to the pads with certain residues. Figure 4-19 shows an extreme example of roll-off failures due to chip-wide contamination. The make up of the contamination is unknown -- the appearance was a whitish film. The suspected source of the contamination is the plasma cleaner.

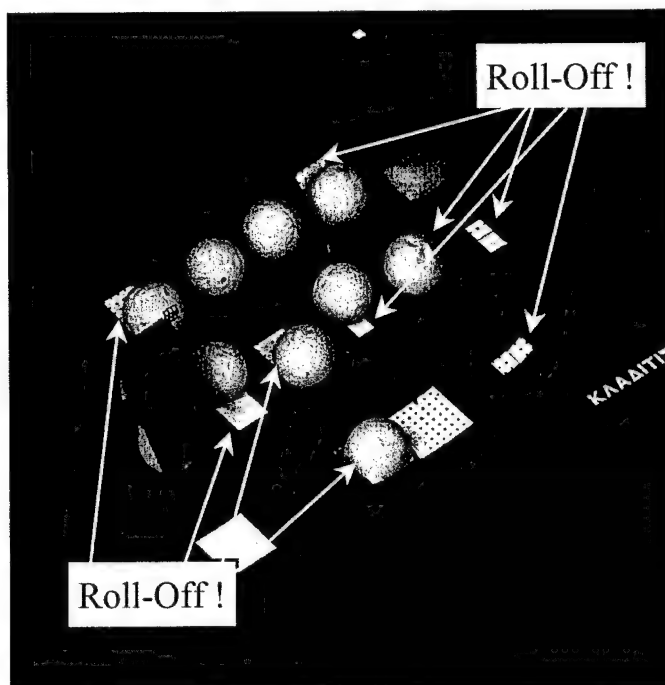


**Figure 4-19:** SEM showing an extreme example of roll-off due to contamination.

#### 4.5.4 Unreleased Solder Joints

The various combinations of angles designed into the test structure versions, revealed a special releasing requirement for the multiple joint solder self-assembled structures. Normally, etch holes are designed into large-surface-area surface micromachined structures so that HF may readily etch away the sacrificial layer during release. Small angle solder joints require large surface area solder pads. When solder wets to a solder pad during preflow, any etch holes that were on the solder pad will be blocked. During the release, the HF will not be able to etch away the sacrificial layer in a timely manner, resulting in unreliable etch times in excess of 5 minutes. An example of multiple joint solder self-assembled structures, that have not been fully released, is shown in Figure 3-4. To ensure that etch times remain short and guarantee fully released structures, a pre-release sequence was added to the

multiple joint solder self-assembled MEMS processing. Structures with solder pads over 131  $\mu\text{m}$  long or wide require a pre-release.

#### 4.6 Summary

This chapter provides general guidelines for the successful processing of multiple joint solder self-assembled surface micromachined MEMS. First, the benefits and drawbacks of the different solder, solder pad, and flux combinations were described. Then methods of solder deposition were described. Next, the prerelease, preflow, release, and reflow processes were described. Details of the temperature, chemical, and time history for the processes were also given. The different sources of solder joint failure: scavenging, overwetting, preflux wetting, roll-off, and unreleased solder joints were described.

Although the process I developed and outlined in this chapter are optimum for the available resources at the University of Colorado. I would suggest making the following changes to make things better.

- a) Assuming a Sn/Pb on gold pads and formic acid vapor flux process, I would make the following changes to minimize or eliminate scavenging and overwetting:
  - Find another type of flux or reflow environment that minimizes or eliminates scavenging while at the same time allows an oxide free solder surface.
- b) Assuming any process, I would make the following changes to minimize or eliminate scavenging and overwetting:

- Find another type of solder, solder pad, and flux combination. Possibly adding a copper or nickel layer under the gold while keeping a formic acid vapor flux and tin/lead solder.
- c) Many failures are caused by the solder not wetting to one or both solder pads for the tin/lead solder experiments. I would investigate a method of tin/lead solder application that guarantees wetting to both solder pads, such as, electroplated solder or paste ejection.
- d) Prerelease should be performed regardless of solder pad size, thereby, ensuring release by minimizing the effects of process variations such as release temperature.

#### 4.7 References

- [1] M. Ishii, T. Kataoka, and H. Kurihara, "Whisker problem in the ultra-fine pitch circuits," *Proceedings of the 12<sup>th</sup> European Microelectronics & Packaging Conference – iMAPS*, Harrogate, Yorkshire, England, pp. 379-385, 7-9 June, 1999.
- [2] J. Brusse, "Tin whiskers: revisiting an old problem," *Electronic Packaging & Space Parts News - EEE Links*, NASA/GSFC Electrical Systems Center, vol. 4, no. 4, pp. 5-7, December 1998.

## 5 Issues in Modeling

This chapter presents all of the mathematical models used in modeling the assembly shape of the two-solder-joint test structure. The assembly shape model can be applied to any single or multiple joint solder self-assembled MEMS. The results of the modeling and comparisons to the experimental data will be presented in Chapter 6.

### 5.1 Solder Angle Modeling

Figure 5-1 is a SEM of the side view (left) and front view (right) of a solidified solder joint showing important parameters that will be referred to throughout the rest of this work.

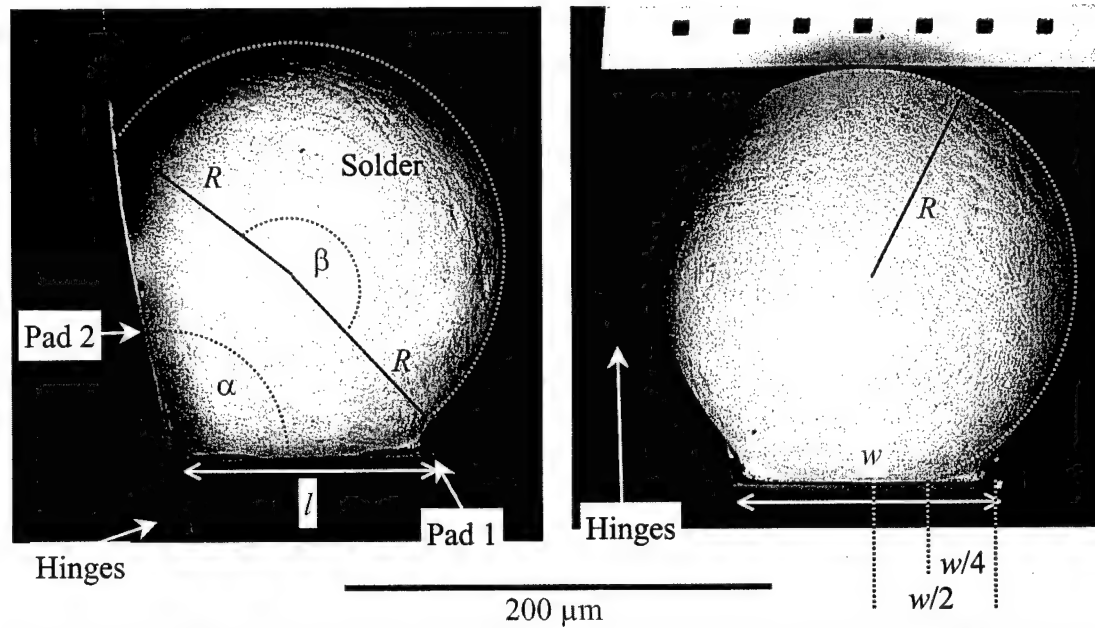


**Figure 5-1:** SEM of the side view (left) and front view (right) of a solidified solder joint showing important parameters that will be referred to throughout the rest of this work.

The parameters are the length of a solder pad ( $l$ ), the width of a solder pad ( $w$ ), the assembly or equilibrium angle ( $\alpha$ ), the radius of curvature of the solder ( $R$ ), and the angle of curvature of the solder ( $\beta$ ). The angle of curvature is defined as the angle between two radii of curvature that emanate from, and intersect at, the center of curvature and end at the interface between the solder surface and solder pad at  $w/2$ . The solder joint, shown in Figure 5-1 is the first joint of a 90°/90° 8 mil warp test structure.

Harnessing the surface tension of liquid solder to assemble MEMS, already introduced as "solder self-assembly", appears to be a reliable and practical method of mass assembly for MEMS. Solder can be strategically deposited on MEMS chips as part of the normal fabrication process, subsequently, the MEMS can be mass assembled in one quick reflow step. The deposited volume of solder controls the angle to which liquid solder rotates microstructures. To use solder assembly for MEMS, one must be able to predict the equilibrium shape of solder during the reflow process, thus, predicting the "assembly angle" or "equilibrium angle"

Models for solder shape can be divided into two general categories: surface energy based and geometry based. In general, surface energy based models find the equilibrium shape of the solder joint by finding the shape with a minimum surface energy. In general, geometry based models find the equilibrium shape of the solder by assuming an ideal geometry whose characteristics are dictated by a balance of fluid dynamic forces.

Several numerical and finite element models have been created to predict the shape of liquid solder joints for the flip-chip process and ball-grid arrays [1 - 15].

Specifically suited to the solder geometry of MEMS solder self-assembly, is the prior work done by Harsh et. al. [16, 17]. Harsh et. al. use *Surface Evolver* [18, 19] to find the solder shape that has the minimum surface area for a set of plate angles and a fixed volume. I consider this method an accurate method, since the minimum surface energy is directly proportional to the minimum surface area:

$$E_{\text{surface}} = \gamma \times \text{Area}_{\text{surface}} \quad (5-1)$$

where  $\gamma$  is the surface tension coefficient of the solder air surface. Furthermore, since  $\gamma$  is irrelevant, and body forces are negligible at the micro-scale, *Surface Evolver* is able to make very close approximations of solder shape without making any assumptions about forces. A more detailed explanation of the *Surface Evolver* model, and models similar to the ones I will be presenting next, is given in my paper [20] included as a reference in Appendix C of this work. The *Surface Evolver* model has drawbacks however – several hour computation times, solution progress monitoring to ensure that the surface evolution is well behaved, and relatively complex model geometry definition for the solver.

In an effort to create a designer's tool that can predict the equilibrium angle in a fraction of a second and be used during real time MEMS design, this research follows the approach used by Syms et. al. [21 - 23]. Syms uses a simple two-dimensional model, represented in Figure 5-2, consisting of:

- a) A two dimensional torque balance equation between internal pressure and surface tension force of a solder joint between two plates.
- b) An equation relating the initial cross sectional area when the angle between the plates is  $180^\circ$  and final cross sectional area when the angle is at equilibrium.

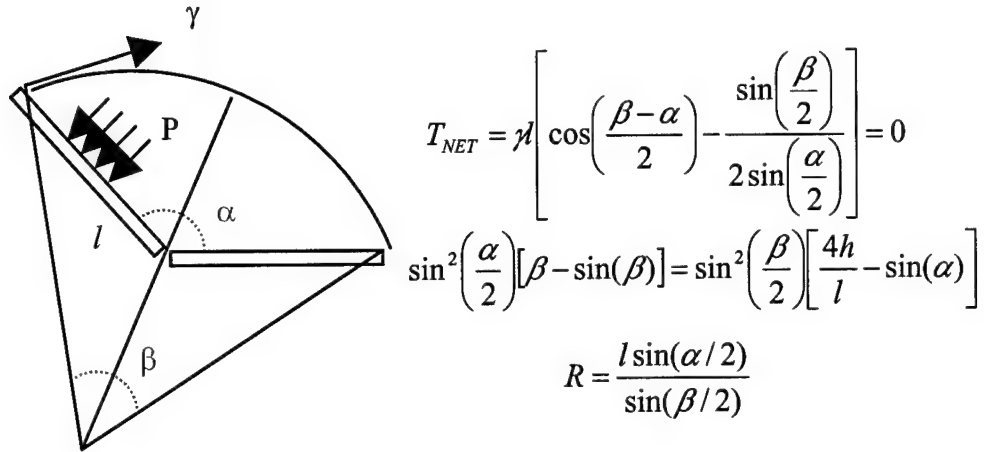


**Figure 5-2:** Geometric equilibrium angle prediction model used by Syms, where  $\gamma$  is the surface tension coefficient,  $\beta$  is the angle of curvature,  $\alpha$  is the angle between the solder pads of length  $l$ ,  $P$  is the internal pressure of the liquid,  $h$  is the height of the initial electroplated solder volume, and  $T_{NET}$  is the net torque per unit length (into the page) between the internal pressure and surface tension.

Syms's method yields two simple equations and two unknowns that may be solved numerically in a fraction of a second. I would like to state that I have utilized Syms's model, and end this section here. This however, is not the case. Syms models long cylindrically shaped (foot long hot dog like) solder joints ( $w \gg l$ ) where the effects of the ends of the joint are negligible, and a model of the central cross section of that joint is reasonable. The solder joints used for this research are spherical in shape and wetted to square or nearly square solder pads where the full three dimensional shape of the solder joint must be considered to get reasonable predictions. Figure 5-3 (top) shows a comparison of *Surface Evolver* equilibrium angle predictions to Syms's model for a fixed solder volume, equivalent to an 8 mil diameter ( $203.2 \mu\text{m}$ ) sphere, while changing the length of square solder pads. Figure 5-3 (bottom) is a plot of Syms's radius of curvature ( $R$ ) as the length of square solder pads is varied. The radius of an 8 mil diameter sphere is also plotted for reference.

Deposited solder height ( $h$ ), for the equations in Figure 5-2, is calculated as  $h=V/(2wl)$ , where  $V$  is the volume of an 8 mil diameter sphere and  $w = l$  for square pads. The equivalent volume of solder that would be electroplated  $h$  thick onto a pad area of  $w$  wide and  $2l$  long is  $hw2l$ .

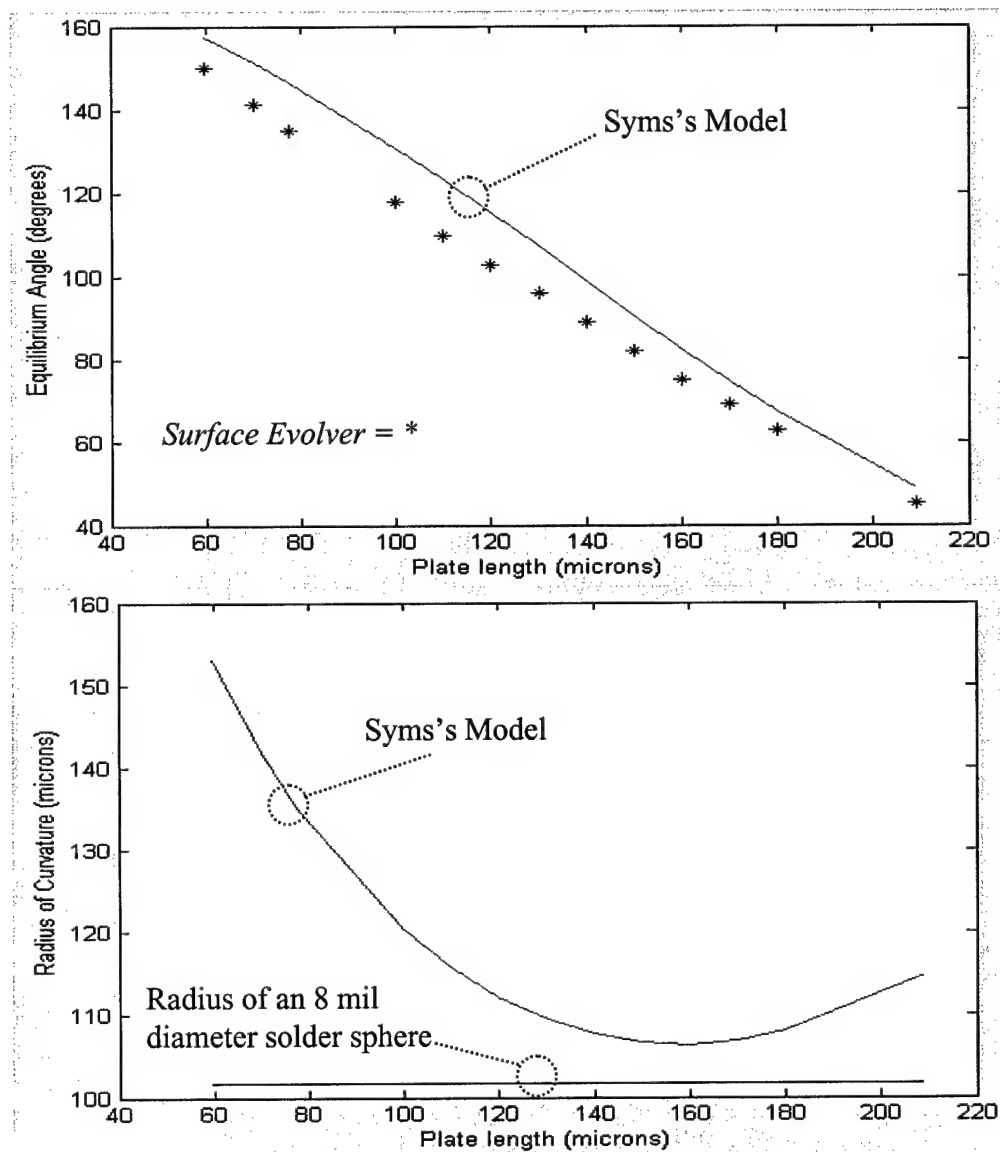


**Figure 5-3:** Comparison of *Surface Evolver* equilibrium angle predictions to Syms's model (top), and a plot of Syms's radius of curvature.

As one can see from the figure, the average error in the equilibrium angle is approximately  $15^\circ$ , and the radius of curvature does not behave in a realistic manner

as the length of the solder pads change. For a fixed volume of solder, as the square solder pad length/width decreases, the radius of curvature of the solder should approach that of radius of a perfect sphere of the same volume. Furthermore, as can be seen from the equations in Figure 5-2, the model is not influenced by the width of the solder pad ( $w$ ). Unfortunately, Syms's simple two-dimensional model is not directly applicable to the three-dimensional nature of the solder joints used in this research.

In this research, simple three-dimensional models, inspired by Syms's work, are developed that can be solved numerically with computing times of less than a second. The model used to determine the equilibrium angle of a solder joint between two adjacently hinged plates is constructed from:

- a) A torque balance equation between internal pressure of a solder joint wetted between two plates and the surface tension forces acting along the perimeter of the plates.
- b) An equation relating the initial deposited volume of solder and an assumed final volume shape when the angle between the plates is at equilibrium.

For this model, the following assumptions are made:

- a) The solder is an incompressible fluid,
- b) The weight of the solder pads and attached structures is negligible,
- c) The effects of body forces on the solder volume are negligible,
- d) The solder surface is able to reach a minimum surface energy shape, and
- e) The internal pressure of the solder can be described by the curvature of the solder surface.

Figure 5-4 is a depiction of important parameters in the development of the three-dimensional geometric solder model. Please refer to this figure for the remainder of this section. It is also helpful to compare Figure 5-4 to Figure 5-1 to see how the diagrams relate to the actual solder joint.

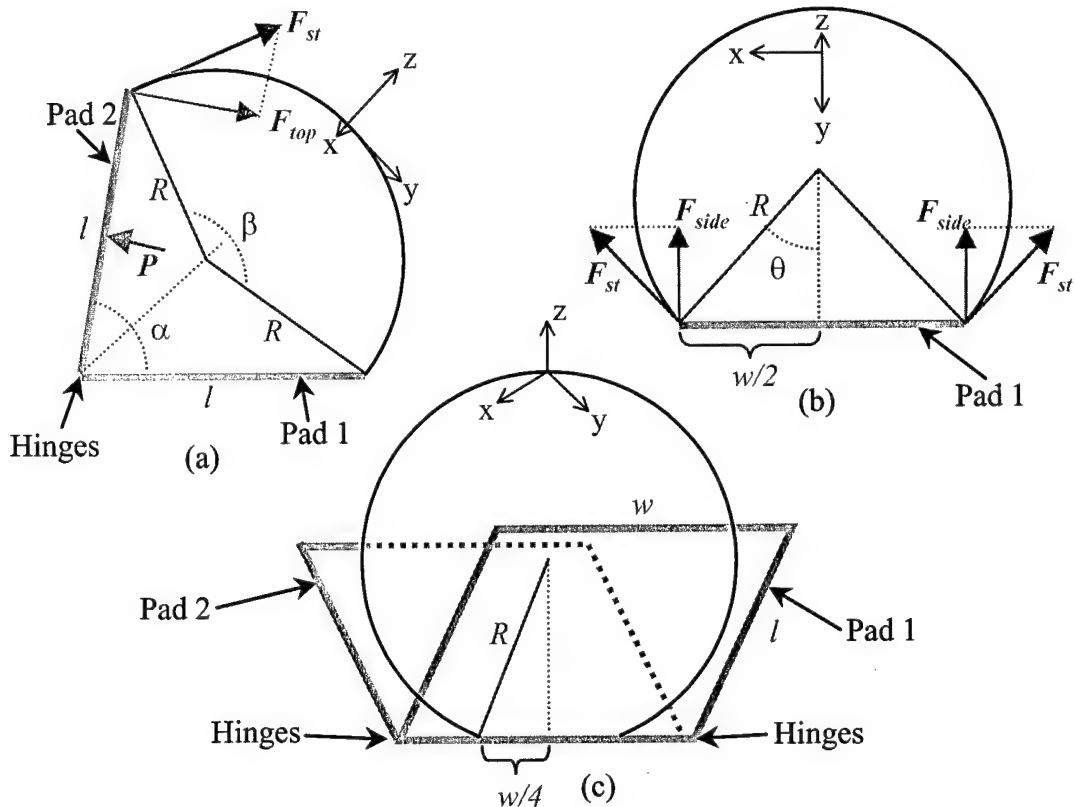


**Figure 5-4:** Depiction of important parameters in the development of the three-dimensional geometric solder model. This figure is best viewed in color.

The difference in pressure ( $P$ ) from within the solder droplet to the surroundings can be described by the Laplace-Young equation, introduced in Chapter 2 [24]:

$$P = \cancel{\rho gh} - \gamma \left( \frac{\partial^2 z}{\partial x^2} + \frac{\partial^2 z}{\partial y^2} \right) = -\gamma \left( \frac{\partial^2 z}{\partial x^2} + \frac{\partial^2 z}{\partial y^2} \right) = \gamma \left( \frac{1}{R_x} + \frac{1}{R_y} \right) = \frac{2\gamma}{R} \quad (5-2)$$

where,  $\rho$  is the density of the solder,  $g$  is acceleration due to gravity,  $h$  is height measured from the top of the solder droplet,  $\gamma$  is coefficient of surface tension of the solder-flux interface,  $R_x$  is the radius of curvature of the solder surface in the xz-plane, and  $R_y$  is the radius of curvature of the solder surface in the yz-plane. Note that the curvature of the solder surface will be negative because of the orientation of the reference axes in Figure 5-4. Also, the hydrostatic pressure term,  $\rho gh$ , is neglected in this analysis for reasons discussed in Chapter 2. Furthermore,  $R = R_x = R_y$  because the solder shape is spherical. From Figure 5-4 (a), the radius of curvature can be related to the angle between the plates ( $\alpha$ ) and the angle of curvature ( $\beta$ ) by:

$$R = \frac{l \sin(\alpha/2)}{\sin(\beta/2)} = R_l . \quad (5-3)$$

From Figure 5-4 (c), the radius of curvature can be related to the angle between the plates ( $\alpha$ ) and the angle of curvature ( $\beta$ ) in a different way, which I will denote as  $R_w$  to distinguish from Equation (5-3):

$$R_w^2 = (l \cos(\alpha/2) - R_w \cos(\beta/2))^2 + (w/4)^2 . \quad (5-4)$$

From Figure 5-4 (a) and (b) the surface tension force ( $F$ ) acting normal to a plate surface at the top edge of a plate ( $F_{top}$ ) and along the edge ( $F_{side}$ ) of both sides is:

$$F = F_{top} + 2F_{side} = \gamma d\xi \cos[(\alpha-\beta)/2] + 2\gamma d\eta w/(2R) \quad (5-5)$$

where,  $w$  is the width of a plate (into the page),  $l$  is the length of a plate,  $(\alpha-\beta)/2$  is the contact angle of the solder surface with the plate,  $w/(2R) = \sin(\theta)$ , and  $d\xi$  and  $d\eta$  are differential distances along the width and length of a plate, respectively.

The total torque on a plate due to the surface tension force ( $T_{ST}$ ) is found by integrating  $F$ , from Equation (5-4), times the appropriate moment arm, along the perimeter of a plate:

$$T_{ST} = \gamma \cos\left(\frac{\alpha - \beta}{2}\right) \int_0^w l d\xi + \frac{\gamma w}{R} \int_0^l \eta d\eta = \gamma wl \cos\left(\frac{\alpha - \beta}{2}\right) + \frac{\gamma wl^2}{2R}. \quad (5-6)$$

The torque on a plate due to the internal pressure of the solder ( $T_P$ ) is:

$$T_P = \int_0^w \int_0^l \eta P d\eta d\xi = \frac{1}{2} wl^2 P = \frac{\gamma wl^2}{R}. \quad (5-7)$$

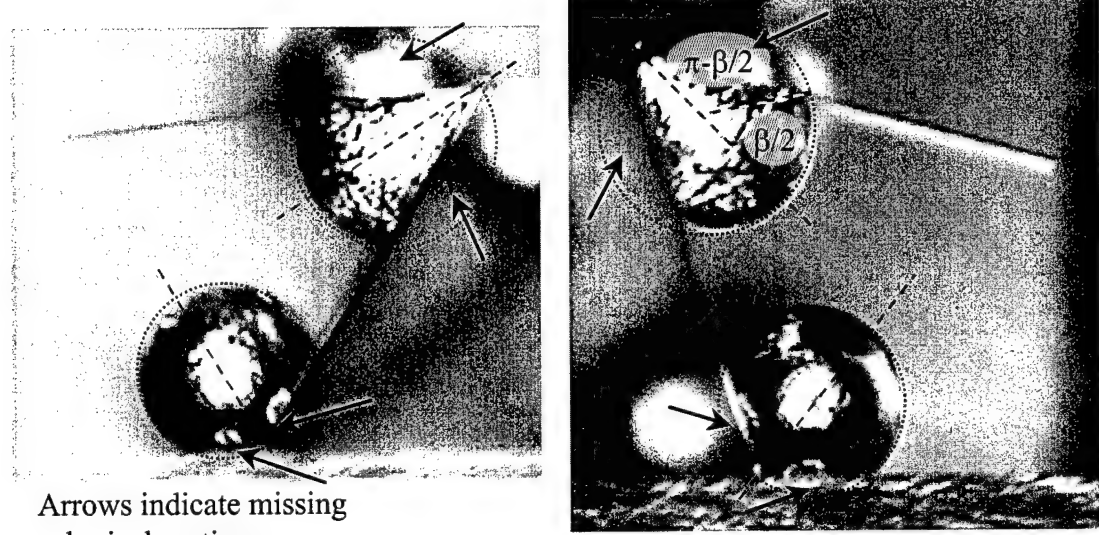
The net torque on a plate ( $T_{NET}$ ) is:

$$T_{NET} = T_{ST} - T_P = \gamma wl \cos[(\alpha - \beta)/2] - (1/2)\gamma wl^2/R. \quad (5-8)$$

Substitution of Equation (5-3) into (5-8) yields:

$$T_{NET} = \gamma wl \cos[(\alpha - \beta)/2] - (1/2)\gamma wl \sin(\beta/2)/\sin(\alpha/2). \quad (5-9)$$

The volume of a solder joint may be modeled in several ways. If a sphere is superimposed over a solder joint at equilibrium, the intersection of the two volumes suggests that solder occupies a volume of space that is approximately a sphere with two equal spherical sections lopped off – as shown in Figure 5-5 and depicted in Figure 5-6.



Arrows indicate missing spherical sections

**Figure 5-5:** Captured video images showing two-dimensional depictions of missing spherical sections from spheres superimposed on solder joints.

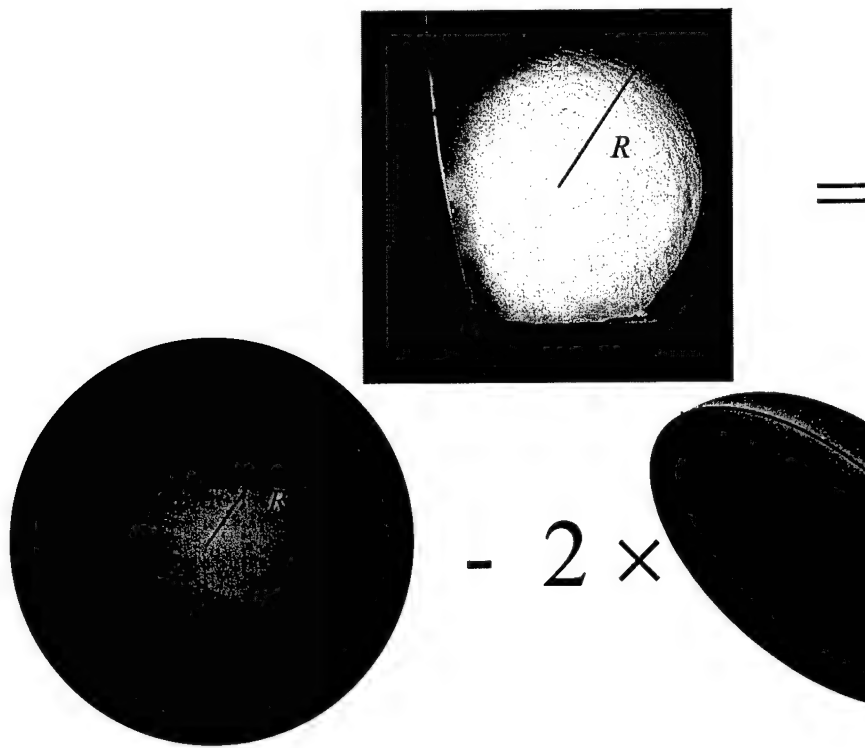


**Figure 5-6:** Pictorial equation showing the modeling of a solder joint shape by the volume of a sphere – 2 x the volume of a section of sphere.

The volume of a general section of a sphere described by a radius of curvature  $R$  and an angle  $\omega$  is depicted in Figure 5-6 and found from:

$$V_{SpherePortion} = 4 \int_0^{\omega/2} \int_{\frac{R \cos(\omega/2)}{\cos(\phi)}}^R \int_0^{\pi/2} \rho^2 \sin(\phi) d\theta d\rho d\phi \\ = \frac{2}{3} \pi R^3 \left( 1 - \frac{3}{2} \cos(\omega/2) + \frac{1}{2} \cos^3(\omega/2) \right) \quad (5-10)$$

To dictate how much of a sphere gets loped off, we let  $\omega = \pi - \beta/2$ , as illustrated in Figure 5-5. The volume of the solder joint is then:

$$V = V_{Sphere} - 2V_{SpherePortion} \\ = \frac{4}{3} \pi R^3 - \frac{4}{3} \pi R^3 \left( 1 - \frac{3}{2} \cos(\pi/2 - \beta/4) + \frac{1}{2} \cos^3(\pi/2 - \beta/4) \right) \\ = \frac{2}{3} \pi R^3 \left( 3 \sin(\beta/4) - \sin^3(\beta/4) \right) \quad (5-11)$$

Equations (5-4), (5-9), and (5-11), letting  $R = R_w$ , are three equations with five unknowns ( $\alpha$ ,  $\beta$ ,  $R$ ,  $V$ , and  $T_{NET}$ ), that can be solved numerically given two of the unknowns. At equilibrium,  $T_{NET} = 0$ , and the volume,  $V$ , is equal to the initial deposited volume of solder. Figure 5-7 is a plot comparing geometric model equilibrium angle predictions to *Surface Evolver* predictions [25] for different square solder pad lengths while keeping a fixed volume of solder equivalent to an 8 mil diameter sphere. Figure 5-8 is a plot of error between geometric model equilibrium angle predictions and the *Surface Evolver* predictions. Figure 5-9 shows the behavior of the radius of curvature,  $R_w$ , of the geometric model for different square solder pad lengths while keeping a fixed volume of solder equivalent to an 8 mil diameter sphere.

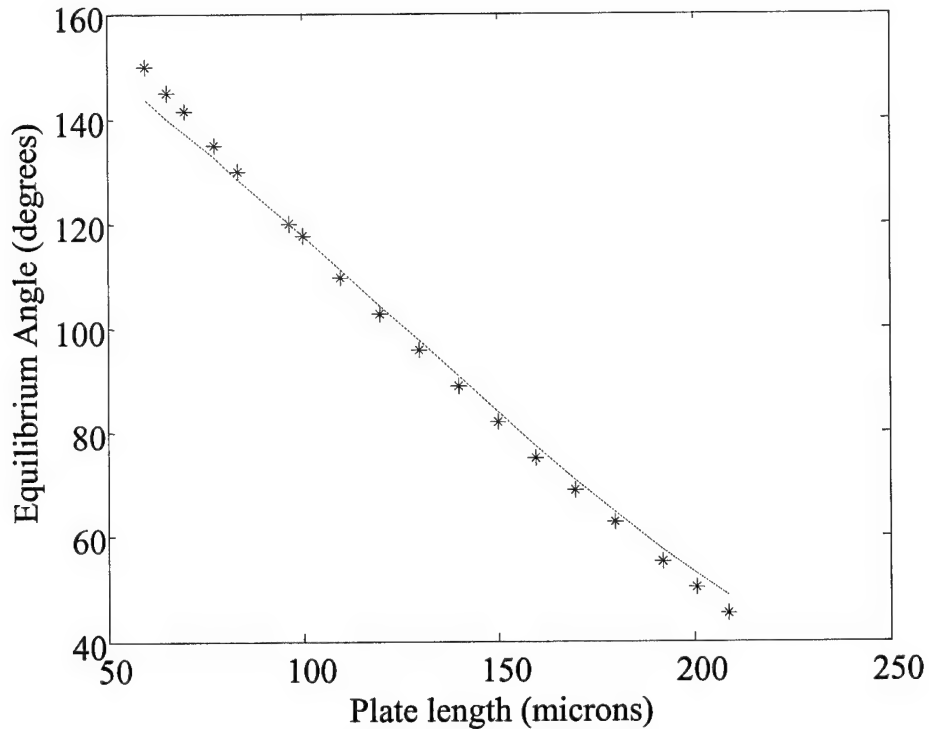


**Figure 5-7:** Plot comparing geometric model equilibrium angle predictions to *Surface Evolver* (\*) predictions for different square solder pad lengths while keeping a fixed volume of solder equivalent to an 8 mil diameter sphere.

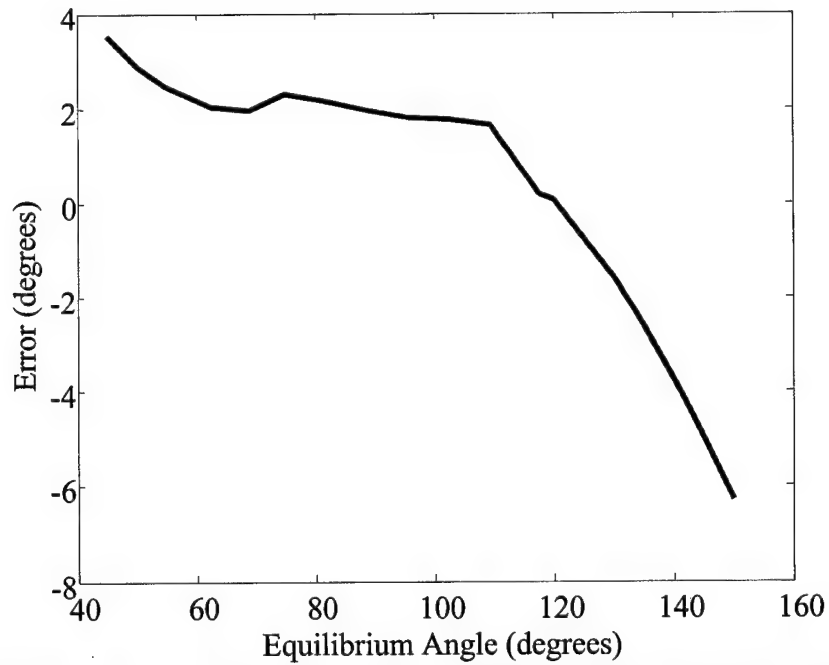


**Figure 5-8:** Plot of error between geometric model equilibrium angle predictions and *Surface Evolver* predictions for different square solder pad lengths while keeping a fixed volume of solder equivalent to an 8 mil diameter sphere.

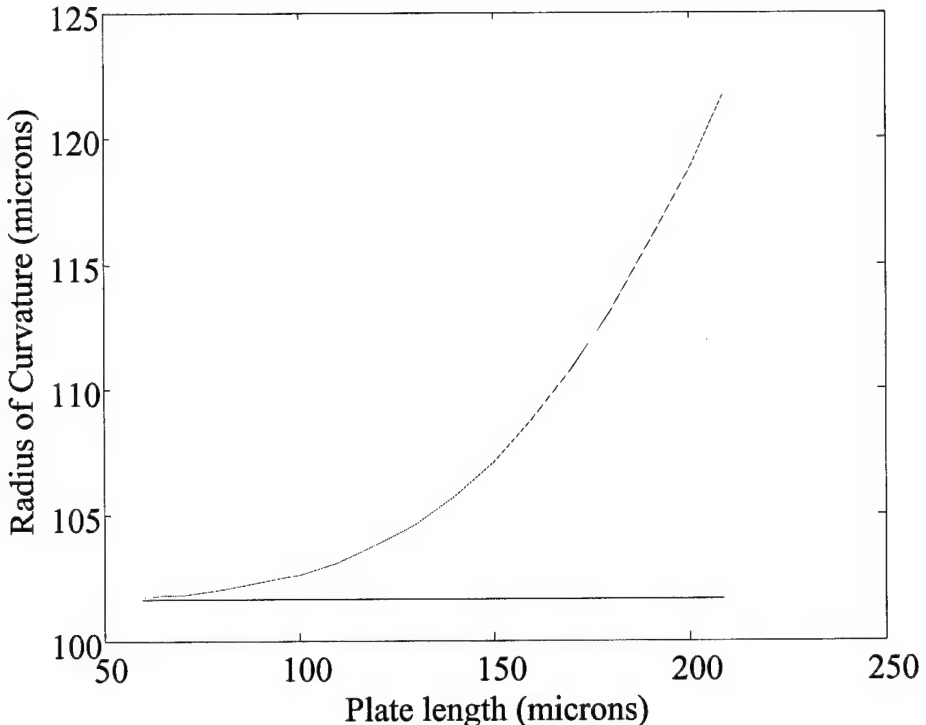


**Figure 5-9:** Plot showing the behavior of the radius of curvature,  $R_w$ , of the geometric model for different square solder pad lengths while keeping a fixed volume of solder equivalent to an 8 mil diameter sphere. The radius of an 8 mil sphere is also plotted as a straight line.

Figure 5-10 is a plot comparing geometric model equilibrium angle predictions to *Surface Evolver* predictions for different square solder pad lengths while keeping a fixed volume of solder equivalent to a 4 mil diameter sphere. Figure 5-11 shows the behavior of the radius of curvature,  $R_w$ , of the geometric model for different square solder pad lengths while keeping a fixed volume of solder equivalent to a 4 mil diameter sphere.

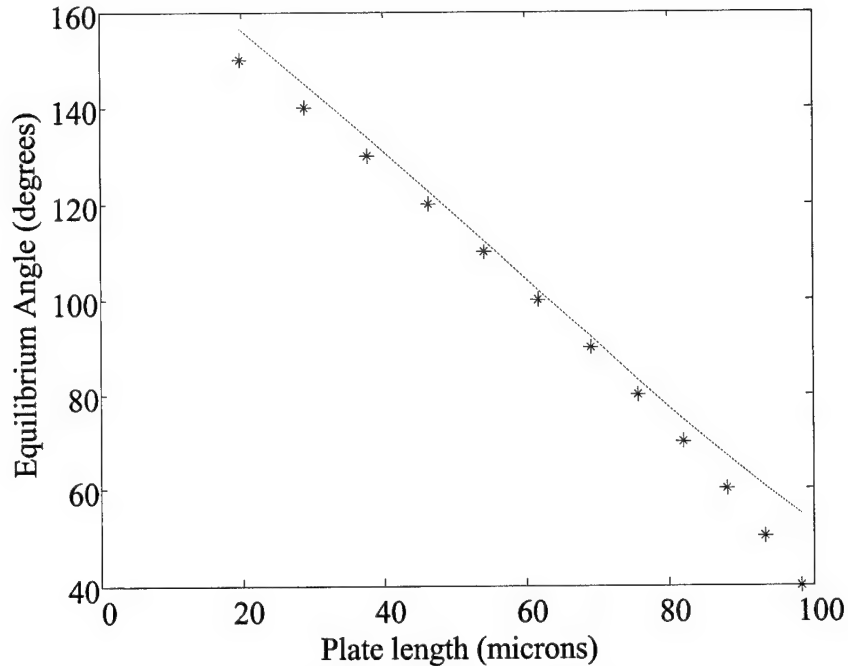


**Figure 5-10:** Plot comparing geometric model equilibrium angle predictions to *Surface Evolver* (\*) predictions for different square solder pad lengths while keeping a fixed volume of solder equivalent to a 4 mil diameter sphere.

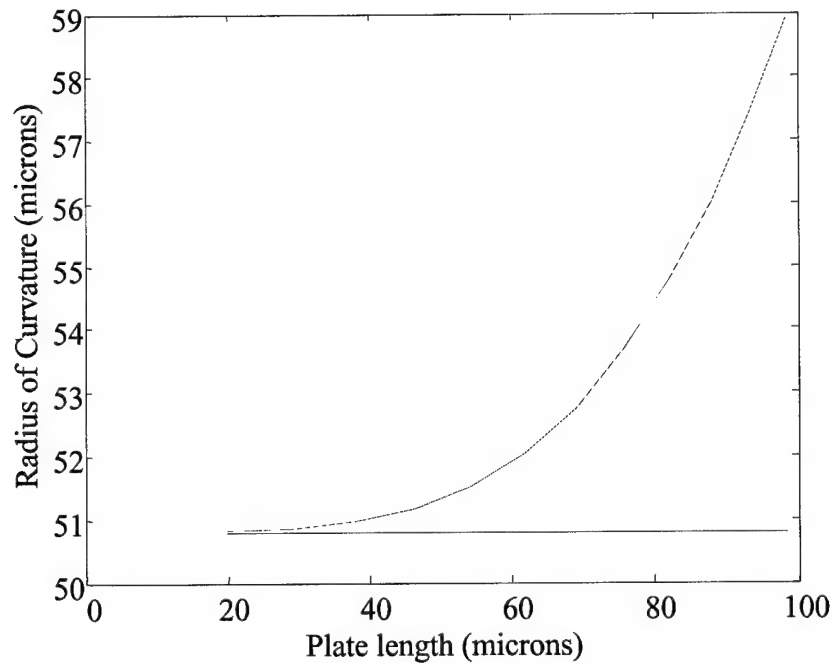


**Figure 5-11:** Plot showing the behavior of the radius of curvature,  $R_w$ , of the geometric model for different square solder pad lengths while keeping a fixed volume of solder equivalent to a 4 mil diameter sphere. The radius of a 4 mil sphere is also plotted as a straight line.

Equations (5-4), (5-9), and (5-11) are posed as a non-linear least-squares problem and minimized using a Gauss-Newton method for finding the search direction. The nonlinear optimization algorithm used is *fsolve* from the *MATLAB* optimization toolbox. A good starting point for the optimization is  $\alpha = \pi/2$ ,  $\beta = \pi$ , and  $R_w$  = the radius that the deposited volume of solder would have if it were a sphere. The solution is typically obtained in 5 steps and 28 function evaluations.

The spherical segment model, depicted in Figure 5-6, is not new, and has been utilized by L. S. Goldman [26] to model the profile of controlled collapse chip joints for flip chipping onto ceramic substrates. In Goldman's paper, the solder pad on the chip and the wetted solder area on the substrate land are modeled as circular. In my case, the actual solder joint is wetted to square pads. Furthermore, the solder of the actual joint must transition from a perfect sphere shape to the constraining shape of the square gold pads. My model does not account for the volume of the wedges that are created when the solder surface transitions from a spherical surface to a surface constrained to square corners and straight edges. The six wedge volumes that are not accounted for are located at the four independent corners of the solder pads and the two mutually shared sets of corners at the hinges. Accurately accounting for these wedge regions would make the model predictions more accurate. Furthermore, the spherical segment model is only valid when body forces or external forces on the joint are not excessive. Therefore, the error in my model would further increase if the weight of the upper solder joints, and structures, of a series-connected multiple-joint solder self-assembled structure, becomes significant.

When experimental data or more accurate predictions are available, the error in  $\alpha$ , from the geometric model, can be removed or minimized by modeling the error by a best fit curve, and adding it back to  $\alpha$  during the solution of the three equations. The error in  $\alpha$  for an 8 mil volume and a 4 mil volume is modeled by Equations (5-12) and (5-13), respectively:

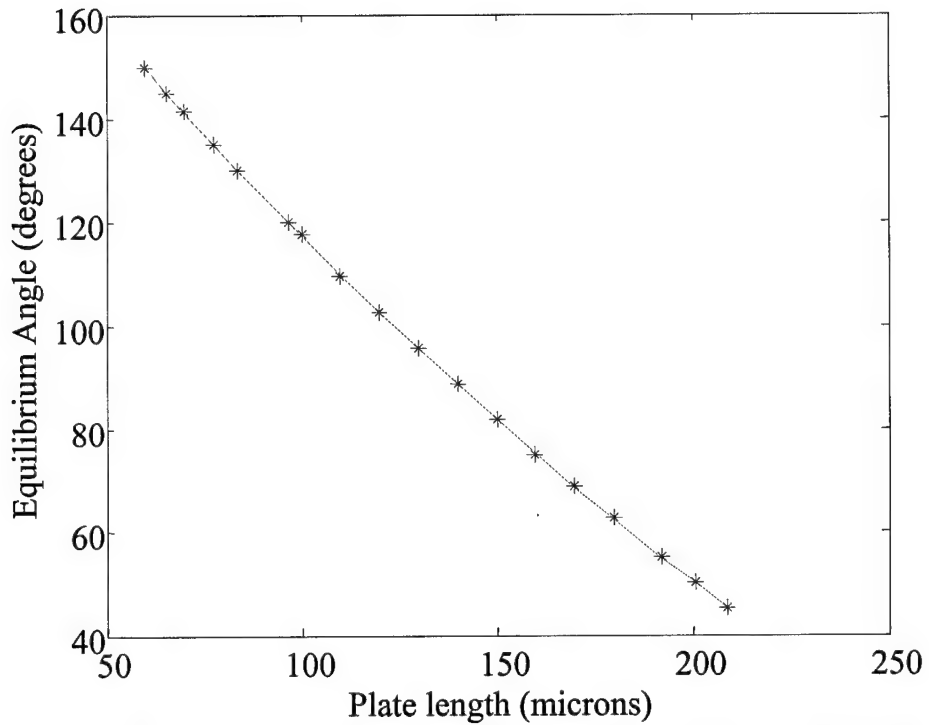
$$E_{\alpha 8} = -7.3091 \times 10^{-2} \alpha^3 + 3.0236 \times 10^{-1} \alpha^2 - 4.2628 \times 10^{-1} \alpha + 2.4056 \times 10^{-1} \quad (5-12)$$

$$E_{\alpha 4} = -5.2903 \times 10^{-2} \alpha^3 + 4.2576 \times 10^{-1} \alpha^2 - 1.0056 \alpha + 7.7192 \times 10^{-1} \quad (5-13)$$

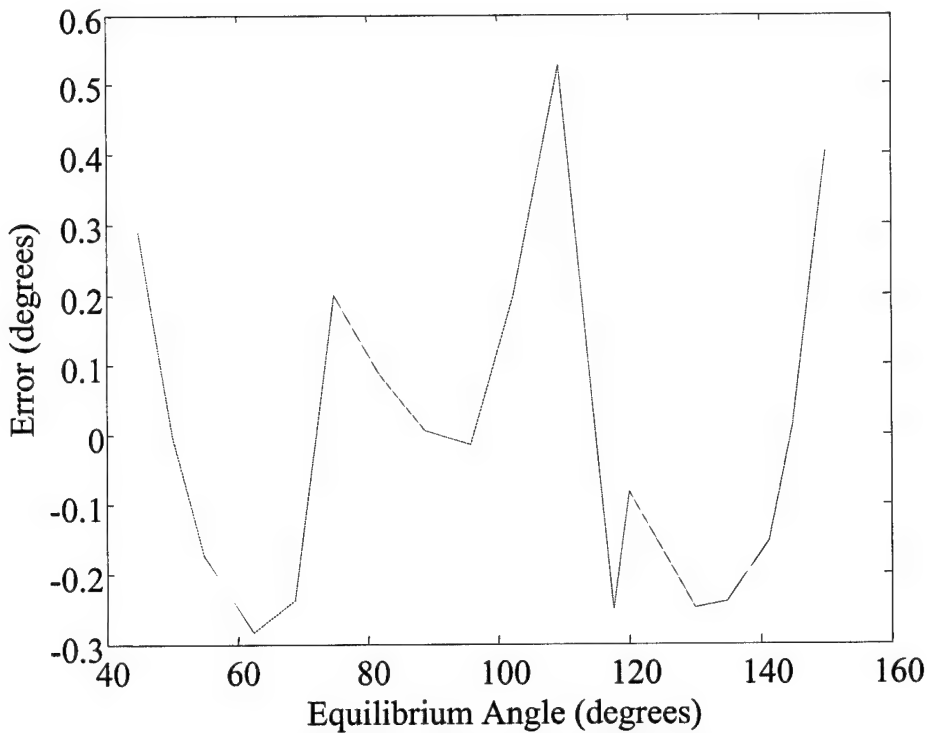
Figure 5-12 shows a plot comparing corrected geometric model equilibrium angle predictions to *Surface Evolver* predictions for different square solder pad lengths while keeping a fixed volume of solder equivalent to an 8 mil diameter sphere. Figure 5-13 shows a plot of the error between corrected geometric model equilibrium angle predictions and *Surface Evolver* predictions for the 8 mil volume. Figure 5-14 shows a plot comparing corrected geometric model equilibrium angle predictions to *Surface Evolver* predictions for different square solder pad lengths while keeping a fixed volume of solder equivalent to a 4 mil diameter sphere. Figure 5-15 shows a plot of the error between corrected geometric model equilibrium angle predictions and *Surface Evolver* predictions for the 4 mil volume. The corrected model is used to make the predictions for the final shape of the test structure presented in the next chapter.

Figure 5-16 and Figure 5-17 are graphs of the two dimensional solution space when the corrected geometric model equations are posed as a least squares minimization problem. The crossing of the red lines locates the minimum, in this case at an equilibrium angle of  $90^\circ$ , while  $R_w$  is kept constant at the value that it

would have at the solution. Furthermore, the volume of solder is equivalent to an 8 mil diameter sphere. The well-behaved surface is ideal for the unconstrained optimization.



**Figure 5-12:** Plot comparing corrected geometric model equilibrium angle predictions to *Surface Evolver* (\*) predictions for different square solder pad lengths while keeping a fixed volume of solder equivalent to an 8 mil diameter sphere.



**Figure 5-13:** Plot of error between corrected geometric model equilibrium angle predictions and *Surface Evolver* predictions for different square solder pad lengths while keeping a fixed volume of solder equivalent to an 8 mil diameter sphere.

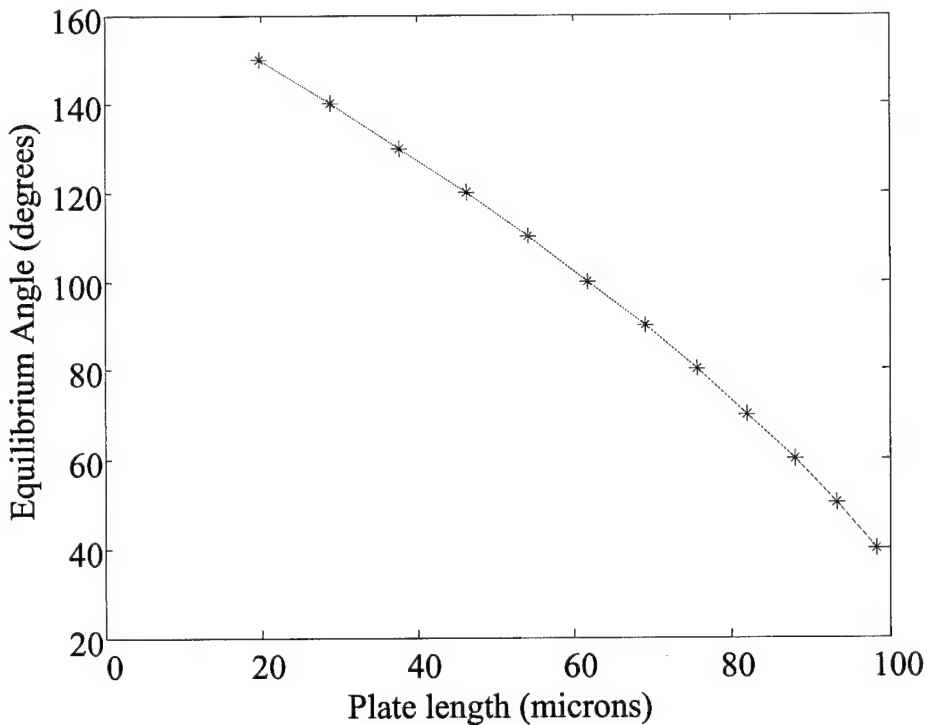


**Figure 5-14:** Plot comparing corrected geometric model equilibrium angle predictions to *Surface Evolver* (\*) predictions for different square solder pad lengths while keeping a fixed volume of solder equivalent to a 4 mil diameter sphere.

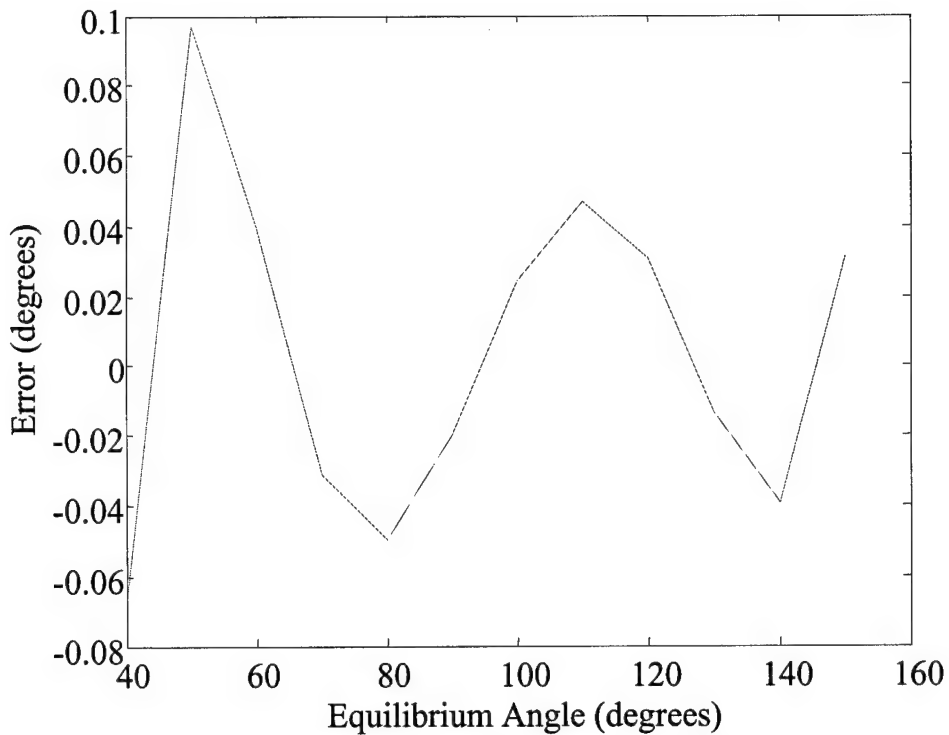


**Figure 5-15:** Plot of error between corrected geometric model equilibrium angle predictions and *Surface Evolver* predictions for different square solder pad lengths while keeping a fixed volume of solder equivalent to a 4 mil diameter sphere.

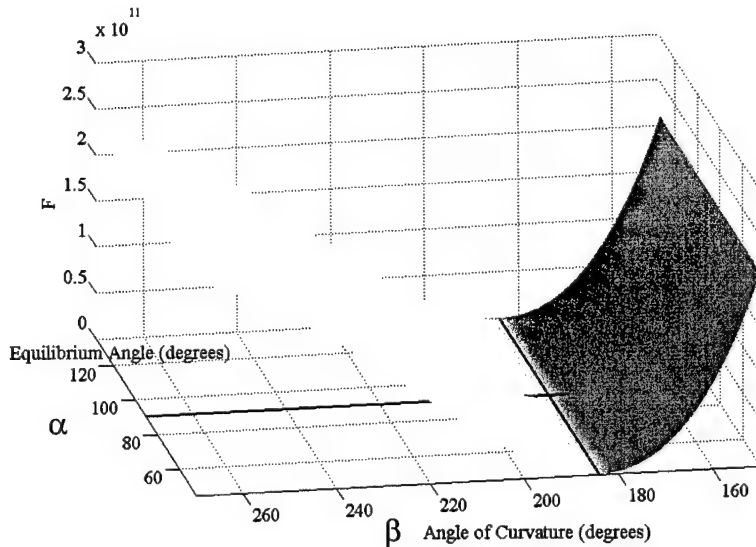


**Figure 5-16:** Graph of the two-dimensional solution space when the corrected geometric model equations are posed as a least squares minimization problem. The crossing of the red lines locates the minimum, in this case at an equilibrium angle of  $90^\circ$ , while  $R_w$  is kept constant at the value that it would have at the solution. Furthermore, the volume of solder is equivalent to an 8 mil diameter sphere.

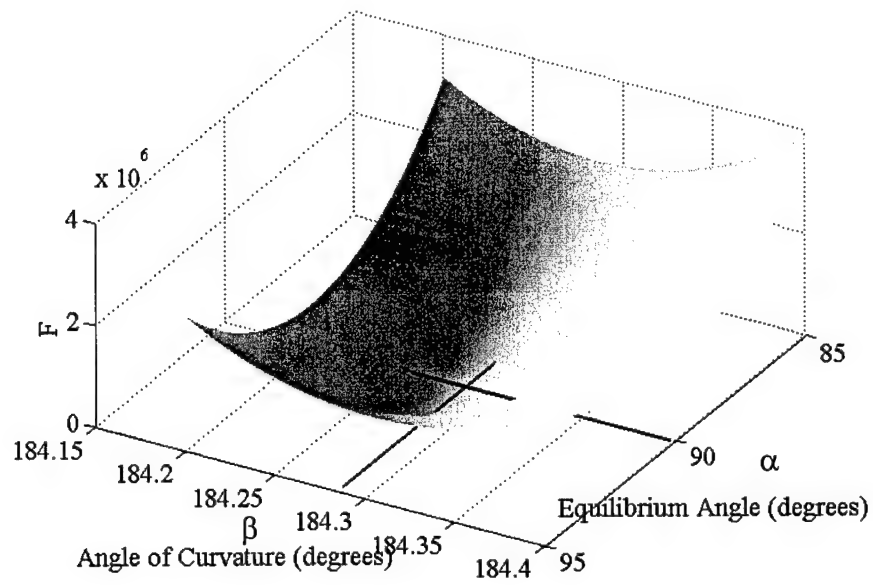


**Figure 5-17:** Closer view of the location of the minimum of Figure 5-16.

## 5.2 Modeling Deformation

In order to predict the assembly shape of the test structure, I have decided to take into account three types of deformation:

- Deformation of a polysilicon layer due to internal stress from fabrication,
- Deformation of gold on polysilicon bilayer structures due to the stress caused by misfit strains between the gold and polysilicon layers, and
- Deformation of polysilicon due to solder.

The models to be presented are very simple analytical linear models, for more accurate nonlinear modeling of the above-mentioned deformations in plate like structures, please see the work of Dunn et al. [27, 28, 29]. The time dependence of the deformations due to creep, for example, is neglected in these models. For more

information on the time dependence of the deformation of gold on polysilicon bilayer structures, see Zhang's work [30]. Furthermore, the processing dependence of the deformations due to heat treatment (annealing), for example, is also neglected in these models. For more information on the processing dependence of the deformation of gold on polysilicon bilayer structures, see Miller's work [31].

Figure 5-18 depicts a bilayer structure of a gold film of thickness  $t_f$  on a polysilicon layer of thickness  $t_s$ . The composite structure is said to have tensile residual stress  $\sigma_{res}$ , and is curved in the direction of positive "y". Also depicted in Figure 5-18 is a single layer of polysilicon with thickness  $t_s$ . The single layer is said to have compressive residual stress  $\sigma_{res}$ , and is curved in the direction of negative "y". Please refer to Figure 5-18 for the following derivations.

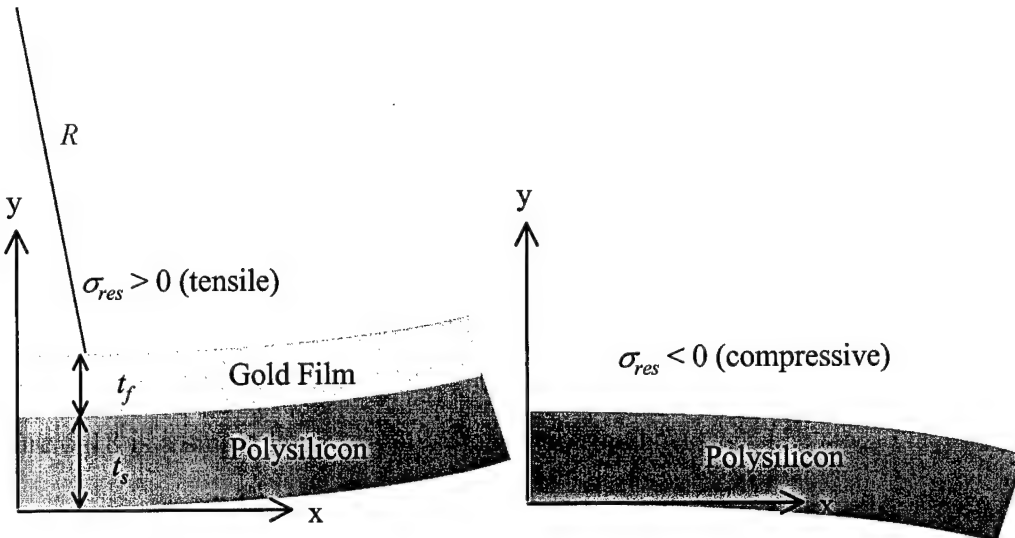


**Figure 5-18:** Depiction of nomenclature and conventions used in the derivation of the deformation models in the following sections.

### 5.2.1 Deformation Of A Bilayer Structure Due To Internal Residual Stress And Stress Due To Misfit Strain

Beginning with Stoney's Equation [32]:

$$\sigma_{res} = \frac{E'_s t_s^2}{6t_f R} \quad (5-14)$$

where

$$\sigma_{res} = \sigma_{th} + \sigma_{int} \quad (5-15)$$

where  $\sigma_{th}$  is the part of residual stress due to misfit strain between the gold film and the polysilicon layer,  $\sigma_{int}$  is the internal stress of the polysilicon layer inherent from fabrication,  $R$  is the radius of curvature of the bilayer structure, and  $E'_s = E_s/(1-\nu_s)$  is the biaxial modulus derived from the Young's Modulus of polysilicon ( $E_s$ ) and Poisson's ratio ( $\nu_s$ ) for polysilicon. Use of the biaxial modulus is a way to take into account that there is also bending taking place, along the "z" axis, into and out of the page, restricting the bending along the "x" axis from being as great as it would if just Young's Modulus were used in Equation (5-14). Since  $\nu$  is always less than unity, the biaxial modulus is always greater or stiffer than Young's Modulus alone. From the basic beam bending equation:

$$\frac{d^2y}{dx^2} = \frac{M}{EI}, \text{ for } \left. \frac{dy}{dx} \right|_{x=0} = y|_{x=0} = 0, \quad y = \frac{M}{2EI} x^2 \quad (5-16)$$

where  $M$  is a moment,  $E$  is Young's Modulus,  $I$  is the second area moment of inertia,  $x$  is the independent variable along the "x" axis, and  $y$  is the dependent variable describing the displacement of the structure, or deformation. Using the beam bending approximation of curvature:

$$\frac{d^2y}{dx^2} = \frac{1}{R} = \frac{M}{EI}, \quad (5-17)$$

then substituting Equation (5-17) into (5-16), yields:

$$\frac{1}{R} = \frac{2y}{x^2} \quad (5-18)$$

Substituting Equation (5-18) into (5-14), and solving for  $y$  gives:

$$y = \frac{3t_f\sigma_{res}}{E'_s t_s^2} x^2. \quad (5-19)$$

I will now derive an expression for  $\sigma_{th}$ . Due to thermal expansion, the length of the gold film ( $L$ ) can change by:

$$L = L_0 + L_0 \alpha_f \Delta T \quad (5-20)$$

where  $L_0$  is the initial length,  $\alpha_f$  is the coefficient of thermal expansion of the gold film,  $\Delta T = (T - T_0)$ ,  $T$  is the dependent variable of temperature, and  $T_0$  is the temperature where the misfit strain between the layers is zero. The strain developed in a film that is fixed to a substrate of smaller coefficient of thermal expansion is:

$$\varepsilon_f = (L_0 - L)/L_0 = -\alpha_f \Delta T. \quad (5-21)$$

Assuming the substrate may also expand or contract, the film strain is relieved by the substrate strain giving:

$$\varepsilon_f = -\alpha_f \Delta T - (-\alpha_s \Delta T) = (\alpha_s - \alpha_f) \Delta T. \quad (5-22)$$

The residual stress in the film or equivalently the stress in the top surface of the polysilicon substrate is:

$$\sigma_{th} = E'_f (\alpha_s - \alpha_f) \Delta T. \quad (5-23)$$

Substituting Equation (5-23) into (5-15) and both into (5-19) yields the deformation for a bilayer structure with residual stress due to the internal stress of the polysilicon layer and the misfit strain between the gold film and the polysilicon layer:

$$y = \frac{3t_f(E'_f(\alpha_s - \alpha_f)\Delta T + \sigma_{int})}{E'_s t_s^2} x^2. \quad (5-24)$$

In the above analysis, I have assumed that  $\sigma_{int}$  is not a function of temperature.

Given  $\sigma_{res}$  and  $\sigma_{int}$ ,  $T_0$  may be found from Equations (5-23) and (5-15) as:

$$T_0 = T - \frac{(\sigma_{res} - \sigma_{int})}{E'_f(\alpha_s - \alpha_f)}. \quad (5-25)$$

If  $R$  and  $\sigma_{int}$  are known experimentally, then  $\sigma_{th}$  can be found from Equation (5-24) by taking the second derivative of it with respect to  $x$ , setting it equal to the curvature, and solving for  $\sigma_{th}$ :

$$\sigma_{th} = \frac{E'_s t_s^2}{6t_f R} - \sigma_{int}. \quad (5-26)$$

### 5.2.2 Deformation Of A Single Layer Structure Due To Internal Residual Stress Only

From the beam theory elastic flexure formula:

$$\sigma_x = \frac{Md}{I} \Rightarrow \sigma_{int} = \frac{Mt_s}{2I} \Rightarrow \frac{M}{2I} = \frac{\sigma_{int}}{t_s} \quad (5-27)$$

where  $\sigma_x$  is the normal stress in the bending beam as a function of the distance  $d$  from the neutral axis. Furthermore, I am assuming that the neutral axis is at the center of the polysilicon layer where I am further assuming that  $\sigma_{int}$  is the maximum stress at a distance  $t_s/2$  from the neutral axis. Substituting Equation (5-27) into (5-16), and

using the biaxial Modulus instead of Young's Modulus, yields the deformation for a single layer with internal residual stress only:

$$y = \frac{\sigma_{int}}{E'_s t_s} x^2. \quad (5-28)$$

In a single layer only,  $\sigma_{int}$  can be found experimentally if the curvature of the layer can be measured. Taking the second derivative of Equation (5-28) with respect to  $x$ , setting it equal to the curvature, and solving for  $\sigma_{int}$  yields:

$$\sigma_{int} = \frac{E'_s t_s}{2}. \quad (5-29)$$

Once  $\sigma_{int}$  is found by measurements of the single layer's curvature,  $T_0$  can then be found, after measuring the curvature of the bilayer structure, by taking the second derivative of Equation (5-24) with respect to  $x$ , setting it equal to the curvature, and solving for  $T_0$  yields:

$$T_0 = \frac{-\left(\frac{t_s^2 E'_s}{R} - 3t_f \sigma_{int}\right)}{6t_f E'_f (\alpha_s - \alpha_f)} + T \quad (5-30)$$

### 5.2.3 Deformation Of Polysilicon Due To Solder

In order to have a simple model for this deformation, I will use the following equation derived from Equation (5-17) along with experimental measurements of curvature:

$$y = \frac{1}{2R} x^2. \quad (5-31)$$

Precise deformation models are not needed for this work. The deformation models only need quantify the proper magnitude of deformation. If more precise models are needed they can easily be plugged into the algorithm for finding the assembly shape of a multiple joint solder self-assembled MEMS, discussed next.

### 5.3 N-hinge Model

Speaking in terms of tolerance analysis, presented in Chapter 2, the "assembly function", created for this research, is an algorithm that can predict the shape of an n-plate n-solder-joint solder assembled structure. The test structure, introduced in Chapter 3, is a 2-plate 2-solder-joint structure. The assembly function requires inputs such as plate geometry, solder volumes, plate composition, hinge-play, relationship between plates, and temperature. The assembly function returns a set of two-dimensional coordinates  $\{f^x f^y\}$ , that can be plotted, describing the shape of the final assembly. The nature of the assembly function ( $f_{assy}$ ) is depicted in Figure 5-19.

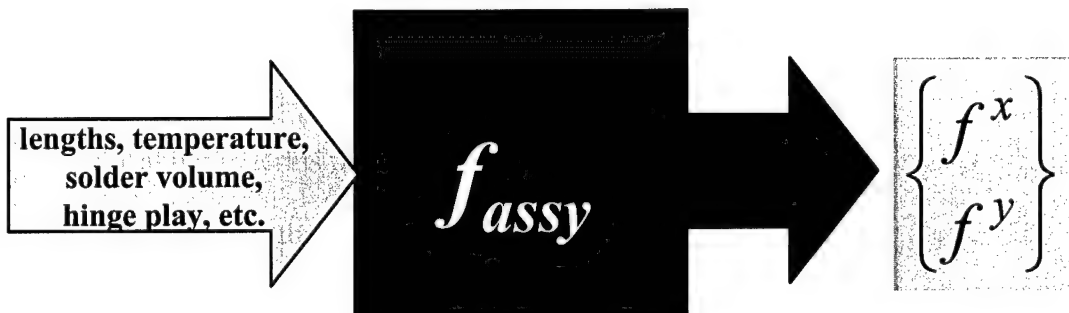


**Figure 5-19:** Depiction of the nature of the assembly function.

The assembly function uses the inputs to determine the following:

- Solder assembly angles

- b) Temperature/non-temperature dependent plate shape (side profile) induced by solder, multilayers, and internal stress in single layers
- c) Displacement between plates due to play in hinges

The assembly function can be trivially extended to three-dimensions, but will be kept two-dimensional as not to add unnecessary complexity and computation. The assembly function algorithm is implemented in the MATLAB programming environment. The code is not MATLAB specific, and can easily be implemented in any programming language. MATLAB is utilized because of its graphical output capabilities.

### 5.3.1 General Overview Of The Assembly Function Algorithm

A block diagram of the assembly function organization is shown in Figure 5-20. The "Assembly Builder" is the main algorithm (file and function name *assybuild.m*) and currently calls on two subroutines that calculate plate shapes due to deformation "Plate-Shape Solver" (file and function name *getshape.m*) and solder assembly angles "Angle Solver" (file and function name *angsolv.m* and *geoequations.m*).

*Getshape.m* utilizes Equations (5-24), (5-28), and (5-31). *Angsolv.m* is where the nonlinear equation solver is called to solve Equations (5-4), (5-9), and (5-11) defined in *geoequations.m*. The output of the Assembly Builder is a  $3 \times$  (user defined number of points) of x-y coordinates of the final assembly's shape. The third row is all ones, necessary for a homogeneous transformation, and can be neglected. The code for the main algorithm and subroutines is included in Appendix B.

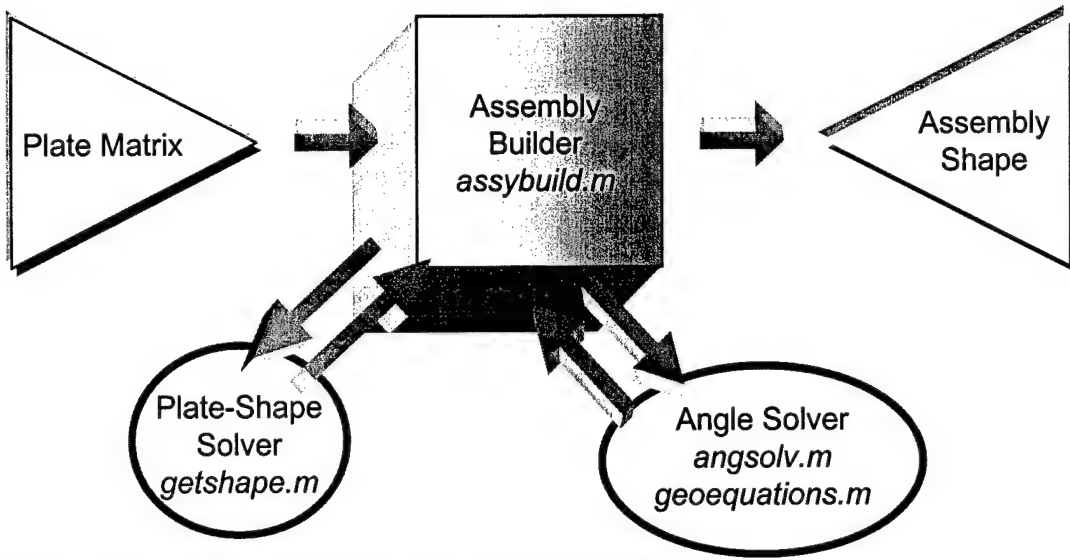


**Figure 5-20:** A block diagram of the assembly function organization.

The Assembly Builder is passed the "Plate Matrix". The Plate Matrix is the user input to the Assembly Builder that defines regions (or plates) of the assembly, their relationship to each other, and the environmental conditions of each plate. Each row of the matrix describes one plate and requires 16 elements of input. The first row is the plate hinged to the substrate. The assembly function can handle any number of plates. When defining the plate matrix, all of the plates must be thought of as being in an unassembled position. The information required to define an i-th plate of an assembly is as follows:

```
plate(i,:)=[L, Shape, elnum, σpoly, σgold, Rsol/poly, T, [Hplay], sw1, α, sw2, V, γ, l, w]
elements: 1, 2 , 3 , 4 , 5 , 6 , 7, [ 8 9 ], 10, 11, 12, 13,14,15,16
```

where

- a) **L** is the length of a plate (micrometers).
- b) **Shape** determines the deformation model that will be used: 1 = undeformed, 2 = poly1 with internal stress, 3 = poly2 with internal stress, 4 = gold on poly2 with internal stress in poly and stress due to misfit strain between gold and

`poly, 5 = solder on poly2 using experimental observations of curvature.`

Requires an integer input.

- c) `elenum` allows the user to decide the number of elements a single plate is divided up into. An input of 1 means the plate will be composed of a single element with a beginning point and an end point. Requires an integer input.
- d)  $\sigma_{\text{poly}}$  is the internal stress (Pa) in a single polysilicon layer where the sign of the stress is determined by the convention in Figure 5-18.
- e)  $\sigma_{\text{gold}}$  is the stress (Pa) in the gold layer where the sign of the stress is determined by the convention in Figure 5-18.
- f)  $R_{\text{sol/poly}}$  is the measured radius of curvature (micrometers) of a plate that has solder where + means curved up and – means curved down.
- g)  $T$  is the temperature in Celsius.
- h) `[Hplay]` stands for hinge play (micrometers) [x, y] and is the 2-D coordinate position of the beginning point of this plate with respect to a local coordinate system whose origin coincides with the end of previous plate and whose local y-axis is perpendicular to the slope of the end of the previous plate.
- i) `sw1` is a switch where 1 = allows the hinge play to affect solder angle by converting the hinge location into a shortening or lengthening of the solder pad. `Sw2` must also be 1 for this to work.
- j)  $\alpha$  is a manual angle (radians) between this plate and previous plate when, and only works when `sw2` = 0.

- k) **sw2** is a switch where 1 = calculate the equilibrium angle using the following parameters  $\{\text{plate}(i, 12-16)\}$  and 0 = use  $\alpha$  instead. The assembly angle is always defined at the beginning of the i-th plate.
- l)  $V$  is the volume of solder microns<sup>3</sup>.
- m)  $\gamma$  is the surface tension coefficient (Newton/microns) of the solder and can be set to 1 because it is not currently needed in any of the models.
- n)  $l$  is the length of the solder pads (microns).
- o)  $w$  is the width of the solder pads (microns)

Figure 5-21 is an example of a plate matrix defining a warp version of the test structure. The test structure is actually subdivided up into 9 distinct plates or regions with distinct deformation behavior. An addressable array named *dims* happens to be used, in this example, to provide the input values to the plate matrix.

**plate(i,:)= [L, Shape, elnum,  $\sigma_{\text{poly}}$ ,  $\sigma_{\text{gold}}$ ,  $R_{\text{sol/poly}}$ , T, [Hplay], sw1,  $\alpha$ , sw2, V,  $\gamma$ , l, w]**

```

plate(1,:)=[hingegap, 1, 1, 0, 0, 0, dims(18), dims(8:9), 0, 0, 1, 4/3*pi*(dims(12)/2)^3, 1, dims(14), dims(16)];
plate(2,:)=[dims(14), 5, 50, 0, 0, dims(5), dims(18), [0,0], 0, pi, 0, 1, 0, 0];
plate(3,:)=[gap, 3, 10, dims(3), 0, 0, dims(18), [0,0], 0, pi, 0, 0, 1, 0, 0];
plate(4,:)=[dims(1)-dims(14)-dims(15)-2*gap, 4, 100, dims(3), dims(4), 0, dims(18), [0,0], 0, pi, 0, 0, 1, 0, 0];
plate(5,:)=[gap, 3, 10, dims(3), 0, 0, dims(18), [0,0], 0, pi, 0, 0, 1, 0, 0];
plate(6,:)=[dims(15), 5, 50, 0, 0, dims(6), dims(18), [0,0], 0, pi, 0, 0, 1, 0, 0];
plate(7,:)=[dims(15), 5, 50, 0, 0, dims(7), dims(18), dims(10:11), 0, 0, 1, 4/3*pi*(dims(13)/2)^3, 1, dims(15), dims(17)];
plate(8,:)=[gap, 3, 10, dims(3), 0, 0, dims(18), [0,0], 0, pi, 0, 0, 1, 0, 0];
plate(9,:)=[dims(2)-dims(15)-gap, 4, 100, dims(3), dims(4), 0, dims(18), [0,0], 0, pi, 0, 0, 1, 0, 0];

```

**Figure 5-21:** An example of a plate matrix defining a warp version of the test structure.

### 5.3.2 Specific Description Of The Assembly Function Algorithm

The Assembly Builder algorithm (*assybuild.m*) is represented graphically in Figure 5-22 and is described in the following steps.

- A. Define the plate matrix as a variable matrix, for example *PlateM*.

B. Call *assybuild.m* at the MATLAB command line or from a MATLAB .m-file using the plate matrix as an argument:  $V = \text{assybuild}(PlateM)$ , where  $V$  is the output of the Assembly Builder: a  $3 \times (\text{user defined number of points})$  of x-y coordinates of the final assembly's shape, that can be plotted.

C. *assybuild.m* receives the plate matrix and performs the following steps:

- a)  $m = \text{number of rows of plate matrix.}$
- b) Get the shape of the  $m^{\text{th}}$  plate ( $V_i$ ).  $V_i = \text{getshape}(\text{row } m \text{ of } PlateM)$ , where the last row of  $V_i$  is all ones.
- c) **for  $i = m$  to 1, decrement by 1**
- d) Get the shape of the  $i-1^{\text{th}}$  plate ( $V_{i-1}$ ) – the first time at this step, the  $i-1^{\text{th}}$  plate is the  $m-1^{\text{th}}$  plate.
  - (i) If  $i \neq 1$ , then  $V_{i-1} = \text{getshape}(\text{row } i-1 \text{ of } PlateM)$  , where the last row of  $V_{i-1}$  is all ones.
  - (ii) If  $i = 1$ , then  $V_{i-1} = \begin{pmatrix} 0 & 0 \\ 0 & 0 \\ 1 & 1 \end{pmatrix}$  (this represents the substrate).
- e)  $\theta_i = \text{the angle at the beginning of } V_i$ . Calculated using a 4-quadrant arc tangent and the first two points of  $V_i$ .
- f)  $\theta_{i-1} = \text{the angle at the end of } V_{i-1}$ . Calculated using a 4-quadrant arc tangent and the last two points of  $V_{i-1}$ .
- g) Calculate the assembly angle between  $V_{i-1}$  and  $V_i$ .
  - (i) If  $PlateM_{i,12} = 1$ , then  $\alpha = \text{angsolv}(PlateM_{i,13}, PlateM_{i,14}, PlateM_{i,15}, PlateM_{i,16})$ .
  - (ii) If  $PlateM_{i,12} \neq 1$ , then  $\alpha = PlateM_{i,11}$ .

h)  $\theta_R = \pi - \alpha + \theta_{i-1} + \theta_i$ , and a rotation matrix is:  $R = \begin{bmatrix} \cos \theta_R & -\sin \theta_R \\ \sin \theta_R & \cos \theta_R \end{bmatrix}$ .

i) Another rotation matrix is:  $R_{i-1} = \begin{bmatrix} \cos \theta_{i-1} & -\sin \theta_{i-1} \\ \sin \theta_{i-1} & \cos \theta_{i-1} \end{bmatrix}$ .

j) Rotate and shift  $V_i$  to the end of  $V_{i-1}$  by the following conceptual steps:  
 rotating  $V_i$  with  $R$ , rotating the hinge play ( $PlateM_{i,8:9}$ ) to be perpendicular to  
 the end of  $V_{i-1}$  using  $R_{i-1}$ , and translating  $V_i$  to the very end of  $V_{i-1}$  using the  
 location of the last point of  $V_{i-1}$ . The new  $V_i$  is then:

$$[V_i] = \begin{bmatrix} [R](\text{end point of } V_{i-1}) + [R_{i-1}][PlateM_{i,8:9}] \\ 00 \end{bmatrix} [V_i].$$

k) If  $i \neq 1$  then combine  $V_{i-1}$  and new  $V_i$  into yet another new  $V_i$ :  $V_i = [V_{i-1} \ V_i]$ .  
 l) Go to c) until  $i = 1$ .

D. *assybuild.m* returns  $V_i$  to the MATLAB command line or .m-file memory space:  $V = V_i$  from step B. All or some of the points in  $V$  can now be plotted, used to calculate partial derivatives, or as points on the trajectory of an optimization problem.

The following discussion is an elaboration on step C. j) above. The heart of the *assybuild.m* algorithm is the rigid body rotation and translation task -- homogeneous transformation. In 2-D, the general form of a homogeneous transformation is:

$$(3 \times n) = (3 \times 3)(3 \times n)$$

$$\begin{bmatrix} [A_2] \\ \bar{1}' \end{bmatrix} = \begin{bmatrix} [R] \bar{P}_0 - [R]\bar{P}_0 + \bar{T} \\ 00 \end{bmatrix} \begin{bmatrix} [A_1] \\ \bar{1}' \end{bmatrix} \quad (5-32)$$

where  $[A_1]$  is a  $2 \times n$  matrix of 2-D coordinates of the portion of assembly before transformation,  $[A_2]$  is a  $2 \times n$  matrix of 2-D coordinates of the portion of assembly after transformation,  $[R]$  is a  $2 \times 2$  rotation matrix,  $\bar{P}_0$  is a  $2 \times 1$  position vector of the assembly's endpoint,  $\bar{T}$  is a  $2 \times 1$  position vector of the translation, and  $\bar{1}$  is an  $n \times 1$  vector of ones. Conceptually, the transformation, in Equation (5-32), rotates a set of points about a point other than the origin, and then translates the set of points.

In the *assybuild.m* algorithm, the homogeneous transformation is performed as follows:

$$(3 \times n) = (3 \times 3)(3 \times n)$$

$$\begin{bmatrix} [A_2] \\ \bar{1}' \end{bmatrix} = \begin{bmatrix} [R_\theta] & \bar{T}_{i-1}^{end} + [R_{\theta_{i-1}}]\bar{h} \\ 0 & 1 \end{bmatrix} \begin{bmatrix} [A_1] \\ \bar{1}' \end{bmatrix} \quad (5-33)$$

where  $[R_\theta]$  is a  $2 \times 2$  rotation matrix were  $\theta = \pi - \alpha + \theta_{i-1} + \theta_i$ ,  $\alpha$  is the solder angle,  $\theta_{i-1}$  is the angle of the end of the  $i-1^{\text{th}}$  plate,  $\theta_i$  is the angle of the beginning of the  $i^{\text{th}}$  plate,  $\bar{T}_{i-1}^{end}$  is a  $2 \times 1$  position vector of the last point of the  $i-1^{\text{th}}$  plate,  $[R_{\theta_{i-1}}]$  is a  $2 \times 2$  rotation matrix were  $\theta_{i-1} = \theta_{i-1}$ , and  $\bar{h}$  is a  $2 \times 1$  position vector of the hinge play. Conceptually, the transformation, in Equation (5-33), rotates a set of points about the origin, and then translates the set of points.

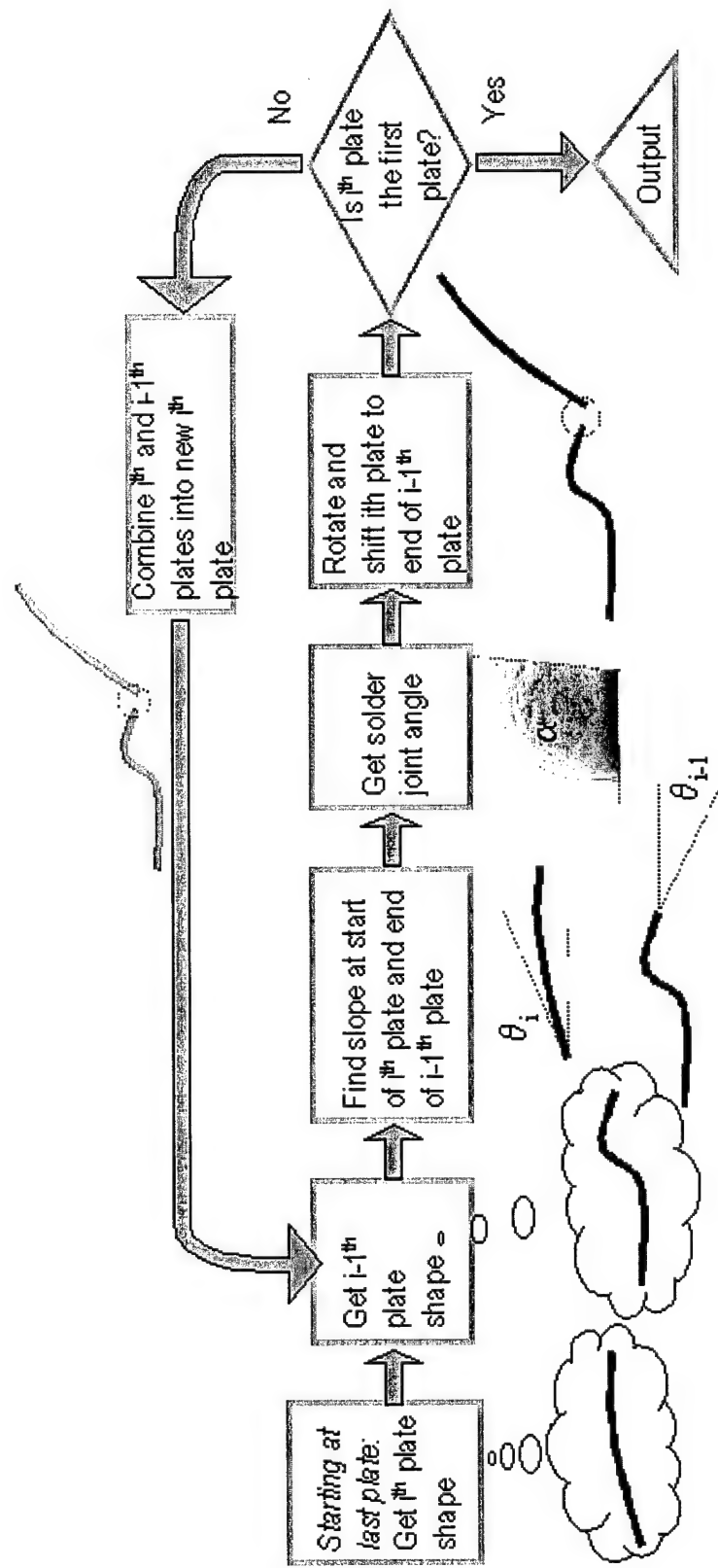


**Figure 5-22:** The Assembly Builder algorithm.

## 5.4 Summary

This chapter described all of the models used to predict the assembly shape of the two-solder-joint test structure and in general n-solder-joint test structures. Three major groups of models were discussed: solder angle models, polysilicon deformation models, and assembly shape modeling. The assembly shape model combines homogeneous transformations with the solder angle and deformation models to get the final assembly shape.

The solder angle model is valid for any type of solder joint with square pads. To improve the accuracy of the solder angle model, I would use circular solder pads instead of square solder pads. The circular solder pads would also have an added benefit of reducing scavenging by eliminating the high surface energy shaped corners and edges where the solder is constrained to the square pads. Furthermore, The solder deformation models can also easily be improved, if needed, by changing from "beam theory" based deformation models to other types of deformation models, such as discussed in the works given in section 5.2.

## 5.5 References

- [1] S. M. Heinrich, A. F. Elkouh, N. J. Nigro, and P. S. Lee, "Solder joint formation in surface mount technology -- Part I: Analysis," *Journal of Electronic Packaging*, vol. 112, no. 3, pp. 210-218, Sep 1990.
- [2] S. M. Heinrich, N. J. Nigro, A. F. Elkouh, and P. S. Lee, "Solder joint formation in surface mount technology -- Part II: Design," *Journal of Electronic Packaging*, vol. 112, no. 3, pp. 219-222, Sep 1990.
- [3] S. M. Heinrich, P. E. Liedtke, N. J. Nigro, A. F. Elkouh, and P. S. Lee, "Effect of chip and pad geometry on solder joint formation in SMT," *Journal of Electronic Packaging*, vol. 115, no. 4, pp. 433-439, Dec 1993.

- [4] L. S. Goldmann, "A heuristic force-height equation for molten axisymmetric solder joints," *Proceedings of the 43rd Electronic Components and Technology Conference*, Orlando, FL, pp. 1120-1124, 1-4 Jun 1993.
- [5] W. Lin, S. K. Patra, and Y. C. Lee, "Design of solder joints for self-aligned optoelectronic assemblies," *IEEE Transactions on Components, Packaging, and Manufacturing Technology Part B: Advanced Packaging*, vol. 18, no. 3, pp. 543-551, Aug 1995.
- [6] S. K. Patra, S. S. Sritharan, and Y. C. Lee, "Quantitative characterization of a flip-chip solder joint," *Journal of Applied Mechanics*, vol. 62, no. 2, pp. 390-397, Jun. 1995.
- [7] H. Shimokawa, C. Lee, K. Yamamoto, and T. Soga, "New estimation method of wetting and surface tension by measuring area of spreading solder in flux atmosphere based on ellipse approximation of sessile drop configurations," *Proceedings of the 1995 Japan International Electronic Manufacturing Technology Symposium*, pp. 421-424, 4-6 Dec. 1995.
- [8] S. M. Heinrich, M. Schaefer, S. A. Schroeder, and P. S. Lee, "Prediction of solder joint geometries in array-type interconnects," *Journal of Electronic Packaging*, vol. 118, no. 3, pp. 114-121, Sep. 1996.
- [9] D. C. Whalley and P. P. Conway, "Simulation and interpretation of wetting balance tests using the surface evolver," *Journal of Electronic Packaging*, vol. 118, no. 3, pp. 134-141, Sep 1996.
- [10] N. J. Nigro, F. J. Zhou, S. M. Heinrich, A. F. Elkouh, R. A. Fournelle, and P. S. Lee, "Parametric finite element method for predicting shapes of three-dimensional solder joints," *Journal of Electronic Packaging*, vol. 118, no. 3, pp. 142-147, Sep 1996.
- [11] G. Subbarayan, "A procedure for automated shape and life prediction in flip-chip and BGA solder joints," *Journal of Electronic Packaging*, vol. 118, no. 3, pp. 127-133, Sep. 1996.
- [12] M. J. Pfeifer, "Solder bump size and shape modeling and experimental validation," *IEEE Transactions on Components, Packaging, and Manufacturing Technology Part B: Advanced Packaging*, vol. 20, no. 4, pp. 452-457, Nov. 1997.
- [13] G. Subbarayan and A. Deshpande, "The nature of centroidal locus in misaligned flip-chip solder joints," *Journal of Electronic Packaging*, vol. 119, no. 3, pp. 156-162, Sep. 1997.
- [14] K. N. Chiang and W. L. Chen, "Electronic packaging reflow shape prediction for the solder mask defined ball grid array," *Journal of Electronic Packaging*, vol. 120, no. 2, pp. 175-178, Jun 1998.
- [15] X. Wu, X. Dou, C. P. Yeh, and K. Waytt, "Solder joint formation simulation and component tombstoning prediction during reflow," *Journal of Electronic Packaging*, vol. 120, no. 2, pp. 141-144, Jun 1998.

- [16] K. F. Harsh, R. S. Irwin, and Y. C. Lee, "Solder self-assembly for MEMS," *Proceedings of the 44th International Instrumentation Symposium*, Reno, NV, vol. 44, pp. 249-255, 3-7 May 1998.
- [17] K. Harsh and Y. C. Lee, "Modeling for solder self-assembled MEMS," *Proceedings of SPIE*, San Jose, CA, vol. 3289, paper 3289-26, Jan. 1998.
- [18] K. A. Brakke, *Surface Evolver Manual*, Version 1.99, The Geometry Center, 1300 South Second Street, Minneapolis, MN 55454, 1 Jun. 1995.
- [19] K. Brakke , "The surface evolver," *Experimental Mathematics*, vol. 1, no. 2 (1992), 141-165.
- [20] P. E. Kladitis, K. F. Harsh, V. M. Bright, and Y. C. Lee, "Three-dimensional modeling of solder shape for the design of solder self-assembled micro-electro-mechanical systems," *Proc. 1999 ASME International Mechanical Engineering Congress and Exposition MEMS Symposium*, Nashville, TN, MEMS-Vol. 1, pp. 11-18, Nov. 1999.
- [21] R. R. A. Syms and E. M. Yeatman, "Self-assembly of three-dimensional microstructures using rotation by surface tension forces," *Electronics Letters*, vol. 29, no. 8, pp. 662-664, 15 Apr. 1993.
- [22] R. R. A. Syms, "Equilibrium of hinged and hingeless structures rotated using surface tension forces," *Journal of Microelectromechanical Systems*, vol. 4, no. 4, pp. 177-184, Dec. 1995.
- [23] P. W. Green, R. R. A. Syms, and E. M. Yeatman, "Demonstration of three-dimensional microstructure self-assembly," *Journal of Microelectromechanical Systems*, vol. 4, no. 4, pp. 170-176, Dec. 1995.
- [24] G. K. Batchelor, *An Introduction to Fluid Dynamics*, Cambridge U. P., pp. 63-65, 1967.
- [25] I would like to acknowledge Brian Schaible for the *Surface Evolver* simulation results. The simulations were performed for work related to the following SBIR: "Novel Joining Method for Self-Assembly of Reliable Three Dimensional Micro-Electro-Mechanical Systems," *Final Report: Phase I Small Business Innovative Research (SBIR) Grant*, Number DMI-9960998, Awarded by the National Science Foundation to Sporian Microsystems, Inc., 1286 Haffner Ct., Loveland, CO, 80537, PI: Brian Schaible, Phone: 303-478-0050, Fax: 603-754-1770, E-mail brian@sporian.com.
- [26] L. S. Goldmann, "Geometric optimization of controlled collapse interconnections," *IBM Journal of Research and Development*, vol. 13, no. 3, pp. 251-265, May 1969.
- [27] M. L. Dunn, Ya. Zhang, J. Roy, P. E. W. Labossiere, and V. M. Bright, "Nonlinear deformation of multilayer MEMS structures," *Proceedings of the 1999 International Mechanical Engineering Congress and Exposition (IMECE 1999)*, MEMS-Vol. 1, pp. 75-79, Nashville, TN, Nov. 1999.
- [28] M. L. Dunn, Y. H. Zhang, and V. M. Bright, "Linear and geometrically nonlinear behavior of metal/polysilicon plate microstructures subjected to

- temperature changes," *Proceedings of the 2000 International Mechanical Engineering Congress and Exposition (IMECE 2000)*, MEMS-Vol. 2, pp. 207-213, Nov. 5-10, 2000, Orlando, Florida.
- [29] M. L. Dunn, Y. H. Zhang, and V. M. Bright, "Nonlinear deformation of metal/polysilicon layered MEMS structures subjected to thermal loading," *Presented at the 2000 ASTM Symposium on Mechanical Properties of Structural Films*, Orlando, FL, November, 2000.
- [30] Y. H. Zhang and M. L. Dunn, "Stress relaxation and creep of gold/polysilicon layered MEMS microstructures subjected to thermal loading," *To be published in the Proceedings of the 2000 International Mechanical Engineering Congress and Exposition (IMECE 2001)*, Nov. 2001.
- [31] David C. Miller, *Micromachined, Flip-Chip Assembled, Actuatable, Normally-Closed Contacts for Use in High Density Electronics Packaging*, Master's Thesis, University of Colorado at Boulder, Dept. of Mechanical Engineering, 2000.
- [32] E. Obermeier, "Mechanical and thermophysical properties of thin film materials for MEMS: techniques and devices," *Proceedings of the Materials Research Society Symposium*, vol. 444, pp. 39-57, 1997.

## **6 Issues In Assembly Precision**

In this chapter the experimental measurements of the endpoints of the different variants of the two-solder-joint test structure will be compared to the model predictions. The end positions of the test structures were measured using the procedures and equipment described in Appendix A, Section A.11: Optical Measurement. The model predictions agree with the experimental data – thereby validating the model. The results of the model are then used to make general statements about the possible precision of multiple joint solder self-assembled MEMS. Next, the specific inputs used for the model are discussed.

### **6.1 The Precision Issues That Are Not Being Considered**

This work addresses the following issues that affect the assembly precision of a multiple joint solder-self assembled MEMS:

- a) Solder volume variation
- b) Solder pad size variation by scavenging and overwetting
- c) Variation of structure deformation due to residual stresses
- d) Hinge location variation
- e) Variation of structure dimensions
- f) Temperature variation

There are methods available to increase the precision of a solder self-assembled MEMS. These methods, which are not being addressed in this work, are:

- a) Increasing assembly angle control using mechanical stops (kick-stands).

- b) Minimizing deformation in solder self-assembled plates by finding an optimum placement of hinges, solder pad, and mechanical stops.
- c) Minimizing deformation in solder self-assembled plates by finding an optimum shape for the solder pads.

Kevin Harsh already addresses the above issues in his dissertation *Design Optimization For MEMS Solder Self-Assembly* [1]. Furthermore, the issues I am addressing are more fundamental. For example, one can not have an optimized solder self-assembled MEMS if one can not reliably process them. Also, mechanical stops are useless if the structures can not even achieve the assembly angle necessary to lock the stops in place.

## 6.2 The Precision Issues That Are Being Considered

The different precision issues that are being addressed have been listed in the previous section. I will now discuss them one at a time by describing them and presenting the parameters used to model them.

### 6.2.1 Solder Volume Variation

The solder volumes used to assemble the test structures were manufactured by Alphametals and are claimed to be at the eutectic mixture of 63Sn/37Pb. Two sizes are used. The sizes, reported by the manufacturer, are  $8 \text{ mil} \pm 1 \text{ mil}$  diameters and  $4 \text{ mil} \pm 0.5 \text{ mil}$  diameters. However, over the course of this research, I became suspicious about the size of the solder spheres, due to the fact that solder joints would always assemble to an angle larger than what was predicted by modeling.

The solder balls were measured using the optical measurement system described in Appendix A, Section A.11. Figure 6-1 shows examples of the captured video images used to measure the actual diameters of the manufactured solder spheres. Table 6-1 lists the measured results, which are also used as inputs to the model. Figure 6-2 and Figure 6-3 show the histograms of the 4 mil and 8 mil measurements, respectively.

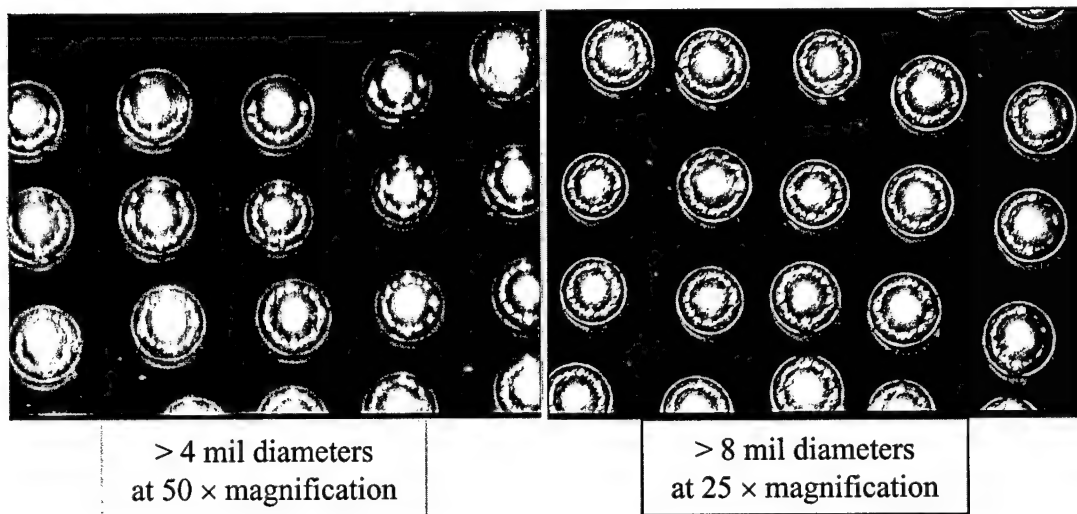


**Figure 6-1:** Captured video images used to measure the actual diameters of the manufactured solder spheres.

Advertised Ball Size (mil)	Sample Size	Measured Mean Diameter $\mu_D$ (mil)	Measured Standard Deviation $\sigma_D$ (mil)	$3\sigma_D$ Tolerance $t_{0D}$ (mil)
$8 \pm 1$	145	8.4547	0.3406	$\pm 1.0217$
$4 \pm 0.5$	121	4.3878	0.1497	$\pm 0.4491$

**Table 6-1:** Tabulation of measured solder sphere diameter parameters.

By now, the reader may be wondering how much does a change in solder ball diameter affect the assembly angle. Figure 6-4 and Figure 6-5 are plots of

equilibrium angle while varying square solder pad dimensions and varying the solder ball diameter by  $4.3878 \pm 0.4491$  mil and  $8.4547 \pm 1.0217$  mil, respectively.

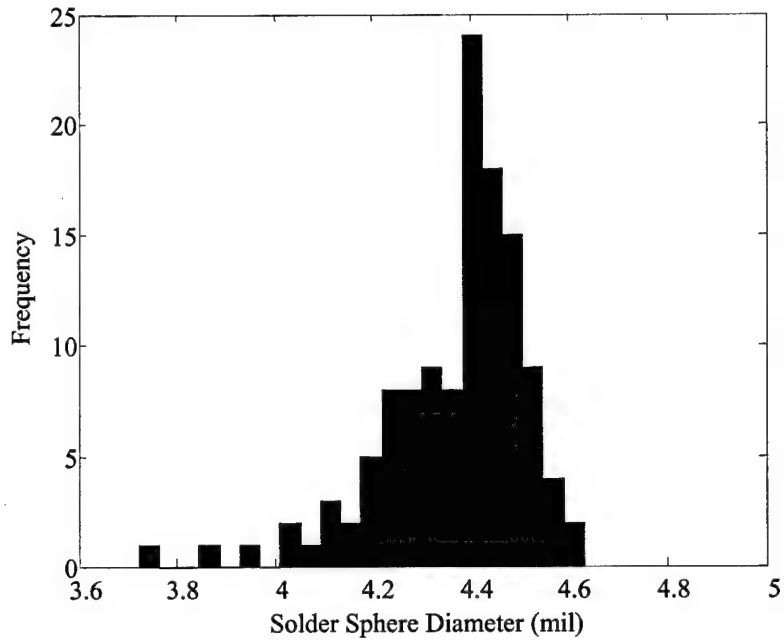


**Figure 6-2:** Histogram of 4 mil ball measurements.

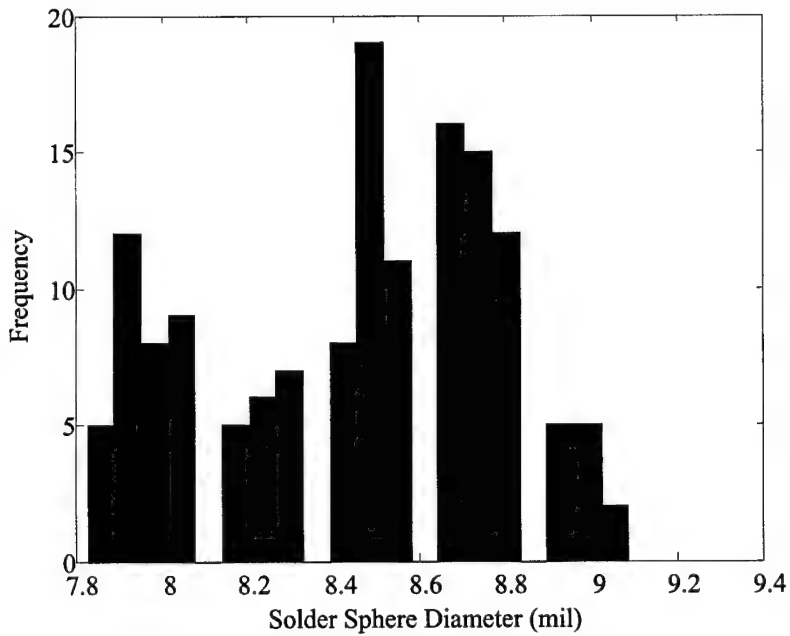


**Figure 6-3:** Histogram of 8 mil ball measurements.

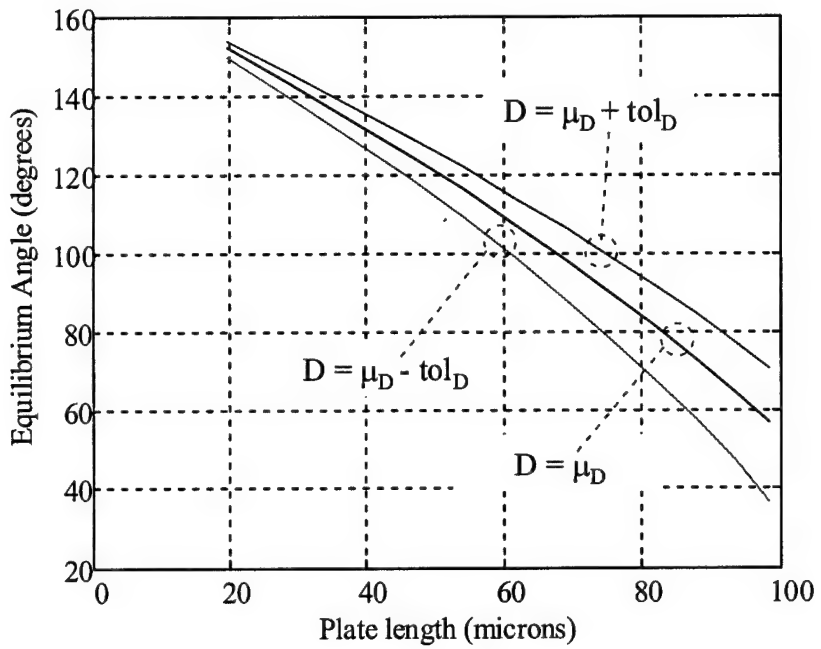


**Figure 6-4:** Plot of equilibrium angle while varying square solder pad dimensions and varying the solder ball diameter by  $4.3878 \pm 0.4491$  mil.

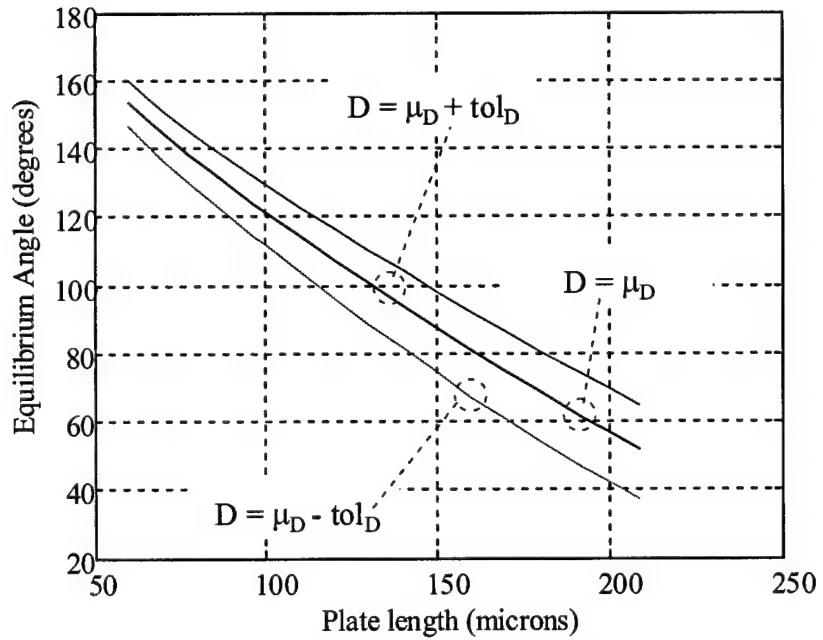


**Figure 6-5:** Plot of equilibrium angle while varying square solder pad dimensions and varying the solder ball diameter by  $8.4547 \pm 1.0217$  mil.

### 6.2.2 Solder Pad Size Variation By Scavenging And Overwetting

Scavenging and overwetting were already discussed in Chapter 4. Table 4-2 lists the amount of scavenging and overwetting observed for different solder pads, solder volumes, and process refinements. Scavenging or overwetting is represented in the model by a simple change in solder pad length or width:

$$l = l_{nominal} - \mu_{scav} \pm tol_{scav}, \text{ and} \quad (6-1)$$

$$w = w_{nominal} - \mu_{scav} \pm tol_{scav}. \quad (6-2)$$

As can be seen from the negative sign of overwetting, in Table 4-2, Equations (6-1) and (6-2) will ensure that  $\mu_{scav}$  is added to  $l$  or  $w$ . Recall that overwetting is where the solder has actually wet to the polysilicon, out further than the solder pads, thereby increasing the effective length and/or width of the original solder pad.

When the length of the solder pad changes, the area of non-solder-covered structure changes. The model accounts for this by defining the lengths, of the portions of the plates, relative to each other in the plate matrix – so when one segment shrinks, another lengthens by an equal amount and vice versa.

### 6.2.3 Variation Of Structure Deformation Due To Residual Stresses

The developments in the following sections use these material properties and values for calculations:

- a)  $E_s = 169 \text{ GPa}$  and  $\nu_s = 0.22$  [2]
- b)  $\alpha_s = 2.33 \times 10^{-6}$ ,  $E_f = 79 \text{ GPa}$ ,  $\nu_f = 0.42$ ,  $\alpha_f = 14.2 \times 10^{-6}$  [3]
- c)  $T = 27^\circ\text{C}$  (measurement temperature)

### 6.2.3.1 Residual Stress Of A Bilayer Structure: Gold On Poly2

The average and standard deviation of the reported gold stress for the MUMPs process runs 10 – 42 was calculated to be  $\mu_{\text{gold}} = 48.21 \text{ MPa}$  (tensile) and  $stdev_{\text{gold}} = 20.44 \text{ MPa}$ . MUMPs fabrication run 8 reported a value for gold stress of 166 MPa (tensile). Here, I am assuming that this stress is measured with the gold on poly2, since the gold can only be patterned on the poly2. The average and standard deviation of the reported poly2 stress was calculated to be  $\mu_{\text{poly2}} = -7.9 \text{ MPa}$  (compressive) and  $stdev_{\text{poly2}} = 2.82 \text{ MPa}$ .

Interferometric microscope measurements of curvature of gold on poly2 yielded an average radius of curvature of  $R = 1700 \mu\text{m}$ . Figure 6-6 shows an example output of the Zygo interferometric microscope where the radius of curvature of gold on poly2 bilayer structure is being measured. The equipment and measurement procedures used can be found in Appendix A, Section A.12.  $R$  was found by taking the average of measured radius of curvatures from all of the gold on poly2 regions of two released warp version chips. The two chips were also plasma cleaned for 1 minute and re-measured. The radius of curvature was more uniform, but virtually the same in magnitude. The residual stress due to misfit strain was then calculated as 103.5 MPa from Equation 5-26, using  $\mu_{\text{poly2}}$  and  $R$ . Using  $T$ ,  $T_0$  was found from Equation (5-25) as  $95.9^\circ\text{C}$ . The nominal stress and tolerance used in the model is:

$$\sigma_{\text{gold}} = 103.5 \pm 20.44 \text{ MPa} . \quad (6-3)$$

This nominal and tolerance value for gold does not take into account any annealing or quenching that occurs during the thermal cycling of the pre-release,

preflow, release, and reflow. In fact, as may be noticed from some of the result figures, if my assumed gold stress value were higher, the predicted results would line up even better with the experimental results.

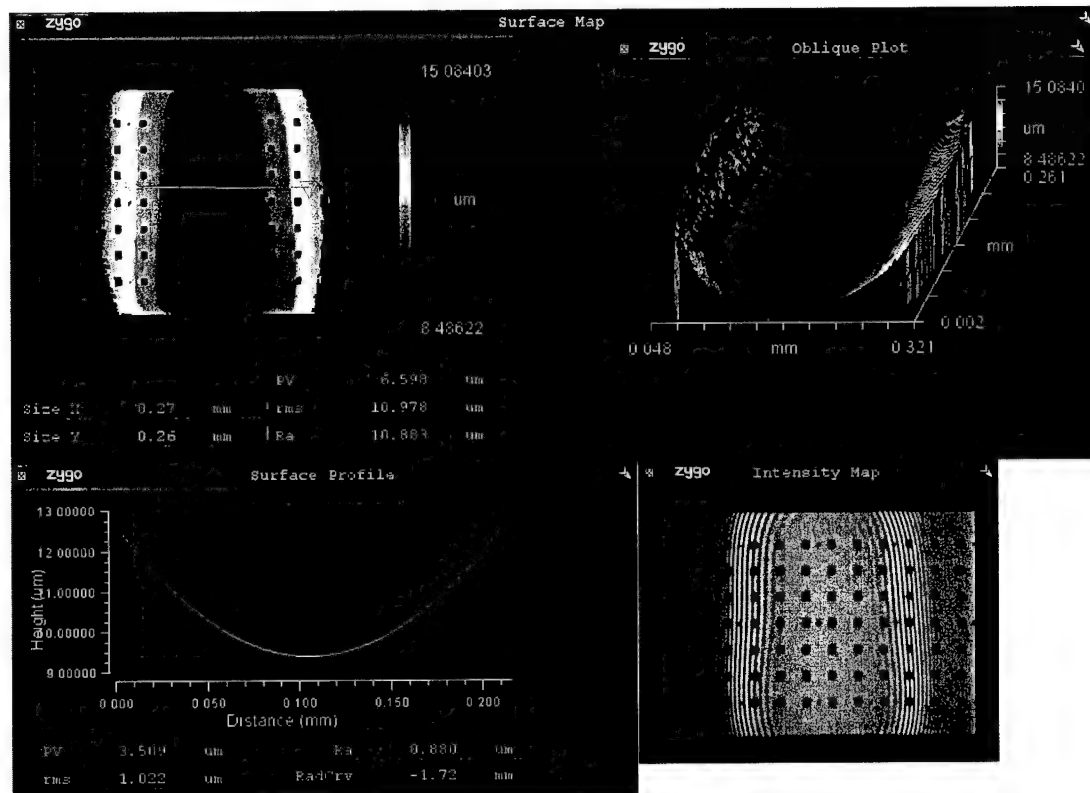


**Figure 6-6:** Output of the Zygo interferometric microscope showing the measurement of radius of curvature of gold on poly2 bilayer structure.

### 6.2.3.2 Residual Stress Of A Single Layer Structure

The nominal stress and tolerance used in the model come from the reported stress values given above:

$$\sigma_{\text{poly}} = -7.9 \pm 2.82 \text{ MPa} . \quad (6-4)$$

### 6.2.3.3 Deformation Of Poly2 Due To Solder

The radius of curvature of the back-side of solder joints was measured from a random sample of assembled 8 mil and 4mil test structures. The average curvature and tolerance used in the model is:

$$R_{\text{sol/poly}} = 6000 \pm 1000 \mu\text{m}. \quad (6-5)$$

An example output of the Zygo interferometric microscope is shown in Figure 6-7.

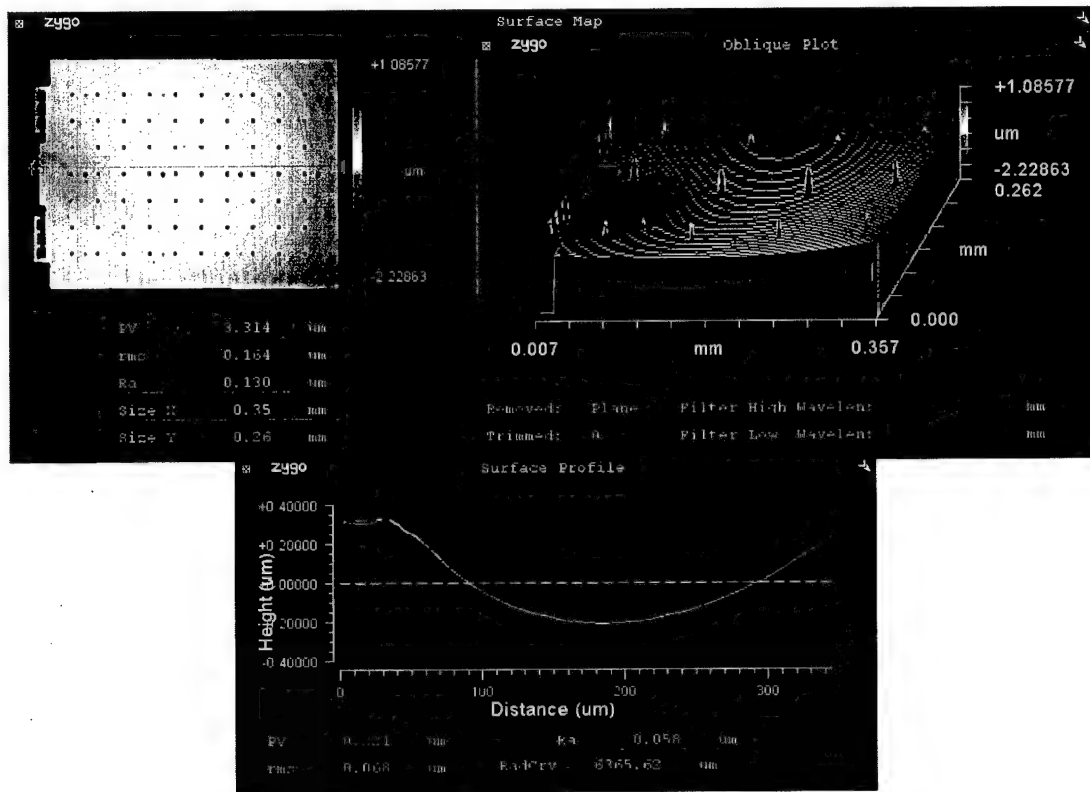


**Figure 6-7:** Output of the Zygo interferometric microscope showing the measurement of radius of curvature of solder on poly2.

### 6.2.4 Hinge Location Variation

Frankly, hinge play at a solder joint is not an issue. Syms proves it [4], and I have experimentally confirmed that the surface tension of the solder will always pull

the hinged ends of the solder pads together – this is the minimum surface energy condition.

However, there may be hinged parts of a multiple joint solder self-assembled structure that are not involved in a solder joint. Depending on the exact design, a substrate hinge has approximately  $\pm 0.5 \mu\text{m}$  of play from a nominal position. To investigate the impact that hinge play would have on an assembled structure, I have included it at each hinge, even though in reality, it would not happen:

$$h_x = h_y = 0 \pm 0.5 \mu\text{m} . \quad (6-6)$$

where  $h_x$  is the hinge play in the x-direction, and  $h_y$  is the hinge play in the y-direction.

### 6.2.5 Variation Of Structure Dimensions

The minimum feature spacing in the MUMPs process is  $2 \mu\text{m}$ . If a structure is somehow  $1 \mu\text{m}$  too long, in any direction, it may not be able to be resolved apart from a neighboring structure during fabrication. From this simplistic reasoning, a tolerance for the length of the test structure plates is deduced:

$$L = 500 \pm 2 \mu\text{m} . \quad (6-7)$$

### 6.2.6 Temperature Variation

For the following simulations, room temperature is assumed to be  $27^\circ\text{C}$ . A somewhat arbitrary tolerance on temperature was chosen from observed fluctuations in room temperature:

$$T = 27 \pm 6^\circ\text{C} . \quad (6-8)$$

### **6.3 Comparison Of Model Predictions With Experimental Measurements**

All of the nominal values, standard deviations, and tolerances, described above, are used as inputs to the n-hinge model. The output of the model is now compared to experimental measurements. Figure 6-9 through Figure 6-13 are plots of experimentally measured endpoints of the two-solder-joint test structure compared to the predicted nominal position; a predicted worst-case tolerance region; and a predicted one, two, and three standard deviation region. The three standard deviation ( $3\sigma$ ) is the statistical tolerance region.

There are a total of 21 figures showing results. Figure 6-9 through Figure 6-13 are 5 examples. The other 16 result figures can be found in Appendix D: Experimental Results. The result figures are designated by their approximate angle combination, i.e. "90/45"; the version, i.e. "warp"; and the approximate volume of solder, i.e. "8 mil" or "4 mil". The legend, shown in Figure 6-8, is used for all of the result figures.

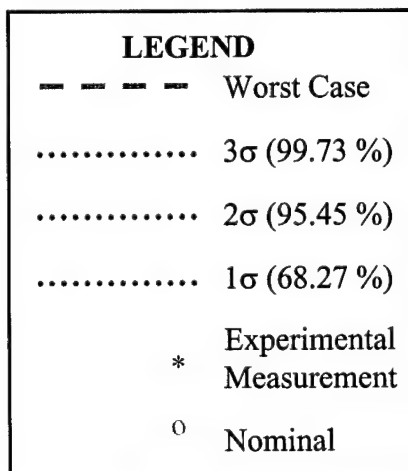


**Figure 6-8:** Legend for the result figures.

Included, in the output of the model, are predictions of the nominal position, partial derivatives, statistical tolerance region, worst-case tolerance region, and individual impacts. Each plot of experimentally measured endpoints has an associated table of model predictions. The following is an explanation of notations used in the tables.

Many of the notations have already been defined previously, and I will not repeat those definitions. All components of the test structure are numbered from the substrate, so a subscript "1" or "2" indicates the 1<sup>st</sup> or 2<sup>nd</sup> item. A subscript or superscript "x" means in the x-direction, similarly for "y". For example, " $h_{2y}$ " denotes the hinge play of the 2<sup>nd</sup> set of hinges in the y-direction. "Impact  $f_i^x$ " is the absolute value of the product of the  $i^{th}$  ( $x_i$ ) variable's tolerance ( $\text{tol}_i$ ) and the partial derivative of the assembly function's x-displacement with respect to  $x_i$ , and similarly for "Impact  $f_i^y$ ". "pl1" and "pl2" mean plate 1 and 2, respectively. "pd1" and "pd2" mean solder pad 1 and 2, respectively. "T0" (not to be confused with " $T_\theta$ ", the zero misfit strain temperature) is the nominal position of the end of the assembly, "T\_WC" is the worst-case tolerance ( $\pm$ ), "T\_S3" is the statistical tolerance ( $\pm 3\sigma_{\text{assembly function}}$ ), "T\_S2" is  $\pm 2\sigma_{\text{assembly function}}$ , and "T\_S1" is  $\pm \sigma_{\text{assembly function}}$ . Furthermore, the first and second rows associated with T0, T\_WC, T\_S3, T\_S2, and T\_S1 are in the "x" and "y" directions in microns, respectively.

The partial derivatives used to calculate the impacts, worst-case tolerance, and statistical tolerances are calculated numerically using central differences. The differential used for the finite differences is:

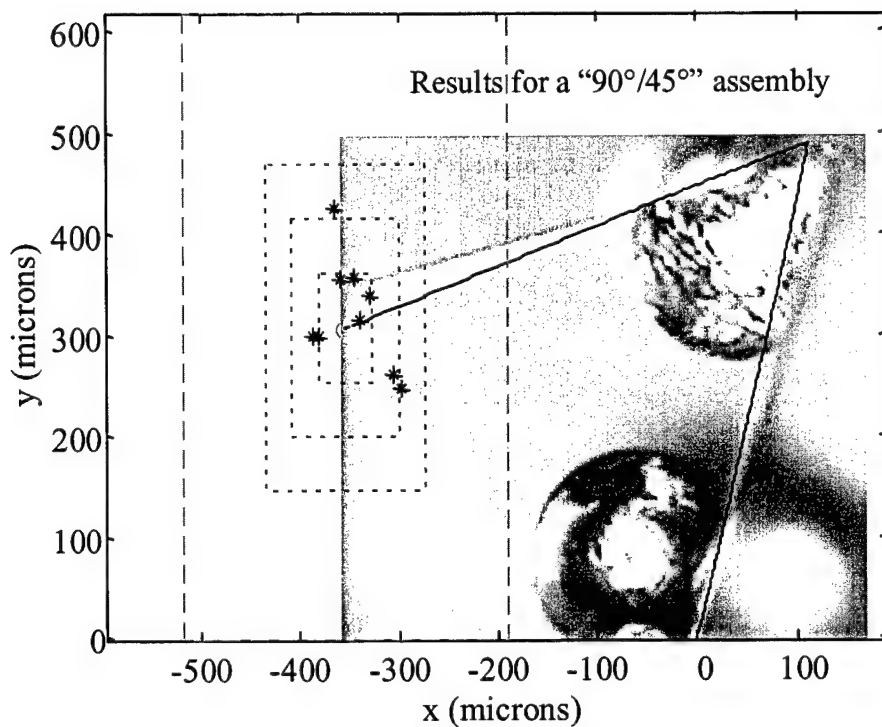
$$\text{Typical Variable Value} \times (\varepsilon_{\text{machine}})^{\frac{1}{2}} \quad (6-9)$$

### 6.3.1 8 Mil Test Structures

The following figures and numerical results were generated using the i/o file *assyio\_2h8.m*. *assyio\_2h8.m* contains the Plate Matrix, calls the Assembly Builder routine, plots output, and calculates derivative information. *assyio\_2h8.m* is included in Appendix B. Again, the end positions of the test structures were measured using the procedures and equipment described in Appendix A, Section A.11: Optical Measurement.

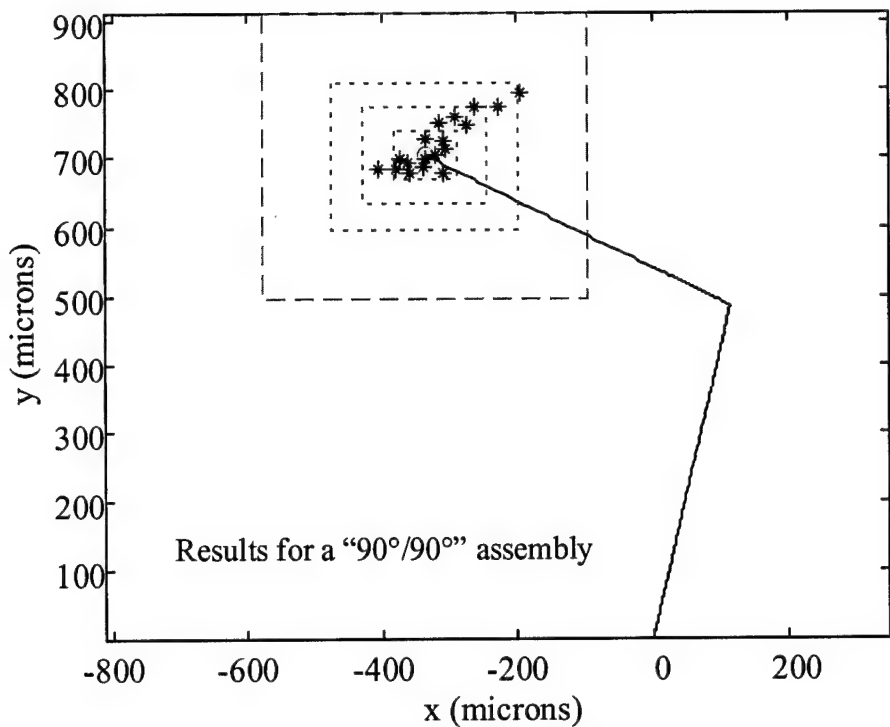
Figure 6-9 is a plot of experimentally measured endpoint positions (\*) for the  $90^\circ/45^\circ$  8 mil variant of the test structure. The nominal predicted position for the endpoint is  $(-345.11, 306.27)$   $\mu\text{m}$ . The largest and 2<sup>nd</sup> largest boxed regions are the worst-case and statistical tolerance regions, respectively. Superimposed, in the background, is one of the captured video images used to measure one of the end position data points. The superimposed image is provided to help the reader orient the model predicted shape to the actual shape. As one can see, in this case, all of the measured data points lie in the statistical tolerance region.

Similarly, Figure 6-10 is a plot of experimentally measured endpoint positions (\*) for the  $90^\circ/90^\circ$  8 mil variant of the test structure. The nominal predicted position for the endpoint is  $(-335.82, 704.31)$   $\mu\text{m}$ . Also, in this case, all of the measured data points lie in the statistical tolerance region.



Variable ( $x_i$ )	$df^x/dx_i$	$df^y/dx_i$	$tol_i$	$nominal_i$	impact $f_i^x$	impact $f_i^y$
$L_1$ ( $\mu\text{m}$ )	2.3179E-01	9.9353E-01	2.00	500-5micgap	0.46358796	1.98706242
$L_2$ ( $\mu\text{m}$ )	-9.3380E-01	-3.5810E-01	2.00	500.00	1.86760386	0.71620124
stress <sub>poly</sub> p11 (Pa)	-1.0383E-07	-4.3533E-07	2820000.00	-7900000.00	0.292810893	1.22762888
stress <sub>poly</sub> p12 (Pa)	1.0857E-07	-2.7102E-07	2820000.00	-7900000.00	0.306165088	0.764268899
R <sub>sol/poly</sub> p1pd1 ( $\mu\text{m}$ )	8.3893E-04	1.2805E-03	1000.00	6000.00	0.83893267	1.2805233
R <sub>sol/poly</sub> p1pd2 ( $\mu\text{m}$ )	-4.5550E-04	2.3979E-03	1000.00	6000.00	0.45549711	2.3979479
R <sub>sol/poly</sub> p12pd1 ( $\mu\text{m}$ )	-7.8704E-04	2.0426E-03	1000.00	6000.00	0.78703753	2.0426254
$h_{1x}$ ( $\mu\text{m}$ )	1.0000E+00	0.0000E+00	0.50	0.00	0.5	0
$h_{1y}$ ( $\mu\text{m}$ )	0.0000E+00	1.0000E+00	0.50	0.00	0	0.5
$h_{2x}$ ( $\mu\text{m}$ )	1.9944E-01	9.7990E-01	0.50	0.00	0.09972191	0.489952085
$h_{2y}$ ( $\mu\text{m}$ )	-9.7992E-01	1.9943E-01	0.50	0.00	0.48995781	0.099716185
$D_1$ ( $\mu\text{m}$ )	2.1014E+00	2.4297E+00	25.95	214.75	54.53244066	63.05083178
$D_2$ ( $\mu\text{m}$ )	-1.6768E+00	4.3168E+00	25.95	214.75	43.5120258	112.0200024
$I_1$ ( $\mu\text{m}$ )	-3.2540E+00	-3.7994E+00	6.00	131-6	19.5242724	22.79646
$I_2$ ( $\mu\text{m}$ )	1.6267E+00	-4.2860E+00	22.00	217-22	35.7868016	94.2918856
$w_1$ ( $\mu\text{m}$ )	-3.9547E-01	-4.5724E-01	6.00	131-6	2.37281394	2.74346592
$w_2$ ( $\mu\text{m}$ )	2.2386E-01	-5.7632E-01	7.00	217-7	1.56702791	4.03425155
	T0	T_WC	T_S3	T_S2	T_S1	
	-354.11	163.41	80.90	53.93	26.97	
	306.27	310.47	161.19	107.46	53.73	

**Figure 6-9:** 90/45 8 mil variant.



Variable ( $x_i$ )	$df^x/dx_i$	$df^y/dx_i$	$tol_i$	$nominal_i$	impact $f_i^x$	impact $f_i^y$
$L_1$ ( $\mu\text{m}$ )	2.5122E-01	9.9266E-01	2.00	500.00	0.50243324	1.98531842
$L_2$ ( $\mu\text{m}$ )	-8.9656E-01	4.4331E-01	2.00	500.00	1.79311346	0.88661532
$\text{stress}_{\text{poly}} \text{ p11}$ (Pa)	-6.9525E-07	-5.9443E-07	2820000.00	-7900000.00	1.960597696	1.676282476
$\text{stress}_{\text{poly}} \text{ p12}$ (Pa)	-1.8837E-07	-3.9912E-07	2820000.00	-7900000.00	0.531212227	1.125531175
$R_{\text{sol/poly}} \text{ p11pd1}$ ( $\mu\text{m}$ )	2.2204E-03	1.2171E-03	1000.00	6000.00	2.2204329	1.2170588
$R_{\text{sol/poly}} \text{ p11pd2}$ ( $\mu\text{m}$ )	9.7028E-04	1.5108E-03	1000.00	6000.00	0.97027906	1.5107791
$R_{\text{sol/poly}} \text{ p12pd1}$ ( $\mu\text{m}$ )	6.6451E-04	1.3703E-03	1000.00	6000.00	0.66450946	1.3703092
$h_{1x}$ ( $\mu\text{m}$ )	1.0000E+00	0.0000E+00	0.50	0.00	0.5	0
$h_{1y}$ ( $\mu\text{m}$ )	0.0000E+00	1.0000E+00	0.50	0.00	0	0.5
$h_{2x}$ ( $\mu\text{m}$ )	2.1417E-01	9.7679E-01	0.50	0.00	0.10708618	0.48839569
$h_{2y}$ ( $\mu\text{m}$ )	-9.7681E-01	2.1417E-01	0.50	0.00	0.48840332	0.10708618
$D_1$ ( $\mu\text{m}$ )	4.8326E+00	2.3042E+00	25.95	214.75	125.4055911	59.79496572
$D_2$ ( $\mu\text{m}$ )	1.4927E+00	3.0891E+00	25.95	214.75	38.73642914	80.16315965
$I_1$ ( $\mu\text{m}$ )	-7.5179E+00	-3.6036E+00	6.00	131-6	45.1074654	21.6213066
$I_2$ ( $\mu\text{m}$ )	-2.3927E+00	-4.8897E+00	6.00	131-6	14.3563686	29.3383296
$w_1$ ( $\mu\text{m}$ )	-9.0944E-01	-4.3363E-01	6.00	131-6	5.45664462	2.6017965
$w_2$ ( $\mu\text{m}$ )	-2.8092E-01	-5.8134E-01	6.00	131-6	1.68549846	3.48805812
T0	T_WC	T_S3	T_S2	T_S1		
-335.82	240.51	139.71	93.14	46.57		
704.31	207.90	106.61	71.08	35.54		

Figure 6-10: 90/90 8 mil variant.

### 6.3.2 8 Mil Warp Test Structures

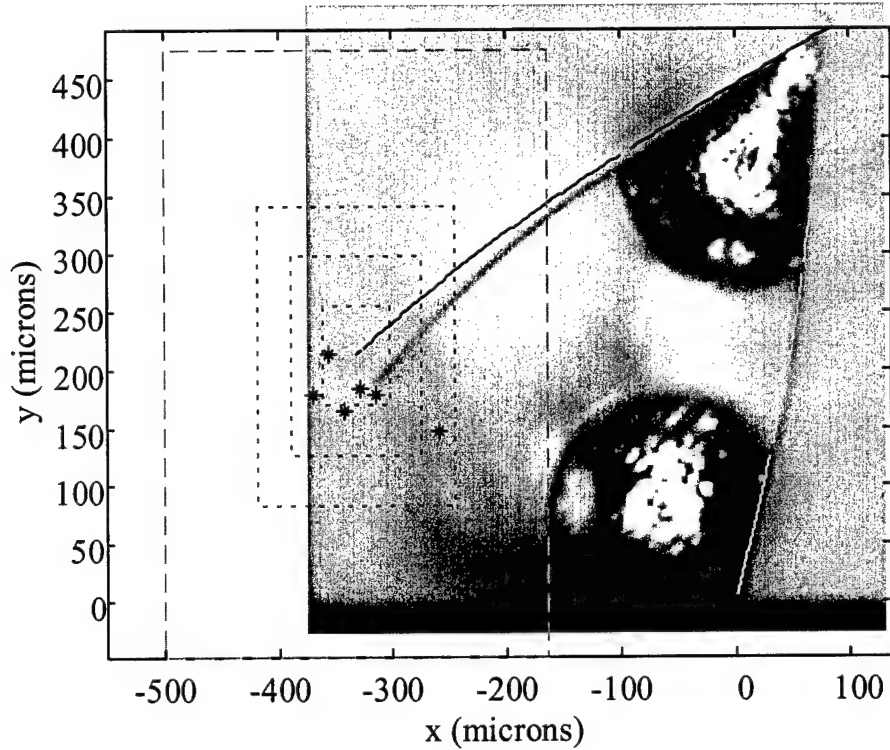
The following figures and numerical results were generated using the i/o file *assyio\_2h8warp.m*. *assyio\_2h8warp.m* contains the Plate Matrix, calls the Assembly Builder routine, plots output, and calculates derivative information. *assyio\_2h8warp.m* is included in Appendix B. Again, the end positions of the test structures were measured using the procedures and equipment described in Appendix A, Section A.11: Optical Measurement.

Figure 6-11 is a plot of experimentally measured endpoint positions (\*) for the  $90^\circ/45^\circ$  8 mil warp variant of the test structure. The nominal predicted position for the endpoint is  $(-331.93, 212.91)$   $\mu\text{m}$ . As one can see, in this case, all of the measured data points lie in the statistical tolerance region.

Similarly, Figure 6-12 is a plot of experimentally measured endpoint positions (\*) for the  $45^\circ/135^\circ$  8 mil variant of the test structure. The nominal predicted position for the endpoint is  $(-818.02, 365.27)$   $\mu\text{m}$ . Also, all of the measured data points lie in the statistical tolerance region. Included in this figure is a second plot of the assembly, modeled with all of its components at their worst case. This second plot is included to show that if the structure were allowed, and all of the components, in the right combination, happened to be at their worst case, the structure could actually reach the worst-case tolerance region.

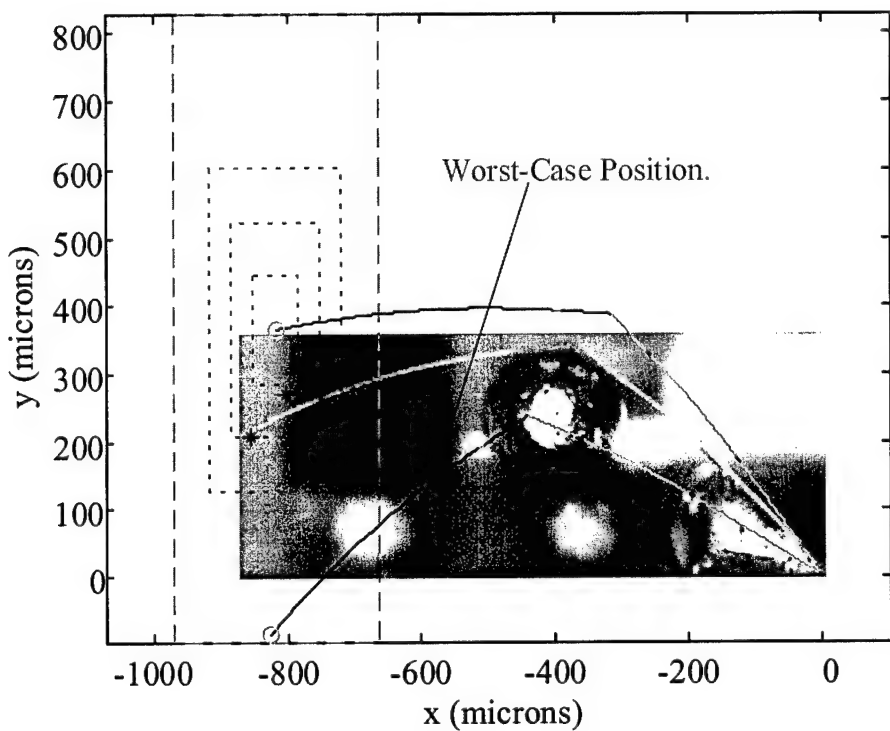
Recall that overwetting, described in Section 4.5.1, causes the failure of the warp version assemblies to assemble to a proper assembly shape. Further recall, that overwetting occurs mostly with the small solder pads of the  $135^\circ$  degree solder joints.

Because of this failure due to overwetting, test variants including an assembly angle of 135°, usually failed, therefore data is limited for these variants.



Variable ( $x_i$ )	$df^x/dx_i$	$df^y/dx_i$	$tol_i$	$nominal_i$	impact $f^x_i$	impact $f^y_i$
$L_1$ ( $\mu\text{m}$ )	1.7416E-01	7.4927E-01	2.00	500.00	0.3483	1.4985
$L_2$ ( $\mu\text{m}$ )	-7.5811E-01	-6.7755E-01	2.00	500.00	1.5162	1.3551
stress <sub>poly</sub> (Pa)	1.0259E-08	-6.1013E-08	2820000.00	-7900000.00	0.0289	0.1721
stress <sub>gold</sub> (Pa)	1.3029E-07	-5.5761E-07	21000000.00	103500000.00	2.7361	11.7098
$R_{\text{sol/poly}} p1pd1$ ( $\mu\text{m}$ )	5.1491E-04	1.2036E-03	1000.00	6000.00	0.5149	1.2036
$R_{\text{sol/poly}} p1pd2$ ( $\mu\text{m}$ )	-9.9466E-04	2.2509E-03	1000.00	6000.00	0.9947	2.2509
$R_{\text{sol/poly}} p1pd1$ ( $\mu\text{m}$ )	-1.2792E-03	1.8530E-03	1000.00	6000.00	1.2792	1.8530
$h_{1x}$ ( $\mu\text{m}$ )	1.0000E+00	0.0000E+00	0.50	0.00	0.5000	0.0000
$h_{1y}$ ( $\mu\text{m}$ )	0.0000E+00	1.0000E+00	0.50	0.00	0.0000	0.5000
$h_{2x}$ ( $\mu\text{m}$ )	9.7935E-02	9.9519E-01	0.50	0.00	0.0490	0.4976
$h_{2y}$ ( $\mu\text{m}$ )	-9.9520E-01	9.7937E-02	0.50	0.00	0.4976	0.0490
$D_1$ ( $\mu\text{m}$ )	1.4609E+00	2.2776E+00	25.95	214.75	37.9097	59.1025
$D_2$ ( $\mu\text{m}$ )	-2.6031E+00	3.8629E+00	25.95	214.75	67.5507	100.2430
$l_1$ ( $\mu\text{m}$ )	-2.2009E+00	-3.3187E+00	6.00	131-6	13.2054	19.9120
$l_2$ ( $\mu\text{m}$ )	2.3303E+00	-3.3078E+00	15.00	217-15	34.9548	49.6175
$w_1$ ( $\mu\text{m}$ )	-2.7492E-01	-4.2861E-01	6.00	131-6	1.6495	2.5717
$w_2$ ( $\mu\text{m}$ )	3.2710E-01	-4.8540E-01	7.00	217-7	2.2897	3.3978
Temperature ( $^{\circ}\text{C}$ )	-2.1065E-01	9.0153E-01	6.00	27.00	1.2639	5.4092
T0	T_WC	T_S3	T_S2	T_S1		
-331.93	167.30	86.15	57.43	28.72		
212.91	261.37	128.85	85.90	42.95		

Figure 6-11: 90/45 8 mil warp variant.



Variable ( $x_i$ )	$df^x/dx_i$	$df^y/dx_i$	$tol_i$	$nominal_i$	impact $f^x_i$	impact $f^y_i$
$L_1$ ( $\mu\text{m}$ )	-7.2507E-01	3.7168E-01	2.00	500.00	1.4501	0.7434
$L_2$ ( $\mu\text{m}$ )	-1.0148E+00	-2.0102E-01	2.00	500.00	2.0296	0.4020
stress <sub>poly</sub> (Pa)	-1.2267E-08	-1.0300E-07	2820000.00	-7900000.00	0.0346	0.2905
stress <sub>gold</sub> (Pa)	-1.7374E-07	-1.2693E-06	21000000.00	103500000.00	3.6485	26.6559
$R_{\text{sol/poly}}$ p1pd1 ( $\mu\text{m}$ )	1.5676E-03	4.2257E-03	1000.00	6000.00	1.5676	4.2257
$R_{\text{sol/poly}}$ p1pd2 ( $\mu\text{m}$ )	1.1192E-05	1.1019E-03	1000.00	6000.00	0.0112	1.1019
$R_{\text{sol/poly}}$ p1pd2 ( $\mu\text{m}$ )	-5.1104E-05	9.7024E-04	1000.00	6000.00	0.0511	0.9702
$h_{1x}$ ( $\mu\text{m}$ )	1.0000E+00	0.0000E+00	0.50	0.00	0.5000	0.0000
$h_{1y}$ ( $\mu\text{m}$ )	0.0000E+00	1.0000E+00	0.50	0.00	0.0000	0.5000
$h_{2x}$ ( $\mu\text{m}$ )	-7.0313E-01	7.1106E-01	0.50	0.00	0.3516	0.3555
$h_{2y}$ ( $\mu\text{m}$ )	-7.1107E-01	-7.0312E-01	0.50	0.00	0.3555	0.3516
$D_1$ ( $\mu\text{m}$ )	3.3993E+00	7.6128E+00	25.95	214.75	88.2127	197.5532
$D_2$ ( $\mu\text{m}$ )	-1.1082E-01	2.5132E+00	25.95	214.75	2.8759	65.2180
$I_1$ ( $\mu\text{m}$ )	-3.0791E+00	-6.7868E+00	15.00	217-15	46.1863	101.8024
$I_2$ ( $\mu\text{m}$ )	3.1970E-01	-5.7392E+00	5.00	70+5	1.5985	28.6958
$w_1$ ( $\mu\text{m}$ )	-4.2715E-01	-9.5661E-01	7.00	217-7	2.9900	6.6962
$w_2$ ( $\mu\text{m}$ )	3.7845E-02	-8.5823E-01	18.00	70+18	0.6812	15.4481
Temperature ( $^{\circ}\text{C}$ )	2.8090E-01	2.0522E+00	6.00	27.00	1.6854	12.3133
T0	T_WC	T_S3	T_S2	T_S1		
-818.02	154.24	99.81	66.54	33.27		
365.27	463.36	235.90	157.26	78.63		

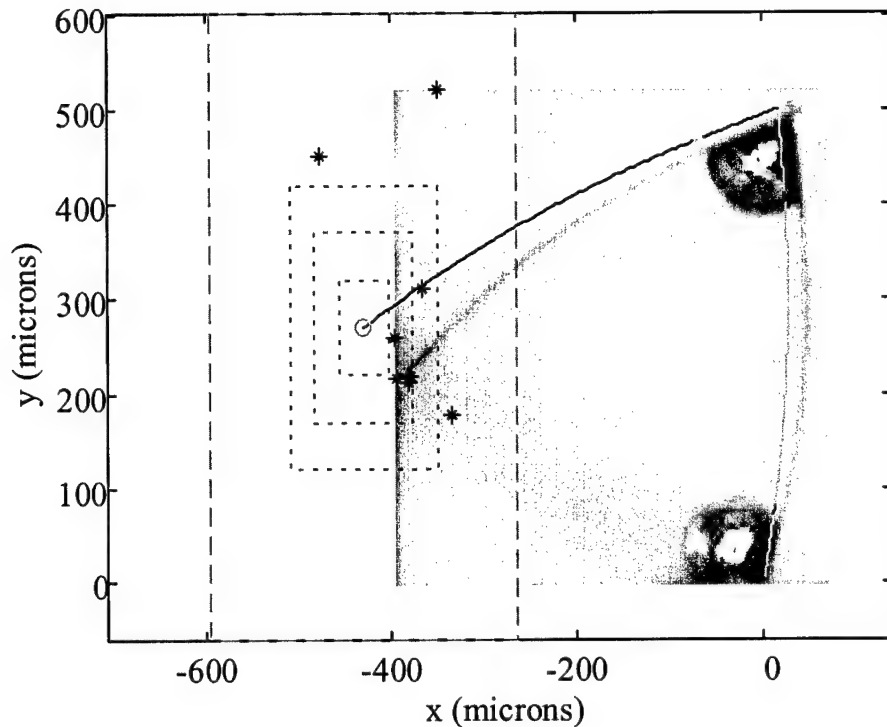
Figure 6-12: 45/135 8 mil warp variant.

### 6.3.3 4 Mil Warp Test Structures

The following figures and numerical results were generated using the i/o file *assyio\_2h4warp.m*. *assyio\_2h4warp.m* contains the Plate Matrix, calls the Assembly Builder routine, plots output, and calculates derivative information. *assyio\_2h4warp.m* is included in Appendix B. Again, the end positions of the test structures were measured using the procedures and equipment described in Appendix A, Section A.11: Optical Measurement.

Figure 6-13 is a plot of experimentally measured endpoint positions (\*) for the  $90^\circ/45^\circ$  4 mil warp variant of the test structure. The nominal predicted position for the endpoint is  $(-429.53, 269.91)$   $\mu\text{m}$ . As one can see, in this case, some of the data points lie outside of the statistical tolerance region, but all of the measured data points lie in the worst-case tolerance region.

Again, recall that overwetting, described in Section 4.5.1, causes the failure of the warp version assemblies to assemble to a proper assembly shape. Further recall, that overwetting occurs mostly with the small solder pads of the  $135^\circ$  degree solder joints. Because of this failure due to overwetting, test variants including an assembly angle of  $135^\circ$ , usually failed, therefore data is limited for these variants. This is the reason that the  $135^\circ/135^\circ$  variant has no data, see Appendix D.



Variable ( $x_i$ )	$df^x/dx_i$	$df^y/dx_i$	tol <sub>i</sub>	nominal <sub>i</sub>	Impact $f^x_i$	Impact $f^y_i$
L <sub>1</sub> ( $\mu\text{m}$ )	1.6692E-02	7.4089E-01	2.00	500.00	0.0334	1.4818
L <sub>2</sub> ( $\mu\text{m}$ )	-8.3603E-01	-6.0575E-01	2.00	500.00	1.6721	1.2115
stress <sub>poly</sub> (Pa)	8.7443E-09	-7.7173E-08	2820000.00	-7900000.00	0.0247	0.2176
stress <sub>gold</sub> (Pa)	1.2274E-07	-1.2768E-06	21000000.00	103500000.00	2.5775	26.8130
R <sub>sol/poly</sub> pl1pd1 ( $\mu\text{m}$ )	4.4362E-04	8.3350E-04	1000.00	6000.00	0.4436	0.8335
R <sub>sol/poly</sub> pl1pd2 ( $\mu\text{m}$ )	-4.5361E-04	1.0982E-03	1000.00	6000.00	0.4536	1.0982
R <sub>sol/poly</sub> pl2pd1 ( $\mu\text{m}$ )	-5.2456E-04	9.9349E-04	1000.00	6000.00	0.5246	0.9935
h <sub>1x</sub> ( $\mu\text{m}$ )	1.0000E+00	0.0000E+00	0.50	0.00	0.5000	0.0000
h <sub>1y</sub> ( $\mu\text{m}$ )	0.0000E+00	1.0000E+00	0.50	0.00	0.0000	0.5000
h <sub>2x</sub> ( $\mu\text{m}$ )	-7.5405E-02	9.9716E-01	0.50	0.00	0.0377	0.4986
h <sub>2y</sub> ( $\mu\text{m}$ )	-9.9715E-01	-7.5397E-02	0.50	0.00	0.4986	0.0377
D <sub>1</sub> ( $\mu\text{m}$ )	3.6541E+00	5.8150E+00	11.41	111.45	41.6935	66.3496
D <sub>2</sub> ( $\mu\text{m}$ )	-4.5773E+00	8.8727E+00	11.41	111.45	52.2270	101.2374
l <sub>1</sub> ( $\mu\text{m}$ )	-5.1648E+00	-8.1828E+00	2.00	69.00	10.3296	16.3655
l <sub>2</sub> ( $\mu\text{m}$ )	5.0953E+00	-9.7398E+00	8.00	96-tol	40.7621	77.9183
w <sub>1</sub> ( $\mu\text{m}$ )	-6.4949E-01	-1.0336E+00	8.00	69.00	5.1959	8.2686
w <sub>2</sub> ( $\mu\text{m}$ )	6.2153E-01	-1.2048E+00	13.00	96-tol	8.0799	15.6622
Temperature (°C)	-1.9844E-01	2.0643E+00	6.00	27.00	1.1906	12.3859
T <sub>0</sub>	T <sub>WC</sub>	T <sub>S3</sub>	T <sub>S2</sub>	T <sub>S1</sub>		
-429.53	166.22	79.60	53.07	26.53		
269.91	331.83	148.92	99.28	49.64		

Figure 6-13: 90/45 4 mil warp variant.

### 6.3.4 Tabular Comparison Of Experimental Data With Model Predictions

Table 6-2 compares the estimated mean and standard deviation of the experimental data with the assembly model predicted mean and standard deviation from Equations (2-10) and (2-11). The mean and standard deviation are shown for both the "x" and "y" directions. The mean of the experimental data is approximated using a simple average. The variance of the experimental data is approximated using the following formula:

$$(\text{Standard Deviation})^2 = \frac{n \sum x^2 - (\sum x)^2}{n(n-1)} \quad (6-10)$$

where  $n$  is the number of samples and  $x$  represents the data. Results for test variants that had more than three data points are shown in Table 6-2. Data points lying outside of or close to the worst case tolerance region were not included in the sample because they did not reflect the majority behavior of the data.

Test Variant	Sample Size	Experimental Measurements ( $\mu\text{m}$ )				Model Predictions ( $\mu\text{m}$ )				
		Mean <sub>x</sub>	Mean <sub>y</sub>	Standard Dev <sub>x</sub>	Standard Dev <sub>y</sub>	Mean <sub>x</sub>	Mean <sub>y</sub>	Standard Dev <sub>x</sub>	Standard Dev <sub>y</sub>	
8 mil warp	90°/45°	9	-345.08	321.14	31.03	54.20	-354.11	306.27	26.97	53.73
	90°/90°	18	-315.70	720.97	53.40	37.39	-335.82	704.31	46.57	35.54
	90°/135°	15	-108.76	918.51	80.11	30.23	-141.67	915.40	63.09	17.58
	135°/135°	12	397.34	823.27	108.38	29.68	376.31	846.83	57.53	22.00
	135°/90°	19	129.04	760.79	146.04	30.20	98.74	774.65	52.70	17.46
	135°/45°	9	-122.27	430.67	66.44	43.69	-132.34	450.04	28.37	51.82
	45°/135°	12	-731.65	555.02	76.25	106.11	-758.76	529.64	55.43	84.04
4 mil warp	90°/45°	6	-328.34	178.06	39.44	22.03	-331.93	212.91	28.72	42.95
	90°/90°	5	-423.07	569.01	38.43	54.08	-414.36	595.74	38.22	41.00
	90°/135°	4	-330.13	800.74	50.10	34.52	-284.90	846.65	56.79	25.85
	90°/45°	6	-374.29	232.19	22.83	45.60	-429.53	269.91	26.53	49.64
	90°/90°	5	-467.52	430.77	45.31	68.25	-486.02	471.43	25.51	39.09

**Table 6-2:** Tabulated comparison of estimated mean and standard deviation of experimental measurements with model predictions in the x and y directions.

The experimental results and model predictions are in agreement with each other. Differences from the mean and standard deviation, as well as an explanation for the data points that lie outside of the worst-case tolerance region will be explained in this chapter's summary.

#### **6.4 Hierarchy And Impact Of Contributors To The Precision Of An Assembly**

The impact is the first order approximation of the amount of variation in the end position of the test structure contributed by any one single component variation. The worst-case tolerance region can also be determined from a summation of the absolute value of the impacts, see Equation (2-8). Table 6-3, Table 6-4, and Table 6-5 are tabulations of the average impacts, ranked from greatest to least, for the 8 mil, 8 mil warp, and 4 mil warp test structures, respectively. The number "1" is being the greatest. The first set of columns ranks the average impact, across all angle combinations and across the x and y directions, for each component variation. The second set of columns is where the like components are averaged together, and their impacts are also ranked. Notice that the amount of impact the internal stress of poly has is greater in the 8 mil results than in the 8 mil warp and 4 mil warp. This is because Equation 5-28 is used to model deformation in the 8 mil variations, and Equation 5-24 is used to model deformation in the 8 mil warp and 4 mil warp variations – two slightly different equations.

Variable ( $x_i$ )	Average impacts from both directions and across all angles (microns)	Rank	Average impacts from both directions, across all angles, and combined joints (microns)		Rank
$L_1$ ( $\mu\text{m}$ )	1.35	9	1.30		4
$L_2$ ( $\mu\text{m}$ )	1.26	10			
$\text{stress}_{\text{poly}}$ $\text{pl1}$ (Pa)	1.68	7	1.23		5
$\text{stress}_{\text{poly}}$ $\text{pl2}$ (Pa)	0.79	13			
$R_{\text{sol/poly}}$ $\text{pl1pd1}$ ( $\mu\text{m}$ )	1.49	8	1.17		6
$R_{\text{sol/poly}}$ $\text{pl1pd2}$ ( $\mu\text{m}$ )	1.08	11			
$R_{\text{sol/poly}}$ $\text{pl2pd1}$ ( $\mu\text{m}$ )	0.94	12			
$h_{1x}$ ( $\mu\text{m}$ )	0.25	16	0.29		7
$h_{1y}$ ( $\mu\text{m}$ )	0.25	16			
$h_{2x}$ ( $\mu\text{m}$ )	0.33	15			
$h_{2y}$ ( $\mu\text{m}$ )	0.33	14			
$D_1$ ( $\mu\text{m}$ )	82.55	1	69.03		1
$D_2$ ( $\mu\text{m}$ )	55.51	2			
$I_1$ ( $\mu\text{m}$ )	52.11	3	45.38		2
$I_2$ ( $\mu\text{m}$ )	38.66	4			
$w_1$ ( $\mu\text{m}$ )	7.85	5	6.54		3
$w_2$ ( $\mu\text{m}$ )	5.23	6			

**Table 6-3:** Tabulation of average impacts ranked from greatest to least for the 8 mil test structure. The number "1" is being the greatest.

Variable ( $x_i$ )	Average impacts from both directions and across all angles (microns)	Rank	Average impacts from both directions, across all angles, and combined joints (microns)		Rank
$L_1$ ( $\mu\text{m}$ )	0.99	12	1.14		6
$L_2$ ( $\mu\text{m}$ )	1.30	10			
$\text{stress}_{\text{poly}}$ (Pa)	0.16	18	0.16		9
$\text{stress}_{\text{gold}}$ (Pa)	15.81	5			
$R_{\text{sol/poly}}$ $\text{pl1pd1}$ ( $\mu\text{m}$ )	1.38	9	1.12		7
$R_{\text{sol/poly}}$ $\text{pl1pd2}$ ( $\mu\text{m}$ )	1.06	11			
$R_{\text{sol/poly}}$ $\text{pl2pd1}$ ( $\mu\text{m}$ )	0.92	13			
$h_{1x}$ ( $\mu\text{m}$ )	0.25	16	0.28		8
$h_{1y}$ ( $\mu\text{m}$ )	0.25	16			
$h_{2x}$ ( $\mu\text{m}$ )	0.31	15			
$h_{2y}$ ( $\mu\text{m}$ )	0.31	14			
$D_1$ ( $\mu\text{m}$ )	76.35	1	65.28		1
$D_2$ ( $\mu\text{m}$ )	54.20	2			
$I_1$ ( $\mu\text{m}$ )	32.18	3	27.80		2
$I_2$ ( $\mu\text{m}$ )	23.41	4			
$w_1$ ( $\mu\text{m}$ )	7.34	6	6.39		5
$w_2$ ( $\mu\text{m}$ )	5.44	8			
Temperature ( $^{\circ}\text{C}$ )	7.30	7	7.30		4

**Table 6-4:** Tabulation of average impacts ranked from greatest to least for the 8 mil warp test structure.

Variable ( $x_i$ )	Average impacts from both directions and across all angles (microns)		Rank	Average impacts from both directions, across all angles, and combined joints (microns)		Rank
$L_1$ ( $\mu\text{m}$ )		0.98	10		1.13	6
$L_2$ ( $\mu\text{m}$ )		1.28	9			
$\text{stress}_{\text{poly}}$ (Pa)		0.17	18	0.17		9
$\text{stress}_{\text{gold}}$ (Pa)		23.02	5	23.02		3
$R_{\text{sol/poly}} \text{ p1pd1}$ ( $\mu\text{m}$ )		0.75	11			
$R_{\text{sol/poly}} \text{ p1pd2}$ ( $\mu\text{m}$ )		0.52	12	0.58		7
$R_{\text{sol/poly}} \text{ p1pd2}$ ( $\mu\text{m}$ )		0.49	13			
$h_{1x}$ ( $\mu\text{m}$ )		0.25	16			
$h_{1y}$ ( $\mu\text{m}$ )		0.25	16	0.28		8
$h_{2x}$ ( $\mu\text{m}$ )		0.31	15			
$h_{2y}$ ( $\mu\text{m}$ )		0.31	14			
$D_1$ ( $\mu\text{m}$ )		62.48	1	52.63		1
$D_2$ ( $\mu\text{m}$ )		42.78	2			
$l_1$ ( $\mu\text{m}$ )		28.68	3	25.87		2
$l_2$ ( $\mu\text{m}$ )		23.06	4			
$w_1$ ( $\mu\text{m}$ )		9.15	7	7.85		5
$w_2$ ( $\mu\text{m}$ )		6.55	8			
Temperature ( $^{\circ}\text{C}$ )		10.63	6	10.63		4

**Table 6-5:** Tabulation of average impacts ranked from greatest to least for the 4 mil warp test structure.

So what do the tables tell us? If someone were to come to me for advice, and say, "I want to begin manufacturing multiple joint solder self-assembled MEMS. Which factors in my process or environment do I need to control the most if I want to ensure repeatable assembly positions?" I would look at Table 6-4, for example, and begin listing the following:

- 1) Solder volume variation contributes the most to the variation in assembly position. Control it!
- 2) Next is scavenging or overwetting. Prevent or minimize it!
- 3) Next is warpage due to misfit stains of gold and polysilicon. Get new material combinations, or anneal, or at least make the residual stress more consistent.
- 4) Next is temperature variation. Your MEMS is actually a thermostat!

- 5) Next, the influence of geometric dimensions of the structure and the warpage of the solder pads are comparable.
- 6) And finally, the influence of residual stress in the polysilicon, and hinge play are comparable.

Table 6-6 is a tabulation of the average of the absolute values of the sensitivities, from all of the angle combinations, of the 8 mil warp variations. The data in this table, Equation (2-11a), and Equation (2-12) are used to calculate the average diminishing statistical tolerance discussed next. Also, with reference to

Table 6-6,  $(\text{impact}/3)^2$  is equivalent to  $\left(\frac{\partial f_{\text{assy}}(x_i)}{\partial x_i}\right)^2 \sigma_i^2$  in Equation (2-11a), and "n" is

the number of contributions of that component variance.

Variable ( $x_i$ )	Average sensitivities from both directions, across all angles, and combined joints (microns/dimension)		tol <sub>i</sub>	n·(Impact/3) <sup>2</sup>	Rank	Diminishing statistical tolerance ( $\mu\text{m}$ )
L <sub>1</sub> ( $\mu\text{m}$ )	5.7E-01		2	0.2912	7	1.72
L <sub>2</sub> ( $\mu\text{m}$ )						
stress <sub>poly</sub> (Pa)	5.6E-08		2820000.00	0.0027	9	0.16
stress <sub>gold</sub> (Pa)	7.5E-07		21000000.00	27.7764	3	17.61
R <sub>solt/poly</sub> p1pd1 ( $\mu\text{m}$ )						
R <sub>solt/poly</sub> p1pd2 ( $\mu\text{m}$ )	1.1E-03		1000	0.4190	6	2.60
R <sub>solt/poly</sub> p2pd1 ( $\mu\text{m}$ )						
R <sub>solt/poly</sub> p2pd2 ( $\mu\text{m}$ )						
h <sub>1x</sub> ( $\mu\text{m}$ )						
h <sub>1y</sub> ( $\mu\text{m}$ )	5.6E-01		0.5	0.0354	8	0.59
h <sub>2x</sub> ( $\mu\text{m}$ )						
h <sub>2y</sub> ( $\mu\text{m}$ )						
h <sub>3x</sub> ( $\mu\text{m}$ )						
D <sub>1</sub> ( $\mu\text{m}$ )	2.5E+00		25.95	946.8579	1	124.92
D <sub>2</sub> ( $\mu\text{m}$ )						
I <sub>1</sub> ( $\mu\text{m}$ )	3.9E+00		15	749.4374	2	84.16
I <sub>2</sub> ( $\mu\text{m}$ )						
w <sub>1</sub> ( $\mu\text{m}$ )	5.4E-01		7	3.1557	5	84.16
w <sub>2</sub> ( $\mu\text{m}$ )						
Temperature ( $^{\circ}\text{C}$ )	1.2E+00		6	5.9271	4	7.75

**Table 6-6:** Tabulation of average sensitivities and diminishing statistical tolerance of the 8 mil warp test structure.

If the question is asked, "On average, in the 'x' or 'y'-directions, what is the variation of the endpoint of the 8 mil warp test structure?"

1. The answer is:  $Tol_{assembly} = \pm 124.92 \mu\text{m}$ .
2. "If solder volume variation can be eliminated?"
  - The answer is:  $Tol_{assembly} = \pm 84.16 \mu\text{m}$ .
3. "If the variation of solder volume, scavenging, and overwetting can be eliminated?"
  - The answer is:  $Tol_{assembly} = \pm 17.61 \mu\text{m}$ .
4. "If the variation of solder volume, scavenging, overwetting, and gold stress can be eliminated?"
  - The answer is:  $Tol_{assembly} = \pm 7.75 \mu\text{m}$ .
5. "If the variation of solder volume, scavenging, overwetting, gold stress, and temperature can be eliminated?"
  - The answer is:  $Tol_{assembly} = \pm 2.60 \mu\text{m}$ .
6. "If the variation of solder volume, scavenging, overwetting, gold stress, temperature, and solder pad warpage can be eliminated?"
  - The answer is:  $Tol_{assembly} = \pm 1.72 \mu\text{m}$ .
7. "If the variation of solder volume, scavenging, overwetting, gold stress, temperature, solder pad warpage, and structure geometry can be eliminated?"
  - The answer is:  $Tol_{assembly} = \pm 0.59 \mu\text{m}$ .
8. "If the variation of solder volume, scavenging, overwetting, gold stress, temperature, solder pad warpage, structure geometry, and hinge play can be eliminated?"

- The answer is:  $Tol_{assembly} = \pm 0.16 \mu\text{m}$ .
9. "If the variation of solder volume, scavenging, overwetting, gold stress, temperature, solder pad warpage, structure geometry, hinge play, and polysilicon internal stress can be eliminated?"
- The answer is:  $Tol_{assembly} = \pm 0 \mu\text{m}$ ?

... and this is how precise we can get.

By using a suitable normalization of the precision results, presented in the last column of Table 6-6, the results may be extrapolated to different size structures consisting of  $n$  solder joints or assembled segments. Figure 6-14 is a depiction of the end position ( $P$ ) of a two-joint structure. Equation (6-11) describes the end position as a function of the length of the structure segments ( $L_1$  and  $L_2$ ) and the joint angles.

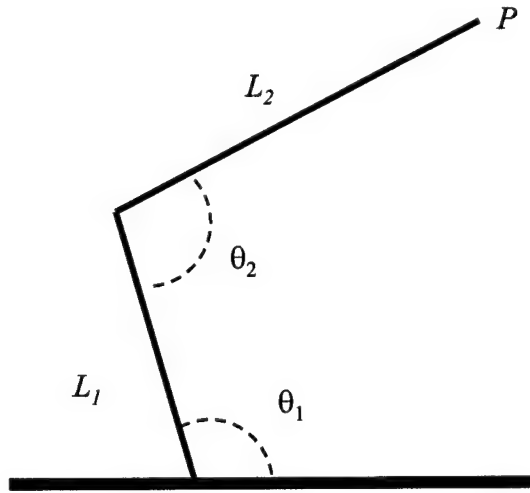


**Figure 6-14:** Depiction of the end position ( $P$ ) of a two-joint structure.

$$P = (L_1 \cos(\theta_1) + L_2 \cos(\theta_1 + \theta_2 - 180), L_1 \sin(\theta_1) + L_2 \sin(\theta_1 + \theta_2 - 180)) . \quad (6-11)$$

Dividing Equation (6-11) by:

$$2 \times (L_1 + L_2) / 2 \quad (6-12)$$

suggests a suitable normalization, where 2 is the number of solder joints, and  $(L_1 + L_2) / 2$  is the average length of the segments. The number of assembled segments and solder joints connecting assembled segments will always be the same and thus cancel out of Equation 6-12. I will define  $\Lambda$  as a characteristic length of a series connected multiple joint solder self-assembled MEMS:

$$\Lambda = \sum L_i \quad (6-13)$$

where  $L_i$  are the lengths of the different assembled sections composing a series connected multiple joint solder self-assembled MEMS. Thus, for the structures used to generate the data presented in the last column of Table 6-6,  $\Lambda_0 = 500 \mu\text{m} + 500 \mu\text{m} = 1000 \mu\text{m}$ . Therefore, by dividing the last column of Table 6-6 by  $\Lambda_0$ , and calculating a specific  $\Lambda$  for a different series connected multiple joint solder self-assembled MEMS, an estimation of the achievable precision may be obtained by:

$$\text{Tol}_{\text{assembly}} = \pm \Lambda \frac{\text{Statistical Tolerance}}{\Lambda_0}. \quad (6-14)$$

## 6.5 Summary

This chapter opened with a description of the component variations being considered for the assembly model. Next the different values picked for the mean and standard deviation of each component were described. The mean, standard deviation, statistical tolerance, and worst-case tolerance of the assembly were then predicted using the assembly model and compared to the experimental data. The

model predictions were found to be reasonable with reality. Components whose variation causes the greatest impact on the assembly variation were identified, see Table 6-4. And finally, predictions on the achievable precision of multiple joint solder self-assembled MEMS were made, see Table 6-6.

Although the model predictions agree with the experimental results, the agreement could be better. The lack of an infinite number of experimental data points prevents me from having a high degree of certainty in the accuracy of the explanations to follow. However, based on my experience in this work, the differences between the model and experiments are probably due to the following factors. The factors are arranged from greatest to least influence, by my judgement.

- 1) **Quenching**, in simple words, the "rapid" cooling of a "hot" object. One can see from the 8 and 4 mil warp results figures, with video image backgrounds, that the curvature of the actual structure segments is greater than the curvature of the modeled assembly shape. This is because the affects of quenching during the preflow and reflow, resulting in an increased curvature of the gold on polysilicon parts of the assembly, are not taken into account in the mean or variation of the gold stress (Equation 6-3). In fact, one can see by looking at the results figures, that if the curvature of the modeled assembly shape were increased, the nominal end position would move closer to the estimated mean of the experimental data.
- 2) **Inaccurate Estimation of Component Variations** can also explain some of the differences. For example, the distribution of solder sphere sizes was measured from a random sample. The solder balls actually used in the assemblies were not from this same measured sample. Furthermore, it was assumed from a random

sample, that all  $135^\circ$  solder joints experienced only overwetting. In reality, under the right conditions, scavenging can also occur causing larger than expected assembly angles. The estimated mean and variation for each assembly component also suffers, in some form, from the same lack of accuracy.

- 3) **The First Order Approximation of Mean and Variance** of the assembly end position may also contribute to the differences, especially since the assembly function is non-linear. Furthermore, even though the components were assumed to be random variables with normal distributions, the actual distribution of the end position of the assembly may not be normal.
- 4) **The Incomplete Reflow of Solder** was a very rare occurrence which I am not able to explain. A few times, I observed reflowing solder joints where the oxide never completely left the solder surface, and the solder joint never reached its modeled equilibrium angle, thus resulting a larger than expected assembly angle.
- 5) **Human Measurement Error:** recall from Appendix A, that there is at least a  $20\text{ }\mu\text{m}$  diameter region of uncertainty for measurements taken with obscured origins.
- 6) **The Beam Theory Based Deformation Models** used in this work are probably less accurate than plate structure based deformation models, especially since the test structures are more plate than beam like.
- 7) **Non-Negligible Forces on the Lower Solder Joint** due to the weight of the upper solder joint and structure segments may also be a cause of differences.

## 6.6 References

- [1] K. F. Harsh, *Design Optimization For MEMS Solder Self-Assembly*, Ph.D. Dissertation, Department of Mechanical Engineering, University of Colorado at Boulder, Engineering Center, Campus Box 427, Boulder, Colorado, 80309-0427, Summer 2001.
- [2] W. Sharpe, B. Yuan, R. Vaidyanathan, and R. Edwards, "Measurement of Young's modulus, Poisson's Ratio, and tensile strength of polysilicon," *Proceedings of the 10th Annual International IEEE MEMS Workshop*, pp. 424-429, 1997.
- [3] J. A. King, *Materials Handbook for Hybrid Microelectronics*, Artech House, Inc., ISBN: 0-89006-325-7, 1988.
- [4] R. R. A. Syms, "Equilibrium of hinged and hingeless structures rotated using surface tension forces," *Journal of Microelectromechanical Systems*, vol. 4, no. 4, pp. 177-184, December 1995.

## **7 Issues In The Realization Of Specific Complex Solder Self-Assembled MEMS**

This chapter is dedicated to the novel inventions that have come out of this research. Obvious and non-obvious issues that are specific to the processing of each invention will be discussed.

### **7.1 Solder Assembled Arrays Of Microrobot Legs Using Photolithographically Patterned Indium On Gold**

This research produced the first mass solder assembled arrays of microrobot legs and the perhaps the smallest solder self-assembled structure and solder joint. Figure 7-1 is a scanning electron micrograph (SEM) of an array of microrobot legs assembled using the surface tension of molten solder. Figure 7-2 is a closer view of one of the robot leg assemblies. The equivalent volume of a sphere of pure indium with diameter of  $37 \mu\text{m}$  was deposited on each set of 25 by  $25 \mu\text{m}$  gold pads for the microrobot leg shown in Figure 7-2. The outline of the location of the gold pads is also shown in Figure 7-2.

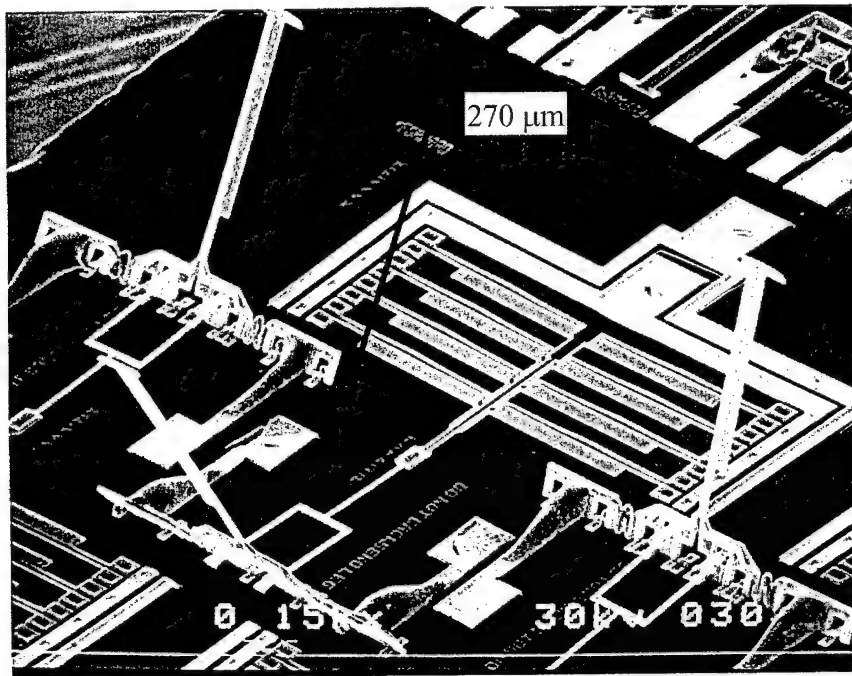


**Figure 7-1:** SEM of an array of microrobot legs assembled using the surface tension of molten solder.

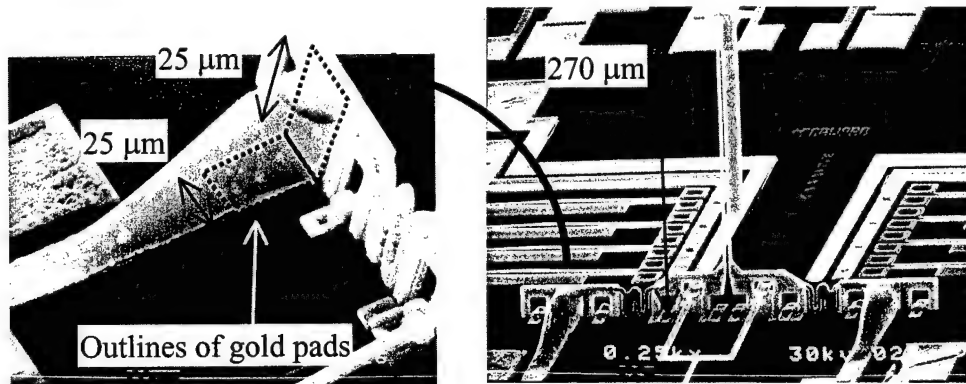


**Figure 7-2:** A close view of one of the robot leg assemblies.

This research also produced the first MEMS device to be assembled with the smallest solder joint, as shown in Figure 7-3. Figure 7-3 is a SEM of a different design of solder self-assembled microrobot leg. The equivalent volume of a sphere of indium with diameter of  $15 \mu\text{m}$  was deposited on each set of 8 by  $10 \mu\text{m}$  gold pads.

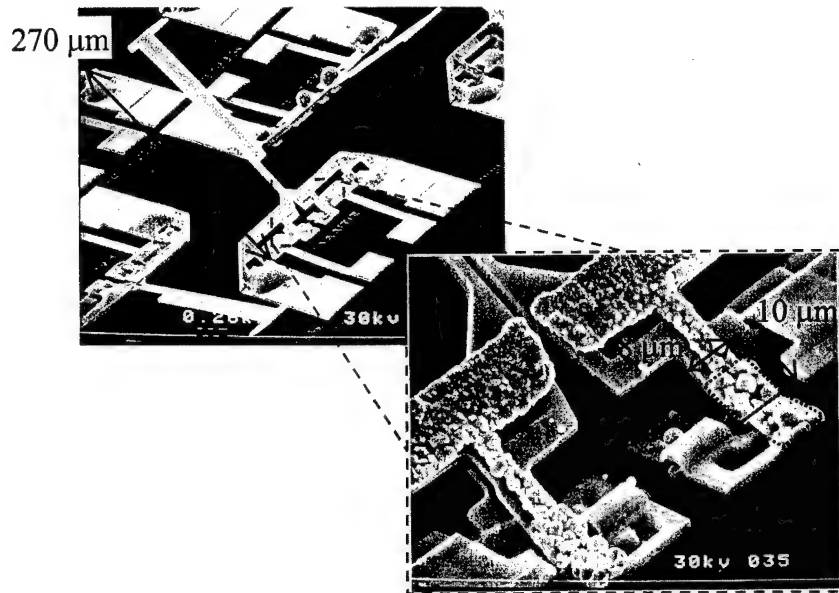


**Figure 7-3:** A SEM of a different design of solder self-assembled microrobot leg.

The pure indium was evaporated, using a BAL-TEC MED 020 Coating System, and patterned on the chip's micromachined surface using a thick photoresist (AZ P4620) metal lift-off process before sacrificial oxide etch (release) of the surface micromachined microrobot legs. More detailed description of the deposition procedures and equipment are given in Chapter 8. Figure 7-4 shows the patterned indium before releasing the chip. The chip was then heated to the melting point of the indium ( $160^{\circ}\text{C}$ ), where the surface tension of the molten indium lifted the legs into place. The microrobot legs, shown in Figure 7-1 - Figure 7-4, are among an array consisting of 25 legs fabricated on a  $2\text{ mm} \times 2\text{ mm}$  chip. The indium solder joints serve as low resistance electrical connections and mechanically rigid supports for the legs, making the robot leg design robust. A curved spring-like electro-

mechanical linkage isolates the mechanically rigid solder joints from the leg, permitting two degrees-of-freedom motion.

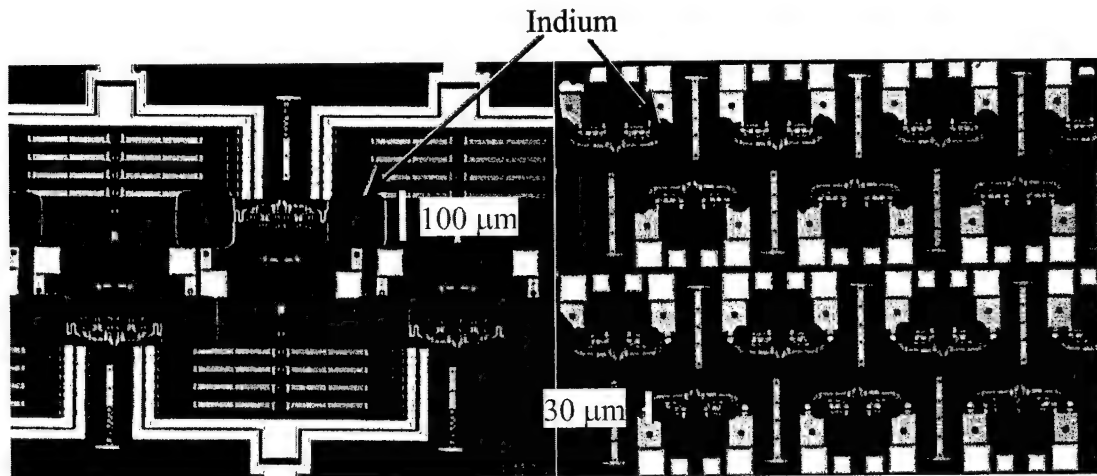


**Figure 7-4:** Captured video images of the patterned indium before release of the microrobot legs.

Another issue concerning this invention, is the indium film that begins coating the surface of the chip during reflow – this issue was discussed in more detail in Chapter 4. For more background on this invention please read my paper [1] included as a reference in Appendix C.

## 7.2 Normally Open And Closed, Electrostatically Actuated, Solder Assembled Switches

Figure 7-5 (a) is a SEM of a normally closed (N.C.) and two normally open (N.O.) electrostatically actuated switches. Figure 7-5 (b) is a top view of the same switches. These switches were assembled with 63Sn/37Pb 4 mil diameter manufactured solder spheres. Mechanical stops are used to dictate the assembly angle since the three plates must be parallel with each other.

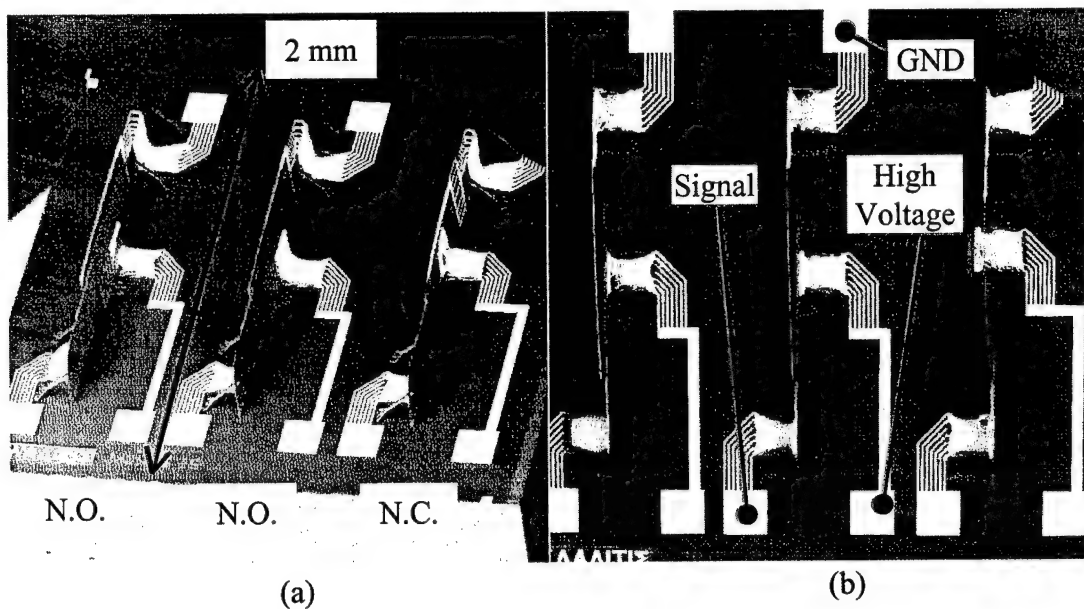


**Figure 7-5:** (a) SEM of a normally closed (N.C.) and two normally open (N.O.) electrostatically actuated switches and (b) a top view of the same switches.

With reference to Figure 7-5 and Figure 7-6 solder self-assembly is used to raise three plates parallel with each other. The resulting solder joints are also used as electrical connections to the three plates. The ground and the signal are attached to the contact plates, and a high voltage is attached to the attraction plate. In the normally open case, the attraction plate pulls the long contact plate into contact with the shorter contact plate. In the normally closed case, the long contact plate is designed to be already in contact with the shorter contact plate by taking advantage of the warpage due to the residual stress of a bilayer gold on polysilicon plate. In this case the attraction plate pulls the long contact plate away from the shorter contact plate.

To be able realize the normally closed switch, a special window had to be made in the long contact plate that allowed the placing of a solder joint to assemble the attraction plate. This window is shown in Figure 7-7.

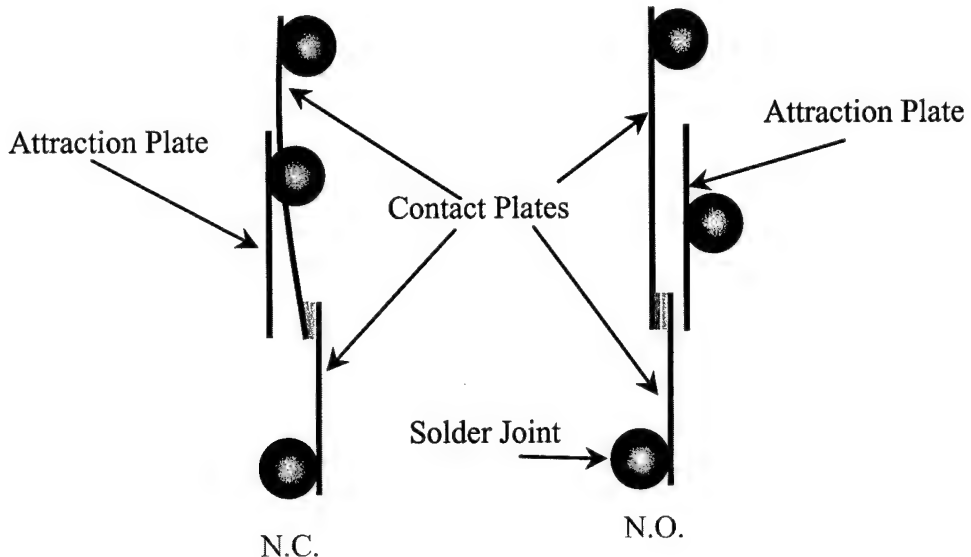


**Figure 7-6:** Depiction of a normally closed (N.C.) and a normally open (N.O.) electrostatically actuated switches.

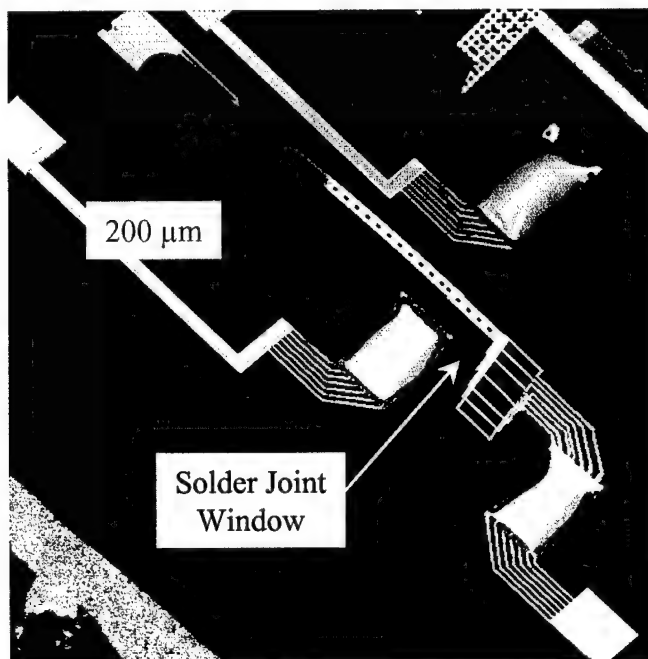


**Figure 7-7:** SEM of a normally closed electrostatically actuated switches.

The total resistance, measured from Signal to GND, of the normally closed switch is  $6\ \Omega$ . The snap-through voltages are 144 V and 55.5 V for the normally open and closed switches, respectively. These switches are far from having acceptable operation, however. The normally open switches often stick closed when actuated one time. In order to achieve relatively low attraction voltages, large plates are used. However, the larger plates become more flimsy causing undesirable contacting of plates, i.e. short circuits. As continuing work, there is a need for a dedicated project on these switches were competing objectives such as actuation voltage, plate spacing, contact plate restoration force, and resistance are optimized to find the best design.

### **7.3 Resistive Point Heaters For MEMS Remote Solder Self-Assembly**

Until this work, it was believed that the reflow of the solder joints, of a complex solder self-assembled MEMS device, had to be restricted to a hotplate or oven. However, I developed microsized resistive point heaters that are designed into, and part of, the solder pads. The term point heaters is used to convey the idea that the heaters only heat up a certain point on a chip. The point heaters can be activated individually, quickly, and no longer is a hot plate or oven needed – the assembly can now even be done remotely. Please read my paper on these heaters in Appendix C [2].

#### **7.4 Solder Self-Assembled Micro Axial Flow Fan Driven By A Scratch-Drive-Actuator Rotary-Motor**

Figure 1-1 shows a scanning electron micrograph of the world's first man-made micro-sized axial flow fan. This fan has been featured in several domestic and international periodicals including the New Scientist, New York Times (Thursday February 15, 2001), Longmont Daily Times-Call, Denver Post, and Rocky Mountain News. Find out more about this complex solder self-assembled MEMS in my paper included in Appendix C [3].

#### **7.5 Solder Assembled Fiber Optic Cable Gripper**

Figure 1-2 is a SEM and captured video images of a solder assembled fiber optic cable gripper assembled with 8 mil 63Sn/37Pb solder spheres. The purpose of the fiber optic cable gripper is to pull a fiber into position and secure it. There are two issues here that I would like to highlight. The gripper design includes the first demonstration of a three-pad two-fold solder joint assembled with one volume of solder. Both Figure 7-8 and Figure 7-9 show this novel joint. To approximate the assembly angle of this total joint I simply assumed that each pair of pads would assemble to an angle close to where they would if that pair was a single solder joint.

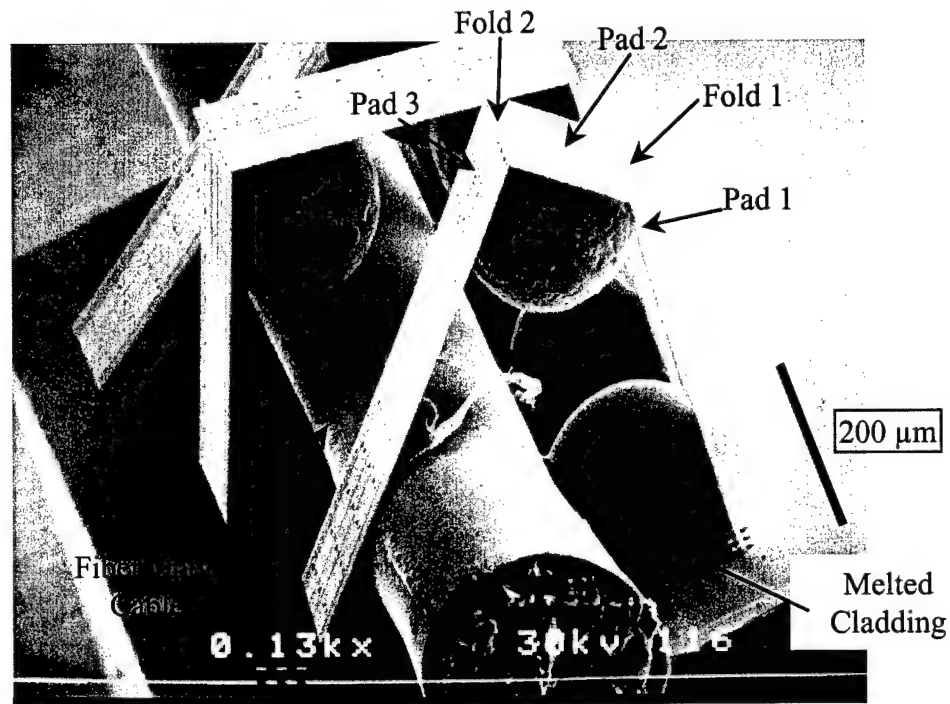


**Figure 7-8:** SEM of a fiber optic cable gripper assembled with 8 mil 63Sn/37Pb manufactured solder spheres.

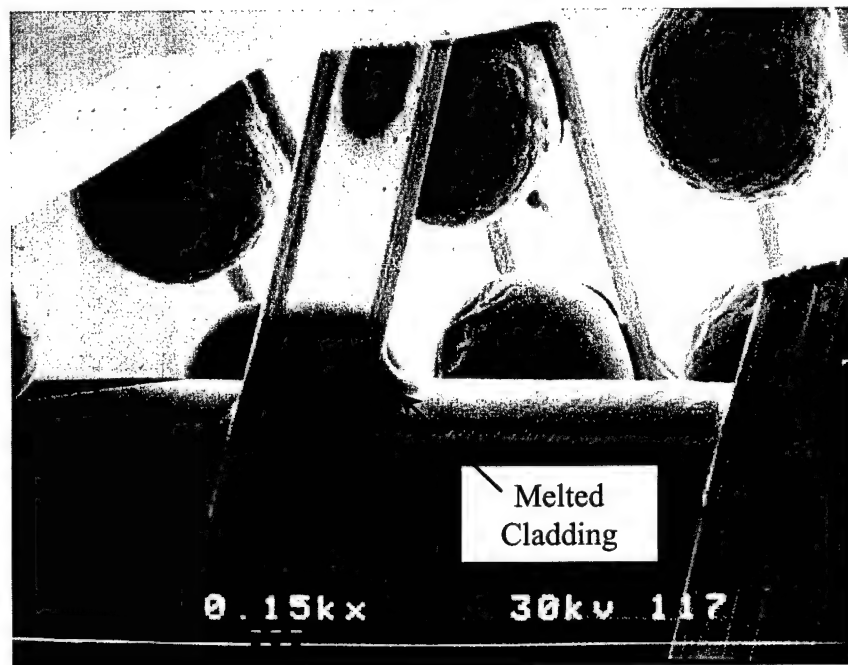


**Figure 7-9:** SEM of another fiber optic cable gripper assembled with 8 mil 63Sn/37Pb manufactured solder spheres.

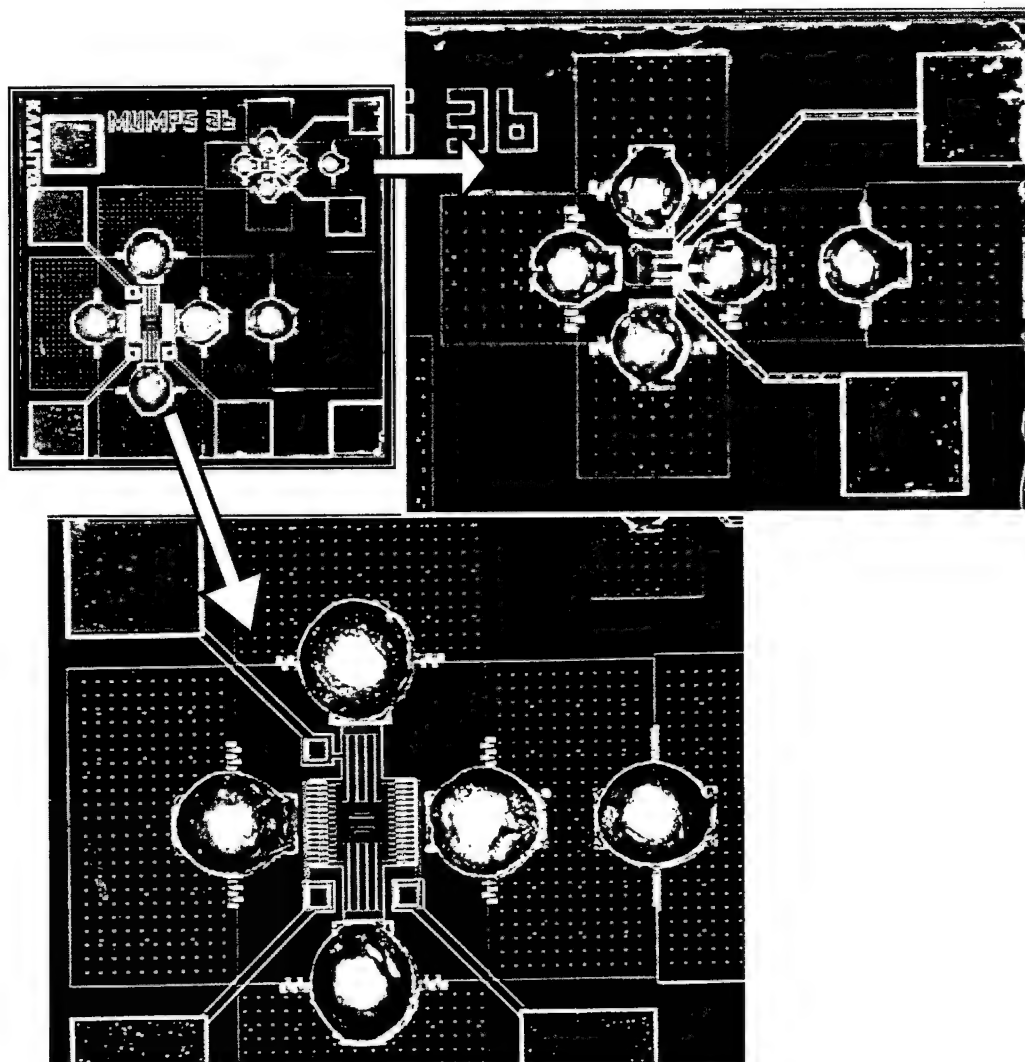
The second issue that I would like to point out is obvious, yet not obvious. When one decides to incorporate solder self-assembly into their design, sometimes it is forgotten that the solder must be heated to temperatures as high as 200 °C for reflow and assembly. This must be kept in mind so that that, if applicable, other components of the design are not damaged or adversely affected. Figure 7-8 and Figure 7-9 both show where parts of the gripper structure and solder have melted the polymer cladding of the fiber optic cable.

## 7.6 Micro Channels & Packages

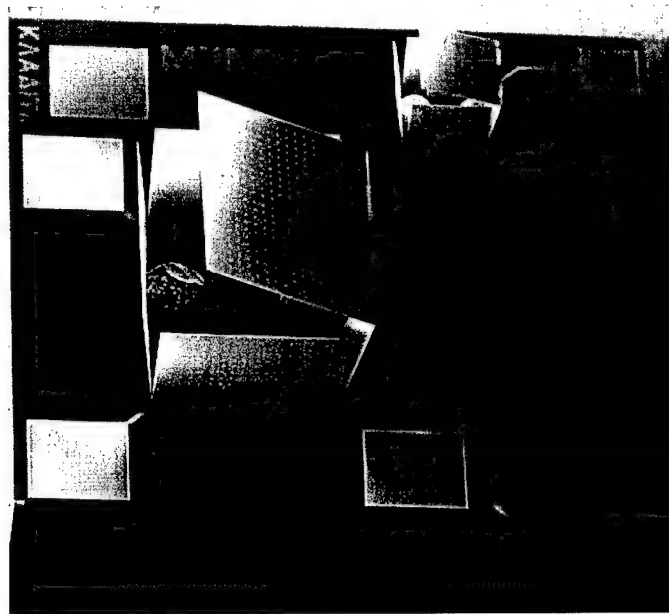
When electronic packaging comes to mind, most people think of encasing a microelectronics or MEMS chip in a dual inline package. With the processing methods and insights that I have developed in this work, it is possible now to begin making packages at the device level. The goal of this project is to demonstrate a technology, using solder self-assembled plates, that enables packaging or encapsulation of individual MEMS devices or individual circuits on a chip.

Figure 7-10 shows captured video images of a preflowed micro package ( $\mu$ package). There are two packages on the chip. One package is preflowed with 63Sn/37Pb 8 mil solder and will enclose a comb drive. The second package is preflowed with 63Sn/37Pb 4 mil solder and will enclose a thermal actuator. Figure 7-11 is a SEM of reflowed  $\mu$ packages. Oversized solder balls and scavenging have kept the sides and top from closing all the way. Figure 7-12 shows closer views of each individual  $\mu$ package. Along the same lines, it is possible to construct channels. Figure 7-13 shows an example of a short section of a micro channel ( $\mu$ channel) that

was inadvertently formed by a test structure suffering from overwetting. Several of these types of enclosures were constructed during my research.



**Figure 7-10:** Captured video images of a preflowed micro package.



**Figure 7-11:** SEM of reflowed micro packages.

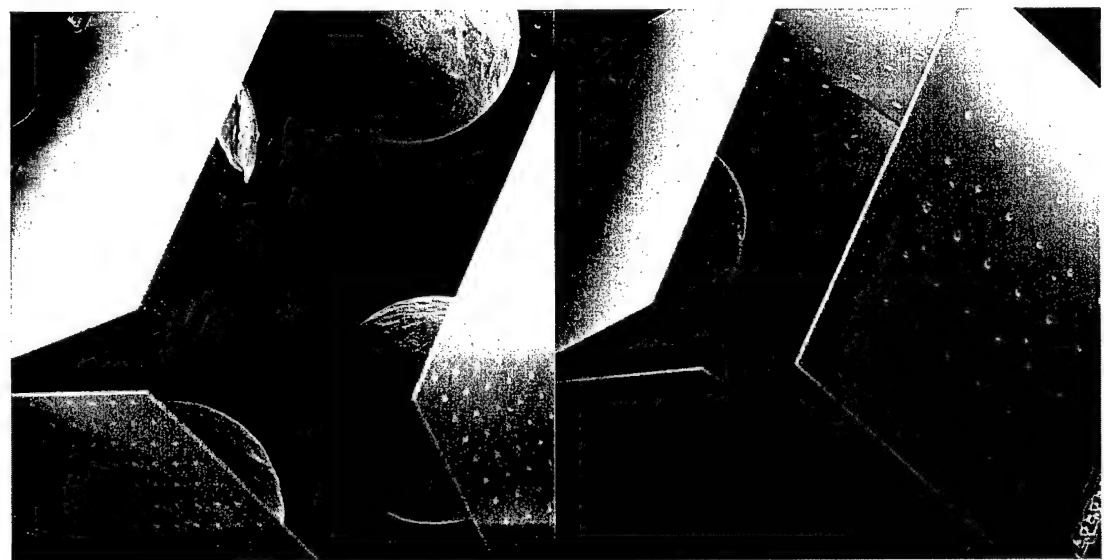


**Figure 7-12:** Close views of reflowed micro packages.

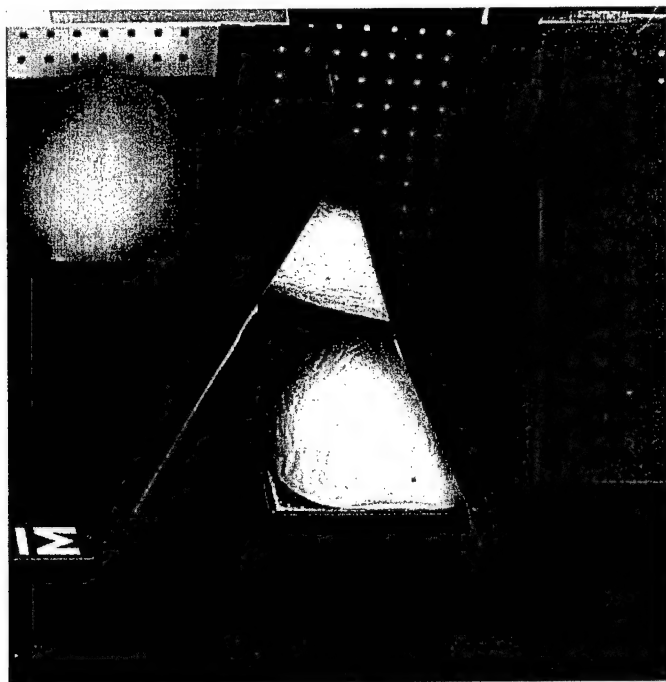


**Figure 7-13:** SEM of a proposed section of a micro channel assembled with two 63Sn/37Pb 8 mil manufactured solder spheres.

## 7.7 References

- [1] P. E. Kladitis and V. M. Bright, "Prototype microrobots for micro positioning and micro unmanned vehicles," *Sensors and Actuators A.*, vol. 80, pp. 132-137, 2000.
- [2] P. E. Kladitis and V. M. Bright, "Novel Resistive Point Heater for MEMS Remote Solder Self-Assembly," *2000 ASME International Mechanical Engineering Congress and Exposition*, MEMS-Vol. 2, pp. 161-167, Orlando, Florida, Nov. 5-10, 2000.
- [3] P. E. Kladitis, R. J. Linderman, and V. M. Bright, "Solder Self-Assembled Micro Axial Flow Fan Driven by a Scratch Drive Actuator Rotary Motor," *Proceedings of the Fourteenth IEEE International Micro Electro Mechanical Systems Conference (MEMS 2001)*, pp. 598-601, Interlaken, Switzerland, 21-25 Jan. 2001.

## **8 Conclusions**

In summary, this work describes the issues in the design, modeling, and manufacture of multiple joint solder self-assembled micro-electro-mechanical systems (MEMS). Chapter 1 introduced the key topics in this work and defined multiple joint solder self-assembled MEMS. Chapter 2 gave some theoretical background and in-depth history on the key topics used in this work: MEMS, surface micromachining, solder self-assembly, and classical tolerance analysis.

Chapters 3, 4, 5, and 6 discussed the different issues involved in the general implementation of a multiple joint solder self-assembled MEMS, but at the same time used 21 variations of a specially designed two-solder-joint test structure to demonstrate the issues. In Chapter 3, I gave guidelines on the important obvious, and not so obvious, design issues specific to the successful implementation of multiple joint solder self-assembled MEMS. The "how to" of manufacturing and processing multiple joint solder self-assembled MEMS was given in Chapter 4. Chapter 5 described all of the modeling used to predict the shape of a multiple joint solder self-assembled MEMS. Then, in Chapter 6, modeled predictions of the end position of the two-solder-joint test structure were compared to the experimentally measured end positions. The modeling was found to be in good agreement. And finally, Chapter 7 describes the issues involved in the processing of specific examples of multiple joint solder self-assembled MEMS.

## 8.1 Limitations

I believe that solder self-assembly is, in general, the most practical method for the assembly of MEMS. However, one of the most valuable contributions this work has made for the scientific and industrial communities was to reveal, without concealment, the possibly serious limitations of this method of assembly.

The biggest limitation, in my opinion, is the relatively large variation in the position of the final assembly. For my test structures, on average, this variance in position was predicted to be  $\pm 124.92 \mu\text{m}$ . This is not very precise relative to the 500  $\mu\text{m}$  segments that the assembly is composed of. Thus, the lack of being able to achieve a precise assembly of a multiple joint solder self-assembled MEMS is a serious limitation that is only further compounded with an increasing number of solder joints. The major sources of assembly variation were revealed to be the variation in solder volume and variation in gold solder pad size due to scavenging and overwetting.

Further limitations, worth noting, are rather application specific. First, multiple joint solder self-assembled MEMS are limited by operating temperature. If the operating temperature reaches the melting temperature of the solder ( $\approx 183^\circ\text{C}$  for eutectic Sn/Pb), the solder joints will not be rigid connections anymore. Second, the temperatures necessary for processing the multiple joint solder self-assembled MEMS (up to  $198^\circ\text{C}$  for eutectic Sn/Pb) may be incompatible with other aspects or materials in the design. Flux contamination may be an issue, for some, because of possible undesired chemical residues or reactions. Although no adverse affects were noted in the processing and operation of most of the devices in this work, tin crystal growth

was promoted by the flux, during the assembly of the microstructures, using the resistive point heaters. And finally, if the weight of the assembly or solder becomes significant, all of the models used in this work must be modified to take weight into account.

## 8.2 Future Paths And Improvements

### A. Design

- a) Design circular solder pads for multiple joint solder self-assembled MEMS.

### B. Modeling

- a) Model circular solder pads. The model for assembly angle, used in this work, already models the volume as if there were circular pads, but the torque balance equation is based on a square pad perimeter (for surface tension) and area (for internal pressure). This is a bit inconsistent. Changing the torque balance equation to be based on a circular pad, a highly accurate and much more simplified model should result.
- b) The assembly function can be used to create an objective function in an optimization problem. The square representation of the worst-case and statistical tolerance regions is not the most accurate representation of the region that an assembly's position can vary in. An optimization problem may be formulated in such a way as to find a more accurate representation of the region of assembly position variation without having to perform a computationally expensive Monte-Carlo analysis. Supposing that  $f^x$  and  $f^y$  are the x and y position output of the assembly function, respectively. A more

efficient method of finding the true tolerance region could be to formulate an objective function that represents a radius emanating from the assembly's nominal position ( $\mu_{xassy}$ ,  $\mu_{yassy}$ ). This radius could be maximized while being constrained to radial lines that have a slope " $a$ ". The radius would also be bounded in the domain by the component's ( $x_i$ ) upper ( $UL_i$ ) and lower ( $LL_i$ ), limits. The problem would be posed as follows:

$$\begin{aligned} \text{min. } & -\sqrt{(f^x - \mu_{xassy})^2 + (f^y - \mu_{yassy})^2} \\ \text{s.t. } & f^y = a(f^x - \mu_{xassy}) + \mu_{yassy} \\ & LL_i \leq x_i \leq UL_i \end{aligned}$$

### C. Manufacture

- a) Investigate and demonstrate methods of manufacturing precise volumes of solder.
- b) Find a different solder, solder pad, and flux combination that eliminates or reduces scavenging and overwetting.
  - (i) To reduce scavenging with Sn/Pb solder, I would suggest adding copper or nickel under the gold pad. Possibly, the copper or nickel will not diffuse as much into the solder, but the gold coating will act to initiate good wetting.
  - (ii) To reduce overwetting, the construction of dams may be necessary. Dams could be designed at the periphery of a solder pad as purely a shape that would discourage solder flow by requiring too much energy to cross over. Dams could also be made out of a material that is less wettable than the polysilicon for the given solder and flux.
- c) Use circular solder pads to minimize scavenging.

- d) Once solder volume variation, scavenging, and overwetting are controlled better, I would suggest performing more careful experiments to gauge the values of component nominal values and variations. I would also include a study to gauge the amount and variation of deformation due to quenching.
- e) Once the component values are more thoroughly controlled and quantified, I would cooperate with industry to batch manufacture a few runs of thousands of copies of an assembled device. Where, this time, the device would be a specific practical device, instead of a general test structure. Then I would compare these measurements with model predictions.

#### D. Integrity

- a) I would perform studies to determine the strength of the solder joint. In this work, the solder joint is stronger than the, at most, 2  $\mu\text{m}$  thick polysilicon structures. However, stronger structure components may be used that are comparable in strength to the joints.

## **Appendix A Equipment and Procedures**

This chapter provides brief descriptions of the equipment used in this research. While reading the previous chapters, the reader is referred here for the description of the mentioned equipment. When not described elsewhere, a description of the operation and procedures will be included.

### **A.1 Dicing Saw**

**Maker:** Assembly Technologies, **Model:** Dicing Saw Model 1006

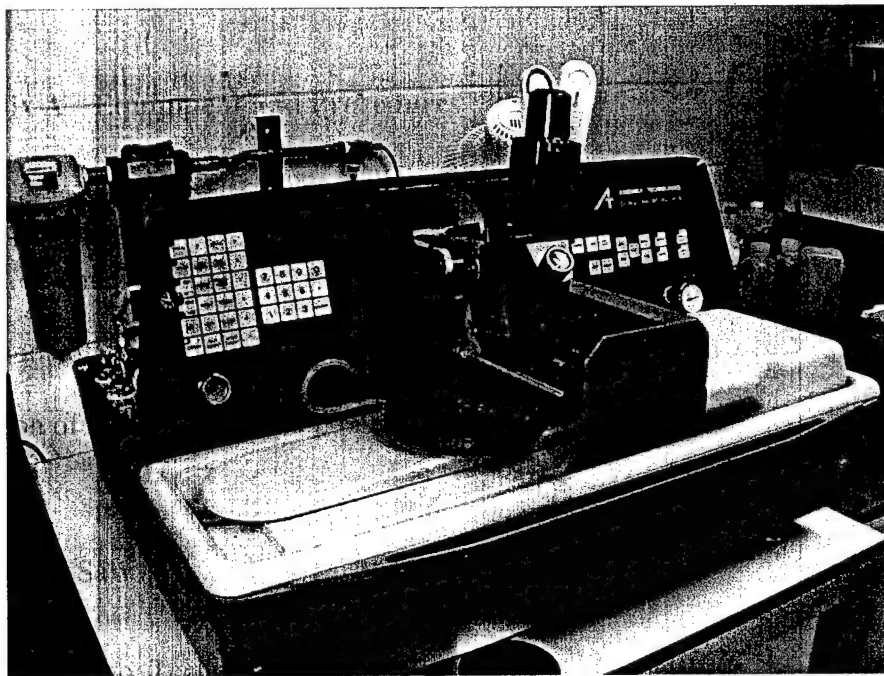


**Figure A-1:** Dicing Saw

Cuts were made manually, using a diamond blade (Semitec S1640) for silicon, with the following operating procedures and settings:

- a) Turn on dicing saw power, compressed air, water, and vacuum pump.

- b) Mount blue sticky film on dicing frame and mount MEMS die onto blue sticky film.
- c) Program parameters: mode=71, 1st=80 mils, 2nd=80 mils, H=18 mils, T=40 mils, theta=90, speed=10, DIA=600, \*=600, phi=11 mils.
- d) Press "reset", press "spindle", place calibration block on stage and press "chuck zero".
- e) Remove calibration block and vacuum mount dicing frame with MEMS die.
- f) Press manual "align" and align using controls while viewing through microscope, make cuts by pressing single cut. A few passes are needed to make a full cut.
- g) When finished, carefully remove the subdice from blue sticky film using tweezers.

## A.2 Scanning Electron Microscope

**Maker:** R. J. Lee Instruments Ltd., **Model:** The personal SEM

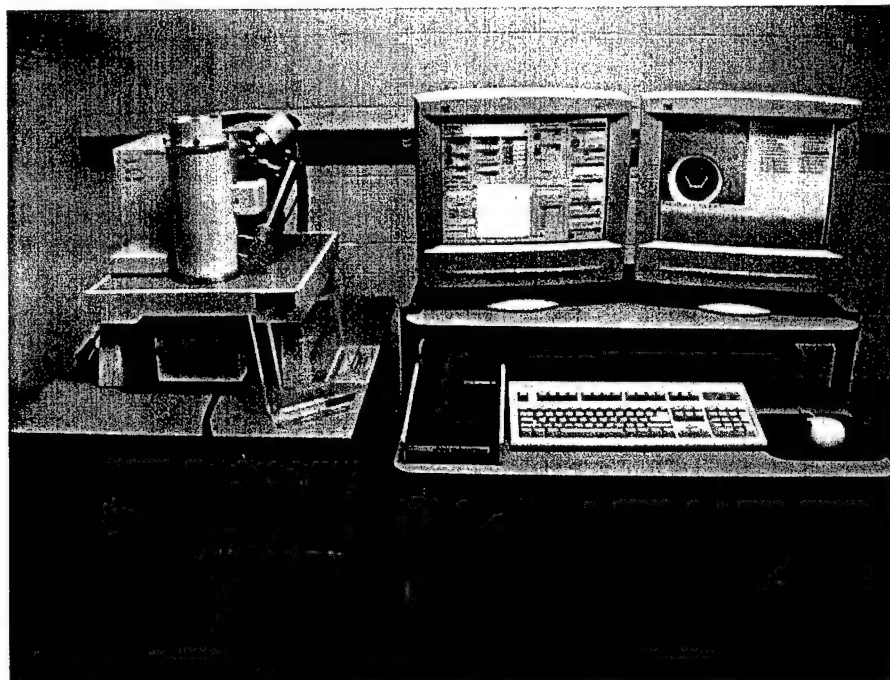


**Figure A-2:** R. J. Lee Scanning Electron Microscope

The operation of the R. J. Lee scanning electron microscope is fully automatic and digitally controlled -- a drawback, since lag time between user interaction and microscope operation is unbearable at times. Typical settings were 15 keV beam energy, 76.5% filament drive, and 50.5  $\mu\text{A}$  emission current at  $2.7 \times 10^{-6}$  torr. This microscope had the capabilities of imaging samples in one of two modes: secondary electron detection (SED) mode or quad-backscatter mode. The major difference that distinguishes quad-backscatter mode from SED, is the ability to visualize relative distinctions between the elemental composition of imaged structures -- the denser the element, the brighter the appearance. Figure A-3 is a comparison between the two types of visualizations: SED (left) and quad-backscatter (right).

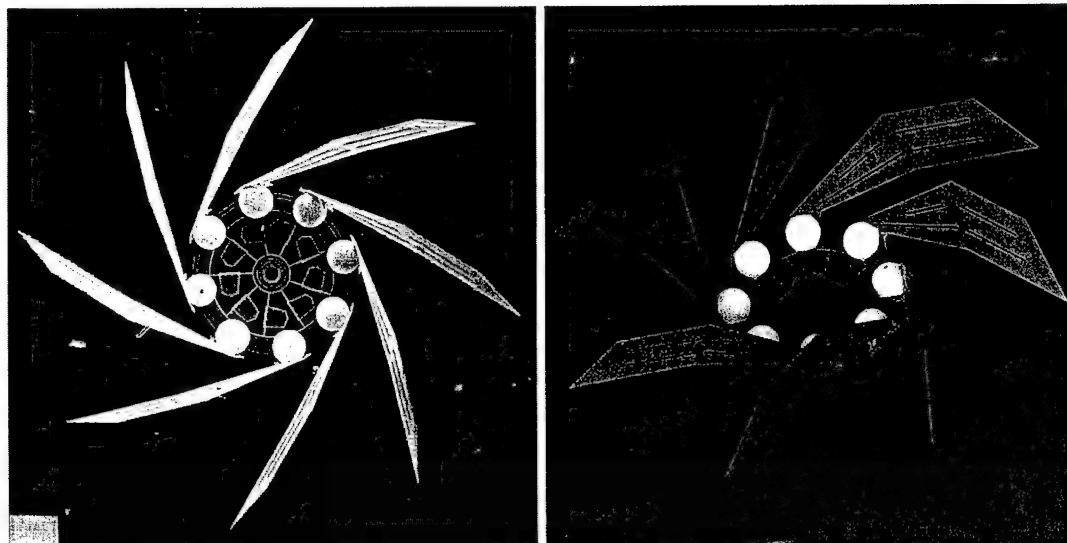


**Figure A-3:** Comparison between SEMs: SED (left) and quad-backscatter (right).

The R. J. Lee scanning electron microscope did not have X-ray fluorescence capabilities (XRF). To determine the rough make-up of elemental composition, an International Scientific Instruments (ISI) scanning electron microscope, with XRF capability, was used. This microscope was also used to capture SEMs. This microscope was similar to the one depicted in Figure A-4. The attachments for XRF capability are not shown in Figure A-4.

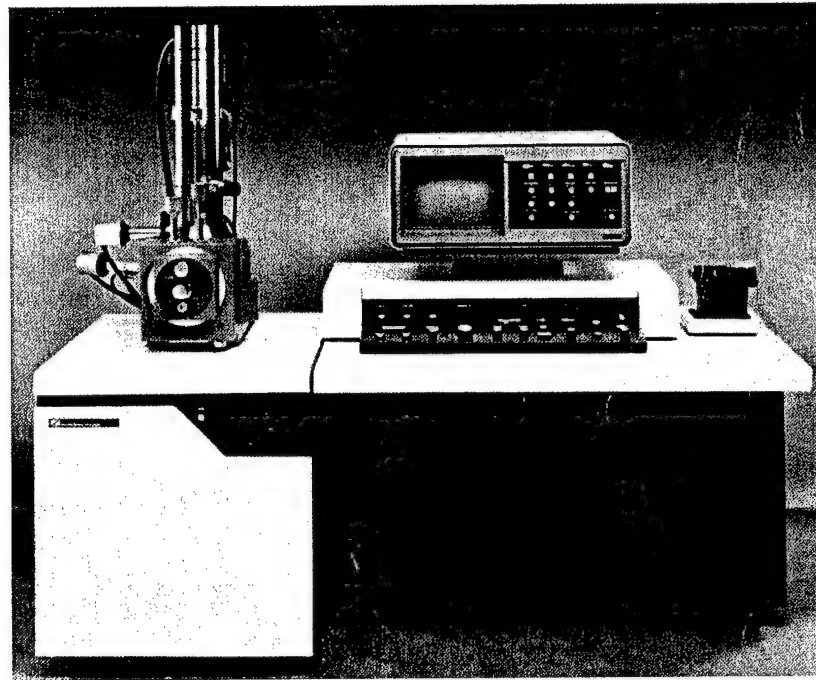


**Figure A-4:** ISI scanning electron microscope.

### A.3 Computing

All data analysis, modeling, design layouts, and most digital image capturing was performed on a personal computer with a 400 MHz Pentium II processor, 128 Mb RAM, and an ATI All-in-Wonder 128 video card.

### A.4 Image Recording And Photography

All captured video images and movies were captured through either a Javelin JE3762DSP or a WATEC WAT-202B CCD color video camera. The video cameras were mounted to either the probe station microscope or a National stereoscopic microscope. All video movies were recorded using JVC HR-VP636U VHS video

recorders. Video was transferred to computer images using either Snappy (stills only) or ATI All-in-Wonder 128 (stills and movie) video capture software and hardware.

#### A.5 MEMS Manipulation And Electrical Characterization

All manipulation and electrical testing of the MEMS in this work was performed using a Micromanipulator Inc. Model no. 6000 probe station shown in Figure A-5. The probe station microscope (USMC) had 2x/0.055 f=200, 10x/0.28 f=200, and 20x/0.42 f=200 apertures.

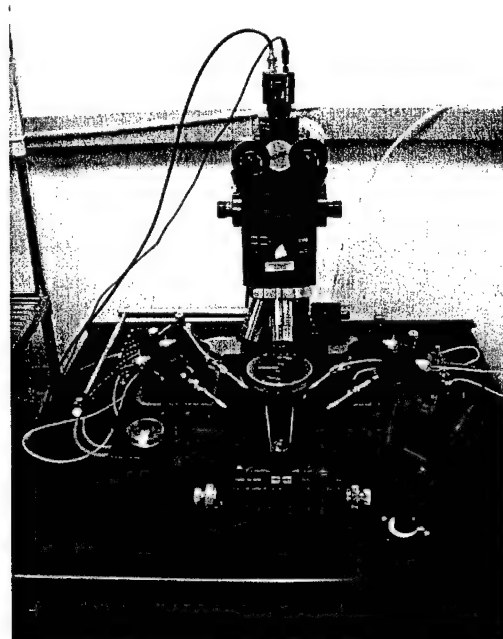


**Figure A-5:** Probe Station.

## A.6 Reflow Station

Figure A-6 and Figure A-7 show the reflow station. All the solder reflow presented in this work was performed at this station. A general description of the sequence of events, of a solder reflow, is presented next, and will guide the reader through a description of the components. One or more MEMS chips are placed on the center of the heating stage. Solder is usually placed on the MEMS chip by impaling solder spheres, located on a neighboring glass slide, with a probe. The probe then transfers the solder sphere to the MEMS chip, and with the help of a second probe, places the solder in an appropriate location.

The glass slide and probes are retracted from the heating stage area. A cylindrical glass chamber or a square glass chamber (for photography) may be lowered over the heating stage. N<sub>2</sub> and/or Formic Acid vapor may be introduced into the chamber and regulated through valves. Gas and vapors are vented out of the chamber through holes in the heating stage stand. The vapors are then collected by an exhaust hose. Temperature of the stage is controlled using a Watlow series 965 temperature controller. Note, the chamber is not a perfectly sealed system, during any reflow experiment, the chamber is slightly open to the atmosphere, including oxygen.

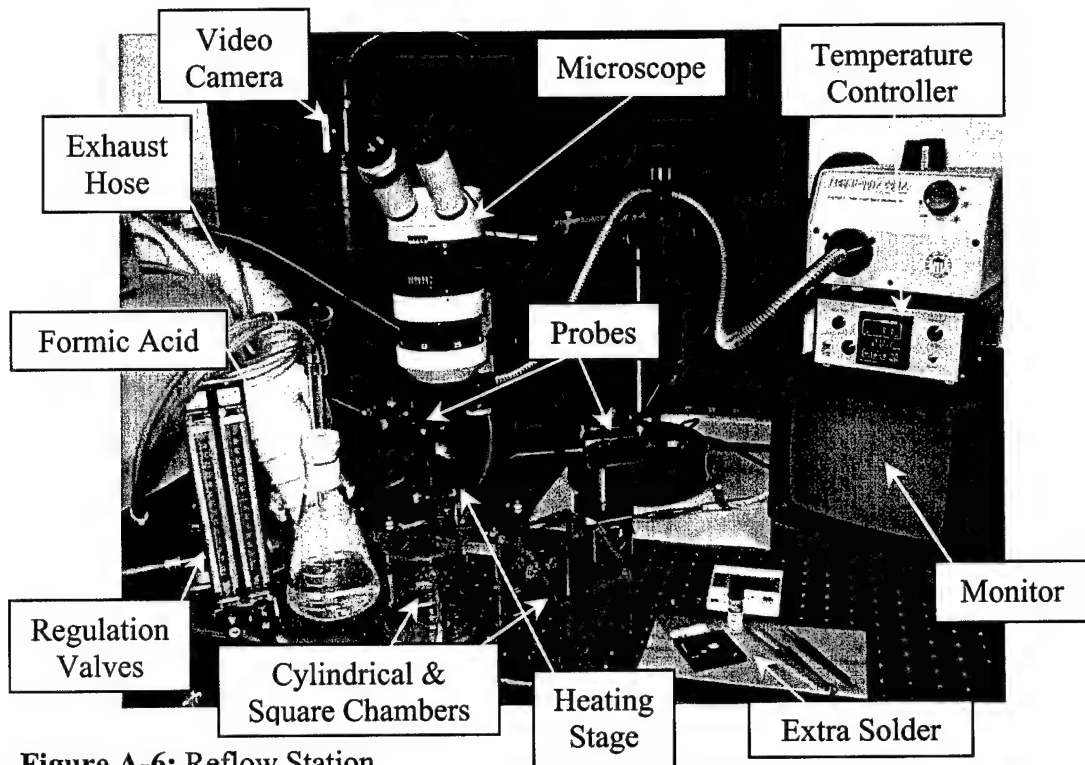


Figure A-6: Reflow Station.

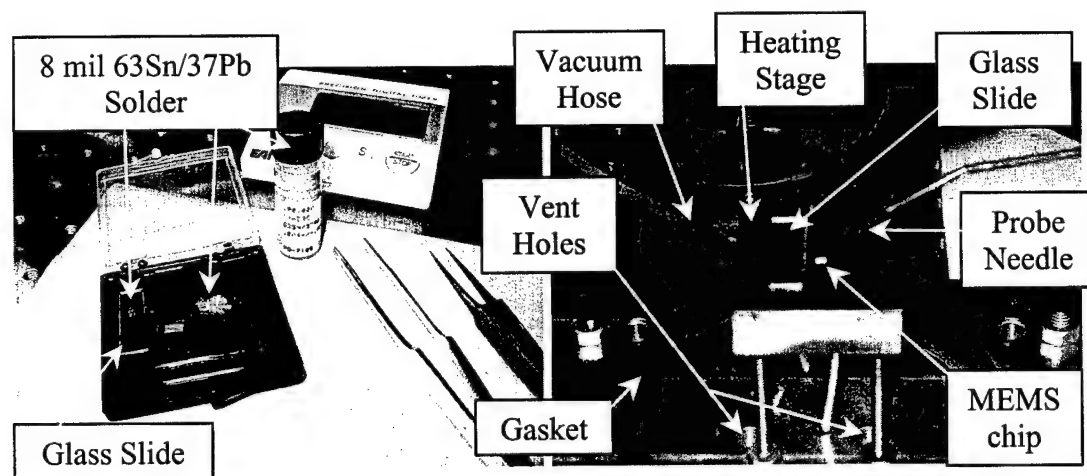
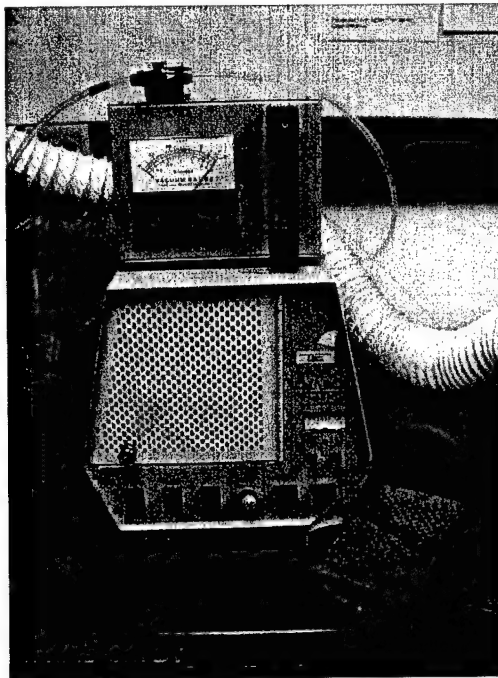


Figure A-7: Reflow Station close views of: manufactured solder sphere storage (left) and heating stage (right).

## A.7 Plasma Cleaner

All plasma cleaning was performed using a March Instruments, Inc. PlasMod shown in Figure A-8. The operation procedures and settings were as follows:

- a) Turn on vacuum, open argon tank regulated at 10 psi, and turn on power to plasma cleaner.
- b) Insert specimen into chamber and activate chamber vacuum.
- c) Regulate chamber argon flow to  $3 \text{ cm}^3 / \text{minute}$ .
- d) When chamber pressure is below 1 mbar, turn on AC power. Iterate between adjusting power and tuning capacitors until the reflected power is a minimum and the forward power is 25 W. A bright violet colored glow should appear in the chamber.
- e) After specimen has been cleaned for a desired amount of time, turn everything off and remove specimen.



**Figure A-8:** Plasma Cleaner.

#### A.8 Thermal Evaporator

All thermal evaporation of indium was performed in a BAL-TEC Evaporative Coating System MED 020. The thickness and thickness rate were monitored using a Sycon Instruments Thickness/Rate Monitor STM-100/MF. Both items are shown in Figure A-9. The operation procedures and settings were as follows:

- a) Turn on power to sensor box and evaporator system. Check sensor life and replace sensor in lid if necessary.
- b) Ensure crucible has In shot in it.
- c) Clean seals on lid and apply new vacuum grease.
- d) Mount specimen in lid, close lid, and plug sensor in "Q".
- e) Push down cover and mount and turn on external lid cooling fan.
- f) Press "Full Speed" and wait till pressure gauge reads  $4 \times 10^{-5}$  mbar.

- g) Block off crucible by turning shutter knob counter clockwise.
- h) Press reset, set Limit=Time, Select=8V, press "On", and press "Up" until current reading is stable at 39 Amps.
- i) Let run for 60 s to burn off unwanted crud, then open shutter. Thickness/Rate monitor should start registering a significant reading.
- j) Increase current until a rate of 40 Å/s is achieved.
- k) Turn off evaporator power by pressing "Reset" when 1000 Å + thickness you wanted is displayed on the Thickness/Rate monitor.
- l) Let system set until pressure gauge indicates  $1.7 \times 10^{-5}$  mbar (approximately 5 minutes). Then press "Stand By" two times, but wait 5 - 10 minutes between first and second push.
- m) Wait till pressure gauge reads approximately 1 bar, then remove specimen.

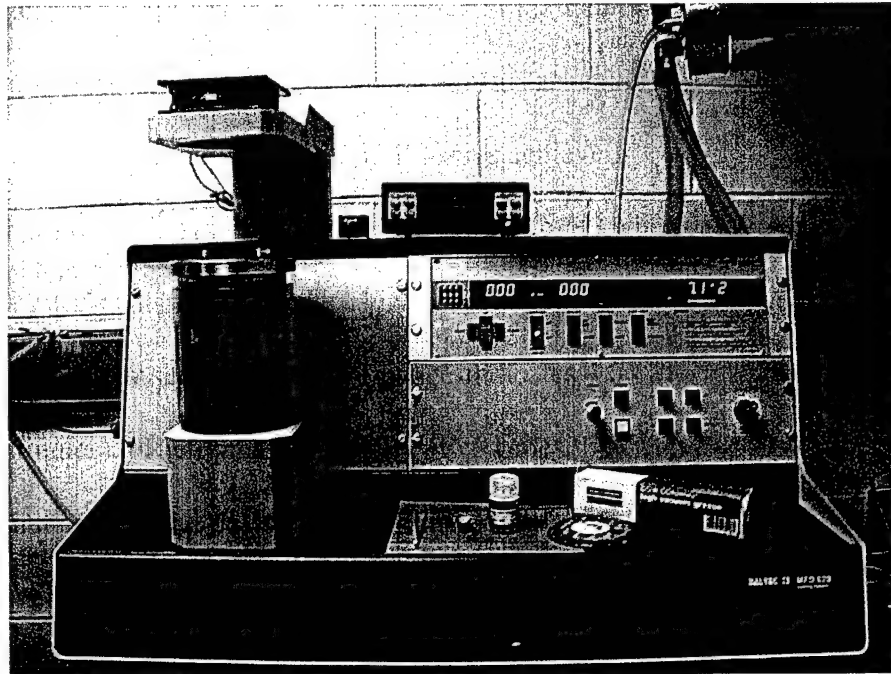


**Figure A-9:** Thermal Evaporator.

## **A.9 Sacrificial Oxide Etching (Also Known As "Release") And Drying**

All releasing and drying of MEMS was performed in a class 100,000 clean room using the equipment and facilities shown in Figure A-10. The most dangerous chemical used is hydrofluoric acid (HF). Besides a clean room suit that includes the wearing of a paper mask, hair net, hood, booties, and powder free latex gloves, eye protection was also worn during the release process.

The drying of the MEMS chips was performed in a BAL-TEC CPD 030 Critical Point Dryer. Special drying is necessary to eliminate device failure by the surface tension forces of a drying liquid causing the MEMS components to permanently stick to the substrate. This undesirable phenomenon is also known as stiction. No more than seven 2 mm by 2 mm surface micromachined chips were released at one time. The release process should be performed using ultra-clean beakers, containers, and utensils. The room temperature during the following procedures was usually around 70 - 75 °F.

### **A.9.1 Pre-Release And Release Procedures**

- a) Starting with an unreleased and photoresist coated silicon surface micromachined MEMS chip, soak in 25 ml Acetone for 15 minutes. This step removes the photo resist coating.
- b) Soak in 25 ml of 2-propanol (isopropyl alcohol) for 5 minutes. This displaces the acetone and any remaining photoresist residue.

- c) Dip in 50 ml deionized and purified water (DIW) for 15 seconds. This step displaces the 2-propanol and conditions the surface of the MEMS chip to be more like the HF.
- d) Let chips air, oven, or hotplate dry or immediately go to step e). Note, if the chips already have the photoresist coating removed and are reasonably clean, the process begins at step e).
- e) Soak in 25 ml of 48% HF, using acid resistant tweezers to place chips. The beaker containing the HF should also be acid resistant. Soak for 30 seconds if pre-releasing. Soak for 2.5 to 4 minutes if performing a full release or final release. The final release time is dependent on structure size and material compatibility. For most of the devices in this work, 4 minutes was used. This step etches away the SiO<sub>2</sub> or sacrificial layer.
- f) Gently and carefully dip in a 50 ml mixture of Methanol:DIW 3:1 for 15 seconds. This step is used to dilute the HF and end the etching.
- g) Gently and carefully place chip or chips in bottom screen cup. The screen cups should be totally immersed in a container of Methanol. The bottom of a glass petri dish works rather well for this. At this point the chips may remain immersed in the methanol indefinitely.
- h) Without disturbing the MEMS chips and contaminating the methanol, carefully screw the top screen cup onto the bottom screen cup. The screen cups prevent the rushing CO<sub>2</sub> in the critical point dryer from turning over the released MEMS chips.

### A.9.2 Drying Procedures

- a) Ensure an unregulated CO<sub>2</sub> supply is attached to the critical point dryer, the metering valve is closed, power is on, and "Gas Out" is off.
- b) Fill the critical point dryer chamber, with methanol, to the half way point of the observation glass. Without leaving the MEMS chips in the screen cups exposed to the air for more than 3 seconds, gently and carefully move the screen cups from the methanol container to the dryer chamber.
- c) Close dryer chamber lid, and press "Cooling" and wait until the temperature reaches 0 °C.
- d) Allow liquid CO<sub>2</sub> to enter chamber by pressing "Medium In". Liquid CO<sub>2</sub> will violently enter the chamber.
- e) When liquid CO<sub>2</sub> fills the chamber to the top of the site glass, press "Medium Out". Liquid will quickly begin to drain from the chamber. Press "Medium Out" again to stop the draining when the level reaches just above the MEMS chip. Do not let the MEMS chips be un-immersed in fluid.
- f) Since "Medium In" was not pressed again, liquid CO<sub>2</sub> is still pouring in. Repeat step e) seven more times or until you are sure the liquid CO<sub>2</sub> has displaced all of the methanol.
- g) Once the liquid CO<sub>2</sub> has filled the chamber to the top of the site glass for the last time, press "Medium In" to stop the input of CO<sub>2</sub>.
- h) Turn off "Cooling" and press "Heating". During the heating, the CO<sub>2</sub> will reach its critical point and change from liquid to gas instantly (without going through a saturation region).

- i) Once the temperature controller indicates 40 °C, press "Gas Out". Slowly open the metering valve allowing the gas to escape in a slow and controlled manner, without letting the CO<sub>2</sub> gas condense back into a liquid.
- j) Once the chamber has reached atmospheric pressure the MEMS chips may be removed.

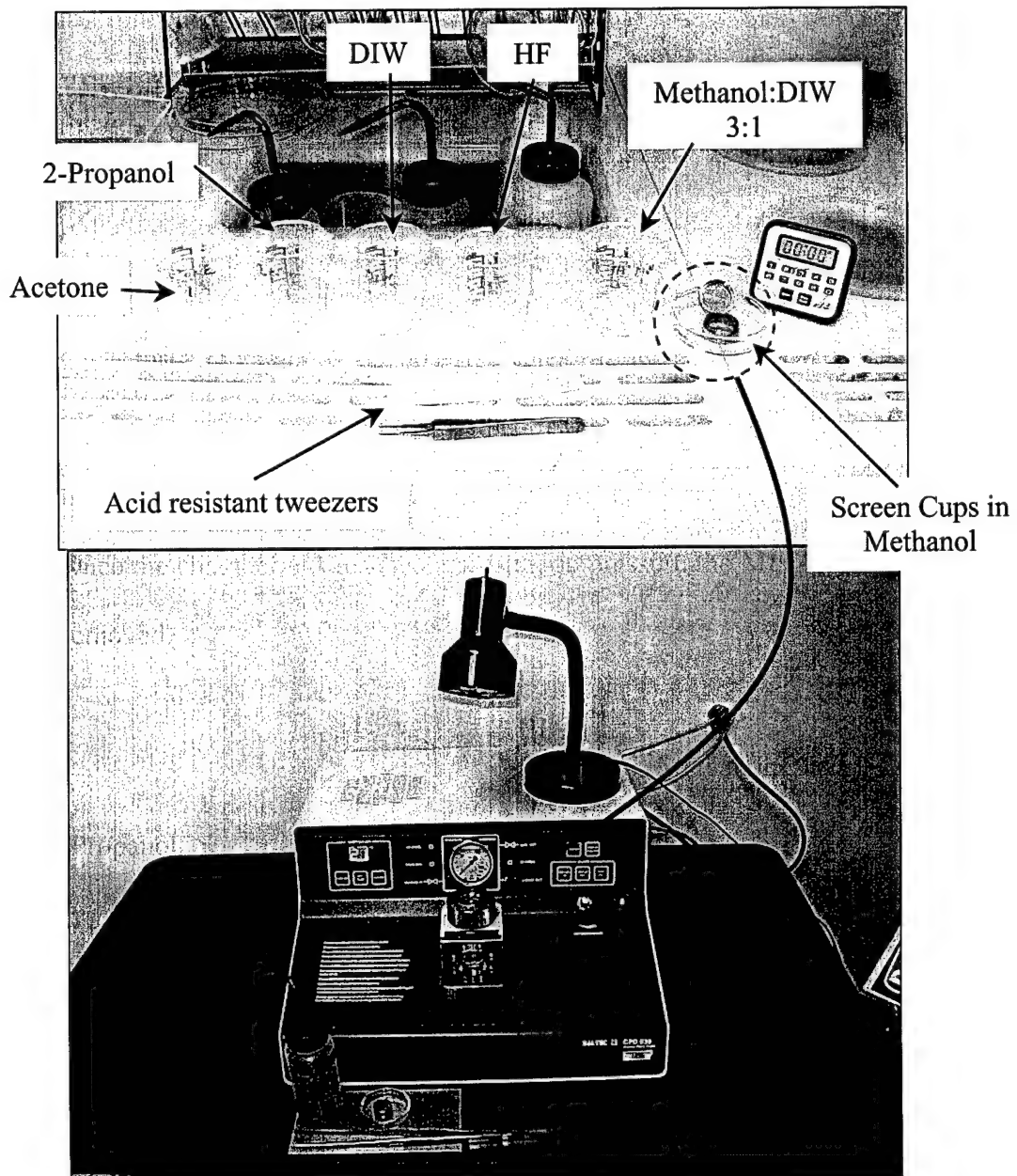


**Figure A-10:** Release station in chemical hood (top) and critical point dryer (below).

### A.10 Wirebonding

All wirebonding was performed on the Marpet Enterprises Inc. Bump/Bonder shown in Figure A-11. Wire bonding was performed using gold wire, a 7/16" capillary, and the manual lever with the following machine settings: Loop=3.15, Reset=13.5, Dual Wt.=10, Bond Force=2, Speed=2, Current=4, Ball Size=5, Power A/B=5/5, Time A/B=5/5, Stage Temp.=130 °C, and Tool Heat=9.



**Figure A-11:** Wirebonder.

### A.11 Optical Measurement

Measurement of the tip displacement of the two solder joint test structures was performed using the setup shown in Figure A-12. The optical measurement station consists of a positioning translation/tilt/rotate specimen holder, a National

stereoscopic microscope (6x, 12x, 25x, 50x magnification), Javelin CCD camera, video monitor, and a personal computer with video capture capability and Paint Shop Pro graphics software.

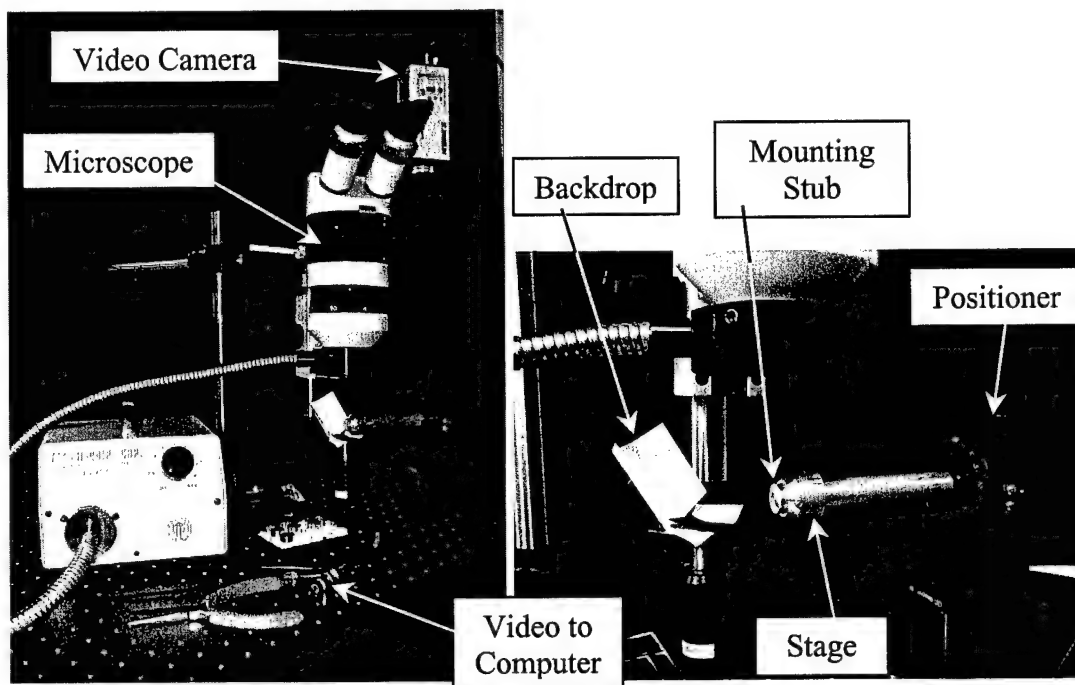
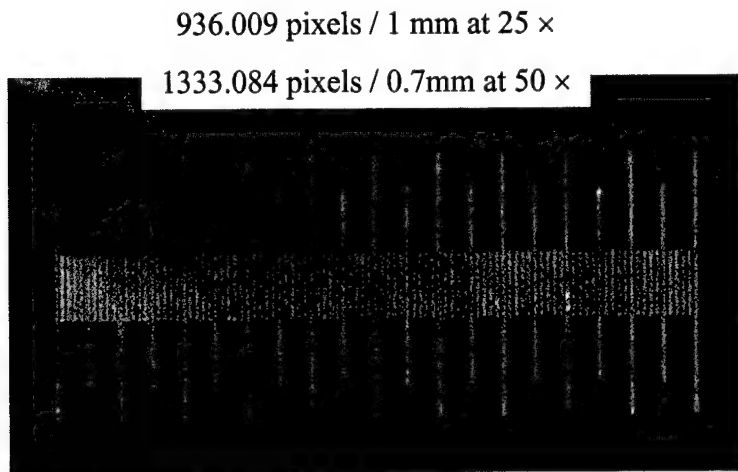


Figure A-12: Optical Measurement System.

The optical measurement station is first calibrated by capturing a 1500 x 1125 pixel image of an Olympus B-0550 0.01mm optical calibration slide and determining the number of pixels per meter using Paint Shop Pro, as shown in Figure A-13. Consequently, the precision of any subsequent measurement will be  $\pm 1$  pixel or approximately  $\pm 1.068 \mu\text{m}$  for images captured at 25x magnification and  $\pm 0.525 \mu\text{m}$  for images captured at 50x magnification. All test structures were measured at 25x magnification.



**Figure A-13:** Captured video image of optical calibration slide.

The procedure for making an optical measurement of the test structures is as follows:

- a) After assembly, the 2 x 2 mm chip containing the array of test structures is attached to a 15 mm diameter aluminum mounting stub using colloidal graphite.
- b) The stub is then mounted in the stage of the positioner and centered under the microscope of the optical measurement station.
- c) The specimen's side profile is aligned until parallel with the plane of view and focal plane, the substrate is also leveled with the horizontal (with respect to the camera image), and a 1500 x 1125 video image is captured and saved as a .jpg graphics file.
- d) The image is then opened in Paint Shop Pro where pixel locations can be determined. The hinge pivot of the first solder joint (at substrate) is considered the origin. The x-y pixel distances from the origin to the tip of the

test structure are then used to determine x-y coordinate in meters using the conversion in Figure A-13.

The means of determining x-y pixel distances is illustrated in Figure A-14. For many measurements, the origin location is obscured. For this reason there is a 20  $\mu\text{m}$  diameter region of uncertainty for measurements taken with obscured origins. However, this 20  $\mu\text{m}$  error is much better than the 60  $\mu\text{m}$  of error obtained when using the scanning electron microscope. The scanning electron microscope would have been the preferred method of measurement because of the large depth of focus, however the amount of error, and difficulty of use for this purpose prevented me from using it.

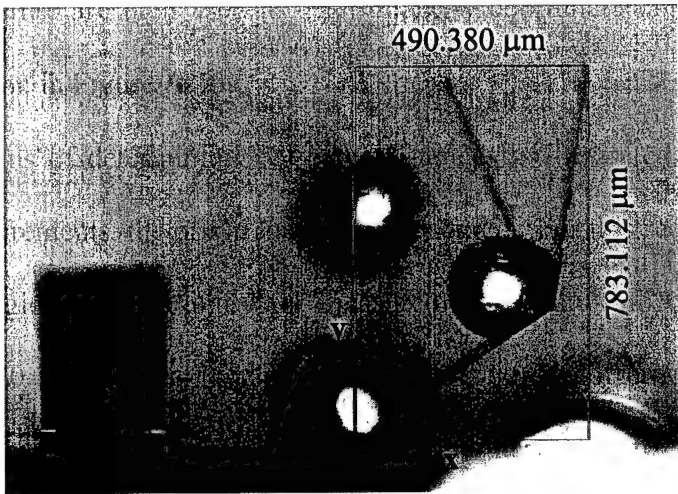


**Figure A-14:** Captured video image of a 135°/135° two-solder-joint structure exemplifying the measurement of x-y position of the end of the last plate with respect to the first solder joint hinges.

### A.12 Interferometric Microscope

All interferometric microscope measurements were made using the Zygo New View 200 Interferometric Microscope with a 10x Mirau objective and 1-2x

magnification, as shown in Figure A-15. The following typical settings procedures were used for most measurements:

- a) Start Zygo software.
- b) Place specimen under objective, move filter to focus, adjust viewing light, and zoom and focus in on desired measurement location.
- c) Planarize measurement area using the planarization knobs until the fringe lines spread out such that there is one giant patch of constructive or destructive interference present in the image. Push filter in to "Measure", close down the noise aperture leaving only the desired measurement area in view, and adjust the viewing light.
- d) Set the scanning depth, objective type, zoom amount, and remove plane in the software.
- e) Set the measurement light intensity to just below 90%. A quick manual scan through the scanning depth, using the fine focus knob, may reveal areas of measurement light saturation -- the light intensity may be reduced further if this is found.
- f) Set focal plane at the center point of the measurement scan.
- g) Begin the measurement while ensuring the isolation table is not disturbed.
- h) Review data, save data, and/or save images.

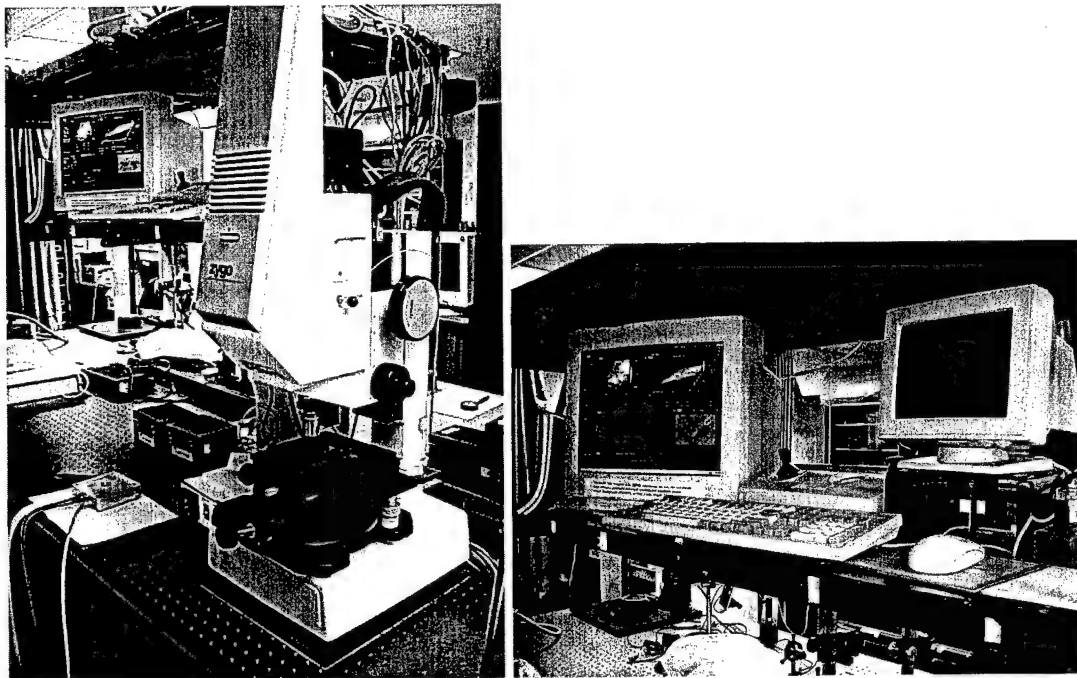


**Figure A-15:** Zygo Interferometric Microscope.

### A.13 Photolithography

All photolithography was performed using the equipment, facilities, and chemicals shown in Figure A-16 Oriel Corporation UV Flood Exposure Machine; Figure A-17 Headway Research Inc. Resist Spinner & Controller, chemicals, hotplate, chemical hood; and Figure A-18 Kasper Instruments Inc. Model 17A Wafer Aligner. The output energy of the Hg bulb of the wafer aligner was measured at 300 nm = 13.1 mW/cm<sup>2</sup>, 365 nm (I-line) = 39.5 mW/cm<sup>2</sup>, 405 nm (h-line) = 68.5 mW/cm<sup>2</sup>, and 436 nm (g-line) = 56 mW/cm<sup>2</sup>. The UV flood exposure machine light source is twice as powerful.

### A.13.1 Mask Making

Masks were designed using L-edit. A "paint" and "scratch" layer were defined using any two layers -- "paint" being everywhere there is black on the mask, and "scratch" being the clear parts of the mask. The usual GDS II levels used for scratch and paint were layers 3 and 4, respectively. The mask design was exported from L-edit into a GDS II file and emailed to a company that could print the mask out on 7 mil thick clear film using positive print, emulsion up, and 1/8 mil resolution. When the plastic film was received, it was transferred to a 2.5 inch soda glass chromium mask using the following procedures:

- a) Cut out film and place emulsion side down on photoresist coating (AZ1350) of new mask plate. Place a clear glass slide on top of film to weight it flat against the new mask plate.
- b) Place plate sandwich under the flood exposure machine, lower light source, and expose for 6 seconds.
- c) Immersion develop new mask plate in CD-30 photoresist developer for 20 seconds or until edge fringes of resist just disappear, rinse in DIW, and immediately blow dry both sides with N<sub>2</sub>.
- d) Bake as indicated -- if desired, this only makes 0.5 μm difference on mask feature dimension. This step was always skipped.
- e) Soak in CR-7 chromium etchant for 3-5 minutes or until chromium just disappears, rinse in DIW, and immediately blow dry both sides with N<sub>2</sub>.
- f) Strip remaining photoresist with acetone, rinse with methanol, and immediately blow dry both sides with N<sub>2</sub>.

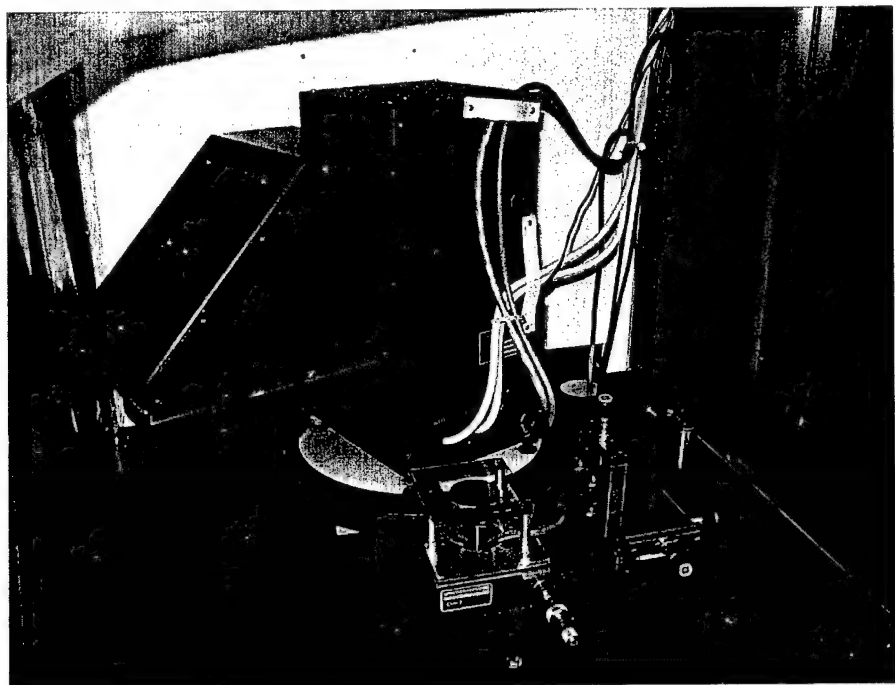


**Figure A-16:** UV Flood Exposure Machine.

### A.13.2 Photoresist Processing



**Figure A-17:** Photoresist spinner, chemicals, hotplate, chemical hood.

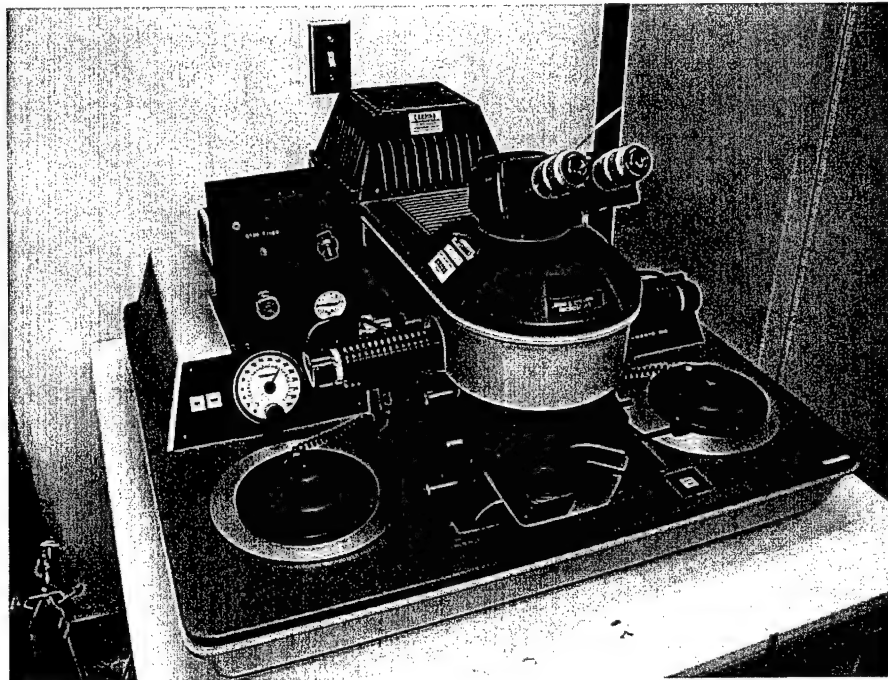


**Figure A-18:** Mask Aligner.

Photolithography is typically done on 2 inch diameter wafers or larger. This research required photolithography on individual 2 mm x 2 mm chips, presenting a difficult problem to overcome. The excellent solution I came up with is outlined in the following procedures:

- a) Start with a cleaned unreleased MEMS chip.
- b) Spin coat a 2 inch wafer with AZP4620 positive photoresist at 2500 RPM for 30 seconds.
- c) Bake wafer on hotplate for 10 seconds at 110 °C, and remove to cool.
- d) Arrange 2 mm x 2 mm chip with four other 1 cm x 1cm chips, of equal thickness, tightly together, on the resist coating of the 2 inch wafer as shown in Figure A-19.

- e) Bake wafer-chip arrangement on hotplate for 3 minutes 15 seconds at 110 °C.  
Remove and let cool. This step glues the chips into place.

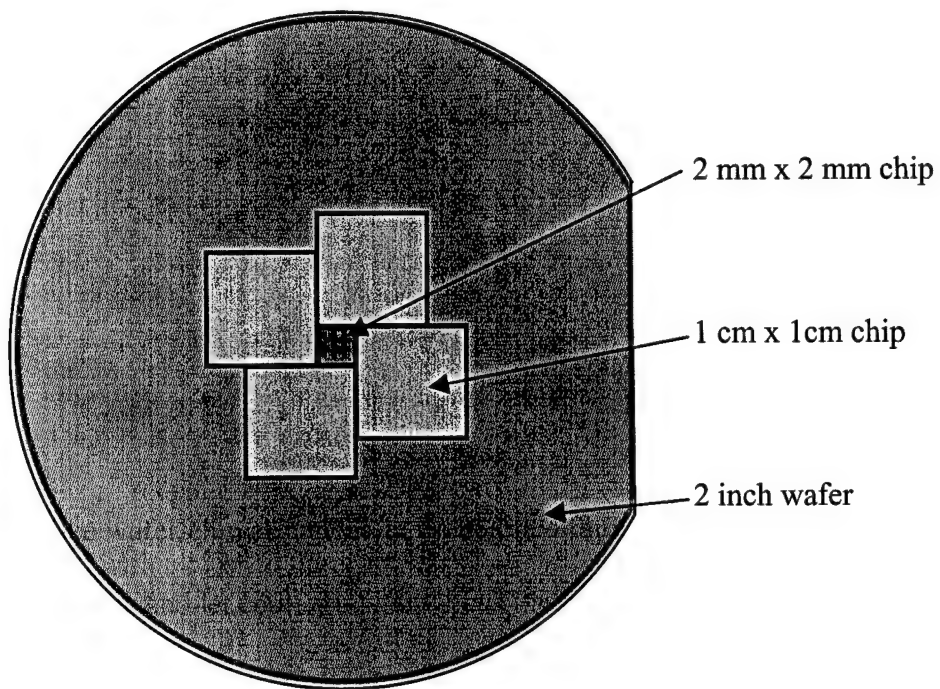


**Figure A-19:** Depiction of chip arrangement on a 2 inch silicon wafer for photolithography on 2 mm x 2 mm chips.

Steps a) - d) are necessary for two reasons. First, photoresist will bead up if applied to small 2 mm x 2 mm surfaces -- this is what is called an edge bead problem. To remedy the edge bead problem, a large surface area is created around the chip using the extra dummy chips. Secondly, contact mask exposure is used. If the mask were to contact a small amount of resist on the chip alone, it would crack or crush it because the force is concentrated over only a 2 mm x 2mm area. By adding more surface area, the force of the mask is distributed over a larger area, thereby relieving the pressure on the 2 mm x 2mm chip.

- f) Spin coat wafer arrangement with AZP4620 positive photoresist at 2000 RPM for 30 seconds. This will give an approximately 20  $\mu\text{m}$  thick layer on the 2 mm x 2 mm chip.
- g) Soft bake wafer on hotplate for 4 minutes 30 seconds at 110 °C, and remove to cool covered from the light.
- h) At this point the wafer aligner should be already to go. Briefly, the procedures for the wafer aligner are as follows. Turn on wafer aligner light source and allow to warm up for 15 minutes. Provide pressurized air and vacuum. Turn on aligner power. Load mask in holder and wafer arrangement on piston. Bring wafer to mask. Align wafer to mask. Contact wafer to mask. Rotate viewer selection to expose and expose for 1 minute.
- i) Spin develop wafer arrangement at 250 RPM for 6 minutes using a mixture of AZ400K developer:DIW 1:4, spray rinse with DIW for 30 sec, and spin dry at 3500 RPM for 30 seconds.

At this point, the photoresist patterns may be used to do photoresist assembly as shown in Figure A-20 or indium may be thermally deposited and the unwanted indium removed by lift off in an acetone bath.

#### A.14 Photoresist Assembly Of MEMS

During this research I also developed an unrefined method of photoresist assembly of MEMS. This section documents the procedures and possible theory behind the assembly mechanisms.

AZP4620 is a positive novolak resin based photoresist. The resist shown in Figure A-20 was first applied to an unreleased MEMS chip and then patterned and developed using the processing outlined above in A.13.2. Subsequently, the chip was released and reheated on a hotplate in air up to 160 °C whereupon a combination of surface tension and shrinking pulls up the plate. The temperature was reduced once the free plate reached an angle of 90°.

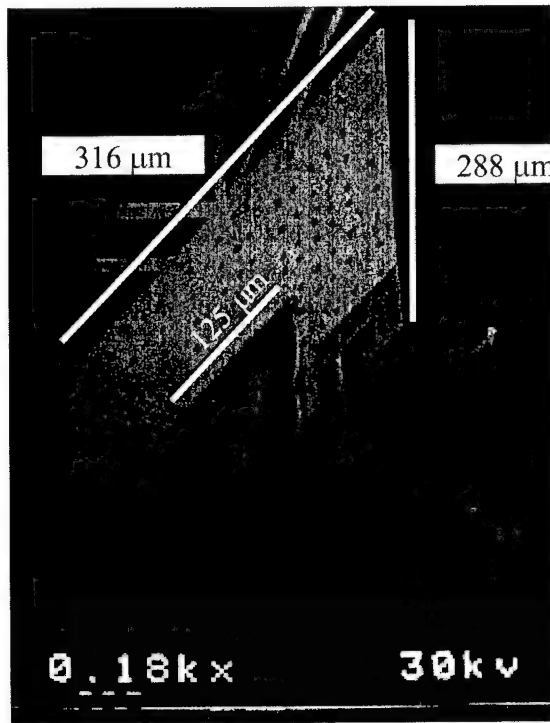


**Figure A-20:** SEM of photoresist assembled MEMS plate.

Any positive photoresist should exhibit this type of shrinking. For AZP4620, there are three mechanisms that cause the shrinking, and these are as follows. For temperatures above 120 °C, the remaining PGMEA solvent evaporates out of the resist and the diazonaphthoquinone sulfonic esters (DNQ) sensitizer begins to

decompose, causing some shrinkage. Furthermore, for temperatures above 125 °C, the three diazo-groups, in the DNQ, begin crosslinking with the novolak resin, resulting in the tripling of the molecular weight, causing shrinking. Finally, for temperatures above 150 °C, the novolak resin begins crosslinking with itself, also contributing to the shrinkage. More information on novolak resin and DNQ based resists, see R. Dammel, *Diazonaphthoquinone-based Resists*, Tutorial Texts in Optical Engineering, vol. TT 11, SPIE Optical Engineering Press, Bellingham, Washington, USA, 1993.

## Appendix B Model Code

### B.1 assybuild.m

```
%assybuild.m
%This function receives the plate matrix (plate) and returns the two-dimensional, shift-ready,
%matrix of points containing the coordinates of the final assembly.
%i.e. v1= [x1 x2 .... xn]
%
% [y1 y2 .... yn]
% [1 1 .... 1]
%This program calls the geometric angle solver (angsolve.m) to solve for the actual rotation angle
%This program calls the deformation solver (getshape.m) to solve for the deformation of structures
%Plate information, plate(1,:)
%plate(i,:)=[length, shape, elnum, pstress, gstress, solcurv, temp, [hplay], sw1, angle, sw2, V, g, l, w]
% 1, 2, 3, 4, 5, 6, 7, 8,9, 10, 11, 12, 13, 14,15,16
%*****
%length - Length of plate (micrometers)
%shape - 1=straight, 2=poly1 with internal stress, 3=poly2 with internal stress,
% 4=gold on poly2 with internal stress, 5=solder on poly2 exp observation of curvature
%elnum - Number of elements 0:length/elnum:length, 1 means a single beam composed
% of a beginning point and an end point
%pstress- Stress in polysilicon: +curved up, -curved down (Pa)
%gstress- Stress in gold: +curved up, -curved down (Pa)
%solcurv- Radius of curvature of plate with solder: +curved up, -curved down (micrometer)
%temp - (temperature in celsius)
%[hplay]- Hinge play (micrometers) [x,y] coordinate of shift of this plate
% with respect to end of previous plate
%sw1 - Switch: 1=allow hinge play to affect solder angle calculation only with sw2=1 also
%angle - Manual angle (radians) between this plate and previous plate when sw2=0
%sw2 - switch: 1=calculate equilibrium angle using plate(i, 12-16), 0=use angle
%V - Volume of solder (micron)^3
%g - Surface tension coefficient (Newton/microns) can be 1, not needed to find angle
%l - Height of solder plate (microns)
%w - Width of a solder plate (microns)
function v1 = assybuild(plate)
error(nargchk(1,1,nargin));

%Assemble m plates
[m,n]=size(plate);

***** Get the shape of plate *****
%v1 is the shape of the mth plate, (last plate, the first plate is hinged to the nitride).
%v1 is a 3 x (elnum+1) matrix of 2-d, shift ready, column vectors [x,y,1]'
v1=getshape(plate(m,:));

for i=m:-1:1

***** Get the shape of plate *****
%v2 is the shape of the i-1th plate.
%v2 is a 3 x (elnum+1) matrix of 2-d, shift ready, column vectors [x,y,1]'
if i==1
    v2=getshape(plate(i-1,:));
else
    v2=[0 0; 0 1];
end
[mv2,nv2]=size(v2);

***** Determine the rotation angle (Rang) and Rotation matrix (R) *****
%for v1 with respect to the slope at the beginning of v1 and the end of v2.
%Theta1 is the slope of the beginning end of v1,
%and theta2 is the slope of the ending end of v2
theta1=atan2( v1(2,2)-v1(2,1) , v1(1,2)-v1(1,1) );
theta2=atan2( v2(2,nv2)-v2(2,nv2-1) , v2(1,nv2)-v2(1,nv2-1) );

%Method 1 calculates the angle between plates due to the volume of solder
%and possibly hinge play,
```

```

%and Method 2 uses the angle supplied in plate(i,11)
%Method 1
if plate(i,12)==1
    a=angsolv(plate(i,13),plate(i,14),plate(i,15),plate(i,16));
    if plate(i,10)==1 %if true, the hinge play changes the length of the plates and recalculates a
        a=angsolv(plate(i,13),plate(i,14), plate(i,15)+plate(i,8)+plate(i,9)/sin(a) ,plate(i,16));
    end
    Rang=pi-a+theta2+theta1;
else
    %Method 2
    Rang=pi-plate(i,11)+theta2+theta1;
end

R=[cos(Rang) -sin(Rang);sin(Rang) cos(Rang)];

%***** Rotate and shift v1 to the end of v2 *****
%by: 1) rotating v1 with R
%     2) rotating hplay to be perpendicular to the end of v2 using theta2 and Rb
%     3) shifting v1 to the very end of v2 using the
%        location of the last point of v2, v2(1:2,length(v2)) plus the hinge play
    Rb=[cos(theta2) -sin(theta2);sin(theta2) cos(theta2)];
v1=[R, v2(1:2,nv2) + Rb*plate(i,8:9)' ; 0 0 1]*v1;

%***** Create new end of structure by attaching v1 to v2
if i~=1
    v1 = [v2, v1];
end

end      %for i=m:-1:1

```

## B.2 angsolv.m

```
%angsolv.m
%a = angsolv(V,g,l,w)
%
%This function calculates the equilibrium angle and angle of curvature
%for a given volume of a liquid wetted between two hinged plates of equal dimensions.
%The model used is sphere - 2 spherical cap segments + corner fills
%a = resulting equilibrium angle (radians)
%V = volume of solder (microns^3)
%g = surface tension coefficient (Newtons/micron)
%l = height of a plate (microns)
%w = width of a plate (microns)

function a = angsolv(V,g,l,w)
nargs = nargin;
error(nargchk(4,4,nargs));

options=foptions;
%options(1)=1; %1 shows output
options(2)=1e-4;options(3)=1e-4;
%options(5)=1; %1 means use Levenberg-Marquardt least squares solution
%options(14)=600;      %Number of iterations, default is 100xnumber of variables
%options(18)=1;      %max step length

Dsol=(6*V/pi)^(1/3);
alpha0=(-0.7936*l/Dsol + 1.05)*pi;    %initial guess for equilibrium angle
beta0=(-1.4704*l/Dsol + 2.0292)*pi;  %initial guess for angle of curvature
R0=Dsol/2;
%initial guess for radius of curvature

x=fsolve('geoequations',[alpha0 beta0 R0],options,[],V,g,l,w);

if abs(imag(x(1)))>0
    disp('WARNING! A complex solution of angle reached, taking real part of:')
    disp(num2str(x(1)*180/pi))
    a=real(x(1));
else
    a=x(1);
end
```

### B.3 geoequations.m

```
%This function is called by angsolv
function F=geoequations(x,V,g,l,w)

%x=[a,b]

%Iped sphere and spherical pressure, New R
%(rectangular plates)
%x(1)=x(1)+(-7.3091e-002*x(1)^3+3.0236e-001*x(1)^2-4.2628e-001*x(1)+2.4056e-
001);disp('8mil model') %8mil correction
x(1)=x(1)+(-5.2903e-002*x(1)^3+4.2576e-001*x(1)^2-1.0056*x(1)+7.7192e-001);disp('4mil
model') %4mil correction

a=x(1);b=x(2);R=x(3);

F=[  
    2/3*pi*R^3*(3*cos(pi/2-b/4)-cos(pi/2-b/4)^3)-V %sphere - 2 whole spherical cap segments  
    R^2-(l*cos(a/2) - R*cos(b/2))^2 - (w/4)^2 %w affectable R, the new R  
    w*l*cos((a-b)/2)-0.5*w*l*sin(b/2)/sin(a/2)%Net Torque Equation, using old R  
];
```

## B.4 getshape.m

```
%getshape.m
%This function returns the two dimensional shiftready [x,y,1]' vector
%describing the shape of a plate

%[V] = getshape(P)
%P=[length, shape, elnum, pstress, gstress, solcurv, temp, [hplay], sw1, angle, sw2, V, g, l, w]
%length - Length of plate (micrometers)
%shape - 1=straight, 2=poly1 with internal stress, 3=poly2 with internal stress,
%        4=gold on poly2 with internal stress, 5=solder on poly2 exp observation of curvature
%elenum - Number of elements 0:length/elenum:length, 1 means a single beam composed
%        of a beggining point and an end point
%pstress- Stress in polysilicon: +curved up, -curved down (Pa)
%gstress- Stress in gold: +curved up, -curved down (Pa)
%solcurv- Radius of curvature of plate with solder: +curved up, -curved down (micrometer)
%temp - (temperature in celsius)
%Note, only P(1-7) are relevant for this function

function V = getshape(P)

error(nargchk(1,1,nargin));

x=0:P(1)/P(3):P(1);

switch P(2)
case 1
    V=[x;zeros(1,length(x));ones(1,length(x))];
case 2
    Ep=169e9; %Young's modulus of polysilicon (Pa)
    vp=.22; %Poisson's ratio for polysilicon
    Epb=Ep/(1-vp);
    tp1=2; %thickness of poly1 (micrometers)
    y=P(4)/Epb/tp1*x.^2;
    V=[x;y;ones(1,length(x))];
case 3
    Ep=169e9; %Young's modulus of polysilicon (Pa)
    vp=.22; %Poisson's ratio for polysilicon
    Epb=Ep/(1-vp);
    tp2=1.5; %thickness of poly2 (micrometers)
    y=P(4)/Epb/tp2*x.^2;
    V=[x;y;ones(1,length(x))];
case 4
    Ep=169e9; %Young's modulus of polysilicon (Pa)
    vp=.22; %Poisson's ratio for polysilicon
    Epb=Ep/(1-vp);
    Eg=79e9; %Young's modulus of gold (Pa)
    vg=.42; %Poisson's ratio for gold
    Egb=Eg/(1-vg);
    ap=2.33e-6; %coefficient of thermal expansion for polysilicon (K^-1)
    ag=14.2e-6; %coefficient of thermal expansion for gold (K^-1)
    tg=0.5; %thickness of gold (micrometers)
    tp2=1.5; %thickness of poly2 (micrometers)
    To=27 - (P(5)-P(4))/Egb/(ap-ag);
    y=( 3*tg*( Egb*(ap-ag)*(P(7)-To) + P(4) )*x.^2 ) / (Epb*tp2^2);
    V=[x;y;ones(1,length(x))];
case 5
    Etl=31e9; %Young's modulus of 63Sn/37Pb (Pa)
    vtl=0.4; %Poisson's ratio for 63Sn/37Pb
    Etlb=Etl/(1-vtl);
    atl=24e-6; %coefficient of thermal expansion for 63Sn/37Pb (K^-1)
    y=0.5/P(6)*x.^2;
    V=[x;y;ones(1,length(x))];
end
```

## B.5 assyio\_2h8.m

```
%assyio_2h8
%8mil tolerance analysis
%Worst Case and Statistical Predictions for Dissertation
%
%
%This file provides the input and displays the output for assybuild.m
%The input is a 16 column matrix where each row describes a plate
%assybuild.m receives the plate matrix (plate) and returns the two-dimensional, shift-ready,
%matrix of points containing the coordinates of the final assembly.
%i.e. v1= [x1 x2 .... xn]
%           [y1 y2 .... yn]
%           [1 1 .... 1]
%Plate information, plate(1,:) is hinged to the nitride
%plate(i,:)=[length, shape, elnum, pstress, gstress, solcurv, temp, [hplay], sw1, angle, sw2, V, g, l, w]
%           1, 2, 3, 4, 5, 6, 7, 8,9, 10, 11, 12, 13, 14,15,16
%*****
%length - Length of plate (micrometers)
%shape - 1=straight, 2=poly1 with internal stress, 3=poly2 with internal stress,
%        4=gold on poly2 with internal stress, 5=solder on poly2 exp observation of curvature
%elenum - Number of elements 0:length/elenum:length, 1 means a single beam composed
%        of a beggining point and an end point
%pstress- Stress in polysilicon: +curved up, -curved down (Pa)
%gstress- Stress in gold: +curved up, -curved down (Pa)
%solcurv- Radius of curvature of plate with solder: +curved up, -curved down (micrometer)
%temp - (temperature in celsius)
%[hplay]- Hinge play (micrometers) [x,y] coordinate of shift of this plate
%        with respect to end of previous plate
%sw1 - Switch: 1=allow hinge play to affect solder angle calculation only with sw2=1 also
%angle - Manual angle (radians) between this plate and previous plate when sw2=0
%sw2 - switch: 1=calculate equilibrium angle using plate(i, 12-16), 0=use angle
%V - Volume of solder (micron)^3
%g - Surface tension coefficient (Newton/microns) can be 1, not needed to find angle
%l - Height of solder plate (microns)
%w - Width of a solder plate (microns)

clear
set(0,'defaultaxesfontname','times new roman')
set(0,'defaultaxesfontsize',12)
%*****
%***Change these values for different angle combinations
data=load('45135.txt');
% l1 l2 w1 w2
scav=[15 -9 7 -18];
p1=217;
p2=70;
gap=8; %if p1=217 gap=8, otherwise 5
%*** *** *** ***

%Define nominal dimensions
L=[500-gap 500]; %1,2 length of actual plates (microns)
Ps=[-7.9e6 -7.9e6]; %3,4 poly stress (Pa)
Src=[6000 6000 6000];%5,6,7 solder radius of curvature (microns) for each pad
x=[0,0 , 0,0]; %8,9,10,11 hinge position (microns)
D=[8.4547 8.4547]*(1e-3*0.3048/12*1e-6); %12,13 (microns) measured mean of solder balls
l=[p1-scav(1) p2-scav(2)]; %14,15 solder pad lengths (microns)
w=[p1-scav(3) p2-scav(4)]; %16,17 solder plate width (microns)

Ndims=[L, Ps, Src, x, D, l, w];dims=Ndims; %Vectors of nominal dimensions
%vector of tolerance values corresponding to Nomdim
tol=[2 2 2.82e6 2.82e6 1000 1000 1000 .5 .5 .5 1.0218*25.4 1.0218*25.4 scav];tol=abs(tol);
typval=Ndims;typval(8:11)=[1 1 1 1];del=sqrt(eps)*typval;%typical values for finite differences

%Define the plates of the assembly, plate(1,:) is hinged to the nitride
%plate(i,:)=length, shape, elnum, pstress, gstress, solcurv, temp, [hplay], sw1, angle, sw2, V, g, l, w]
%           1, 2, 3, 4, 5, 6, 7, 8,9, 10, 11, 12, 13, 14,15,16
```

```

plate(1,:)=[gap, 1, 1, 0, 0, 0, 27, dims(8:9), 0, 0, 1, 4/3*pi*(dims(12)/2)^3, 1, dims(14), dims(16)]; %gap and
angle
plate(2,:)=[dims(14), 5, 50, 0, 0, dims(5), 27, [0,0], 0, pi, 0, 0, 1, 0, 0]; %plate1pad1
plate(3,:)=[dims(1)-dims(14)-dims(15), 3, 50, dims(3), 0, 0, 27, [0,0], 0, pi, 0, 0, 1, 0, 0]; %plate1pol2only
plate(4,:)=[dims(15), 5, 50, 0, 0, dims(6), 27, [0,0], 0, pi, 0, 0, 1, 0, 0]; %plate1pad2
plate(5,:)=[dims(15), 5, 50, 0, 0, dims(7), 27, dims(10:11), 0, 0, 1, 4/3*pi*(dims(13)/2)^3, 1, dims(15),
dims(17)];%plate2pad1
plate(6,:)=[dims(2)-dims(15), 3, 50, dims(4), 0, 0, 27, [0,0], 0, pi, 0, 0, 1, 0, 0]; %plate2poly2only
Nplate=plate;
psize=size(plate);

%***** OUTPUT *****
%Get the nominal assembly shape
v=assybuild(Nplate);
[m,n]=size(v);
T0=v(1:2,n);

%Use this to plot each segment individually
in1=1;
for i=1:psize(1)
    plot(v(1,in1:in1+plate(i,3)),v(2,in1:in1+plate(i,3)))
    in1=in1+plate(i,3)+1;
    hold on
end
plot(T0(1),T0(2),'co')
xlabel('x (microns)')
ylabel('y (microns)')

%Plot data
plot(data(1,:), data(2,:),'r*')
hold off
axis equal

%Calculate first partial derivatives (central)
%Where D1c is the derivative matrix D1c=[df/dx1', df/dx2', ..., df/dxn']
for i=1:length(Ndims)
    dims=Ndims;
    dims(i)=Ndims(i)+del(i)/2;
    plate(1,:)=[gap, 1, 1, 0, 0, 0, 27, dims(8:9), 0, 0, 1, 4/3*pi*(dims(12)/2)^3, 1, dims(14), dims(16)]; %gap and
angle
    plate(2,:)=[dims(14), 5, 50, 0, 0, dims(5), 27, [0,0], 0, pi, 0, 0, 1, 0, 0]; %plate1pad1
    plate(3,:)=[dims(1)-dims(14)-dims(15), 3, 50, dims(3), 0, 0, 27, [0,0], 0, pi, 0, 0, 1, 0, 0]; %plate1pol2only
    plate(4,:)=[dims(15), 5, 50, 0, 0, dims(6), 27, [0,0], 0, pi, 0, 0, 1, 0, 0]; %plate1pad2
    plate(5,:)=[dims(15), 5, 50, 0, 0, dims(7), 27, dims(10:11), 0, 0, 1, 4/3*pi*(dims(13)/2)^3, 1, dims(15),
dims(17)];%plate2pad1
    plate(6,:)=[dims(2)-dims(15), 3, 50, dims(4), 0, 0, 27, [0,0], 0, pi, 0, 0, 1, 0, 0]; %plate2poly2only
    vr=assybuild(plate);
    dims(i)=Ndims(i)-del(i)/2;
    plate(1,:)=[gap, 1, 1, 0, 0, 0, 27, dims(8:9), 0, 0, 1, 4/3*pi*(dims(12)/2)^3, 1, dims(14), dims(16)]; %gap and
angle
    plate(2,:)=[dims(14), 5, 50, 0, 0, dims(5), 27, [0,0], 0, pi, 0, 0, 1, 0, 0]; %plate1pad1
    plate(3,:)=[dims(1)-dims(14)-dims(15), 3, 50, dims(3), 0, 0, 27, [0,0], 0, pi, 0, 0, 1, 0, 0]; %plate1pol2only
    plate(4,:)=[dims(15), 5, 50, 0, 0, dims(6), 27, [0,0], 0, pi, 0, 0, 1, 0, 0]; %plate1pad2
    plate(5,:)=[dims(15), 5, 50, 0, 0, dims(7), 27, dims(10:11), 0, 0, 1, 4/3*pi*(dims(13)/2)^3, 1, dims(15),
dims(17)];%plate2pad1
    plate(6,:)=[dims(2)-dims(15), 3, 50, dims(4), 0, 0, 27, [0,0], 0, pi, 0, 0, 1, 0, 0]; %plate2poly2only
    vr=assybuild(plate);
    D1c(:,i)=(vr(1:2,n)-vl(1:2,n))/del(i);
end

%Find Worst Case tolerance analysis with central derivatives
T_WC=0;
for i=1:length(tol)
    T_WC = T_WC + tol(i)*abs(D1c(:,i));
end

%Calculate standard deviation of variables
sd=tol/3;

%Calculate standard deviation and mean for assembly

```

```

%MEAN_A=T0+1/2*D2c*(sd.^2)'
for i=1:length(tol)
    COV(i,i)=sd(i)^2;
end
VAR_A=[D1c(1,:)*COV*D1c(1,:)' ; D1c(2,:)*COV*D1c(2,:)'];

%Plot worst case box
hold on
plot([T0(1)-T_WC(1) T0(1)+T_WC(1) T0(1)+T_WC(1) T0(1)-T_WC(1) T0(1)-T_WC(1)],...
[T0(2)-T_WC(2) T0(2)-T_WC(2) T0(2)+T_WC(2) T0(2)+T_WC(2) T0(2)-T_WC(2)],...
'g-')
hold off

%Plot Statistical 3sigma tolerance box
T_S3=3*sqrt(VAR_A);
hold on
plot([T0(1)-T_S3(1) T0(1)+T_S3(1) T0(1)+T_S3(1) T0(1)-T_S3(1) T0(1)-T_S3(1)],...
[T0(2)-T_S3(2) T0(2)-T_S3(2) T0(2)+T_S3(2) T0(2)+T_S3(2) T0(2)-T_S3(2)],...
'm:')
hold off

%Plot Statistical 2sigma tolerance box
T_S2=2*sqrt(VAR_A);
T_S=T_S2;
hold on
plot([T0(1)-T_S(1) T0(1)+T_S(1) T0(1)+T_S(1) T0(1)-T_S(1) T0(1)-T_S(1)],...
[T0(2)-T_S(2) T0(2)-T_S(2) T0(2)+T_S(2) T0(2)+T_S(2) T0(2)-T_S(2)],...
'm:')
hold off

%Plot Statistical 1sigma tolerance box
T_S1=sqrt(VAR_A);
T_S=T_S1;
hold on
plot([T0(1)-T_S(1) T0(1)+T_S(1) T0(1)+T_S(1) T0(1)-T_S(1) T0(1)-T_S(1)],...
[T0(2)-T_S(2) T0(2)-T_S(2) T0(2)+T_S(2) T0(2)+T_S(2) T0(2)-T_S(2)],...
'm:')
hold off

specs=[T0,T_WC,T_S3,T_S2,T_S1];
save -ascii -tabs specs.txt specs
D1c=D1c';
save -ascii -tabs derivatives.txt D1c

```

## B.6 assyio\_2h8warp.m

```
%assyio_2h8warp
%8mil tolerance analysis
%Worst Case and Statistical Predictions for Dissertation
%
%
%This file provides the input and displays the output for assybuild.m
%The input is a 16 column matrix where each row describes a plate
%assybuild.m receives the plate matrix (plate) and returns the two-dimensional, shift-ready,
%matrix of points containing the coordinates of the final assembly.
%i.e. v1= [x1 x2 .... xn]
%
%                                [y1 y2 .... yn]
%                                [1 1 .... 1]
%Plate information, plate(1,:)
%plate(i,:)=[length, shape, elnum, pstress, gstress, solcurv, temp, [hplay], sw1, angle, sw2, V, g, l, w]
%      1, 2, 3, 4, 5, 6, 7, 8, 9, 10, 11, 12, 13, 14, 15, 16
%*****
%length - Length of plate (micrometers)
%shape - 1=straight, 2=poly1 with internal stress, 3=poly2 with internal stress,
%        4=gold on poly2 with internal stress, 5=solder on poly2 exp observation of curvature
%elnum - Number of elements 0:length/elnum:length, 1 means a single beam composed
%       of a beginning point and an end point
%pstress- Stress in polysilicon: +curved up, -curved down (Pa)
%gstress- Stress in gold: +curved up, -curved down (Pa)
%solcurv- Radius of curvature of plate with solder: +curved up, -curved down (micrometer)
%temp - (temperature in celsius)
%[hplay]- Hinge play (micrometers) [x,y] coordinate of shift of this plate
%       with respect to end of previous plate
%sw1 - Switch: 1=allow hinge play to affect solder angle calculation only with sw2=1 also
%angle - Manual angle (radians) between this plate and previous plate when sw2=0
%sw2 - switch: 1=calculate equilibrium angle using plate(i, 12-16), 0=use angle
%V - Volume of solder (micron)^3
%g - Surface tension coefficient (Newton/microns) can be 1, not needed to find angle
%l - Height of solder plate (microns)
%w - Width of a solder plate (microns)

clear
set(0,'defaultaxesfontname','times new roman')
set(0,'defaultaxesfontsize',12)
%*****
%***Change these values for different angle combinations
data=load('warp45135.txt');
% l1 l2 w1 w2
scav=[ 15 -5 7 -18 ];
%scav=[0 0 0];
p1=217;
p2=70;
hingegap=8; %5 if p1 = 131 or 70, 8 if p1=217
gap=10; %does not change
%*** *** *** ***

%Define nominal dimensions
L=[500-hingegap 500]; %1,2 length of actual plates - substrate hinge gap(microns)
Ps=[-7.9e6]; %3 plain poly2 stress (Pa)
GPs=[103.5e6]; %4 stress of gold on poly
Src=[6000 6000 6000];%5,6,7 solder radius of curvature (microns) for each pad
x=[0,0 , 0,0]; %8,9,10,11 hinge position (microns)
D=[8.4547 8.4547]*25.4; %12,13 (microns) measured mean of solder balls
l=[p1-scav(1) p2-scav(2)]; %14,15 solder pad lengths (microns)
w=[p1-scav(3) p2-scav(4)]; %16,17 solder plate width (microns)
T=27; %18 temperature (degrees celsius)

Ndims=[L, Ps, GPs, Src, x, D, l, w, T];dims=Ndims; %Vectors of nominal dimensions
%vector of tolerance values corresponding to Nomdim
tol=[2 2 2.82e6 21e6 1000 1000 1000 .5 .5 .5 1.0218*25.4 1.0218*25.4 scav 6];tol=abs(tol);
typval=Ndims;typval(8:11)=[1 1 1 1];del=sqrt(eps)*typval;%typical values for finite differences
```

```

%Define the plates of the assembly, plate(1,:) is hinged to the nitride
%plate(i,:)=[length, shape, elnum, pstress, gstress, solcurv, temp, [hplay], sw1, angle, sw2, V, g, l, w]
%           1, 2, 3, 4, 5, 6, 7, 8, 9, 10, 11, 12, 13, 14, 15, 16
plate(1,:)=hingegap, 1, 1, 0, 0, 0, dims(18), dims(8:9), 0, 0, 1, 4/3*pi*(dims(12)/2)^3, 1, dims(14),
dims(16)];%hingegap and angle
plate(2,:)=[dims(14), 5, 50, 0, 0, dims(5), dims(18), [0,0], 0, pi, 0, 0, 1, 0, 0]; %plate1 pad1
plate(3,:)=[gap, 3, 10, dims(3), 0, 0, dims(18), [0,0], 0, pi, 0, 0, 1, 0, 0]; %gap1 poly2 only
plate(4,:)=[dims(1)-dims(14)-dims(15)-2*gap, 4, 100, dims(3), dims(4), 0, dims(18), [0,0], 0, pi, 0, 0, 1, 0, 0];%gold on
poly
plate(5,:)=gap, 3, 10, dims(3), 0, 0, dims(18), [0,0], 0, pi, 0, 0, 1, 0, 0; %gap2 poly2 only
plate(6,:)=[dims(15), 5, 50, 0, 0, dims(6), dims(18), [0,0], 0, pi, 0, 0, 1, 0, 0]; %plate1 pad2
plate(7,:)=[dims(15), 5, 50, 0, 0, dims(7), dims(18), dims(10:11), 0, 0, 1, 4/3*pi*(dims(13)/2)^3, 1, dims(15),
dims(17)];%plate2 pad1
plate(8,:)=gap, 3, 10, dims(3), 0, 0, dims(18), [0,0], 0, pi, 0, 0, 1, 0, 0; %gap3 poly2 only
plate(9,:)=[dims(2)-dims(15)-gap, 4, 100, dims(3), dims(4), 0, dims(18), [0,0], 0, pi, 0, 0, 1, 0, 0]; %plate2 gold
on poly
Nplate=plate;
psize=size(plate);

***** OUTPUT *****
%Get the nominal assembly shape
v=assybuild(Nplate);
[m,n]=size(v);
T0=v(1:2,n);

%Use this to plot each segment individually
in1=1;
for i=1:psize(1)
    plot(v(1,in1:in1+plate(i,3)),v(2,in1:in1+plate(i,3)),'Color',[0 rem(i,2) == 0 1])
    in1=in1+plate(i,3)+1;
    hold on
end
plot(T0(1),T0(2),'co')
xlabel('x (microns)')
ylabel('y (microns)')

%Plot data
plot(data(1,:), data(2,:),'r*')
hold off
axis equal

%Calculate first partial derivatives (central)
%Where D1c is the derivative matrix D1c=[df/dx1', df/dx2', ..., df/dxn']
for i=1:length(Ndims)
    dims=Ndims;
    dims(i)=Ndims(i)+del(i)/2;
    plate(1,:)=hingegap, 1, 1, 0, 0, 0, dims(18), dims(8:9), 0, 0, 1, 4/3*pi*(dims(12)/2)^3, 1, dims(14),
dims(16)];%hingegap and angle
    plate(2,:)=[dims(14), 5, 50, 0, 0, dims(5), dims(18), [0,0], 0, pi, 0, 0, 1, 0, 0]; %plate1 pad1
    plate(3,:)=gap, 3, 10, dims(3), 0, 0, dims(18), [0,0], 0, pi, 0, 0, 1, 0, 0; %gap1 poly2 only
    plate(4,:)=[dims(1)-dims(14)-dims(15)-2*gap, 4, 100, dims(3), dims(4), 0, dims(18), [0,0], 0, pi, 0, 0, 1, 0, 0];%gold on
poly
    plate(5,:)=gap, 3, 10, dims(3), 0, 0, dims(18), [0,0], 0, pi, 0, 0, 1, 0, 0; %gap2 poly2 only
    plate(6,:)=[dims(15), 5, 50, 0, 0, dims(6), dims(18), [0,0], 0, pi, 0, 0, 1, 0, 0]; %plate1 pad2
    plate(7,:)=[dims(15), 5, 50, 0, 0, dims(7), dims(18), dims(10:11), 0, 0, 1, 4/3*pi*(dims(13)/2)^3, 1, dims(15),
dims(17)];%plate2 pad1
    plate(8,:)=gap, 3, 10, dims(3), 0, 0, dims(18), [0,0], 0, pi, 0, 0, 1, 0, 0; %gap3 poly2 only
    plate(9,:)=[dims(2)-dims(15)-gap, 4, 100, dims(3), dims(4), 0, dims(18), [0,0], 0, pi, 0, 0, 1, 0, 0]; %plate2 gold
on poly
    vr=assybuild(plate);
    dims(i)=Ndims(i)-del(i)/2;
    plate(1,:)=hingegap, 1, 1, 0, 0, 0, dims(18), dims(8:9), 0, 0, 1, 4/3*pi*(dims(12)/2)^3, 1, dims(14),
dims(16)];%hingegap and angle
    plate(2,:)=[dims(14), 5, 50, 0, 0, dims(5), dims(18), [0,0], 0, pi, 0, 0, 1, 0, 0]; %plate1 pad1
    plate(3,:)=gap, 3, 10, dims(3), 0, 0, dims(18), [0,0], 0, pi, 0, 0, 1, 0, 0; %gap1 poly2 only
    plate(4,:)=[dims(1)-dims(14)-dims(15)-2*gap, 4, 100, dims(3), dims(4), 0, dims(18), [0,0], 0, pi, 0, 0, 1, 0, 0];%gold on
poly
    plate(5,:)=gap, 3, 10, dims(3), 0, 0, dims(18), [0,0], 0, pi, 0, 0, 1, 0, 0; %gap2 poly2 only
    plate(6,:)=[dims(15), 5, 50, 0, 0, dims(6), dims(18), [0,0], 0, pi, 0, 0, 1, 0, 0]; %plate1 pad2

```

```

plate(7,:)=[dims(15), 5, 50, 0, 0, dims(7), dims(18), dims(10:11), 0, 0, 1, 4/3*pi*(dims(13)/2)^3, 1, dims(15),
dims(17)];%plate2 pad1
plate(8,:)=[gap, 3, 10, dims(3), 0, 0, dims(18), [0,0], 0, pi, 0, 0, 1, 0, 0]; %gap3 poly2 only
plate(9,:)=[dims(2)-dims(15)-gap, 4, 100, dims(3), dims(4), 0, dims(18), [0,0], 0, pi, 0, 0, 1, 0, 0]; %plate2 gold
on poly
vl=assybuild(plate);
D1c(:,i)=(vr(1:2,n)-vl(1:2,n))/del(i);
end

%Find Worst Case tolerance analysis with central derivatives
T_WC=0;
for i=1:length(tol)
    T_WC = T_WC + tol(i)*abs(D1c(:,i));
end

%Calculate standard deviation of variables
sd=tol/3;

%Calculate standard deviation and mean for assembly
%MEAN_A=T0+1/2*D2c*(sd.^2)
for i=1:length(tol)
    COV(i,i)=sd(i)^2;
end
VAR_A=[D1c(1,:)*COV*D1c(1,:)'; D1c(2,:)*COV*D1c(2,:)'];

%Plot worst case box
hold on
plot([T0(1)-T_WC(1) T0(1)+T_WC(1) T0(1)+T_WC(1) T0(1)-T_WC(1) T0(1)-T_WC(1),...
[T0(2)-T_WC(2) T0(2)-T_WC(2) T0(2)+T_WC(2) T0(2)+T_WC(2) T0(2)-T_WC(2)],...
'g-')
hold off

%Plot Statistical 3sigma tolerance box
T_S3=3*sqrt(VAR_A);
hold on
plot([T0(1)-T_S3(1) T0(1)+T_S3(1) T0(1)+T_S3(1) T0(1)-T_S3(1) T0(1)-T_S3(1),...
[T0(2)-T_S3(2) T0(2)-T_S3(2) T0(2)+T_S3(2) T0(2)+T_S3(2) T0(2)-T_S3(2)],...
'm:')
hold off

%Plot Statistical 2sigma tolerance box
T_S2=2*sqrt(VAR_A);
T_S=T_S2;
hold on
plot([T0(1)-T_S(1) T0(1)+T_S(1) T0(1)+T_S(1) T0(1)-T_S(1) T0(1)-T_S(1),...
[T0(2)-T_S(2) T0(2)-T_S(2) T0(2)+T_S(2) T0(2)+T_S(2) T0(2)-T_S(2)],...
'm:')
hold off

%Plot Statistical 1sigma tolerance box
T_S1=sqrt(VAR_A);
T_S=T_S1;
hold on
plot([T0(1)-T_S(1) T0(1)+T_S(1) T0(1)+T_S(1) T0(1)-T_S(1) T0(1)-T_S(1),...
[T0(2)-T_S(2) T0(2)-T_S(2) T0(2)+T_S(2) T0(2)+T_S(2) T0(2)-T_S(2)],...
'm:')
hold off

specs=[T0,T_WC,T_S3,T_S2,T_S1];
save -ascii -tabs specs.txt specs
D1c=D1c';
save -ascii -tabs derivatives.txt D1c

```

## B.7 assyio\_2h4warp.m

```
%assyio_2h4warp
%8mil tolerance analysis
%Worst Case and Statistical Predictions for Dissertation
%
%
%This file provides the input and displays the output for assybuild.m
%The input is a 16 column matrix where each row describes a plate
%assybuild.m receives the plate matrix (plate) and returns the two-dimensional, shift-ready,
%matrix of points containing the coordinates of the final assembly.
%i.e. v1= [x1 x2 .... xn]
% [y1 y2 .... yn]
% [1 1 .... 1]
%Plate information, plate(1,:) is hinged to the nitride
%plate(i,:)=[length, shape, elnum, pstress, gstress, solcurv, temp, [hplay], sw1, angle, sw2, V, g, l, w]
% 1, 2, 3, 4, 5, 6, 7, 8, 9, 10, 11, 12, 13, 14,15,16
%*****
%length - Length of plate (micrometers)
%shape - 1=straight, 2=poly1 with internal stress, 3=poly2 with internal stress,
%        4=gold on poly2 with internal stress, 5=solder on poly2 exp observation of curvature
%elnum - Number of elements 0:length/elnum:length, 1 means a single beam composed
%       of a beggining point and an end point
%pstress- Stress in polysilicon: +curved up, -curved down (Pa)
%gstress- Stress in gold: +curved up, -curved down (Pa)
%solcurv- Radius of curvature of plate with solder: +curved up, -curved down (micrometer)
%temp - (temperature in celsius)
%[hplay]- Hinge play (micrometers) [x,y] coordinate of shift of this plate
%       with respect to end of previous plate
%sw1 - Switch: 1=allow hinge play to affect solder angle calculation only with sw2=1 also
%angle - Manual angle (radians) between this plate and previous plate when sw2=0
%sw2 - switch: 1=calculate equilibrium angle using plate(i, 12-16), 0=use angle
%V - Volume of solder (micron)^3
%g - Surface tension coefficient (Newton/microns) can be 1, not needed to find angle
%l - Height of solder plate (microns)
%w - Width of a solder plate (microns)

clear
set(0,'defaultaxesfontname','times new roman')
set(0,'defaultaxesfontsize',12)
%*****
%***Change these values for different angle combinations
data=load('warp9045_4.txt');
% l1 l2 w1 w2
scav=[0 8 0 13]; %subtract from nominal
tol=[2 8 8 13]; %+-
%scav=[0 0 0];
p1=69; %96,69,33
p2=96;
hingegap=5; %5 if p1 = 131 or 70, 8 if p1=217
gap=10; %does not change
%*** *** ***
%Define nominal dimensions
L=[500-hingegap 500]; %1,2 length of actual plates - substrate hinge gap(microns)
Ps=[-7.9e6]; %3 plain poly2 stress (Pa)
GPs=[103.5e6]; %4 stress of gold on poly
Src=[6000 6000 6000];%5,6,7 solder radius of curvature (microns) for each pad
x=[0,0 , 0,0]; %8,9,10,11 hinge position (microns)
D=[4.3878 4.3878]*25.4; %12,13 (microns) measured mean of solder balls
l=[p1-scav(1) p2-scav(2)]; %14,15 solder pad lengths (microns)
w=[p1-scav(3) p2-scav(4)]; %16,17 solder plate width (microns)
T=27; %18 temperature (degrees celsius)

Ndims=[L, Ps, GPs, Src, x, D, l, w, T];dims=Ndims; %Vectors of nominal dimensions
%vector of tolerance values corresponding to Nomdim
tol=[2 2 2.82e6 21e6 1000 1000 1000 .5 .5 .5 .5 0.4491*25.4 0.4491*25.4 tol 6];tol=abs(tol);
typval=Ndims;typval(8:11)=[1 1 1 1];del=sqrt(eps)*typval;%typical values for finite differences
```

```

%Define the plates of the assembly, plate(1,:) is hinged to the nitride
%plate(i,:)=[length, shape, elnum, pstress, gstress, solcurv, temp, [hplay], sw1, angle, sw2, V, g, l, w]
%   1, 2, 3, 4, 5, 6, 7, 8, 9, 10, 11, 12, 13, 14, 15, 16
plate(1,:)=[hingegap, 1, 1, 0, 0, 0, dims(18), dims(8:9), 0, 0, 1, 4/3*pi*(dims(12)/2)^3, 1, dims(14),
dims(16)];%hingegap and angle
plate(2,:)=[dims(14), 5, 50, 0, 0, dims(5), dims(18), [0,0], 0, pi, 0, 0, 1, 0, 0]; %plate1 pad1
plate(3,:)=[gap, 3, 10, dims(3), 0, 0, dims(18), [0,0], 0, pi, 0, 0, 1, 0, 0]; %gap1 poly2 only
plate(4,:)=[dims(1)-dims(14)-dims(15)-2*gap, 4, 100, dims(3), dims(4), 0, dims(18), [0,0], 0, pi, 0, 0, 1, 0, 0];%gold on
poly
plate(5,:)=[gap, 3, 10, dims(3), 0, 0, dims(18), [0,0], 0, pi, 0, 0, 1, 0, 0]; %gap2 poly2 only
plate(6,:)=[dims(15), 5, 50, 0, 0, dims(6), dims(18), [0,0], 0, pi, 0, 0, 1, 0, 0]; %plate1 pad2
plate(7,:)=[dims(15), 5, 50, 0, 0, dims(7), dims(18), dims(10:11), 0, 0, 1, 4/3*pi*(dims(13)/2)^3, 1, dims(15),
dims(17)];%plate2 pad1
plate(8,:)=[gap, 3, 10, dims(3), 0, 0, dims(18), [0,0], 0, pi, 0, 0, 1, 0, 0]; %gap3 poly2 only
plate(9,:)=[dims(2)-dims(15)-gap, 4, 100, dims(3), dims(4), 0, dims(18), [0,0], 0, pi, 0, 0, 1, 0, 0]; %plate2 gold
on poly
Nplate=plate;
psize=size(plate);

***** OUTPUT *****
%Get the nominal assembly shape
v=assybuild(Nplate);
[m,n]=size(v);
T0=v(1:2,n);

%Use this to plot each segment individually
in1=1;
for i=1:psize(1)
    plot(v(1,in1:in1+plate(i,3)),v(2,in1:in1+plate(i,3)),'Color',[0 rem(i,2) == 0 1])
    in1=in1+plate(i,3)+1;
    hold on
end
plot(T0(1),T0(2),'co')
xlabel('x (microns)')
ylabel('y (microns)')

%Plot data
plot(data(1,:), data(2,:),'r')
hold off
axis equal

%Calculate first partial derivatives (central)
%Where D1c is the derivative matrix D1c=[df/dx1', df/dx2', ..., df/dxn']
for i=1:length(Ndims)
    dims=Ndims;
    dims(i)=Ndims(i)+del(i)/2;
    plate(1,:)=hingegap, 1, 1, 0, 0, 0, dims(18), dims(8:9), 0, 0, 1, 4/3*pi*(dims(12)/2)^3, 1, dims(14),
dims(16));%hingegap and angle
    plate(2,:)=[dims(14), 5, 50, 0, 0, dims(5), dims(18), [0,0], 0, pi, 0, 0, 1, 0, 0]; %plate1 pad1
    plate(3,:)=[gap, 3, 10, dims(3), 0, 0, dims(18), [0,0], 0, pi, 0, 0, 1, 0, 0]; %gap1 poly2 only
    plate(4,:)=[dims(1)-dims(14)-dims(15)-2*gap, 4, 100, dims(3), dims(4), 0, dims(18), [0,0], 0, pi, 0, 0, 1, 0, 0];%gold on
poly
    plate(5,:)=[gap, 3, 10, dims(3), 0, 0, dims(18), [0,0], 0, pi, 0, 0, 1, 0, 0]; %gap2 poly2 only
    plate(6,:)=[dims(15), 5, 50, 0, 0, dims(6), dims(18), [0,0], 0, pi, 0, 0, 1, 0, 0]; %plate1 pad2
    plate(7,:)=[dims(15), 5, 50, 0, 0, dims(7), dims(18), dims(10:11), 0, 0, 1, 4/3*pi*(dims(13)/2)^3, 1, dims(15),
dims(17)];%plate2 pad1
    plate(8,:)=[gap, 3, 10, dims(3), 0, 0, dims(18), [0,0], 0, pi, 0, 0, 1, 0, 0]; %gap3 poly2 only
    plate(9,:)=[dims(2)-dims(15)-gap, 4, 100, dims(3), dims(4), 0, dims(18), [0,0], 0, pi, 0, 0, 1, 0, 0]; %plate2 gold
on poly
    vr=assybuild(plate);
    dims(i)=Ndims(i)-del(i)/2;
    plate(1,:)=hingegap, 1, 1, 0, 0, 0, dims(18), dims(8:9), 0, 0, 1, 4/3*pi*(dims(12)/2)^3, 1, dims(14),
dims(16));%hingegap and angle
    plate(2,:)=[dims(14), 5, 50, 0, 0, dims(5), dims(18), [0,0], 0, pi, 0, 0, 1, 0, 0]; %plate1 pad1
    plate(3,:)=[gap, 3, 10, dims(3), 0, 0, dims(18), [0,0], 0, pi, 0, 0, 1, 0, 0]; %gap1 poly2 only
    plate(4,:)=[dims(1)-dims(14)-dims(15)-2*gap, 4, 100, dims(3), dims(4), 0, dims(18), [0,0], 0, pi, 0, 0, 1, 0, 0];%gold on
poly
    plate(5,:)=[gap, 3, 10, dims(3), 0, 0, dims(18), [0,0], 0, pi, 0, 0, 1, 0, 0]; %gap2 poly2 only
    plate(6,:)=[dims(15), 5, 50, 0, 0, dims(6), dims(18), [0,0], 0, pi, 0, 0, 1, 0, 0]; %plate1 pad2

```

```

plate(7,:)=[dims(15), 5, 50, 0, 0, dims(7), dims(18), dims(10:11), 0, 0, 1, 4/3*pi*(dims(13)/2)^3, 1, dims(15),
dims(17)];%plate2 pad1
plate(8,:)=[gap, 3, 10, dims(3), 0, 0, dims(18), [0,0], 0, pi, 0, 0, 1, 0, 0]; %gap3 poly2 only
plate(9,:)=[dims(2)-dims(15)-gap, 4, 100, dims(3), dims(4), 0, dims(18), [0,0], 0, pi, 0, 0, 1, 0, 0]; %plate2 gold
on poly
    vl=assybuild(plate);
    D1c(:,i)=(vr(1:2,n)-vl(1:2,n))/del(i);
end

%Find Worst Case tolerance analysis with central derivatives
T_WC=0;
for i=1:length(tol)
    T_WC = T_WC + tol(i)*abs(D1c(:,i));
end

%Calculate standard deviation of variables
sd=tol/3;

%Calculate standard deviation and mean for assembly
%MEAN_A=T0+1/2*D2c*(sd.^2)
for i=1:length(tol)
    COV(i,i)=sd(i)^2;
end
VAR_A=[D1c(1,:)*COV*D1c(1,:)'; D1c(2,:)*COV*D1c(2,:)'];

%Plot worst case box
hold on
plot([T0(1)-T_WC(1) T0(1)+T_WC(1) T0(1)+T_WC(1) T0(1)-T_WC(1) T0(1)-T_WC(1),...
[T0(2)-T_WC(2) T0(2)-T_WC(2) T0(2)+T_WC(2) T0(2)+T_WC(2) T0(2)-T_WC(2)],...
'g-')
hold off

%Plot Statistical 3sigma tolerance box
T_S3=3*sqrt(VAR_A);
hold on
plot([T0(1)-T_S3(1) T0(1)+T_S3(1) T0(1)+T_S3(1) T0(1)-T_S3(1) T0(1)-T_S3(1),...
[T0(2)-T_S3(2) T0(2)-T_S3(2) T0(2)+T_S3(2) T0(2)+T_S3(2) T0(2)-T_S3(2)],...
'm:')
hold off

%Plot Statistical 2sigma tolerance box
T_S2=2*sqrt(VAR_A);
T_S=T_S2;
hold on
plot([T0(1)-T_S(1) T0(1)+T_S(1) T0(1)+T_S(1) T0(1)-T_S(1) T0(1)-T_S(1),...
[T0(2)-T_S(2) T0(2)-T_S(2) T0(2)+T_S(2) T0(2)+T_S(2) T0(2)-T_S(2)],...
'm:')
hold off

%Plot Statistical 1sigma tolerance box
T_S1=sqrt(VAR_A);
T_S=T_S1;
hold on
plot([T0(1)-T_S(1) T0(1)+T_S(1) T0(1)+T_S(1) T0(1)-T_S(1) T0(1)-T_S(1),...
[T0(2)-T_S(2) T0(2)-T_S(2) T0(2)+T_S(2) T0(2)+T_S(2) T0(2)-T_S(2)],...
'm:')
hold off

specs=[T0,T_WC,T_S3,T_S2,T_S1];
save -ascii -tabs specs.txt specs
D1c=D1c';
save -ascii -tabs derivatives.txt D1c

```

## **Appendix C Selected Published Papers**

The papers presented in this appendix have been left in identical form and content as published in the proceedings or journals.

### **C.1 Solder Angle Modeling**

P. E. Kladitis, K. F. Harsh, V. M. Bright, and Y. C. Lee, "Three-Dimensional Modeling of Solder Shape for the Design of Solder Self-Assembled Micro-electro-mechanical Systems," *Proc. 1999 ASME International Mechanical Engineering Congress and Exposition MEMS Symposium*, Nashville, TN, MEMS-Vol. 1, pp. 11-18, Nov. 1999.

# Three-Dimensional Modeling of Solder Shape for the Design of Solder Self-Assembled Micro-electro-mechanical Systems

Paul E. Kladitis, Kevin F. Harsh, Victor M. Bright, and Y. C. Lee

NSF Center for Advanced Manufacturing and Packaging of Microwave, Optical, and Digital  
Electronics

Department of Mechanical Engineering, University of Colorado, Boulder, CO 80309-0427, USA.

Tel: (303) 735-1734, Fax: (303) 492-3498, e-mail: victor.bright@colorado.edu

## ABSTRACT

Micro-electro-mechanical systems (MEMS) can be assembled by harnessing the surface tension of liquid solder. In order to assemble the MEMS to precise positions, the shape of the solder, of a given volume, must be known. This paper presents two methods of modeling the shape of solder wetted between two MEMS plates. One method accurately models the solder shape by finding the minimum surface energy shape. A second, less accurate but faster, method approximates the solder shape using simple geometric shapes. The geometric shape model can be trained to be just as accurate as the minimum surface energy model.

## INTRODUCTION

Currently there exists no practical method to mass assemble complex three-dimensional micro-electro-mechanical systems (MEMS). Harnessing the surface tension of molten solder to assemble MEMS, also known as "solder assembly," promises to make possible a reliable and practical method of mass assembly for MEMS.

Solder assembly is a powerful and compact method for providing actuation, eliminating the need for thermal or electrostatic assembly schemes that usually take up more chip real-estate than the assembled device. Solder assembly requires no external electrical control lines that also take up chip real-estate nor does solder assembly require impractical actuation voltages. The resulting solder joints in solder assembly also serve as robust low resistance electrical and mechanically rigid connections.

Solder can be strategically deposited on MEMS as part of the fabrication process. Subsequently, the MEMS can be mass assembled in one quick solder reflow step. The deposited volume of solder controls the angle to which liquid solder rotates microstructures. To use solder assembly for MEMS, one must be able to predict the equilibrium shape of solder during the reflow process, hence this work.

Two three-dimensional methods of modeling solder shape are presented in this paper. The first method uses *The Surface Evolver* (Brakke, 1995) to accurately find the minimum surface energy solder shape. However, this method requires several hours of computational time. A second method, inspired by the work of Syms (1995), requiring computation times of less than a second, but less accurate, approximates the solder shape with simple three-dimensional geometric shapes. The geometric shape approximation can be trained to *Surface Evolver* predictions or experimental data yielding an accurate and fast designer's tool for predicting solder shape. Furthermore, both methods are compared with experimental data and compared against each other. All microstructures presented in this paper are fabricated, prior to solder deposition and assembly, using

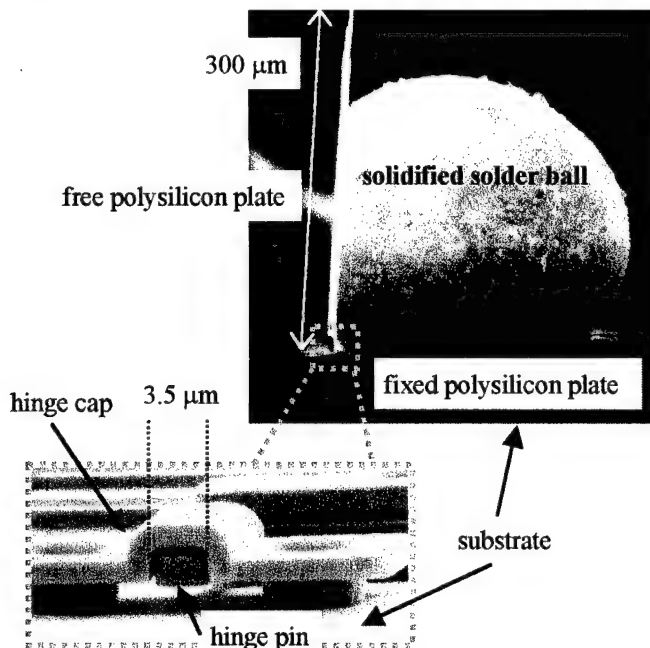
## NOMENCLATURE

$\cos$	cosine	$m$	meter	$T_{ST}$	torque on the free plate from the surface tension of the solder (Newton-meters)
$f$	a function	$\text{mil}$	$1 \times 10^{-3}$ inches	$T_{NET}$	net torque (Newton-meters)
$F$	surface tension force at the solder-MEMS plate interface (Newtons)	$N$	Newtons	$V$	volume of the solder (meters <sup>3</sup> )
$F_1$	surface tension force at the solder-MEMS plate interface along the width edge (N)	$P$	internal pressure of solder joint (Pascals)	$w$	width of MEMS plate (meters)
$F_2$	surface tension force at the solder-MEMS plate interface along a length edge (N)	$Pb$	lead	$x, y, z$	Cartesian reference axes
$g$	acceleration of gravity (meters/second <sup>2</sup> )	$R$	radius of curvature of solder shape	$\alpha$	angle between MEMS plates
$h$	height measured from top of solder joint (meters)	$R_x$	radius of curvature in the xz plane	$\beta$	angle of curvature of solder shape
$kg$	$1 \times 10^3$ grams	$R_y$	radius of curvature in the yz plane	$\gamma$	surface tension coefficient of solder (Newtons/meter)
$l$	length of MEMS plate (meters)	$\sin$	sine	$\mu$	$1 \times 10^{-6}$
		$\text{Sn}$	tin	$\pi$	pi (3.14...)
		$T_P$	torque on the free plate from the internal pressure of the solder (Newton-meters)	$\rho$	density of solder (kilograms/meter <sup>3</sup> )
				$^\circ$	degrees
				$\infty$	infinity

a commercially available polycrystalline silicon surface micromachining process: the Multi-User MEMS Process (MUMPs) by MCNC (Koester et al., 1996).

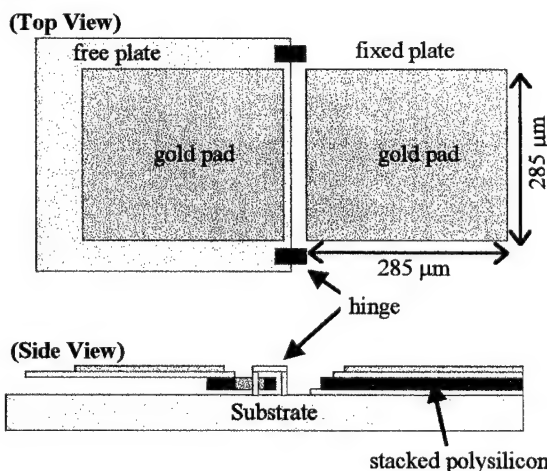
### DESCRIPTION OF SOLDER ASSEMBLY

Figure 1 shows a scanning electron micrograph (SEM) of the basic element of solder assembly: the side view of a solidified solder joint wetted between two gold coated polycrystalline silicon (polysilicon) plates, or MEMS plates. One plate is fixed to the substrate, while another plate of equal size is free to rotate about hinges adjacent to the fixed plate. Figure 1 also shows a close up of the type of hinge used to allow the free plate to rotate.



**Figure 1:** SEM of the side view of a solidified solder joint wetted between two gold-coated polysilicon plates and a close view of a hinge.

The free plate was initially lying parallel to the substrate, with a fixed volume of solder, placed on top of, and across both plates. The tops of the plates are coated with a  $0.5 \mu\text{m}$  thick layer of gold. The substrate was subsequently heated to the melting temperature of the solder, the solder wetted to the gold coating of the plates, and the surface tension forces of the solder raised the free plate into the position shown in Figure 1. Finally, the substrate is allowed to cool, solidifying the solder. Figure 2 is a drawing of a polysilicon solder-wettable plate pair.



**Figure 2:** Drawing of a polysilicon solder-wettable plate pair.

Known volumes of solder can be placed on the wettable plates as commercially available ball grid array (BGA) solder spheres or deposited and patterned using standard metal lift-off techniques. The volume of solder will determine the final resting angle, or equilibrium angle, between the two plates. The solder wettable plates can be attached to larger structures and be used to rotate, or assemble, the larger structures.

Both modeling methods presented in this paper assume perfect wetting of the solder to the gold surface, an incompressible solder material, constant material properties of the solder, rigid plates, and the weight of the plates and solder is negligible.

It is helpful to keep in mind the following question when reading the remainder of this paper. Given a set of MEMS plates with gold-coated solder wettable areas of certain dimensions, and certain volume of solder on the wettable areas, what “equilibrium angle” will the plates make with each other after reflow of the solder? The following sections present two different methods for determining that “equilibrium angle.”

### SOLDER SHAPE MODELING BY FINDING THE MINIMUM SURFACE ENERGY

The basis of the model presented in this section is the known tendency of liquids to minimize their surface energy. Henceforth, this model will be referred to as the “surface energy minimization model.” Given a set of constraints (wetted area, solder volume, solder density, and molten solder surface tension coefficient), if the precise shape of the molten solder for a range of angles between plates can be calculated, then the corresponding surface energies can be calculated. These energies can then be compared to each other to find the angle between the plates where the surface energy is at a minimum. This angle will be the equilibrium position of the free hinged plate. Harsh and Lee (1998) give additional information on this model.

The surface energy minimization model can be broken into two steps. The first step is to precisely model the shape of the molten solder wetted between the two plates at a fixed angle. For this shape prediction, an existing software called *The Surface Evolver* (Brakke, 1995) is used. The *Surface Evolver* public domain software, is a very powerful tool for studying surface tension-defined shapes (Lin et al., 1995). By generating an initial, user-defined surface based on wetted area, solder volume, and plate geometry, the program can then evolve the surface toward a minimum surface energy profile, which we will call a “local minimum surface energy.”

Numerically, *Surface Evolver* uses a gradient decent on a space of admissible surfaces to try to find a local minimum of the energy function. Therefore, solder shape at a given rotation angle is defined by surface energy minimization. An example of finding the minimized surface solder shape from an initial guess shape is shown in Figure 3.

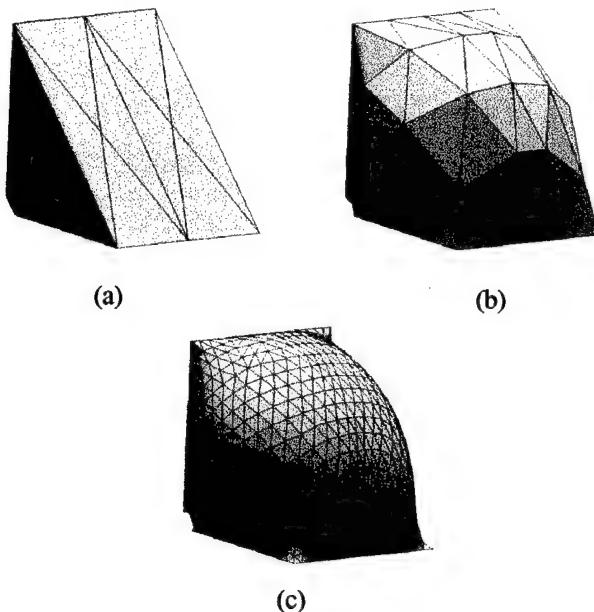


**Figure 3:** Example of finding the minimized surface solder shape from an initial guess shape using *Surface Evolver*. (a) Initial, user-generated solder shape, (b) intermediate calculated solder shape after several iterations, (c) final converged solder shape.

Figure 3(a) shows an initial solder shape input to *Surface Evolver* defined at a plate angle of 90°. This initial shape does not need to closely approximate the final shape as long as the constraints are set appropriately (wetted area, solder volume, solder surface tension coefficient, and solder density). Figure 3(b) shows the same surface after an evolution of several iterations to a lower surface energy shape. After additional iterations until an acceptable convergence of the calculated value of surface energy is reached, the final energy-minimized shape calculated by *Surface Evolver* is shown in Figure 3(c).

The second step is to use the *Surface Evolver* predictions to gauge the equilibrium angle, from a range of angles between plates, for a fixed volume of solder. At each given angle between plates, *Surface Evolver* calculates the stable shape and its corresponding local minimum surface energy. When the local minimum surface energies for the range of angles are compared against each other, a global minimum surface energy can be identified, therefore, the equilibrium angle is found.

For example, Figure 4 presents the surface area (surface energy / surface tension coefficient) of two different solder volumes, as a function of plate angle, wetted between 285 μm by 285 μm plates. With reference to Figure 4, the top and bottom plots correspond to volumes of solder equivalent to 14 mil ( $2.35 \times 10^{-11} \text{ m}^3$ ) and 12 mil ( $1.48 \times 10^{-11} \text{ m}^3$ ) diameter spheres, respectively. The final shapes with plate angles of 72.2° and 64.3° are identified as the minimum global surface energy shapes. Thus, 72.2° and 64.3° are the equilibrium angles.

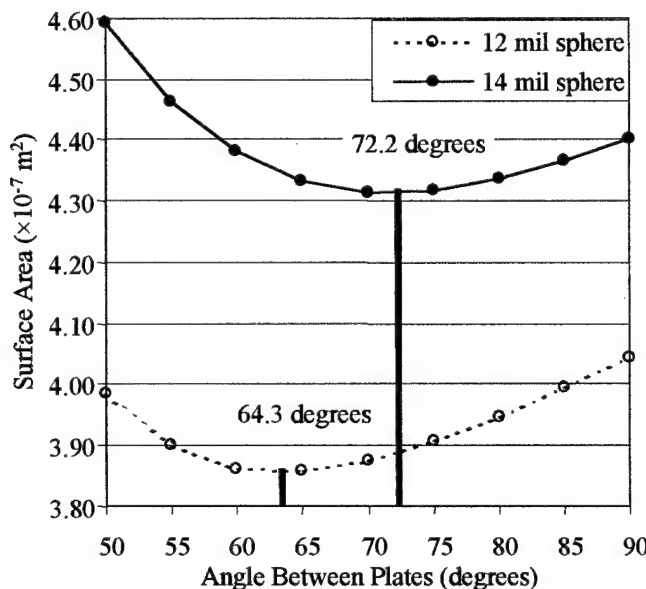


**Figure 4:** Example of surface area of two different solder volumes as a function of plate angle showing locations of minimum global surface energies.

#### CONFIRMATION OF THE SURFACE ENERGY MINIMIZATION MODEL WITH EXPERIMENTAL DATA

As a verification of the surface energy minimization model, a range of solder volumes was used to assemble polysilicon plates, and the resulting equilibrium angles of the plates were measured. Three sets of plates with gold wettable pads (285 x 285 μm), as shown in Figures 1 and 2, were assembled at each of five different solder volumes: 0.439, 0.879, 1.318, 1.757, and  $2.197 \times 10^{-11} \text{ m}^3$ . The solder volumes were constructed from eutectic 63Sn/37Pb solder spheres manufactured by the Indium Corporation. The manufactured diameters ranged from 4 mil (101.6 μm) to 16 mil (406.4 μm) with a manufacturer specified tolerance of ±1 mil ( $\pm 25.4 \mu\text{m}$ ).

The process for assembling the MEMS involves placing the solder spheres onto the gold plated pads on the MEMS plates. The solder was subsequently reflowed at its melting temperature using a fluxless soldering process developed for optoelectronic packaging (Tan and Lee, 1996). After the MEMS devices were assembled, the angle of the plate was measured. The method employed was to take a SEM of the assembled MEMS and then expand the picture to a larger size. The equilibrium angles between the plates were measured directly from the expanded picture.

Comparisons of the surface energy minimization model predictions with the final angular positions of the actual plates, for a given solder volume, are shown in Figure 5. The equilibrium angle measurements taken from the three sets of plates, described above, are averaged together in Figure 5.

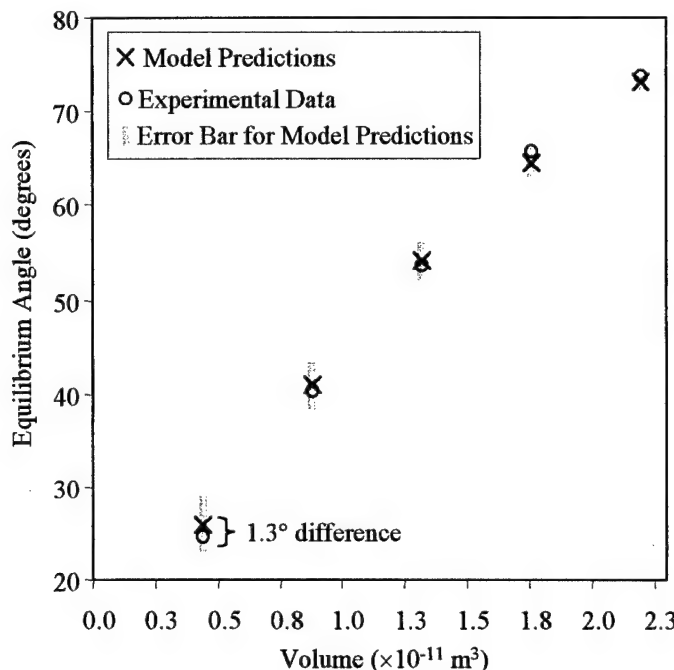


**Figure 5:** Comparisons of the surface energy minimization model predictions with the experimentally measured angular positions of the MEMS plates.

The error bars, in Figure 5, represent the calculated equilibrium angle sensitivity to the manufacturer-specified  $\pm 1$  mil variation in the solder sphere diameter. The equilibrium angle sensitivity was calculated using surface energy minimization model. The experimental errors resulting from solder volume variation, as estimated by the model, are between  $\pm 3^\circ$  for the smallest volume ( $0.439 \times 10^{-11} \text{ m}^3$ ), and  $\pm 0.8^\circ$  for the largest volume ( $2.197 \times 10^{-11} \text{ m}^3$ ). The maximum difference between the model predictions and averaged experimental data is  $1.3^\circ$  as shown in Figure 5.

Finding the equilibrium angle for a certain size set of plates and a certain volume of solder using the *Surface Evolver* method takes several hours of computation time using a 500 MHz DEC-alpha processor. A second, less accurate method of predicting the equilibrium angle, with computation times of less than a second, is presented in the next section.

### SOLDER SHAPE MODELING USING GEOMETRIC SHAPE APPROXIMATION

A second method of predicting the equilibrium angle employs simple, three-dimensional geometric shapes for representing the volume and shape of a molten solder joint wetted between two plates. Henceforth, this model will be referred to as the “geometric shape approximation model.” The three-dimensional geometric shape approximation model is based on net torque equilibrium of the internal pressure of a liquid and the surface tension forces. This model is inspired by the two-dimensional model presented by Syms (1995).

The geometric shape approximation model is constructed from two equations:

1. A three dimensional torque balance equation between internal pressure and surface tension force of a solder joint between two plates, and
2. An equation relating the initial deposited volume of solder to the total volume of the three-dimensional geometric shapes that collectively represent the volume of the liquid solder wetted between the two MEMS plates.

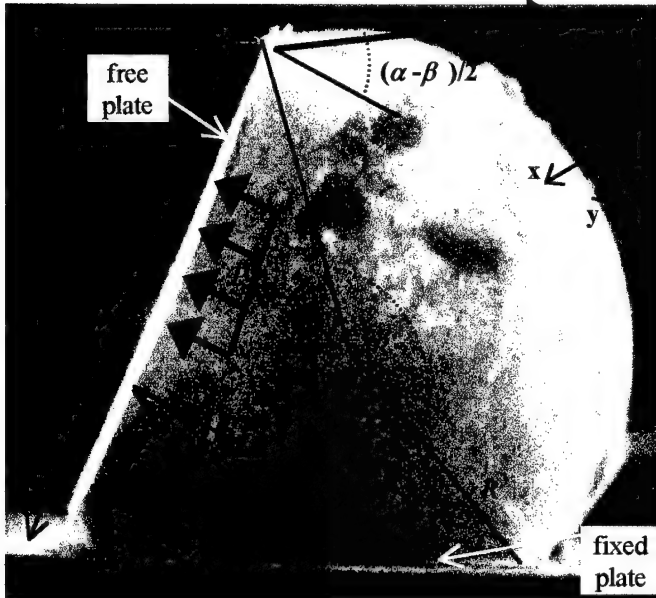
This model further assumes that the internal pressure of the solder can be represented by hydrostatic pressure and a pressure described by the curvature of the solder surface. Approximating the shape of the solder is necessary in order to derive the curvature of the solder surface.

Figure 6 shows a SEM of a solder joint between two polysilicon plates labeled with the parameters used in the following development of the model. Please refer to this figure for the remainder of this discussion.

The difference in pressure ( $P$ ) from within the solder droplet to the surroundings can be described by (Batchelor, 1967):

$$P = \rho gh - \gamma \left( \frac{\partial^2 z}{\partial x^2} + \frac{\partial^2 z}{\partial y^2} \right) = \rho gh - \gamma \left( \frac{1}{R_x} + \frac{1}{R_y} \right) \quad (1)$$

where,  $\rho$  is the density of the solder,  $g$  is acceleration due to gravity,  $h$  is height measured from the top of the solder droplet,  $\gamma$  is coefficient of surface tension of the solder,  $R_x$  is the radius of curvature of the solder surface in the  $xz$ -plane, and  $R_y$  is the radius of curvature of the solder surface in the  $yz$ -plane.



**Figure 6:** SEM of a solder joint between two polysilicon plates with important design parameters used in the development of the geometric shape approximation model.

Note that the curvature of the solder surface will be negative because of the orientation of the reference axes in Figure 6. Also, the hydrostatic pressure term,  $\rho gh$ , can be neglected in this analysis, but is retained for completeness. If we model the solder volume as a cylindrical shape, then  $R_x = \infty$  and  $R = R_y$ . If we model the solder volume as a spherical shape, then  $R = R_x = R_y$ . The radius of curvature is related to the angle between the plates ( $\alpha$ ) and the angle of curvature ( $\beta$ ) by:

$$R = \frac{l \sin(\alpha / 2)}{\sin(\beta / 2)} \quad (2)$$

The total surface tension force ( $F$ ) acting normal to the free plate's surface at the top horizontal edge ( $F_1$ ) and along the edge ( $F_2$ ) of both vertical sides is (refer to Figure 6):

$$F = F_1 + 2F_2 = (\gamma w + 2\gamma l) \cos[(\alpha - \beta)/2] \quad (3)$$

where,  $w$  is the width of a plate (into the page),  $l$  is the length of the plate, and  $(\alpha - \beta)/2$  is the contact angle of the solder surface with the plate.

The torque on the free plate due to the internal pressure of the solder, assuming a spherical solder shape ( $T_P$ ), is shown in Equations (4).  $T_P$  is found by integrating  $P$ , from Equation (1), times the moment arm, over the surface area of the free plate:

$$T_P = (1/6)\rho g w l^3 \sin\alpha + wl^2\gamma/R \quad (4)$$

The torque on the free plate due to the surface tension force ( $T_{ST}$ ) is found by integrating  $F$ , from Equation (3), times the moment arm, along the perimeter of the free plate:

$$T_{ST} = (\gamma wl + \gamma l^2) \cos[(\alpha - \beta)/2] \quad (5)$$

The net torque on the free plate ( $T_{NET}$ ) is given in Equation (6):

$$T_{NET} = T_{ST} - T_P = (\gamma wl + \gamma l^2) \cos[(\alpha - \beta)/2] - (1/6)\rho g w l^3 \sin\alpha - wl^2\gamma/R \quad (6)$$

Finally, the volume and shape of the solder may be modeled in several different ways. During the rotation of the plate by the liquid solder, the shape of the solder must be such that the volume of the solder at any point during the rotation must be equal to the initial deposited volume of solder ( $V$ ), therefore:

$$V = f(\alpha, \beta, R) \quad (7)$$

Substituting Equation (2) into Equations (6) and (7) yields two equations with four unknowns ( $\alpha$ ,  $\beta$ ,  $V$ , and  $T_{NET}$ ) that can be solved numerically given two of the unknowns. The plate dimensions,  $l$  and  $w$ , can also be unknowns, but are assumed to be known for this discussion.

One model may be found by approximating the volume and shape of the solder joint by the volume of a wedge, a slice of a sphere, and conic side lobes, as illustrated in Figure 7.

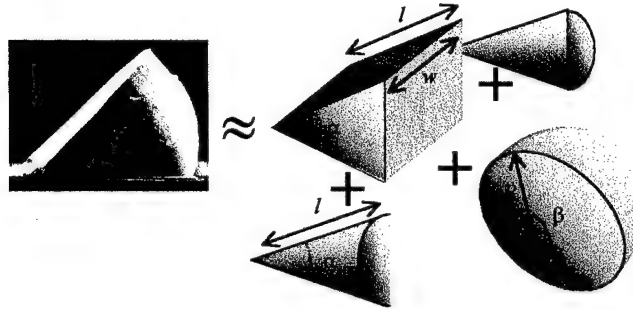


**Figure 7:** Illustration of the approximation of the volume of a solder joint by a wedge, a slice of sphere, and conic side lobes.

Equation (7) then becomes:

$$V = (1/2)wl^2 \sin\alpha + (2/3)\pi R^3 [1 - (3/2)\cos(\beta/2) + (1/2)\cos^3(\beta/2)] + (\pi/3)l^3 [\cos(\alpha/2) - \cos(\alpha/2)^3] \quad (8)$$

Substituting Equation (2) into (8) yields:

$$V = (1/2)wl^2 \sin\alpha + (2/3)\pi l^3 \sin^3(\alpha/2) [1 - (3/2)\cos(\beta/2) + (1/2)\cos^3(\beta/2)] / \sin^3(\beta/2) + (\pi/3)l^3 [\cos(\alpha/2) - \cos(\alpha/2)^3] \quad (9)$$

After eliminating  $R$  in Equation (6), Equations (6) and (9) can be solved numerically for  $\alpha$  and  $\beta$  when  $V$  and  $T_{NET}$  are specified. With  $V$  specified with a specific volume of solder and  $T_{NET} = 0$ , solving for  $\alpha$  yields the equilibrium angle.

### CONFIRMATION OF THE GEOMETRIC SHAPE APPROXIMATION MODEL WITH EXPERIMENTAL DATA

The same plate dimensions ( $l = 285 \mu\text{m}$  and  $w = 285 \mu\text{m}$ ) and solder volumes ( $V = 0.439, 0.879, 1.318, 1.757$ , and  $2.197 \times 10^{-11} \text{ m}^3$ ) used to confirm the surface energy minimization model can be used as inputs to the geometric shape approximation model. Solving for the equilibrium angle using the geometric shape

approximation model and comparing the results to the measured data from Figure 5 yields the plot in Figure 8. The maximum difference between the model predictions and averaged experimental data is  $5.9^\circ$  as shown in Figure 8.

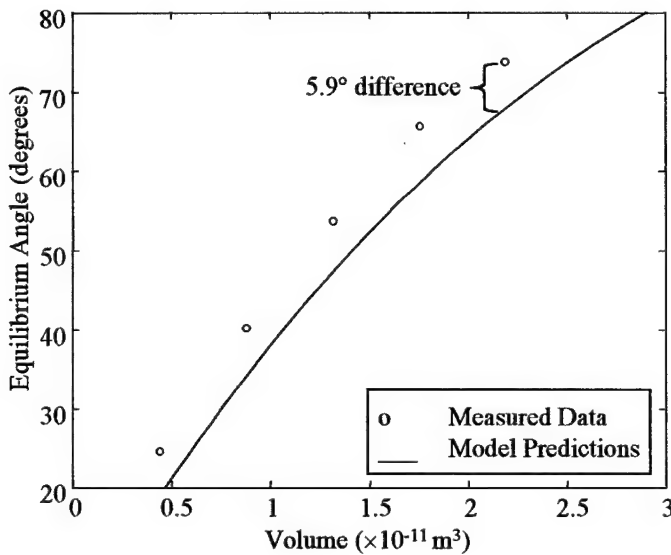


**Figure 8:** Comparison of geometric shape approximation model predictions with experimentally measured data.

Since Equation (9) is an approximation of the solder volume and shape, it can be scaled or trained to refine the approximation. By trial and error, a scaling factor of 0.7 was found that brings the predictions into very close agreement with the measured data. Figure 9 shows the comparison between the trained geometric shape approximation model predictions and experimentally measured data and surface energy minimization model predictions.

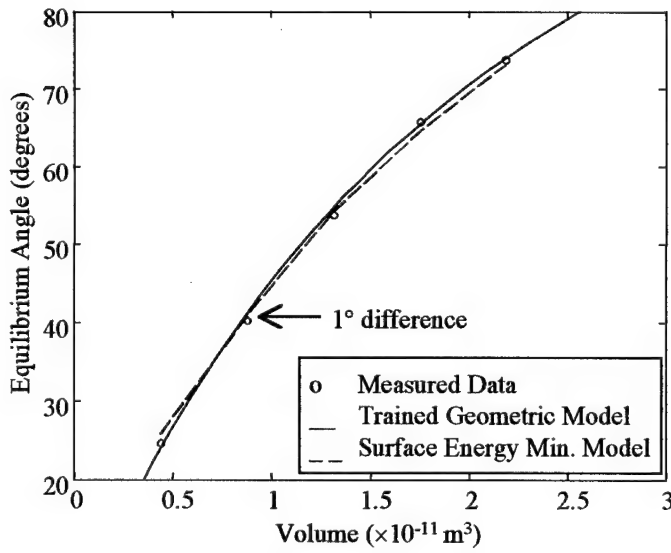


**Figure 9:** Comparison of trained geometric shape approximation model predictions with experimentally measured data and surface energy minimization model predictions.

The scaled model used is given in Equation (10):

$$V = 0.7 \left( \frac{1}{2}wl^2 \sin\alpha + \frac{2}{3}\pi l^3 \sin^3(\alpha/2) [1 - (3/2)\cos(\beta/2) + (1/2)\cos^3(\beta/2)]/\sin^3(\beta/2) + (\pi/3)l^3 [\cos(\alpha/2) - \cos(\alpha/2)^3] \right) \quad (10)$$

where the volume of the wedge shape is scaled by 0.7. For square pads,  $w = l$ , Equation 10 can be solved in terms of dimensionless volume by factoring out the  $l^3$  term.

The ability to non-dimensionalize Equation 10 suggests that the trained geometric shape approximation model should be able to make good equilibrium angle predictions for any square plate dimensions. The trained model results in a powerful equilibrium angle predicting tool that has the accuracy of the surface energy minimization model but computation time of less than a second (0.05 seconds on a 400 MHz Pentium II processor). Figure 10 is a plot of useful assembly angles versus dimensionless volume.

To support the idea that the trained geometric shape approximation model will make acceptable predictions for different size square plates, the surface energy minimization model was used to calculate the equilibrium angle for different solder volumes wetted to  $25 \mu\text{m} \times 25 \mu\text{m}$  plates. Both model predictions are plotted in Figure 11. The maximum difference between the models is  $5^\circ$ .

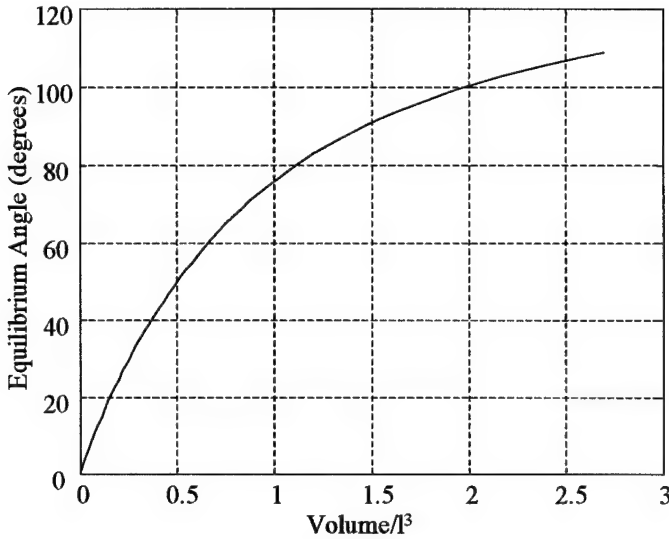


**Figure 10:** Plot of useful assembly angles versus dimensionless volume using the trained geometric shape approximation model.

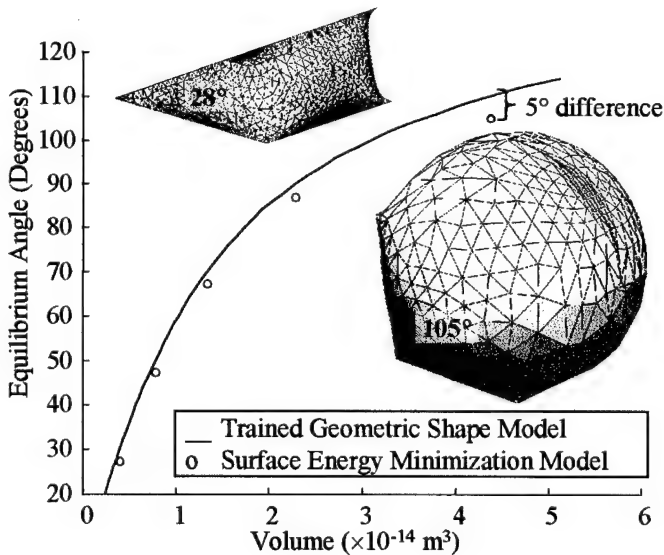


**Figure 11:** Comparison of trained geometric shape approximation model with the surface energy minimization model predictions of equilibrium angle for different solder volumes wetted to  $25 \mu\text{m} \times 25 \mu\text{m}$  plates. Inserts show solder shapes predicted by *Surface Evolver* for volumes of solder resulting in equilibrium angles of  $28^\circ$  and  $105^\circ$ .

When solving only for the necessary volume needed to reach a certain equilibrium angle, and the hydrostatic pressure term in Equation 6 is negligible, the exact value of the surface tension coefficient is not needed. When  $T_{NET} = 0$ ,  $\gamma$  can be factored out of Equation 6. Only when a torque prediction is important does one need to know accurate material properties such as surface tension coefficient. The exact value of density ( $\rho$ ) is not critical either unless the physical dimensions become large enough so that hydrostatic pressure is no longer negligible. Figure 12 compares the net torque predictions for both models with a volume of indium ( $2.2824 \times 10^{-14} \text{ m}^3$ ) wetted between  $25 \mu\text{m} \times 25 \mu\text{m}$  plates as the angle between the plates changes from  $45^\circ$  to

180°. The equilibrium angle for this volume and plate size is approximately 90°, as shown in Figure 12 where the net torque is zero.

The net torque was approximated from the surface energy minimization model's predictions of surface energy by finding the change in surface energy per change in plate angle. The trained geometric shape approximation model solves for the net torque directly from Equations (6) and (10). The material properties for pure indium, used for the net torque predictions, are:  $\gamma = 0.559 \text{ N/m}$  and  $\rho = 7310 \text{ kg/m}^3$ .

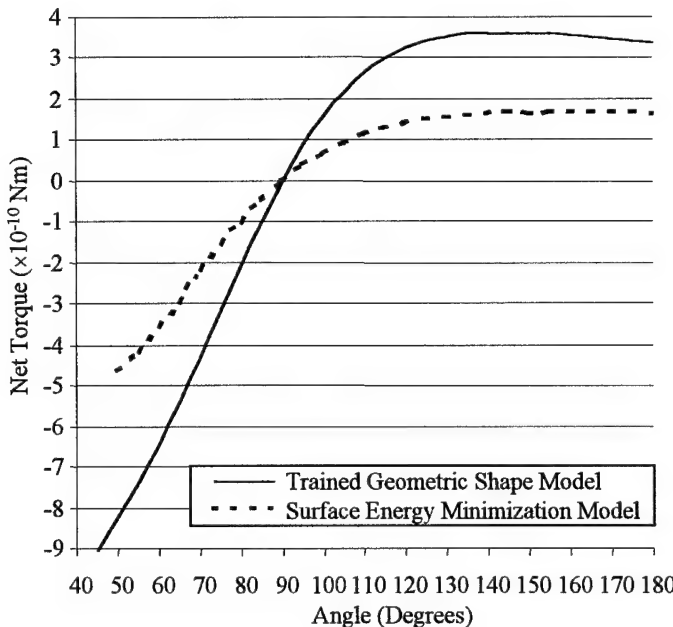


**Figure 12:** Comparison of trained geometric shape approximation model with the surface energy minimization model predictions of net torque for a volume of indium ( $2.2824 \times 10^{-14} \text{ m}^3$ ) wetted between  $25 \mu\text{m} \times 25 \mu\text{m}$  plates.

## CONCLUSIONS

Two methods of modeling the shape of solder wetted between two MEMS plates in order to determine the equilibrium angle between the plates for a given volume of solder were presented in this paper. The surface energy minimization model is very accurate, however, requires long computation times. The geometric shape approximation model has a very fast computation time, however, is not as accurate as the surface energy minimization model.

The geometric shape approximation model can be trained to experimental data to yield an accurate and fast method of determining the equilibrium angle. This model is thus useful as a real-time tool when designing solder self-assembled MEMS. Both the surface energy minimization and geometric shape approximation models can also be used to predict the torque on the free plate – useful for incorporating externally applied moments that may be part of the assembled MEMS design.

## ACKNOWLEDGEMENTS

Effort sponsored by the Defense Advanced Research Projects Agency (DARPA) and Air Force Research Laboratory, Air Force Materiel Command, USAF, under agreement number F30602-98-1-0219.

## REFERENCES

- Brakke K. A., June 1, 1995, *The Surface Evolver Manual*, Version 1.99, University of Minnesota Geometry Center, Minneapolis, MN 55455.
- Syms, R. R. A., Dec. 1995, "Equilibrium of Hinged and Hingeless Structures Rotated Using Surface Tension Forces," *Journal of Microelectromechanical Systems*, vol. 4, no. 4, pp. 177-184.
- Koester, D., Mahadevan, R., and Markus, K., 1996, *SmartMUMPs design handbook including MUMPs introduction and design rules*, rev. 4, DARPA project (DABT 63-93-C-0051) of MEMS Technology Applications Center MCNC, 3021 Cornwallis Road, Research Triangle Park, NC 27709.

Harsh, K. F. and Lee, Y. C., Jan. 1998, "Modeling for Solder Self-Assembled MEMS," *Proceedings of the International Society for Optical Engineering (SPIE '98)*, vol. 3289, pp. 177-184.

Lin, W., Patra, S. K., and Lee, Y. C., Aug. 1995, "Design of Solder Joints for Self-aligned Optoelectronic Assemblies," *IEEE Trans. on Components, Packaging and Manufacturing Technology, Part A*, pp. 543-551.

Tan, Q. and Lee, Y. C., May 1996, "Soldering for Optoelectronics Packaging," *IEEE Transactions on Components, Packaging and Manufacturing Technology, Part C*, pp. 28-30.

Batchelor, G. K., 1967, *An Introduction to Fluid Dynamics*, Cambridge U. P., pp. 63-65.

## C.2 Solder Self-Assembled Microrobot Legs

P. E. Kladitis and V. M. Bright, "Prototype microrobots for micro positioning and micro unmanned vehicles," *Sensors and Actuators A.*, vol. 80, pp. 132-137, 2000.

# Prototype microrobots for micro-positioning and micro-unmanned vehicles

Paul E. Kladitis <sup>\*</sup>, Victor M. Bright <sup>1</sup>

*NSF Center for Advanced Manufacturing and Packaging of Microwave, Optical, and Digital Electronics (CAMPMode),  
Department of Mechanical Engineering, University of Colorado at Boulder, Boulder, CO 80309-0427, USA*

Received 15 April 1999; accepted 19 July 1999

---

## Abstract

The design and performance of two prototype microrobots are presented in this paper. The microrobots were implemented by surface micromachining arrays of 270  $\mu\text{m}$  long, polycrystalline silicon legs across the surface of a silicon chip. The method of motion of the microrobots is designed to mimic the way six-legged insects walk. One microrobot leg design has two degrees-of-freedom motion, and the other leg design has one degree-of-freedom motion. Both microrobot designs are able to transport objects across their bellies while lying on their backs. The microrobot with one degree-of-freedom motion is able to support several times its own weight, making available the option to carry an autonomous power supply (such as a solar cell), microprocessor, control circuitry, test equipment, and sensing or surveillance devices. Results of the self-assembly of the microrobot legs using the surface tension of molten indium are also presented.

© 2000 Elsevier Science S.A. All rights reserved.

**Keywords:** Microrobot; Electro-thermal actuator; Self-assembly; Solder; Insects

---

## 1. Introduction

The realization of the microrobot, presented herein, is a new and revolutionary tool useful for a variety of applications. Examples include micro-unmanned-surveillance vehicles and micro-weapons for military applications; small machines that help build smaller machines and small-quarters inspectors for industrial applications; and micro-surgeons for medical applications [1–3].

Several microrobot schemes, miniature robot designs, and microrobot components have been developed [4–9]. Some implementations have revealed important design considerations, for example, Teshigahara et al. [10] have determined that wheels are not a suitable method of propulsion for micrometer sized vehicles.

The method of motion for the robots in this research is modeled after the optimum designs already existing in nature. Mimicking nature is not a new concept in the field of Micro-Electro-Mechanical-Systems (MEMS). For example, Suzuki et al. [11,12] and Shimoyama et al. [6] replicate insect exoskeletons and insect wing muscle motion, and Ataka et al. [13] duplicate ciliary motion to transport objects across a chip.

This paper presents two microrobots designed to walk on a flat surface. The paper will discuss the method of motion and microrobot layout, the microrobot leg designs, and experimental performance of each microrobot. The microrobots in this research were fabricated using a commercially available silicon surface micromachining process: the Multi-User MEMS Process (MUMPs) by MCNC [14].

## 2. Method of motion and microrobot layout

The method of motion of both microrobots is designed to mimic the way six legged insects walk. In this method,

<sup>\*</sup> Corresponding author. Tel.: +1-303-735-1734; fax: +1-303-492-3498; E-mail: kladitis@colorado.edu

<sup>1</sup> E-mail: victor.bright@colorado.edu

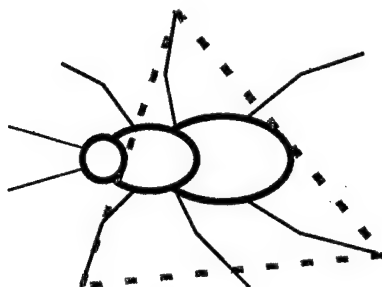


Fig. 1. Schematic of a six legged insect with three legs arranged in a tripod.

three legs, positioned like a tripod, are in contact with the walking surface at any one time. To copy this motion, the microrobots use large arrays of legs, electrically wired into six groups, to effectively act as six legs. Fig. 1 is a top view of a six-legged insect with three legs positioned in a tripod.

Fig. 2 shows a simplified wiring diagram used for both microrobots. Each leg of the microrobot is electrically powered. All the legs are grounded through the substrate. The six groups of legs are divided into two larger groups, where one group is powered with a signal through "line A", and the other group is powered through "line B" with a different signal, as shown in Fig. 2.

Power is applied to the microrobot through the three bondpads on the chip. Fig. 3 shows a scanning electron micrograph (SEM) of a belly-up view of a microrobot.

### 3. Microrobot leg designs

The wiring scheme and arrangement of leg groups are the same for both microrobot designs. The microrobots differ in leg design, size of the chip body, and the total number of legs. In both designs, the total number of legs is evenly divided into six groups.

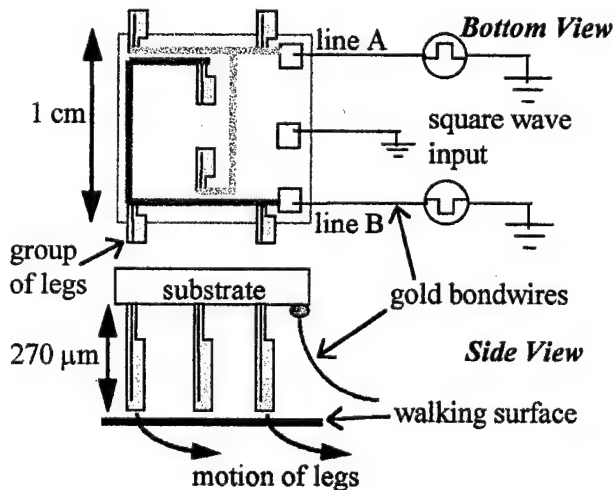


Fig. 2. Simplified wiring diagram for the microrobots showing a bottom or belly-up view and a side view.

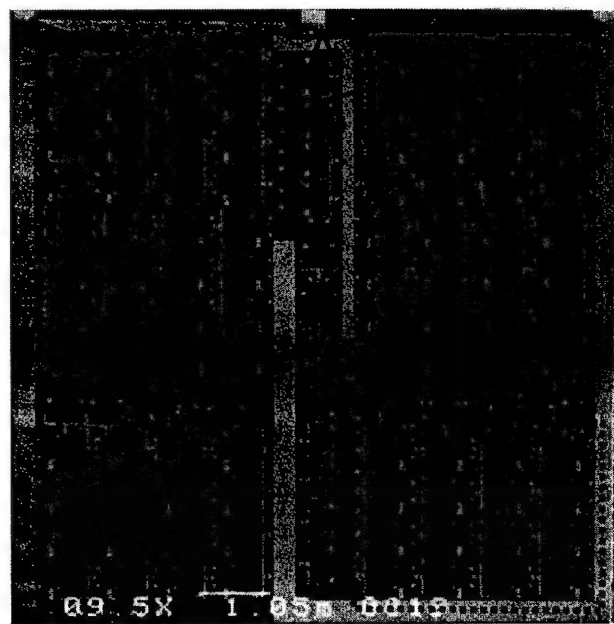


Fig. 3. SEM of a belly-up view of a microrobot. One of the six groups of legs is outlined by a dotted box.

#### 3.1. Two degrees-of-freedom microrobot leg design

The two degrees-of-freedom microrobot design consists of a 1 cm × 1 cm × 0.5 mm silicon chip body with an array of 96 legs arranged into six groups of sixteen legs. Each leg is an electro-thermal actuator. An electro-thermal actuator takes advantage of the thermal expansion of polycrystalline silicon (polysilicon) when supplied by electric current [15]. The mass of this microrobot is 127.5 mg.

The 270 μm long by 18.5 μm wide by 2.0 μm thick legs are fabricated on one side of the chip using a polysilicon surface micromachining process. The legs are manually erected or assembled to a normal position with respect to the chip's surface and locked into place using micromachined spring wires.

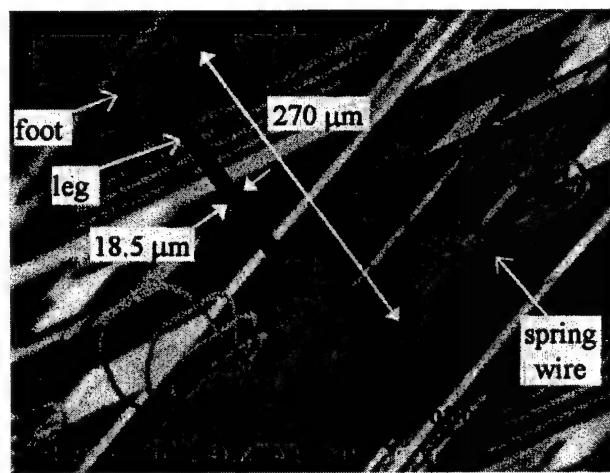


Fig. 4. SEM of an assembled microrobot leg with two degrees-of-freedom motion.

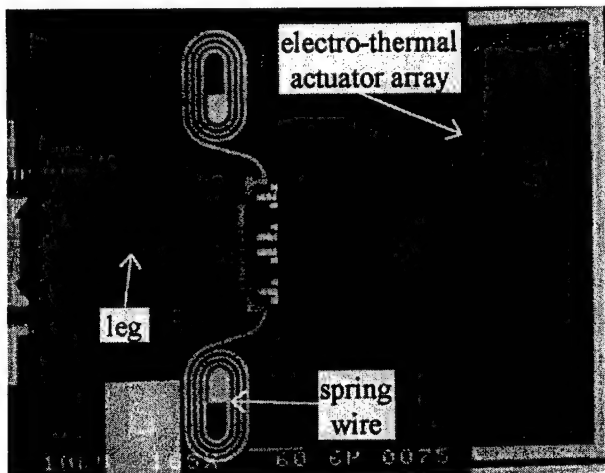


Fig. 5. SEM of an unassembled microrobot leg with two degrees-of-freedom motion.

nipulator probes. Electrical power is provided to each leg by two, gold covered, polysilicon connections called "spring wires". The spring wires provide flexible and low resistance electrical connections from the leg to gold and polysilicon interconnects anchored to the substrate.

Fig. 4 shows an assembled microrobot leg. Fig. 5 shows an unassembled microrobot leg. The leg itself provides motion in the forward direction, and the electro-thermal actuator array, that can be seen in Fig. 5, provides motion in a sideways direction. Fig. 6 shows a portion of the microrobot (belly up) with several legs in view.

### 3.2. One degree-of-freedom microrobot leg design

The second microrobot design consists of a  $5 \times 5 \times 0.5$  mm silicon chip body with an array of 90 electro-thermal actuators serving as legs. The legs are also fabricated using a polysilicon surface micromachining process, and have the same dimensions, as described for the two degrees-of-freedom case with the exception of being  $3.5 \mu\text{m}$  thick.

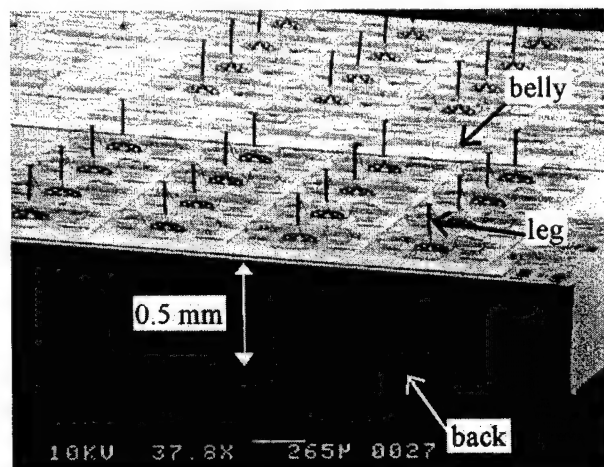


Fig. 6. A portion of the microrobot (belly up) with several legs in view.

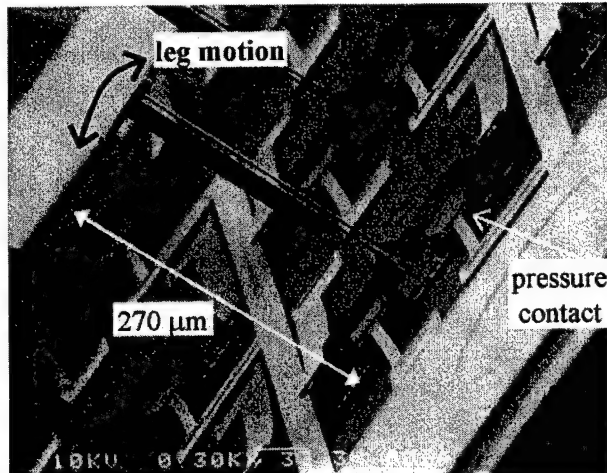


Fig. 7. SEM of a single one degree-of-freedom leg.

The mass of this microrobot design is 32 mg. The legs are manually erected to a normal position, with respect to the chip's surface, using micromanipulator probes. Electrical power is provided to each leg by two polysilicon pressure contacts located at the base of each leg. Fig. 7 shows a SEM of one leg.

## 4. Experimental performance

### 4.1. Two degrees-of-freedom microrobot leg design

While positioned on its back (belly up), the two degrees-of-freedom microrobot legs were able to transport a 3.06 mg piece of kapton film ( $9.25 \times 9 \times 0.023$  mm thick) across the microrobot belly. While carrying the piece of kapton film, the legs moved with a maximum step size of

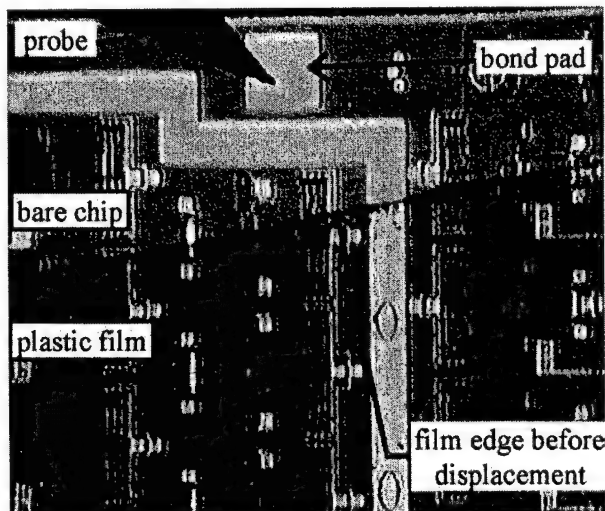


Fig. 8. Captured video image of a plastic film over the microrobot's belly before being transported. Note the probe is supplying power to the microrobot through the bondpad.

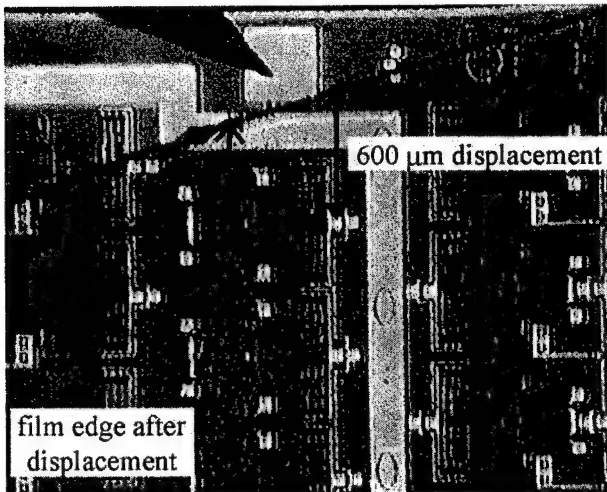


Fig. 9. Captured video image of a plastic film over the microrobot's belly after being transported.

$3.75 \mu\text{m}$  at  $453 \mu\text{m}/\text{min}$  powered by a  $0\text{--}5 \text{ V}$  square wave input with a 50% duty cycle and frequency of 2 Hz. Thus, this experiment demonstrated a voltage-controlled micropositioner. The signal applied to "line A" is  $180^\circ$  out of phase with the signal to "line B". Figs. 8 and 9 are a series of video images showing the plastic film before and after transport over the microrobot's belly. In Figs. 8 and 9, the belly of the robot can be seen through the plastic film while being transported by the microrobot's feet. The maximum DC power that may be supplied to this design, before the electro-thermal actuator polysilicon legs melt, was measured as being  $10 \text{ V} \times 287 \text{ mA} = 2.87 \text{ W}$ .

Both microrobot designs were also tested by placing them, legs down, on a walking surface while being connected to a remote power supply. The microrobot was connected to the remote power supply using three  $25 \mu\text{m}$  diameter and 5 in. long gold bonding wires. However, the

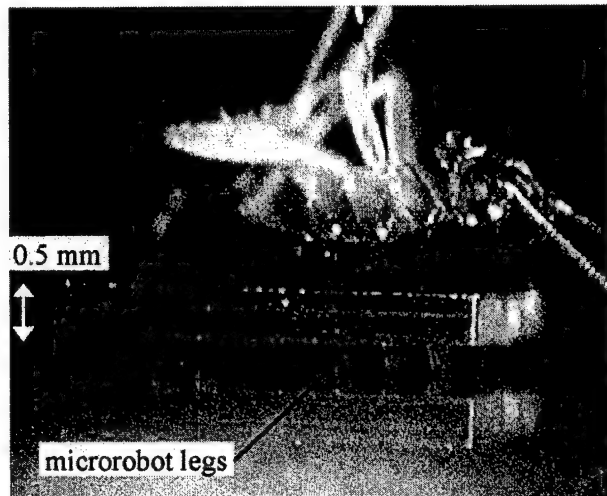


Fig. 11. Video image of the microrobot supporting an insect.

gold wires turned out to be too massive and stiff to permit movement or even allow all the microrobot feet to touch the walking surface. Future designs will carry an autonomous power supply. The future designs will be optimized for power consumption in order to be powered by solar cells or a thin film battery.

#### 4.2. One degree-of-freedom microrobot leg design

While positioned on its back (belly up), the one degree-of-freedom microrobot was able to transport a chip of equal size (32 mg) across its belly while being powered by a square wave input. The signal applied to "line A" was  $180^\circ$  out of phase with the signal applied to "line B". The maximum DC power that may be supplied to this design, before the electro-thermal actuator polysilicon legs melt, was measured as being  $8 \text{ V} \times 74 \text{ mA} = 592 \text{ mW}$ .

Standing on its legs, on a silicon wafer, this microrobot can support several times its own weight. Fig. 10 shows a captured video image of the microrobot supporting four silicon chips plus gold bonding wire. The microrobot legs collapsed after the loading of a fifth chip. Fig. 11 shows the microrobot supporting a cockroach. The chips (32 mg each) and the cockroach (unknown weight) were lowered onto the microrobot's back using tweezers.

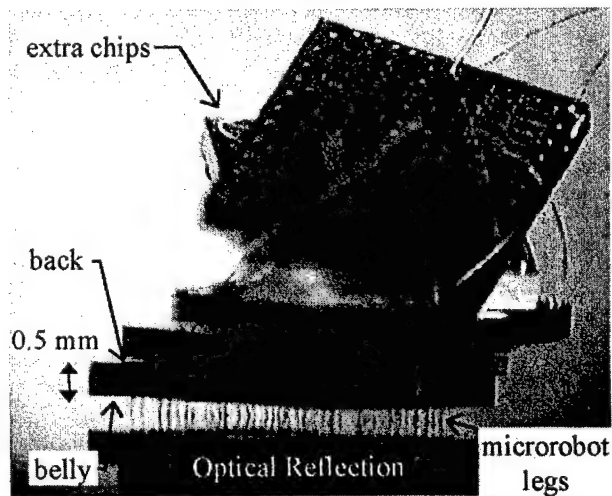


Fig. 10. Captured video image of the microrobot supporting four silicon chips plus gold bonding wire. The microrobot is standing on a silicon wafer.

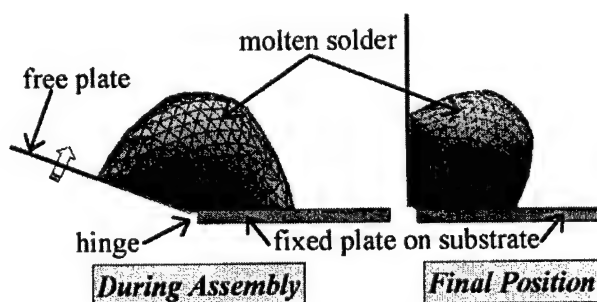


Fig. 12. Illustration of solder self-assembly of a hinged plate.

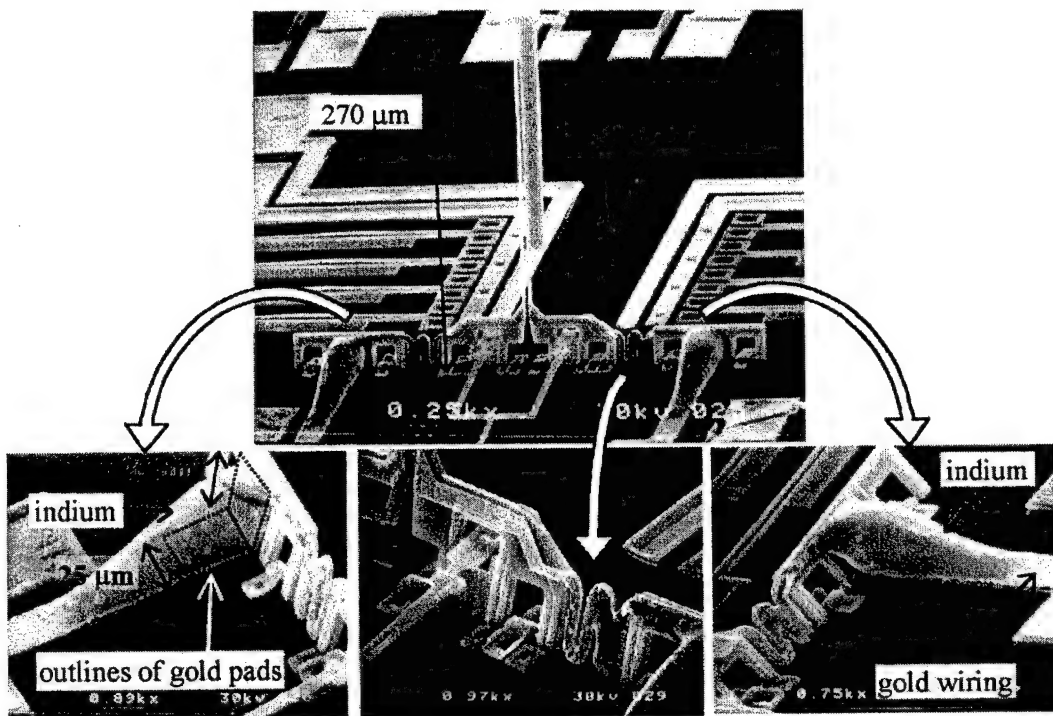


Fig. 13. SEM of a single solder self-assembled microrobot leg showing close views of the left and right indium solder joints and the electro-mechanical linkage isolating the right solder joint from the leg.

#### 4.3. Towards self-assembly of microrobot legs

As stated previously, all of the microrobot legs were manually assembled using micromanipulator probes. The average time for assembly per microrobot was typically 3 h. Damaging the legs during the assembly was a common problem. Current research is directed on massively parallel solder assembly [16–20] of the microrobot legs to make the microrobots commercially manufacturable.

Solder assembly of MEMS involves the use of the surface tension of molten solder as the assembly mechanism. The solder assembly method uses polysilicon plates hinged to the substrate with specific areas metallized as solder wettable pads. Once the solder is in place, it is heated to its melting point, and the force, produced by the natural tendency of liquids to minimize their surface energy, pulls the free plate away from the silicon substrate, as illustrated in Fig. 12. Using solder, hundreds or thousands of precision alignments can be accomplished with a single batch reflow process.

Current results of using surface tension to assemble microrobot legs are shown in Fig. 13. The equivalent of a sphere of indium with diameter of 37  $\mu\text{m}$  was deposited on each set of  $25 \times 25 \mu\text{m}$  gold pads for the microrobot leg shown in Fig. 13. The outline of the location of the gold pads is also shown in Fig. 13.

The pure indium was evaporated, using a BAL-TEC MED 020 Coating System, and patterned on the chip using a thick photoresist (AZ P4620) metal lift-off process be-

fore sacrificial oxide etch of the surface micromachined microrobot legs. The chip was then heated to the melting point of the indium ( $160^\circ\text{C}$ ), where the surface tension of the molten indium lifted the legs into place as shown in Fig. 13. The microrobot leg, shown in Fig. 13, is one of five legs fabricated on a  $2 \times 2 \text{ mm}$  test chip.

This new microrobot leg design combines the sturdiness of the  $3.5 \mu\text{m}$  thick one degree-of-freedom leg design with two degrees-of-freedom motion. The indium solder joints serve as low resistance electrical connections and mechanically rigid supports for the legs, making the robot leg design robust. A curved spring-like electro-mechanical linkage isolates the mechanically rigid solder joints from the leg, permitting the two degrees-of-freedom motion.

#### 5. Conclusions

This paper presented the design and experimental results for two microrobot prototypes. The two degrees-of-freedom microrobot design demonstrated transportation of a piece of plastic film in a single direction. However, the legs possess two degrees-of-freedom motion in the plane of the chip. Depending on the wiring and synchronization of leg movements, the robot could transport or rotate an object in any direction within the plane of the chip, thus realizing a micropositioner. The one degree-of-freedom microrobot design demonstrated transportation of a chip of the same size and was able to support up to four chips.

Providing an autonomous power supply or a power supply that would not impede movement of both micro-robots was a challenge in this research. However, the one degree-of-freedom microrobot design should easily be able to carry an autonomous power supply (such as a solar cell), microprocessor, control circuitry, test equipment and sensing or surveillance devices, thus realizing a micro-unmanned vehicle.

The ability of being able to assemble the microrobot legs using the surface tension of solder makes the mass production of this microrobot a reality by simply adding a solder deposition step and reflow step to a MEMS fabrication process.

### Acknowledgements

This effort was sponsored in part by the Department of Defense (MDA904-97-C-0320) and Defense Advanced Research Projects Agency (DARPA) and Air Force Research Laboratory, Air Force Materiel Command, USAF, under agreement number F30602-98-1-0219.

### References

- [1] P. Dario, R. Valleggi, M.C. Carrozza, M.C. Montesi, M. Cocco, Microactuators for microrobots: a critical survey, *Journal of Micromechanics and Microengineering* 2 (3) (1992) 141–157.
- [2] S. Johansson, Micromanipulation for micro- and nano-manufacturing, Proceedings of the INRIA/IEEE Symposium on Emerging Technologies and Factory Automation, Vol. 3, 1995, pp. 3–8.
- [3] M. Flynn, L. Tavro, S. Bart, R. Brooks, D. Ehrlich, K. Udayakumar, L. Cross, Piezoelectric micromotors for microrobots, *IEEE/ASME Journal of Microelectromechanical Systems* 1 (1) (1992) 44–51.
- [4] T. Fukada, A. Kawamoto, F. Arai, H. Matsuura, Micro mobile robot in fluid (1st report, mechanism and swimming experiment of micro mobile robot in water), *Transactions of the Japan Society of Mechanical Engineers, Part C* 60 (569) (1994) 204–210.
- [5] C. Liu, T. Tsao, Y. Tai, W. Liu, P. Will, C. Ho, Micromachined permalloy magnetic actuator array for micro robotics assembly systems, Proceedings of the International Conference on Solid-State Sensors and Actuators, Eurosensors IX, Vol. 1, 1995, pp. 328–331.
- [6] I. Shimoyama, Y. Kubo, T. Kaneda, H. Miura, Simple microflight mechanism on silicon wafer, Proceedings of the IEEE MEMS Workshop, 1994, pp. 148–152.
- [7] T. Yasuda, I. Shimoyama, H. Miura, Microrobot actuated by a vibration energy field, *Sensors and Actuators, A: Physical* 43 (1) (1994) 366–370.
- [8] R. Yeh, E. Kruglick, K. Pister, Towards an articulated silicon microrobot, Proceedings of ASME Dynamic Systems and Control, Vol. 2, 1994, pp. 747–754.
- [9] R. Yeh, E.J.J. Kruglick, K.S.J. Pister, Surface-micromachined components for articulated microrobots, *IEEE/ASME Journal of Microelectromechanical Systems* 5 (1) (1996) 10–17.
- [10] A. Teshigahara, M. Watanabe, N. Kawahara, Y. Ohtsuka, T. Hattori, Performance of a 7-mm microfabricated car, *IEEE/ASME Journal of Microelectromechanical Systems* 4 (2) (1995) 76–80.
- [11] K. Suzuki, I. Shimoyama, H. Miura, Insect-model based microrobot with elastic hinges, *IEEE/ASME Journal of Microelectromechanical Systems* 3 (1) (1994) 4–9.
- [12] K. Suzuki, I. Shimoyama, H. Miura, Y. Ezura, Creation of an insect based microrobot with an external skeleton and elastic joints, *Proceedings of the IEEE MEMS Workshop, 1992*, pp. 190–195.
- [13] M. Ataka, S. Omofisks, N. Takeshima, H. Fujita, Fabrication and operation of polyimide bimorph actuators for a ciliary motion, *IEEE/ASME Journal of Microelectromechanical Systems* 2 (4) (1993) 146–150.
- [14] D. Koester, R. Mahadevan, K. Markus, SmartMUMPs design handbook including MUMPs introduction and design rules, rev. 4, DARPA project (DABT 63-93-C-0051) of MEMS Technology Applications Center MCNC, 3021 Cornwallis Road, Research Triangle Park, NC 27709, 1996.
- [15] J.H. Comtois, V.M. Bright, Applications for surface micromachined polysilicon thermal actuators and arrays, *Sensors and Actuators, A: Physical* 58 (1997) 19–25.
- [16] R.R.A. Syms, Equilibrium of hinged and hingeless structures rotated using surface tension forces, *Journal of Microelectromechanical Systems* 4 (4) (1995) 177–184.
- [17] P.W. Green, R.R.A. Syms, E.M. Yeatman, Demonstration of three-dimensional microstructure self-assembly, *Journal of Microelectromechanical Systems* 4 (4) (1995) 170–176.
- [18] K. Harsh, R. Irwin, Y.C. Lee, Solder self assembly for MEMS, *Proceedings of the 44th International Instrumentation Symposium, Reno, NV, May 1998*, pp. 249–255.
- [19] K. Harsh, Y.C. Lee, Modeling for solder self-assembled MEMS, *Proceedings of SPIE 3289 (1998)* 177–184.
- [20] P.E. Kladitis, V.M. Bright, K.F. Harsh, Y.C. Lee, Prototype microrobots for micro positioning in a manufacturing process and micro unmanned vehicles, *The 12th IEEE International Conference on MicroElectroMechanical Systems — MEMS '99, Orlando, FL, 17–21 January 1999*, pp. 570–575.

*Paul Kladitis* is currently working on a PhD in Mechanical Engineering at the University of Colorado at Boulder. He received his BS in Electrical Engineering at Wright State University in Dayton, OH in 1996 and his MS in Electrical Engineering at the Air Force Institute of Technology in Dayton, OH in 1997.

*Dr. Victor M. Bright* is an Associate Professor of Mechanical Engineering and the Director of the MEMS R&D Laboratory, University of Colorado at Boulder. Prior to joining the University, he was an Associate Professor and the Director of Microelectronics Research Laboratory in the Department of Electrical and Computer Engineering, Air Force Institute of Technology, Wright-Patterson Air Force Base, OH (6/92–12/97). Prof. Bright's research includes MEMS, silicon micromachining, microsensors, microactuators, MEMS self-assembly, MEMS packaging, opto-electronics, and semiconductor device physics. Dr. Bright received the following awards in the area of MEMS: Best Paper of the MCM'98 — International Conference and Exhibition on Multichip Modules and High Density Packaging, 1998; R.F. Bunshah Best Paper Award at the 1996 International Conference on Metallurgical Coatings and Thin Films. Dr. Bright has authored and co-authored more than 70 papers in the areas of MEMS. He is a member of IEEE, ASME, and SPIE. He serves on the Executive Committee for ASME MEMS Sub-division.

### **C.3 Resistive Point Heater For MEMS Remote Solder Self-Assembly**

P. E. Kladitis and V. M. Bright, "Novel Resistive Point Heater for MEMS Remote Solder Self-Assembly," *2000 ASME International Mechanical Engineering Congress and Exposition*, MEMS-Vol. 2, pp. 161-167, Orlando, Florida, Nov. 5-10, 2000.

## Novel Resistive Point Heater for MEMS Remote Solder Self-Assembly

Paul E. Kladitis and Victor M. Bright

NSF Center for Advanced Manufacturing and Packaging of Microwave, Optical, and Digital Electronics

Department of Mechanical Engineering, University of Colorado, Boulder, CO 80309-0427.

Tel: (303) 735-1763, Fax: (303) 492-3498, E-mail: kladitis@colorado.edu

### ABSTRACT

MEMS structures can be assembled using the surface tension of molten solder (solder self-assembly). Until this novel development, solder self-assembly was performed at the wafer or chip level where the whole chip needed to be heated to melt the micro sized solder droplets used to assemble devices. In this paper we present the design, testing, and modeling of a resistive point heater that is used to assemble an individual device on a chip without affecting neighboring devices. The point heater was packaged in 14 and 24 pin ceramic dual inline packages and tested in air, nitrogen, and formic-acid/nitrogen vapor. The lowest power needed to liquify a 63Sn/37Pb, 8 mil diameter equivalent volume solder droplet and assemble a device in formic-acid/nitrogen vapor was found to be 714 mW. The average power, of several trials, required to liquify a solder droplet is 998 mW at 141 mA and 7.08 V. A steady-state heat transfer model predicts 986.4 mW is required to keep the droplet at 181 °C (the observed minimum temperature at which 63Sn/37Pb solder is in liquid state). Growth of pure Sn platey crystals, verified by X-ray florescence, was noted on the point heater assembly and surroundings during assembly in formic-acid/nitrogen vapor.

### INTRODUCTION

The self-assembly of MEMS structures using surface tension of molten solder (solder self-assembly) is a compact, powerful, and practical assembly method that also results in robust mechanical and electrical connections. The basic components of solder assembly consist of two plates hinged to each other with an appropriate liquid between the plates wetted to defined areas. The minimum surface energy shape for this basic surface tension (BST) assembly unit can be modeled allowing one to predict the final angle between the plates. In this case, surface micromachined polycrystalline silicon (polysilicon) structures serve as the plates, molten solder serves as the liquid between the plates, and gold coating on the plates serves as the wettable defined areas. Figure 1 shows an example where three BST assembly units were combined to form a fiber optic cable gripper. In Figure 1, each volume of 63Sn/37Pb solder is equivalent to an 8 mil diameter solder sphere. Detailed information on solder shape modeling and the solder assembly process is given by Kladitis et al. [1] and Harsh et al. [2].

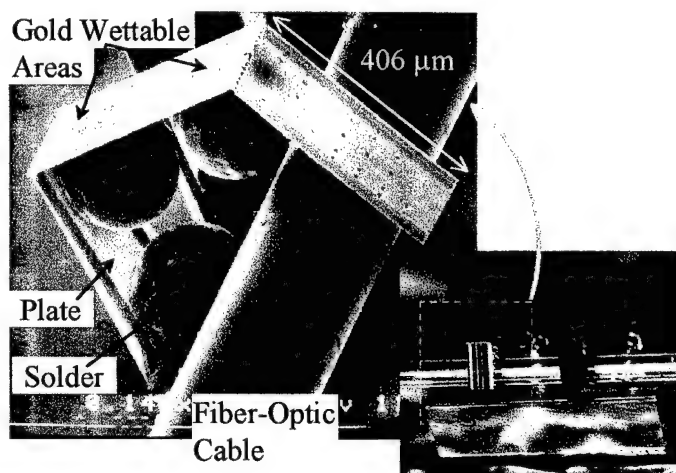


**Figure 1:** Scanning electron micrograph and captured video image of a fiber-optic cable gripper assembled with three solder joints.

Until this novel development, the conventional solder self-assembly method was performed at the wafer or chip level where the whole chip needed to be heated to melt the micro sized solder droplets used to assemble

devices. In this paper we present a resistive point heater (RPH) that is used to assemble an individual device on a chip without affecting neighboring devices. Figure 2 shows a scanning electron micrograph (SEM) of a resistive point heater unit after assembling a polysilicon plate using an 8 mil diameter equivalent volume of 63Sn/37Pb solder.

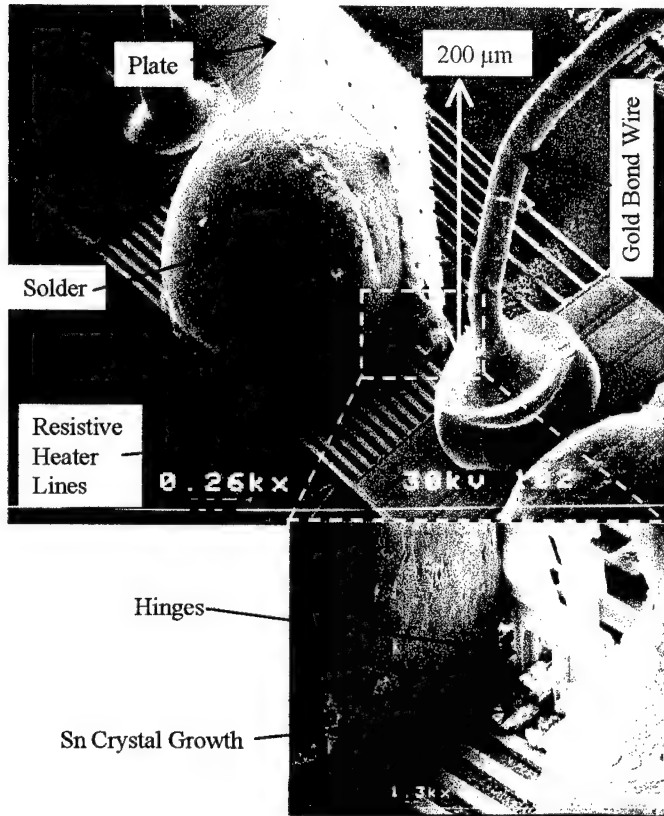


**Figure 2:** SEM of a resistive point heater unit after assembling a polysilicon plate using an 8 mil diameter equivalent volume of 63Sn/37Pb solder.

This RPH unit can now be used to assemble larger and more complex structures using various types of linkages. Anywhere a compact, powerful, and practical assembly method that also results in robust mechanical and electrical connections is needed, the RPH unit can be used. The intended use of the RPH unit involves pre-wetting a volume of solder across both gold wettable areas of an unreleased structure either by physical placement of molten solder [3] or by cold deposition/plating of a solder material as in a BGA bumping process. Once the solder is in place the structure can be packaged and released. As long as the solder is pre-wetted to both wettable pads, the assembly yield will be 100%, barring any mechanical failure of the structure needing assembly. The packaged system can be sent on its mission, and at the appropriate time, power can be applied to the RPH to remotely assemble the structure. The RPH may be operated in air, however, because the solder surface will crust over with oxide while molten, the modeled assembly angle will not be achieved. For best results, the RPH should be operated in a vapor or liquid flux environment or any environment that will disallow oxidation of the solder. Theoretically, a vacuum will prohibit oxidation; therefore, space applications may be best suited for the RPH.

The remainder of this paper will cover the design of the RPH unit, the packaging and testing of the device, and a steady-state heat transfer model. Further more, all references to solder in this paper will imply an 8 mil diameter equivalent volume of 63Sn/37Pb solder. Also, all the microstructures presented in this paper have been fabricated using the MUMPs process – a polysilicon surface micromachining process [4]. The names of the MUMPs layers will be utilized when describing a device.

## DESIGN

Figure 3 shows a captured video image and CAD drawing of the top view of an unassembled RPH. This RPH consists of a 200  $\mu\text{m}$  tall Poly2 free plate and a fixed plate with  $132 \mu\text{m} \times 132 \mu\text{m}$  gold wettable areas.

The free plate is attached to the nitride through six hinges. Fourteen, 2  $\mu\text{m}$  wide Poly1 resistive heater lines, with an identical set of Poly0 heater lines run underneath the gold area of the free plate. The Poly1 heater lines are anchored to the Poly0 heater lines through 6  $\mu\text{m} \times 6 \mu\text{m}$  Anchor1(s) located 121  $\mu\text{m}$  away from both wire-bond pads.

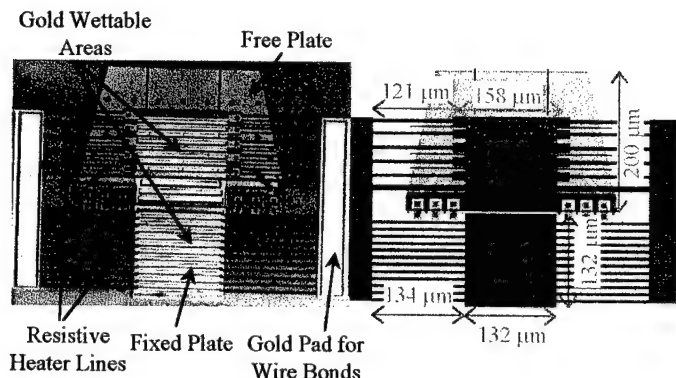


**Figure 3:** Captured video image and CAD drawing of the top view of an unassembled resistive point heater unit.

Twenty-four, 2  $\mu\text{m}$  wide Poly1 resistive heater lines, with an identical set of Poly0 heater lines run underneath the gold area of the fixed plate. These Poly1 and Poly0 heater lines are encased in Oxide1 and Oxide2 underneath the fixed plate. All of the Poly1 and Poly0 resistive heater lines end at trapped-oxide wire-bond pads to be bonded out for electrical connections to the heater lines. This RPH design is a prototype – designs optimized in size, power consumption, and power distribution are under study.

### PACKAGING AND TESTING

Arrays of six RPHs have been fabricated on 2 mm  $\times$  2 mm die and packaged in 14 and 24 pin ceramic dual inline packages (DIP). The experiment using a 24 pin DIP will be described next. Figure 4 shows video pictures of four, 2 mm  $\times$  2 mm packaged and bonded dice in a 24 pin DIP, and a close up of one die wire bonded to the package.

The unreleased dice were first mounted in the package using Poly-Solder Polyblend silver epoxy and cured at 140 °C for 19 minutes. The whole package was then soaked in acetone for 30 minutes and 2-propanol for 10 minutes to remove the photoresist coating on the dice. The package was allowed to air dry. Next the chips were released by immersing the package in 48% HF for 3.5 minutes, de-ionized water for 1 minute, 2-propanol for 5 minutes, and methanol for 30+ minutes as part of the critical point CO<sub>2</sub> drying process in a BAL-TEC CPD 030 critical point dryer.

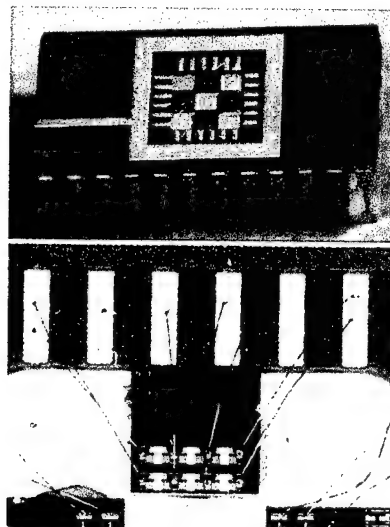


**Figure 4:** Video pictures of four, 2 mm  $\times$  2 mm packaged and bonded dice in a 24 pin DIP, and a close up of one die wire bonded to the DIP.

Next, the dice were wire bonded to the DIP using gold wire in a Marpet Enterprises Inc. Model 1204B wire bonder. The DIP was inserted into a 24 port socket with 24, 22 gauge wires soldered to the leads. While mounted in the socket, and measuring through the wires, the resistance of 20 RPHs was measured yielding an average of  $30.1\ \Omega$  and a standard deviation of  $1.7\ \Omega$ .

For testing, the DIP in socket was fastened to the stage inside a glass chamber ported for  $N_2$  and CHOOH (formic acid) as shown in Figure 5. When testing the RPHs in air, the chamber was removed. When testing in  $N_2$ , the chamber was used with an  $N_2$  flow rate of 3 L/minute. When testing in flux vapor, the chamber was used with an  $N_2$  flow rate of 1 L/minute and  $N_2$  bubbled through formic acid at a rate of 2 L/minute. The temperature of the chamber was monitored at  $28\ ^\circ C$  during the experiment through a thermocouple mounted in the stage and wired to a Watlow Series 965 temperature controller. All resistance measurements were made using a Fluke 77 III multimeter. Power was supplied and measured by connecting a HP E3620A DC power supply, with digital voltage and current readout, to the appropriate RPH through the wires soldered to the leads of the socket.

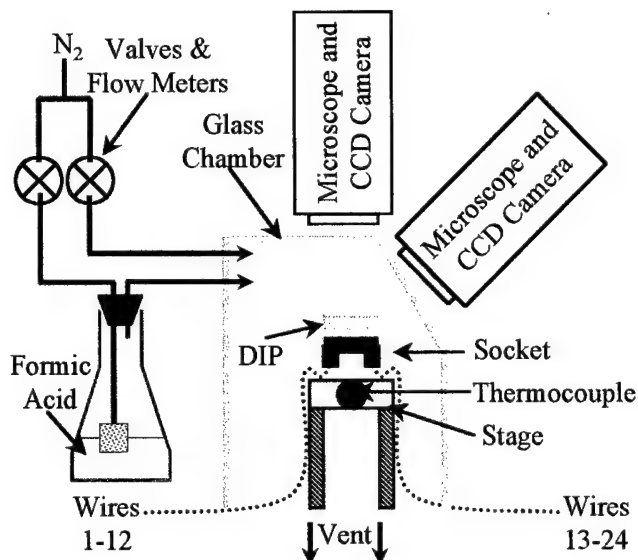


**Figure 5:** Diagram of the setup used for testing the packaged resistive point heaters.

$8\text{ mil} \pm 1\text{ mil}$  diameter solder spheres manufactured by AlphaMetals were smashed between glass microscope slides and manually placed on each RPH using probes as illustrated in Figure 6.

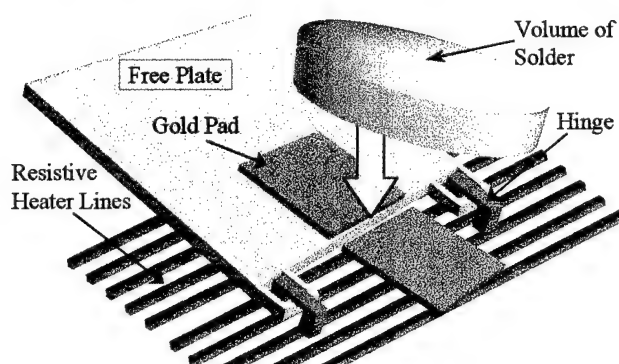


**Figure 6:** Depiction of the application of flattened solder spheres to an RPH unit. Although the solder was not applied to the RPH in the preferred manner, as discussed in the introduction, this solder application method demonstrates the robustness of the RPHs by requiring the additional task of the solder wetting to the gold pads.

## EXPERIMENTAL RESULTS

First, a RPH was tested in air. The power required to begin deforming the flattened solder sphere was  $633.39\text{ mW}$  at  $4.91\text{ V}$  and  $129\text{ mA}$ . The solder sphere wet to the fixed gold pad, but not the free gold pad. The solder did not reach its modeled shape due to oxidation of the solder surface. Figure 7 is a captured video image of the unheated solder that was melted in air. Wetting to only the fixed gold pad was a common

occurrence in the experiments. The reason for this is that the fixed plate gets hotter than the free plate – recall that the fixed plate has 24 heaters underneath it while the free plate has only 14.

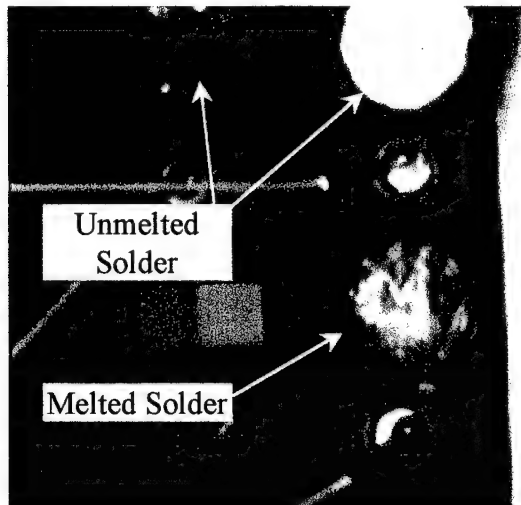


**Figure 7:** Captured video image of unheated solder that was melted in air.

Next an RPH was activated in  $N_2$ . The power required to begin deforming the flattened solder sphere was 670.56 mW at 5.08 V and 132 mA. The melting and wetting behavior was the same as for the air experiments. Finally, 10 RPH trials were performed in flux vapor. Figure 8 is a sequence of captured video images showing the assembly of a RPH unit in flux vapor. Figure 8 also shows an example of an RPH that was activated in  $N_2$  only. Two power measurements were taken for each trial. The first measurement was taken when the power was just enough to cause a slight deformation in the flattened solder, such as Figure 8 (b). The average power of the trials, to cause slight deformation, is 378 mW at 3 V and 126 mA. The second power measurement was taken after the free plate reached its assembly position. The power was adjusted by hand to the point where the entire solder sphere was completely molten as in Figure 8 (e). The average power of the trials, required to keep the assembled solder sphere molten, is 998 mW at 7.08 V and 141 mA.

The voltage and current measurements were taken when queued by the appearance of the molten solder ball; therefore, the measurements can be subjective and may have significant error. With reference to Figure 8, frames (a) – (e) occurred over a 25-second interval, but this is because the power was being increased slowly and deliberately. Frames (c) – (e) occurred over a < 3-second interval, however, the power was also being slowly controlled. The change of state from solid to liquid and liquid to solid appears to be instantaneous when the power is increased or decreased about the phase change point. Experiments to carefully measure the assembly time of pre-wetted solder RPH units are underway. Observations from these preliminary experiments suggest that the assembly time will be less than one second.

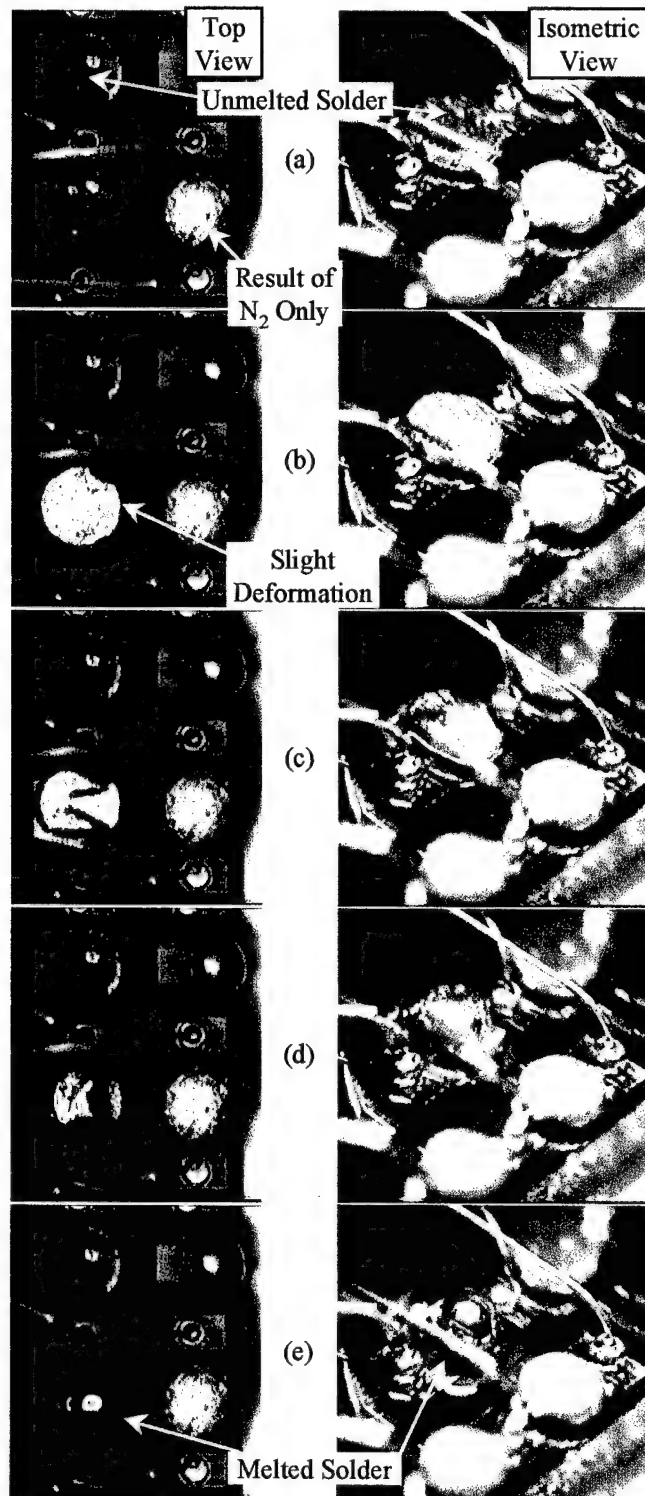


**Figure 8:** A sequence of captured video images showing the assembly of a RPH unit.

Growth of pure Sn crystals was noted on the point heater assembly and surroundings during assembly in formic acid/nitrogen vapor. The Sn crystals grow while power is applied to the RPH. Figure 2 shows a close view of crystal growth on the RPH's hinges. This RPH unit was powered for less than a minute. Crystal growth appears in Figure 8 as a light halo on the substrate surrounding the RPH beginning in frame (b). X-ray

flourescence (XRF) results suggest that the crystals are pure Sn. Figure 9 shows the XRF results for the sample in the inset. The gold spectrum spikes in Figure 9 indicate the gold sputtered coating applied for the purpose of taking good SEMs. The RPH shown in Figure 9 was powered for over 3 minutes in formic acid/N<sub>2</sub> vapor. Note the platey growth of the crystals. Platey growth is characteristic of material with a tetragonal crystal structure such as Sn. The crystal growth has only been observed in formic acid/N<sub>2</sub> vapor, other flux vapors may not encourage crystal growth.

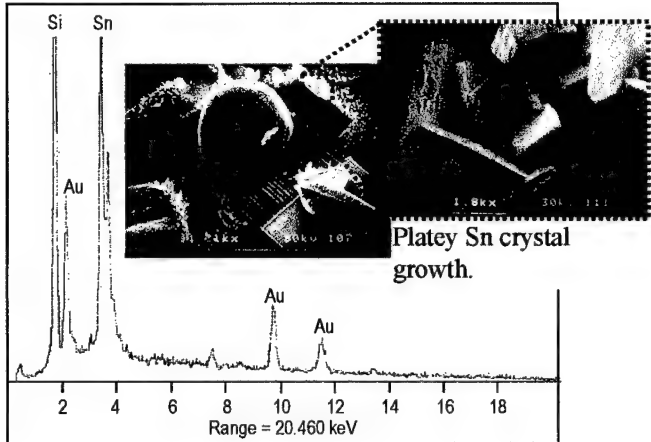


**Figure 9:** XRF elemental spectrum results for the sample in the inset.

## MODELING

A steady-state heat transfer model was developed to predict the power required to keep the assembled solder sphere in a just-molten state, as depicted in Figure 8 (e). The experimentally determined temperature of the solder must be approximately 181 °C to be completely molten. Refer to Figure 3 for dimensions relevant to the following discussion. Figure 10 illustrates the heat transfers accounted for in the development of the model.

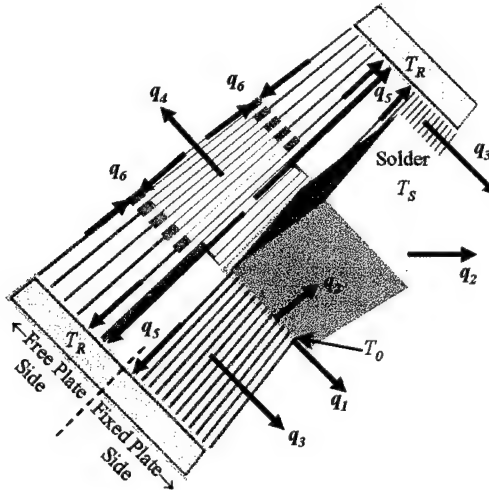


**Figure 10:** Illustration of the heat transfers accounted for in the development of the model.

The heat generated by the Poly0 heater lines will be neglected in this analysis, since the fraction of power being dissipated in them is much less than the power dissipated in the Poly1 heater lines. The fraction of electrical power going to the Poly1 heater lines ( $\eta$ ), available for heat generation, is assumed to be:

$$\eta = \frac{\frac{\rho_{P0}}{A_{P0}}}{\frac{\rho_{P0}}{A_{P0}} + \frac{\rho_{P1}}{A_{P1}}} = 0.72, \quad (1)$$

where  $\rho_{P0}$  is the resistivity of Poly0 ( $1.3 \times 10^{-5} \Omega\text{m}$ ),  $\rho_{P1}$  is the resistivity of Poly1 ( $2 \times 10^{-5} \Omega\text{m}$ ),  $A_{P0}$  is the cross-sectional area of a Poly0 heater line ( $2 \mu\text{m} \times 0.5 \mu\text{m}$ ), and  $A_{P1}$  is the cross-sectional area of a Poly1 heater line ( $2 \mu\text{m} \times 2 \mu\text{m}$ ).

Let  $q_1$  be the heat transfer from all the Poly1 heater lines combined, in the trapped oxide pad, to the substrate. Assuming that the temperature of the whole trapped oxide pad is the same as the Poly1 heater lines ( $T_0$ ), the heat transfer is:

$$q_1 = \frac{1}{R_1} (T_0 - T_R), \quad (2)$$

where  $R_1 = \frac{L_{O1}}{k_O A_1} + \frac{L_N}{k_N A_1} + \frac{L_C}{k_C A_1} + \frac{0.55}{k_C \sqrt{A_1}}$ ,  $T_R$  is room temperature or the far field temperature of the Si

chip ( $28^\circ\text{C}$ ),  $L_{O1}$  is the thickness of Oxide1 ( $2 \mu\text{m}$ ),  $L_N$  is the thickness of the nitride layer ( $0.6 \mu\text{m}$ ),  $L_C$  is the thickness of the Si chip ( $500 \mu\text{m}$ ),  $k_O$  is the thermal conductivity of the oxide ( $1.1 \text{ W/mK}$ ),  $k_N$  is the thermal conductivity of the nitride ( $16 \text{ W/mK}$ ),  $k_C$  is the thermal conductivity of the Si chip ( $153 \text{ W/mK}$ ),  $A_1$  is the area of the fixed gold pad ( $132 \mu\text{m} \times 132 \mu\text{m}$ ), and  $\frac{0.55}{k_C \sqrt{A_1}}$  is an addition spreading thermal resistance suggested by

Dally [5] for small area heat sources used to model conduction to the substrate.

Let  $q_2$  be the heat transfer from all the Poly1 heater lines combined, in the trapped oxide pad, to the top of the solder sphere, then:

$$q_2 = \frac{1}{R_2} (T_0 - T_S), \quad (3)$$

where  $R_2 = \frac{L_{O2}}{k_O A_1} + \frac{L_P}{k_P A_1} + \frac{L_S}{k_S A_1}$ ,  $T_S$  is the temperature of the top of the solder,  $L_{O2}$  is the thickness of Oxide2 ( $0.75 \mu\text{m}$ ),  $L_P$  is the thickness of Poly2 ( $1.5 \mu\text{m}$ ),  $L_S$  is the effective length of the solder ball

$\left( \frac{\frac{4}{3} \pi [4 \times 10^{-3} \text{ in} (0.0254 \text{ m/in})]^3}{A_1} \right)$  assuming a tetragonal shape with base  $A_1$ ,  $k_P$  is the thermal conductivity of the polysilicon ( $34 \text{ W/mK}$ ), and  $k_S$  is the thermal conductivity of the solder ( $49.78 \text{ W/mK}$ ).

Natural convection from the molten solder was modeled as laminar natural convection around a sphere using a correlation suggested by Gebhart et al. [6] for the average Nusselt number with appropriate Grashof number for this micro-scale problem. Therefore,  $q_2$  is also:

$$q_2 = A_S h (T_S - T_R), \quad (4)$$

where  $A_S = (\pi [8 \times 10^{-3} \text{ in} (0.0254 \text{ m/in})]^2 - A_1)$  is the exposed area of the solder sphere and  $h = \frac{k_A}{D} N u_D$  is the heat transfer coefficient of the solder sphere to the surroundings. The thermal conductivity of the air ( $k_A$ ) is  $0.039 \text{ W/mK}$ ,  $D$  is the original unflattened diameter of the solder sphere ( $8 \times 10^{-3} \text{ in} = 203.2 \mu\text{m}$ ), and the average Nusselt number is given by  $N u_D = 2 + G r_R + G r_R^2 (0.139 - 0.4519 P r + 1.1902 P r^2)$ . The Prandtl

number ( $P r$ ) for air is  $0.7$ ,  $G r_R$  is the Grashof number for air  $\left( \frac{g \beta}{\alpha v} R^3 (T_S - T_R) \right)$ ,  $g \beta / \alpha v$  is  $9.53 \times 10^6 \text{ m}^{-3} \text{ K}^{-1}$ , and

$R$  is the radius of the solder sphere ( $101.6 \mu\text{m}$ ). Furthermore, the thermal properties of formic acid/ $\text{N}_2$  vapor are being approximated by the thermal properties of air at  $200^\circ\text{C}$ .

Let  $q_3$  be the heat transfer from all the Poly1 heater lines combined, on both sides of the trapped oxide pad, to the substrate. Assuming heat is being transferred by conduction through the air from three faces of a heater line, and that the temperature of the whole line is approximately uniform at  $T_0$ , the heat transfer is:

$$q_3 = \frac{1}{R_3} (T_0 - T_R), \quad (5)$$

where  $R_3 = \frac{L_{O1}}{k_A A_3} + \frac{L_N}{k_N A_3} + \frac{L_C}{k_C A_3} + \frac{0.55}{k_C \sqrt{A_3}}$  and  $A_3 = (132 \mu\text{m} \times 2 \mu\text{m}) \times 48 \times 3$ , which is, the area of 48, 2

$\mu\text{m}$  wide 132  $\mu\text{m}$  long heater lines including all three faces closest to the nitride.

Let  $q_4$  be the heat transfer from 14 Poly1 heater lines combined, under the free plate, to the substrate. Assuming heat is being transferred by conduction through the air from three faces of a heater line, and that the temperature of the whole line is approximately uniform at  $T_0$ , the heat transfer is:

$$q_4 = \frac{1}{R_4} (T_0 - T_R), \quad (6)$$

where  $R_4 = \frac{L_{O1}}{k_A A_4} + \frac{L_N}{k_N A_4} + \frac{L_C}{k_C A_4} + \frac{0.55}{k_C \sqrt{A_4}}$  and  $A_4 = (400 \mu\text{m} \times 2 \mu\text{m}) \times 14 \times 3$ , which is, the area of 14, 2

$\mu\text{m}$  wide 400  $\mu\text{m}$  long heater lines including all three faces closest to the nitride.

Since the bondpads are anchored to the substrate and bonded to relatively massive gold wires, it is assumed that the bondpads are at  $T_R$ . Total conduction from the heater lines to the bondpads is approximated by:

$$q_5 = \left( \frac{1}{R_{5a}} + \frac{1}{R_{5b}} + \frac{1}{R_{5c}} \right) (T_0 - T_R), \quad (7)$$

where  $R_{5a} = \frac{134 \mu\text{m}}{k_P A_{P1} 48}$ ,  $R_{5b} = \frac{60.5 \mu\text{m}}{k_P A_{P1} 20}$ , and  $R_{5c} = \frac{200 \mu\text{m}}{k_P A_{P1} 8}$ . Furthermore, 134  $\mu\text{m}$  is the length of the 48

heater lines on either side of the fixed plate. Also, 60.5  $\mu\text{m}$  is the length of the 20 segments of heater line located on the free plate side between the bondpads and the anchors to the Poly0 lines. Finally, 200  $\mu\text{m}$  is the length of half of the 4 heater lines located on the free plate side, closest to the hinges. These 4 heater lines are only anchored at the bondpads, and conduction is assumed to be taking place from the center of these lines to the bondpads, therefore, a total of 8 segments.

Total conduction from all the heater lines to the 10 anchors on the free plate side, where two 2  $\mu\text{m}$  wide heater lines are effectively connected to each anchor on either side (total 4 connections per anchor), can be approximated by:

$$q_6 = \left( \frac{1}{R_{6a}} + \frac{1}{R_{6b}} \right) (T_0 - T_R), \quad (8)$$

where

$$R_{6a} = \left( \frac{60.5 \mu\text{m}}{k_P A_{P1}} + \frac{L_N}{k_N A_{P1}} + \frac{L_C}{k_C A_{P1}} + \frac{0.55}{k_C \sqrt{A_{P1}}} \right) / 20 \text{ and}$$

$$R_{6b} = \left( \frac{79 \mu\text{m}}{k_P A_{P1}} + \frac{L_N}{k_N A_{P1}} + \frac{L_C}{k_C A_{P1}} + \frac{0.55}{k_C \sqrt{A_{P1}}} \right) / 20.$$

Furthermore, 60.5  $\mu\text{m}$  is the half-length of the 20 segments of heater line, located on the free plate side, between the bondpads and the anchors to the Poly0 lines. Conduction is assumed to be taking place from the center of these lines to the anchors. Lastly, 79  $\mu\text{m}$  is the half-length of the 10 heater lines located on the free plate side between the anchors to the Poly0 lines. Conduction is also assumed to be taking place from the center of these lines to the anchors, therefore, a total of 20 segments.

Equations (1 – 3) and (5 – 8) yield:

$$\eta q = q_1 + q_2 + q_3 + q_4 + q_5 + q_6 \quad (9)$$

$$= \left( \frac{1}{R_1} + \frac{1}{R_3} + \frac{1}{R_4} + \frac{1}{R_{5a}} + \frac{1}{R_{5b}} + \frac{1}{R_{5c}} + \frac{1}{R_{6a}} + \frac{1}{R_{6b}} \right) \\ \times (T_0 - T_R) + (T_0 - T_S)/R_2$$

where  $q$  is equivalent to the total electrical power dissipated in the RPH. Equations (3) and (4) yield:

$$(T_0 - T_S)/R_2 = A_S h(T_S - T_R). \quad (10)$$

Equations (9) and (10) are two equations with three unknowns. If  $q$  is known, then (9) and (10) can be solved for  $T_0$  and  $T_S$  using a Gauss-Newton method routine. If  $T_S$  is specified, then (9) and (10) can be solved explicitly for  $q$  and  $T_0$ . Specifying  $T_S = 181^\circ\text{C}$ ,  $q$  is solved as 986.4 mW. Figure 11 is a plot of  $T_S$  versus  $q$ .

## CONCLUSIONS

The design, testing, results, and modeling of a prototype resistive point heater has been presented. The resistive point heater can assemble a MEMS device using an 8 mil diameter equivalent solder volume by applying 998 mW. Pure Sn crystal growth will occur when operating the resistive point heater in formic acid/N<sub>2</sub> vapor, however, this crystal growth does not impede the operation of the operating device or neighboring devices if the duration of power to the resistive point heater is approximately less than a minute, during the solder assembly. Less than three seconds are necessary for the actual self-assembly. Designs optimized for size, power consumption, and power distribution are being evaluated. Experiments to accurately determine the assembly time are also underway.

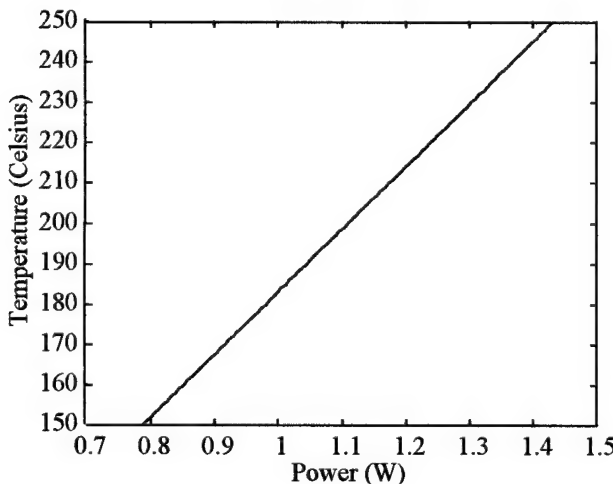


**Figure 11:** A plot of solder temperature ( $T_S$ ) versus dissipated electrical power ( $q$ ).

## ACKNOWLEDGEMENTS

Effort sponsored by the Defense Advanced Research Projects Agency (DARPA) and Air Force Research Laboratory, Air Force Materiel Command, USAF, under agreement number F30602-98-1-0219.

## REFERENCES

- [1] Kladitis, P. E., Harsh, K. F., Bright, V. M., and Lee, Y. C., Nov. 1999, "Three-Dimensional Modeling of Solder Shape for the Design of Solder Self-Assembled Micro-electro-mechanical Systems," *Proc. 1999 ASME IMECE MEMS Symposium*, Nashville, TN, MEMS-Vol. 1, pp. 11-18.
- [2] Harsh, K. F., Bright, V. M., and Lee, Y. C., 1999, "Solder Self-Assembly for Three-Dimensional Microelectromechanical Systems," *Sensors and Actuators A*, vol. 77, pp. 237-244.
- [3] Hayes, D. J., Wallace, D. B., and Cox, W. R., Apr. 1999, "MicroJet Printing of Solder and Polymers for Multi-Chip Modules and Chip-Scale Packages," *Proceedings of the IMAPS International Conference on High Density Packaging and MCMs*, Denver, CO.

- [4] Koester, D. A., Mahadevan, R., Shishkoff, A., and Markus, K. W., May 1999, *MUMPs™ Design Handbook*, Revision 4.0, Cronos Integrated Microsystems, 3021 Cornwallis Road, Research Triangle Park, NC 27709.
- [5] Dally, J. W., 1990, *Packaging of Electronic Systems: A Mechanical Engineering Approach*, McGraw-Hill, Inc., pg. 306.
- [6] Gebhart, B., Jaluria, Y., Mahajan, R. L., and Sammakia, B., 1988, *Buoyancy-Induced Flows and Transport*, Textbook Edition, Hemisphere Publishing Corporation, pg. 215.

#### **C.4 Micro Fan**

P. E. Kladitis, R. J. Linderman, and V. M. Bright, "Solder Self-Assembled Micro Axial Flow Fan Driven by a Scratch Drive Actuator Rotary Motor," *Proceedings of the Fourteenth IEEE International Micro Electro Mechanical Systems Conference (MEMS 2001)*, pp. 598-601, Interlaken, Switzerland, 21-25 Jan. 2001.

# SOLDER SELF-ASSEMBLED MICRO AXIAL FLOW FAN DRIVEN BY A SCRATCH DRIVE ACTUATOR ROTARY MOTOR

Paul E. Kladitis, Ryan J. Linderman, and Victor M. Bright

University of Colorado at Boulder

Department of Mechanical Engineering

Boulder, CO 80309-0427

Tel: 303-735-1763, Fax: 303-492-3498, E-mail: kladitis@colorado.edu, ryan.linderman@colorado.edu

## ABSTRACT

This work presents the first micro-sized axial flow fan driven by a scratch drive actuator rotary motor. The eight fan blades are mass assembled using the surface tension of molten 4 mil diameter 63Sn/37Pb manufactured solder spheres. A sample size of 27 blade angles was measured with a mean assembly angle of 107.24°. The actual mean of the manufactured solder sphere diameters was measured at 4.89 mils, yielding a model predicted, mean blade assembly angle of 107.71°. At resonance, the SDA motor can be driven at 50 RPM forward with a 2kHz AC voltage of 30V<sub>0.P.</sub>, and at 100 RPM reverse with a 3kHz signal. For non-resonant frequencies, the SDA motor can be driven in a forward direction with linear speed control up to 180 RPM using driving signals from 75 – 150 V<sub>0.P.</sub>. Fluid movement by the fan was also experimentally demonstrated.

## INTRODUCTION

As research into the nature of fluid flow at the micro scale continues, the need for experimental devices capable of producing and controlling fluid motion will become increasingly important. Applications for such devices will continue to grow to meet the needs of future chip-based chemical processing operations and micro aerosol collection and sensing systems. Additional applications exist in micro air vehicles designed for advanced atmospheric monitoring, airborne communication relay systems and surveillance tools. A critical design aspect limiting the development of these miniature systems is the need for a low-cost gas propulsion system that allows for precise control of fan blade angle-of-assembly and rotational speed.

Previous microsystem approaches to fluid mixing problems have used macro-sized diaphragm chambers, unique flow channel geometry and electric fields [1–3] to mix fluids. Completely passive macro-sized turbines that convert gas flow into rotational energy have also been demonstrated [4] by anodic-bonding layers of bulk micromachined components together. Flight mechanisms for micro air vehicles, using microelectromechanical systems (MEMS) fabrication techniques, have been previously demonstrated and investigated [5, 6].

Through the combination of key technologies, this research demonstrates the first solder self-assembled micro axial flow fan driven by a scratch drive actuator rotary motor, hereafter referred to as the fan. This fan has the potential for integration into micro-cooling systems, chemical and biological gas sensors, micro combustion mixing chambers, turbine systems, and propulsion systems for micro air vehicles. Not only are these applications further advanced by this research, but also the usefulness of many existing MEMS actuators could also be enhanced. For example, rotor-stator and comb drive electrostatic motors could also potentially be outfitted with similar solder assembled components.

## DESIGN

Figure 1 shows a scanning electron micrograph (SEM) and captured video images of the fan. The fan was fabricated using a commercial polycrystalline surface-micromachine foundry [7].

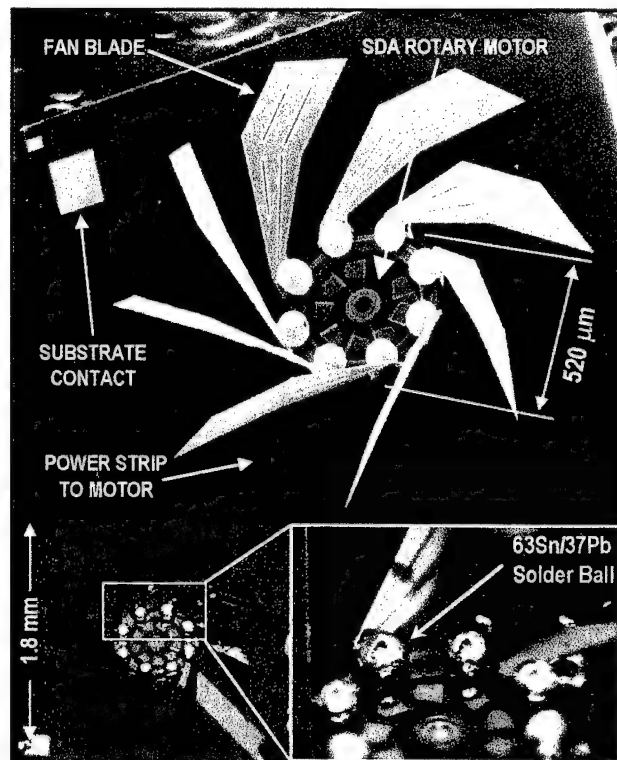


**Figure 1:** SEM and captured video images of a fan.

The design of the micro axial flow fan consists of an optimized scratch drive actuator rotary motor that has an array of eight fan blades solder-assembled to a precise angle around the perimeter of the motor. The entire fan system occupies a  $2 \times 2$  mm chip with dimensions of the fan blades, motor, and solder assembly pads shown in the layouts in Figure 2. This creates a compact design that can be easily arrayed in large numbers and or integrated with chip based systems requiring fluid movement. Figure 3 depicts active aerosol flow channel and micro air vehicle concepts.

The fan motor is driven using a simple AC voltage that produces a cyclic stepping motion with output speed controlled by the frequency of the applied drive signal. The combination of surface micromachining and solder-assembled hinge structures at the base of the fan blades not only allows for batch assembly, but also gives unlimited design options in terms of blade geometry, curvature, and angle of attack.

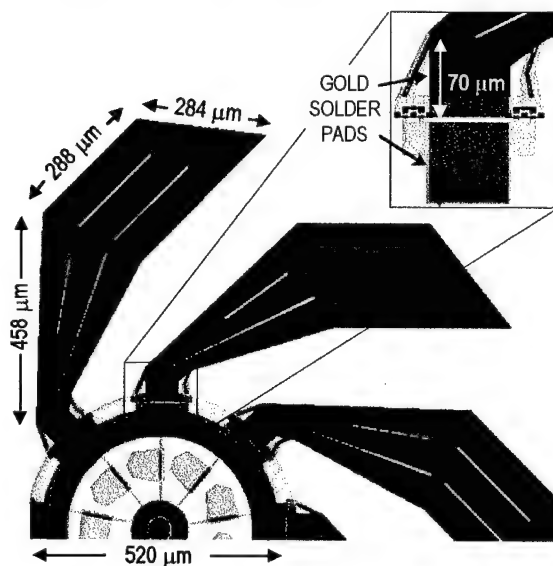


**Figure 2:** Fan component layouts showing design dimensions.

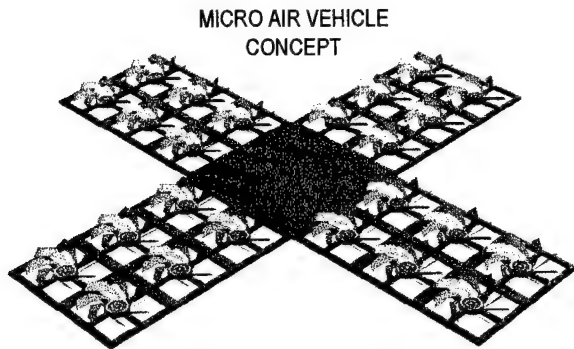
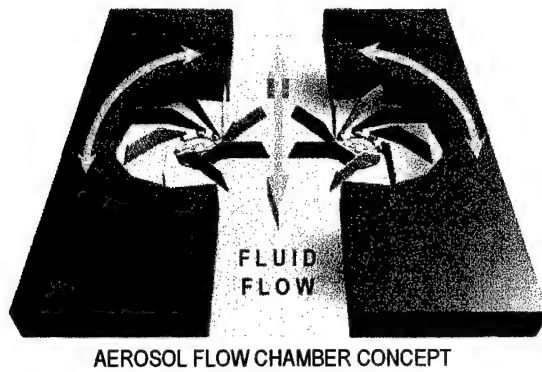


**Figure 3:** Depiction of active aerosol collector flow channel and micro air vehicle concepts.



#### FAN DRIVE PRINCIPLES

The rotary engine designed for the micro axial flow fan utilizes an array of nine optimized scratch drive actuators (SDA). The silicon substrate is used as a ground plane for electrostatic control of surface actuators. The stepping motion of the SDA occurs when the plate (see Figure 4) is deflected against the driving surface to the point where the bushing "scratches" forward storing a strain energy that is used to pull the actuator forward at the end of the stepping cycle.

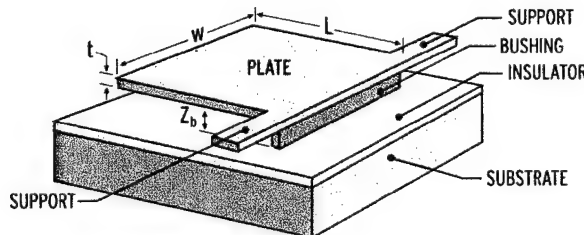


**Figure 4:** SDA terminology and important design parameters.

The critical SDA design aspects that determine performance are the properties and dimensions of the structural polysilicon layer, the bushing, the dielectric layer and the support arms. Typically, the SDA plate and support arm lengths are varied to accommodate fixed fabrication elements such as bushing height and polysilicon thickness.

Because the SDA is electrostatically actuated, a snap-through effect is observed as the voltage is increased. After the snap-through voltage is reached, the plate begins to flatten out against the driving surface and must be designed so that a minimum length remains attached throughout the stepping cycle. Conversely, if the plate is too short, excessive voltages are required to produce stepping deflections that result in increased wear and failure of components. The priming deflection is the state where any additional voltage causes the bushing to scratch forward and begin the stepping cycle. The optimum plate design occurs when the voltage required to reach the snap-through deflection is equal to the priming voltage – resulting in the best balance between drag friction and voltage response. A complete description of analytical modeling tools used to define optimum SDA geometry has been demonstrated by Linderman et al. [8]. A simple sinusoidal voltage is used to repeat the stepping motion of the SDA with output speed controlled by driving signal frequency and step size by the magnitude of the driving signal voltage. The dimensions of the SDA used for the fan rotary motor were 70 $\mu\text{m}$  long by 65 $\mu\text{m}$

wide and a bushing height of  $1.5\mu\text{m}$ . The support arms were  $4\mu\text{m}$  wide and  $30\mu\text{m}$  long with the same  $1.5\mu\text{m}$  thickness as the SDA plate.

In order to create a rotary motor, the SDAs are arranged tangentially around a central hub with a sliding contact at the perimeter of the motor allowing charge to flow into the motor (see Figure 2). The outer perimeter of the motor also provides a structural base for the solder assembly pads. A long strip of polysilicon extends from the perimeter of the motor to the edge of the chip so that wire bonding or probe tips do not obstruct the fan blades.

### SOLDER ASSEMBLY PRINCIPLES AND RESULTS

Figure 5 shows close-up views of the solder assembly joints. Each fan blade has been assembled with  $4 \pm 0.5$  mil diameter, commercially manufactured, 63Sn/37Pb solder spheres. However, the actual solder sphere diameter distribution was measured on a ZYGO interferometric microscope and estimated as  $\mu_{\text{ball}} = 4.89$  mil and  $\sigma_{\text{ball}} = 0.13$  mil. The volume and shape of the molten solder wetted to the gold pads determine the final assembled angle of the fan blade. The gold pads used for solder assembly are arranged as shown in Figure 2 and deposited  $0.5\mu\text{m}$  thick. Using the experimentally determined mean of the manufactured solder sphere diameters, the model predicted a mean fan blade assembly angle of  $107.71^\circ$  – translating to an angle of attack of  $83.3^\circ$  in the fan blade wing. While the upper and lower limits, calculated from a  $\pm 3\sigma_{\text{ball}}$  variation in solder sphere diameter, are  $113.89^\circ$  and  $100.52^\circ$ , respectively.

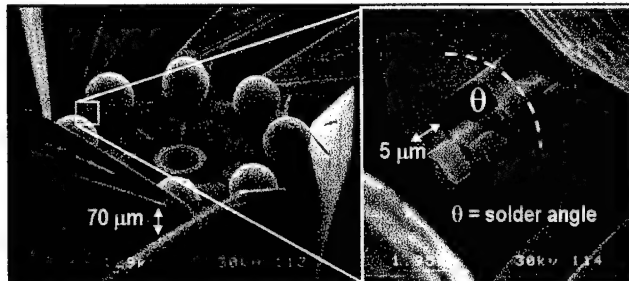


**Figure 5:** SEM close-up views of solder joints and fan blade hinge.

The fan blades are assembled in a three step process: preflow of solder onto unreleased solder pads in a N<sub>2</sub>-Formic Acid vapor environment at  $186^\circ\text{C}$ ; 3.5 minute sacrificial oxide etch in 49% HF, rinse, and critical point CO<sub>2</sub> dry; and finally a 30 second assembly reflow in a N<sub>2</sub>-Formic Acid vapor environment at  $200^\circ\text{C}$ . Kladitis et al. and Harsh et al. detail the modeling of solder shape and the solder self-assembly process [9, 10].

A sample size of 27 blade angles was measured by capturing a side profile of each blade on a video image. The angles were calculated from the pixel distances in the captured video images, and the distribution of the assembly angles was estimated to be  $\mu_{\text{angle}} = 107.24^\circ$  and  $\sigma_{\text{angle}} = 7.95^\circ$ .

### FAN DRIVE TESTING AND RESULTS

The fan was driven in ambient air environments using a sinusoidal AC voltage. Because of the solder masses on the perimeter of the motor and the large fan blade array, the motor showed two distinct operational modes that were much more pronounced than in test motors without solder and fan blades attached. The most promising characteristic demonstrated was the resonant operation that became evident at approximately 3kHz and resulted in controlled forward and reverse rotation of the motor at several times the rotational speeds of traditional drive signals (see Figure 6). Additionally, the resonant control was observed at AC voltages of  $30\text{V}_{\text{0-P}}$  — nearly one fourth the voltage of normal operational modes. During resonant operation, the motor exhibited a forward rotation of approximately 50 RPM at 2kHz with a sudden reversal in rotational direction to 100 RPM at 3kHz. This low voltage directional control is expected to extend the life span of the motor by reducing damages that have been observed as a result of higher drive voltages. More difficult to control low voltage resonant modes were also observed at the 6kHz.

The normal mode of operation was also explored and demonstrated an expected response that is observed in basic test motors without fan blades and solder balls attached. The normal operational mode produces a linear increase in RPM with an increase in driving frequency up to the point where the SDA plate becomes over-damped by the air environment. Rotational speed in the normal mode of operation can also be adjusted by increasing or decreasing the magnitude of the applied voltage which directly controls the step-size made at a given frequency. The arrows and shaded linear region in Figure 6 represent typical ranges in RPM that can be achieved by adjusting the drive voltage at a given frequency. The maximum rotational speed achieved during the fan performance evaluation was 180 RPM. Minimum drive voltages for normal operation occur at approximately  $75\text{ V}_{\text{0-P}}$  and extend beyond  $150\text{ V}_{\text{0-P}}$  at which point the motor is often permanently damaged by the excessive electrostatic forces.

The step frequency limit created by the damping effects of air was observed to begin at approximately 15 kHz in ambient air environments. The damping effect is related to the speed at which air can be forced out and drawn back under the SDA plate required for the stepping motion. Research efforts intended to reduce the frequency limitations of the SDA in air environments and to increase maximum fan RPM are currently underway. From a qualitative standpoint, the fan's SDA motor produced rotational speeds equal to and greater than test motors without fan blades or solder balls attached, indicating the motor is capable of driving arrays of much larger fan blades for increased thrust applications.

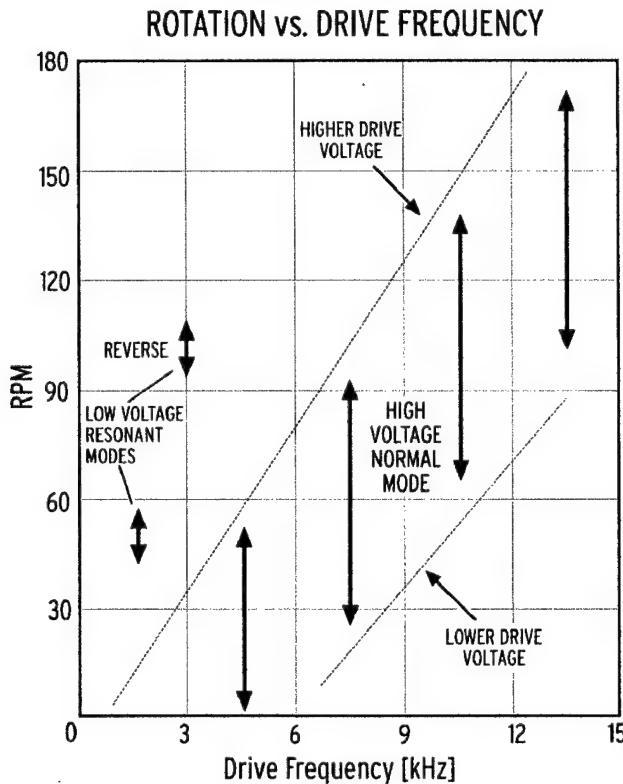


**Figure 6:** Rotary performance of SDA motor controlled fan.

### FLOW VISUALIZATION EXPERIMENTS

To visualize the fan moving fluid, the fan was tested in a chamber consisting of a sealed glass cylinder approximately three inches in diameter and one inch tall. The chamber was placed over the fan chip to prevent flows in the laboratory air from disrupting flow near the fan (see Figure 7). The glass cylinder provided for electrical probe access and a port for the injection of smoke for fluid visualization. The smoke was derived from the smooth rich flavor of second-hand Marlboro™ "reds" and cooled to 0°C before entrance to the chamber.

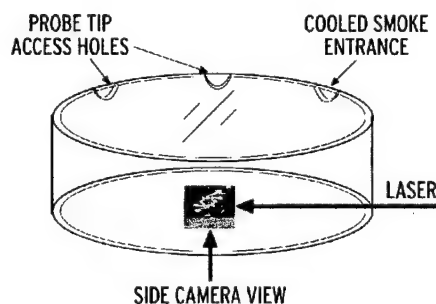


**Figure 7:** Flow visualization experimental set up.

Once the cooled smoke entered the chamber, it gently settled to the bottom surface around the micro fan with individual smoke particles being illuminated by a laser beam directed over the top of the fan. This created an environment where smoke particles could gently drift into the proximity of the fan and could be observed entering the flow produced by the fan motion as shown in Figure 8.

Referring to Figure 8, as the fan was activated at approximately 120 RPM (b), the continuous horizontal drift of the smoke particles was interrupted by an emerging burst of air forced upward (b-e) with peripheral smoke particles being

drawn into the fan flow. As the smoke particles lift over the approaching fan blade they continue to oscillate vertically with the passing of additional blade rotations (f) – providing an image of a very elastic flow environment where viscous forces dominate over weaker inertial forces.

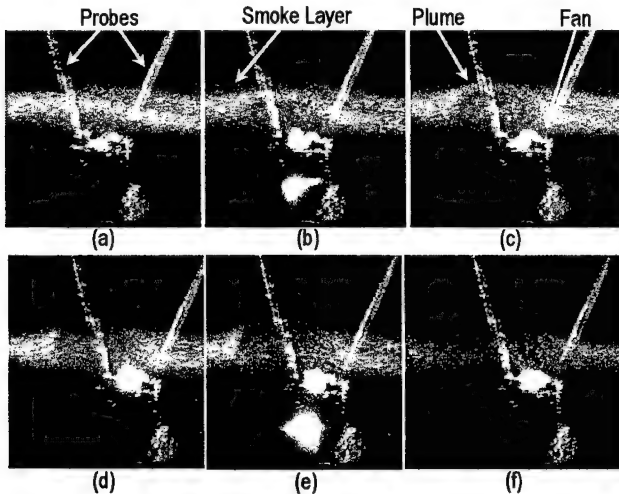


**Figure 8:** Experimental flow visualization sequence – still smoke layer (a), plume formation (b – e), and steady-state oscillation (f).

## CONCLUSIONS

By combining solder self-assembly, polycrystalline surface micromachining, and scratch drive actuation, a novel fluid moving, and truly micro-sized device was designed, fabricated, and tested. The solder self-assembled micro axial flow fan can be batch fabricated and assembled on a single surface micromachined chip. Solder assembly angles were modeled and compared to experimental results. The fan produced linearly controlled rotational speeds up to 180RPM and a resonant mode operation at approximately 3kHz – allowing for reverse and forward rotation with low drive voltages. Future work will involve modeling fluid flow, realizing a flow channel/mixer as conceptualized in Figure 3.

## ACKNOWLEDGEMENTS

Effort sponsored by the Defense Advanced Research Projects Agency (DARPA) and Air Force Research Laboratory, Air Force Materiel Command, USAF, under agreement number F30602-98-1-0219.

## FURTHER INFORMATION

For more information on solder assembly techniques, contact Paul Kladitis. All inquiries related to SDA motors, micro fan design and fluidic testing should be directed to Ryan Linderman (see title).

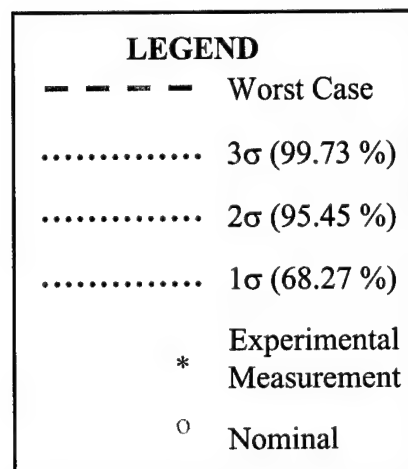
## REFERENCES

1. R. H. Liu, M. A. Stremler, K. V. Sharp, M. G. Olsen, Juang G. Santiago, R. J. Adrian, H. A. Aref, and D. J. Beebe, "Passive Mixing in a Three-Dimensional Serpentine Microchannel," *Journal of MEMS*, vol. 9, no. 2, pp. 190-197, June 2000.
2. J. W. Choi and C. H. Ahn, "An Active Micro Mixer Using Electrohydrodynamic (EHD) Convection," *Proceedings of the Solid-State Sensor and Actuator Workshop*, Hilton Head Isl., SC, pp. 52-55, June 2000.
3. Z. Yang, H. Goto, M. Matsumoto, and R. Maeda, "Ultrasonic Micromixer for Microfluidic Systems," *Proceedings of 13th Annual International Conference on Micro Electro Mechanical Systems*, Miyazaki, Japan, pp. 80-85, January 2000.
4. A. H. Epstein, S. A. Jacobson, J. M. Protz, and L. G. Frechette, "Shirtbutton-Sized Gas Turbines: The Engineering Challenges of Micro High Speed Rotating Machinery," *Proceedings of the 8th International Symposium on Transport Phenomena and Dynamics of Rotating Machinery*, Honolulu, HI, March 2000.
5. N. Miki and I. Shimoyama, "A Micro-Flight Mechanism with Rotational Wings," *Proceedings of 13th Annual International Conference on Micro Electro Mechanical Systems*, Miyazaki, Japan, pp. 158-163, January 2000.
6. T. N. Pornsinsirirak, S. W. Lee, H. Nassef, J. Grasmeyer, Y. C. Tai, C. M. Ho, and M. Keenon, "MEMS Wing Technology for a Battery-Powered Ornithopter," *Proceedings of 13th Annual International Conference on Micro Electro Mechanical Systems*, Miyazaki, Japan, pp. 799-804, January 2000.
7. D. A. Koester, R. Mahadevan, A. Shishkoff, and K. W. Markus, *MUMPs™ Design Handbook*, Revision 4.0, Cronos Integrated Microsystems, 3021 Cornwallis Road, Research Triangle Park, NC 27709, May 1999.
8. R. J. Linderman and V. M. Bright, "Optimized Scratch Drive Actuator for Tethered Nanometer Positioning of Chip Sized Components," *Technical Digest 2000 Solid-State Sensor and Actuator Workshop*, Hilton Head Isl., SC, pp. 214-217, June 2000.
9. P. E. Kladitis, K. F. Harsh, V. M. Bright, and Y. C. Lee, "Three-Dimensional Modeling of Solder Shape for the Design of Solder Self-Assembled Micro-electro-mechanical Systems," *Proc. 1999 ASME IMECE MEMS Symposium*, Nashville, TN, MEMS-Vol. 1, pp. 11-18, November 1999.
10. K. F. Harsh, V. M. Bright, and Y. C. Lee, "Solder Self-Assembly for Three-Dimensional Microelectromechanical Systems," *Sensors and Actuators A*, vol. 77, pp. 237-244, 1999.

## Appendix D Experimental Results

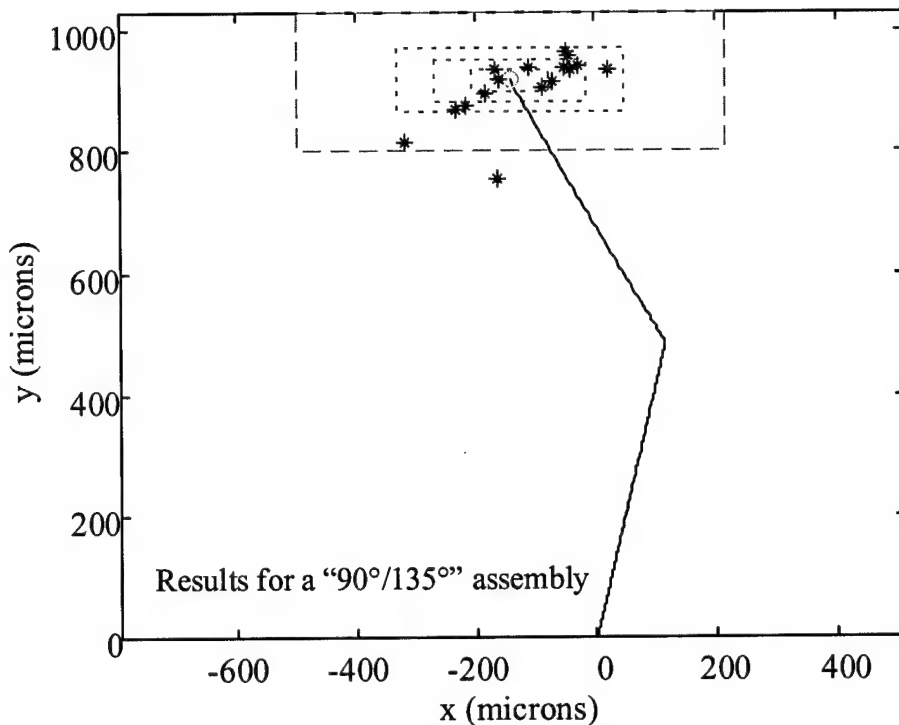
The following plots are described in Chapter 6: Issues In Assembly Precision.

The legend shown in Figure D-1 is for all of the following figures.



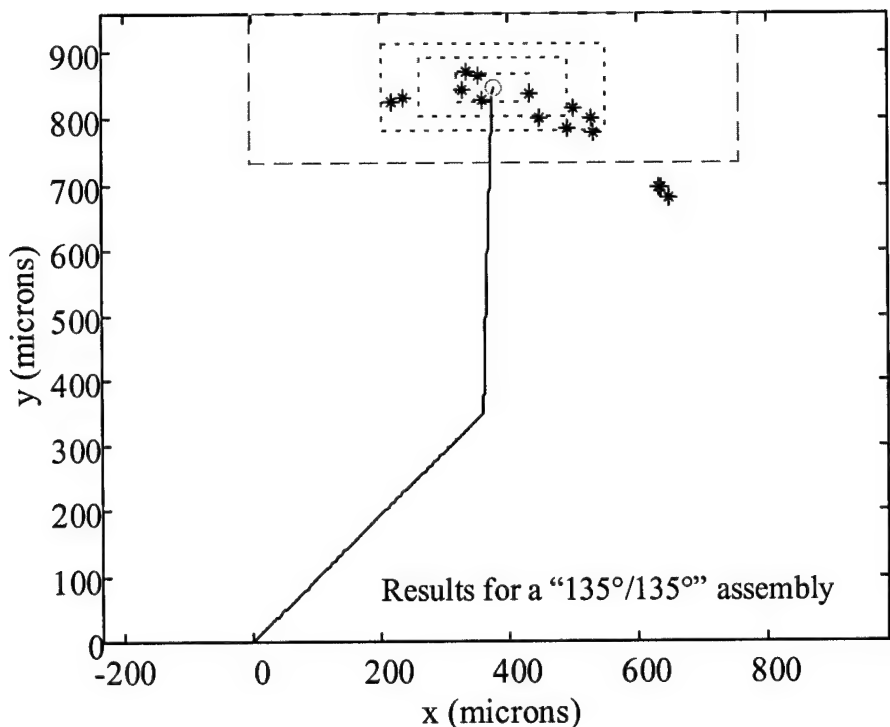
**Figure D-1:** Legend for the following plots.

## D.1 8 Mil Test Structures



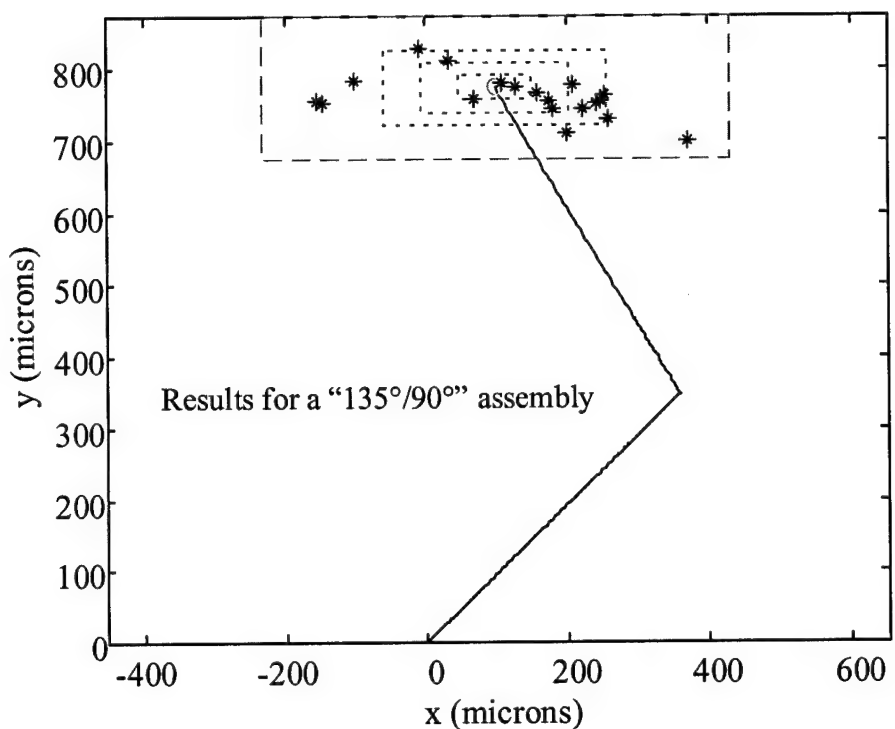
Variable ( $x_i$ )	$df^x/dx_i$	$df^y/dx_i$	$tol_i$	$nominal_i$	impact $f_i^x$	impact $f_i^y$
$L_1$ ( $\mu\text{m}$ )	2.6153E-01	9.8324E-01	2.00	500.00	0.52305272	1.96647796
$L_2$ ( $\mu\text{m}$ )	-5.0470E-01	8.6354E-01	2.00	500.00	1.00939588	1.72708206
stress <sub>poly</sub> p11 (Pa)	-1.1646E-06	-3.6841E-07	2820000.00	-7900000.00	3.28415649	1.03890241
stress <sub>poly</sub> p12 (Pa)	-4.7441E-07	-2.9046E-07	2820000.00	-7900000.00	1.337838907	0.819085582
R <sub>sol/poly</sub> p1pd1 ( $\mu\text{m}$ )	2.9531E-03	5.4319E-04	1000.00	6000.00	2.9530767	0.54318873
R <sub>sol/poly</sub> p1pd2 ( $\mu\text{m}$ )	1.0269E-03	5.4313E-04	1000.00	6000.00	1.0269057	0.54312897
R <sub>sol/poly</sub> p1pd3 ( $\mu\text{m}$ )	8.6860E-04	5.1964E-04	1000.00	6000.00	0.86859926	0.51963806
$h_{1x}$ ( $\mu\text{m}$ )	1.0000E+00	0.0000E+00	0.50	0.00	0.5	0
$h_{1y}$ ( $\mu\text{m}$ )	0.0000E+00	1.0000E+00	0.50	0.00	0	0.5
$h_{2x}$ ( $\mu\text{m}$ )	2.2383E-01	9.7464E-01	0.50	0.00	0.111917495	0.487319945
$h_{2y}$ ( $\mu\text{m}$ )	-9.7463E-01	2.2383E-01	0.50	0.00	0.487317085	0.11191559
$D_1$ ( $\mu\text{m}$ )	6.2810E+00	9.7204E-01	25.95	214.75	162.9913064	25.22447407
$D_2$ ( $\mu\text{m}$ )	2.1908E+00	1.3132E+00	25.95	214.75	56.85243294	34.0770236
$I_1$ ( $\mu\text{m}$ )	-9.7791E+00	-1.5238E+00	6.00	131-6	58.6748982	9.1426632
$I_2$ ( $\mu\text{m}$ )	-5.3769E+00	-3.2087E+00	9.00	70+9	48.3923898	28.8784296
$w_1$ ( $\mu\text{m}$ )	-1.1820E+00	-1.8293E-01	6.00	131-6	7.0920732	1.09756638
$w_2$ ( $\mu\text{m}$ )	-6.8786E-01	-4.1230E-01	18.00	70+18	12.38148054	7.42138956
T0	T_WC	T_S3	T_S2	T_S1		
-141.67	358.52	189.26	126.17	63.09		
915.40	114.11	52.74	35.16	17.58		

Figure D-2: 90/135 8 mil variant.



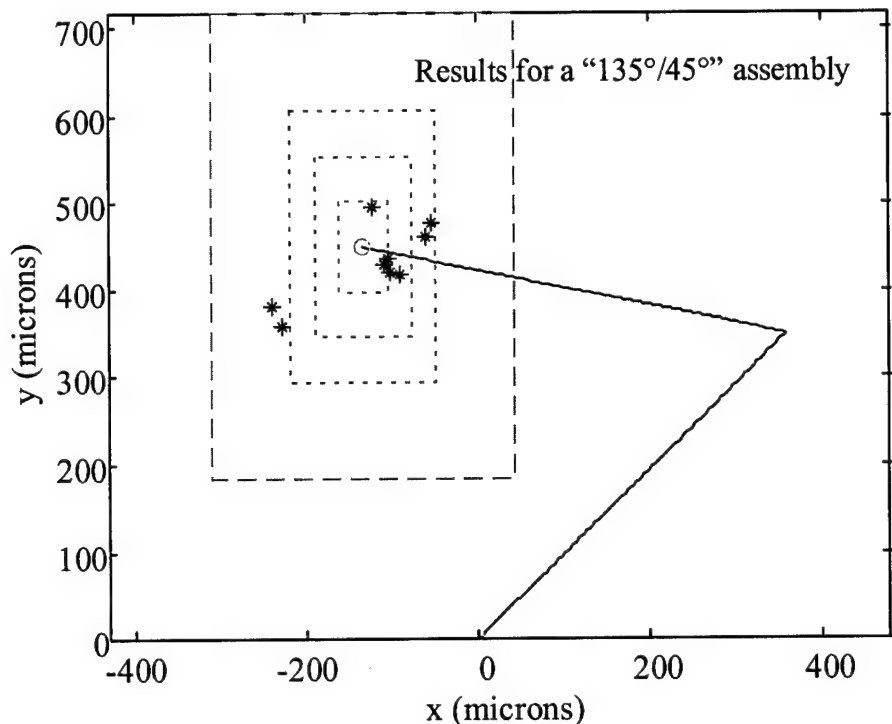
Variable ( $x_i$ )	$df^x/dx_i$	$df^y/dx_i$	$tol_i$	$nominal_i$	impact $f^x_i$	impact $f^y_i$
$L_1$ ( $\mu\text{m}$ )	7.5270E-01	6.8459E-01	2.00	500.00	1.5053993	1.36918628
$L_2$ ( $\mu\text{m}$ )	4.3828E-02	9.9925E-01	2.00	500.00	0.08765506	1.9985017
stress <sub>poly</sub> p11 (Pa)	-1.3991E-06	4.0662E-07	2820000.00	-7900000.00	3.94555224	1.146662083
stress <sub>poly</sub> p12 (Pa)	-5.5611E-07	1.2997E-08	2820000.00	-7900000.00	1.568235502	0.036651574
R <sub>sol/poly</sub> p1pd1 ( $\mu\text{m}$ )	1.7910E-03	-7.5710E-04	1000.00	6000.00	1.7909654	0.75710169
R <sub>sol/poly</sub> p1pd2 ( $\mu\text{m}$ )	1.1574E-03	-1.0006E-04	1000.00	6000.00	1.1573728	0.10006332
R <sub>sol/poly</sub> p1pd3 ( $\mu\text{m}$ )	1.0116E-03	-3.4016E-05	1000.00	6000.00	1.0115967	0.034015656
$h_{1x}$ ( $\mu\text{m}$ )	1.0000E+00	0.0000E+00	0.50	0.00	0.5	0
$h_{1y}$ ( $\mu\text{m}$ )	0.0000E+00	1.0000E+00	0.50	0.00	0	0.5
$h_{2x}$ ( $\mu\text{m}$ )	7.1629E-01	6.9777E-01	0.50	0.00	0.35814476	0.348884585
$h_{2y}$ ( $\mu\text{m}$ )	-6.9779E-01	7.1631E-01	0.50	0.00	0.348896025	0.358154295
$D_1$ ( $\mu\text{m}$ )	4.3259E+00	-1.9223E+00	25.95	214.75	112.2560229	49.88419103
$D_2$ ( $\mu\text{m}$ )	2.5529E+00	-8.3680E-02	25.95	214.75	66.24747215	2.171488864
$I_1$ ( $\mu\text{m}$ )	-1.0416E+01	4.6216E+00	9.00	70+9	93.747852	41.594598
$I_2$ ( $\mu\text{m}$ )	-6.2579E+00	2.1730E-01	9.00	70+9	56.3206635	1.95574455
$w_1$ ( $\mu\text{m}$ )	-1.3582E+00	6.0355E-01	18.00	70+18	24.4474272	10.863918
$w_2$ ( $\mu\text{m}$ )	-8.0153E-01	2.6273E-02	18.00	70+18	14.42755656	0.472916178
T0	T_WC	T_S3	T_S2	T_S1		
376.31	379.75	172.59	115.06	57.53		
846.83	113.60	65.99	43.99	22.00		

**Figure D-3:** 135/135 8 mil variant.



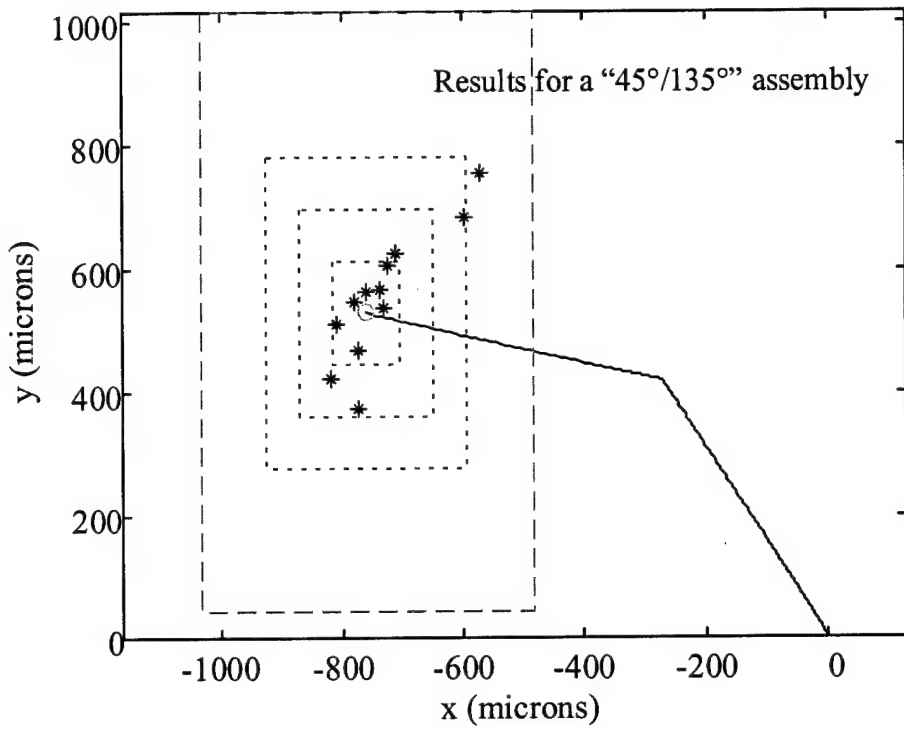
Variable ( $x_i$ )	$df^x/dx_i$	$df^y/dx_i$	$tol_i$	$nominal_i$	impact $f^x_i$	impact $f^y_i$
$L_1$ ( $\mu\text{m}$ )	7.4914E-01	6.9809E-01	2.00	500.00	1.49827434	1.39618636
$L_2$ ( $\mu\text{m}$ )	-5.1324E-01	8.5844E-01	2.00	500.00	1.02647614	1.7168837
stress <sub>poly</sub> p11 (Pa)	-1.1063E-06	-1.1616E-07	2820000.00	-7900000.00	3.119855394	0.327571059
stress <sub>poly</sub> p12 (Pa)	-3.7461E-07	-2.3335E-07	2820000.00	-7900000.00	1.056409816	0.658037074
R <sub>sol/poly</sub> p11pd1 ( $\mu\text{m}$ )	1.6326E-03	-1.4809E-04	1000.00	6000.00	1.63259	0.14808909
R <sub>sol/poly</sub> p11pd2 ( $\mu\text{m}$ )	1.6342E-03	7.4386E-04	1000.00	6000.00	1.6341845	0.74385579
R <sub>sol/poly</sub> p12pd1 ( $\mu\text{m}$ )	1.3011E-03	7.9151E-04	1000.00	6000.00	1.301089	0.79151026
$h_{1x}$ ( $\mu\text{m}$ )	1.0000E+00	0.0000E+00	0.50	0.00	0.5	0
$h_{1y}$ ( $\mu\text{m}$ )	0.0000E+00	1.0000E+00	0.50	0.00	0	0.5
$h_{2x}$ ( $\mu\text{m}$ )	7.0937E-01	7.0486E-01	0.50	0.00	0.35468292	0.352428435
$h_{2y}$ ( $\mu\text{m}$ )	-7.0485E-01	7.0937E-01	0.50	0.00	0.352422715	0.35468292
$D_1$ ( $\mu\text{m}$ )	3.9571E+00	-5.0440E-01	25.95	214.75	102.6874223	13.08924358
$D_2$ ( $\mu\text{m}$ )	2.9286E+00	1.7872E+00	25.95	214.75	75.99824693	46.37789709
$I_1$ ( $\mu\text{m}$ )	-9.5275E+00	1.2034E+00	9.00	70+9	85.7470878	10.8303642
$I_2$ ( $\mu\text{m}$ )	-4.6609E+00	-2.8127E+00	6.00	131-6	27.965208	16.8761538
$w_1$ ( $\mu\text{m}$ )	-1.2424E+00	1.5837E-01	18.00	70+18	22.3635528	2.85061194
$w_2$ ( $\mu\text{m}$ )	-5.5114E-01	-3.3633E-01	6.00	131-6	3.30683388	2.01799368
T0	T_WC	T_S3	T_S2	T_S1		
98.74	330.57	158.09	105.39	52.70		
774.65	99.04	52.39	34.92	17.46		

**Figure D-4:** 135/90 8 mil variant.



Variable ( $x_i$ )	$df^x/dx_i$	$df^y/dx_i$	$tol_i$	$nominal_i$	impact $f_i^x$	impact $f_i^y$
$L_1$ ( $\mu\text{m}$ )	7.3328E-01	7.0935E-01	2.00	500.00	1.46656428	1.4186927
$L_2$ ( $\mu\text{m}$ )	-9.7885E-01	2.0511E-01	2.00	500.00	1.95770562	0.410216
stress <sub>poly</sub> p11 (Pa)	-4.3064E-07	-3.6834E-07	2820000.00	-7900000.00	1.214416954	1.038732195
stress <sub>poly</sub> p12 (Pa)	-5.5632E-08	-2.8660E-07	2820000.00	-7900000.00	0.156881696	0.808226015
$R_{\text{sol/poly}}$ p1pd1 ( $\mu\text{m}$ )	9.2037E-04	3.5893E-04	1000.00	6000.00	0.92037233	0.35892741
$R_{\text{sol/poly}}$ p1pd2 ( $\mu\text{m}$ )	9.1673E-04	2.2621E-03	1000.00	6000.00	0.91672993	2.2621326
$R_{\text{sol/poly}}$ p2pd1 ( $\mu\text{m}$ )	4.4554E-04	2.1432E-03	1000.00	6000.00	0.44553534	2.1431859
$h_{1x}$ ( $\mu\text{m}$ )	1.0000E+00	0.0000E+00	0.50	0.00	0.5	0
$h_{1y}$ ( $\mu\text{m}$ )	0.0000E+00	1.0000E+00	0.50	0.00	0	0.5
$h_{2x}$ ( $\mu\text{m}$ )	6.9867E-01	7.1545E-01	0.50	0.00	0.349333765	0.35772705
$h_{2y}$ ( $\mu\text{m}$ )	-7.1545E-01	6.9866E-01	0.50	0.00	0.357726095	0.349328995
$D_1$ ( $\mu\text{m}$ )	2.2989E+00	6.7604E-01	25.95	214.75	59.65722831	17.54320271
$D_2$ ( $\mu\text{m}$ )	9.3023E-01	4.5366E+00	25.95	214.75	24.13953934	117.7245079
$I_1$ ( $\mu\text{m}$ )	-5.5299E+00	-1.6424E+00	9.00	70+9	49.7689641	14.7815343
$I_2$ ( $\mu\text{m}$ )	-9.5570E-01	-4.4836E+00	22.00	217-22	21.02544268	98.638485
$w_1$ ( $\mu\text{m}$ )	-7.2180E-01	-2.1226E-01	18.00	70+18	12.99231702	3.820608
$w_2$ ( $\mu\text{m}$ )	-1.2419E-01	-6.0567E-01	7.00	217-7	0.86935352	4.23969168
T0	T_WC	T_S3	T_S2	T_S1		
-132.34	176.75	85.10	56.73	28.37		
450.04	266.41	155.45	103.64	51.82		

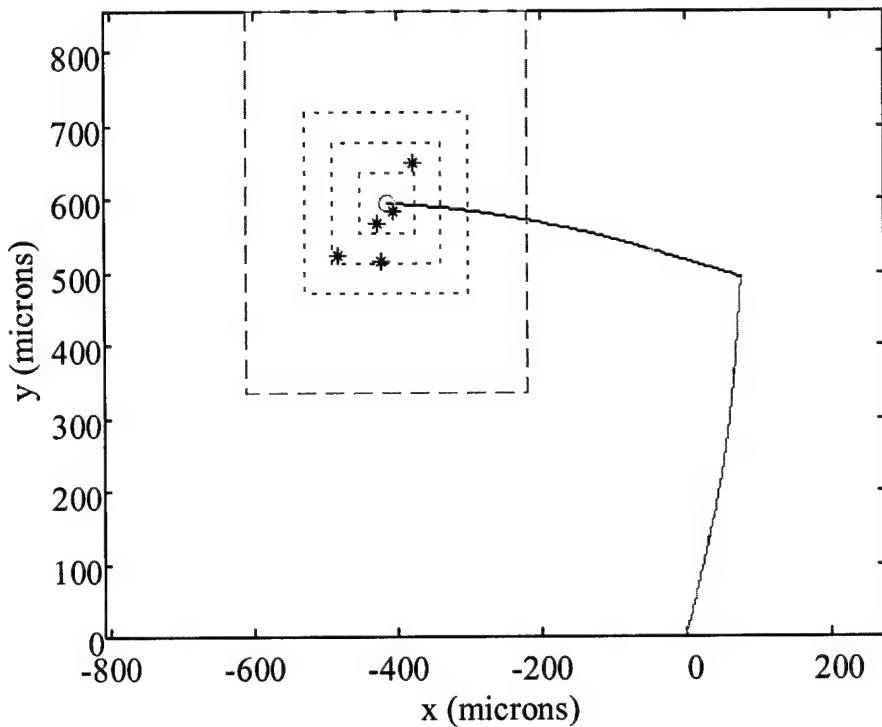
Figure D-5: 135/45 8 mil variant.



Variable ( $x_i$ )	$df^x/dx_i$	$df^y/dx_i$	tol <sub>i</sub>	nominal <sub>i</sub>	impact $f_i^x$	impact $f_i^y$
L <sub>1</sub> (μm)	-5.3222E-01	8.6707E-01	2.00	500.00	1.06443114	1.73414104
L <sub>2</sub> (μm)	-9.7353E-01	2.2947E-01	2.00	500.00	1.94706842	0.45893038
stress <sub>poly</sub> p11 (Pa)	-3.5999E-07	-7.9439E-07	2820000.00	-7900000.00	1.015184293	2.240185073
stress <sub>poly</sub> p12 (Pa)	-1.1651E-07	-5.4393E-07	2820000.00	-7900000.00	0.328556931	1.53387022
R <sub>sol/poly</sub> p1pd1 (μm)	2.3976E-03	3.7987E-03	1000.00	6000.00	2.3975779	3.798748
R <sub>sol/poly</sub> p1pd2 (μm)	3.1421E-04	1.1184E-03	1000.00	6000.00	0.31421026	1.1183879
R <sub>sol/poly</sub> p1pd1 (μm)	2.2213E-04	9.8749E-04	1000.00	6000.00	0.22212728	0.98749415
h <sub>1x</sub> (μm)	1.00000E+00	0.00000E+00	0.50	0.00	0.5	0
h <sub>1y</sub> (μm)	0.00000E+00	1.00000E+00	0.50	0.00	0	0.5
h <sub>2x</sub> (μm)	-5.5193E-01	8.3389E-01	0.50	0.00	0.27596283	0.416942595
h <sub>2y</sub> (μm)	-8.3390E-01	-5.5192E-01	0.50	0.00	0.416950225	0.275959015
D <sub>1</sub> (μm)	4.9052E+00	7.0272E+00	25.95	214.75	127.2904798	182.3561955
D <sub>2</sub> (μm)	5.5844E-01	2.4925E+00	25.95	214.75	14.4916205	64.67948492
I <sub>1</sub> (μm)	-4.7748E+00	-6.8685E+00	22.00	217-22	105.0454482	151.1059286
I <sub>2</sub> (μm)	-1.3808E+00	-6.1073E+00	9.00	70+9	12.427371	54.9660528
w <sub>1</sub> (μm)	-6.5489E-01	-9.3819E-01	7.00	217-7	4.58419724	6.56731593
w <sub>2</sub> (μm)	-1.7533E-01	-7.8256E-01	18.00	70+18	3.15602568	14.08607856
T <sub>0</sub>	T <sub>WC</sub>	T <sub>S3</sub>	T <sub>S2</sub>	T <sub>S1</sub>		
-758.76	275.50	166.28	110.86	55.43		
529.64	486.86	252.13	168.09	84.04		

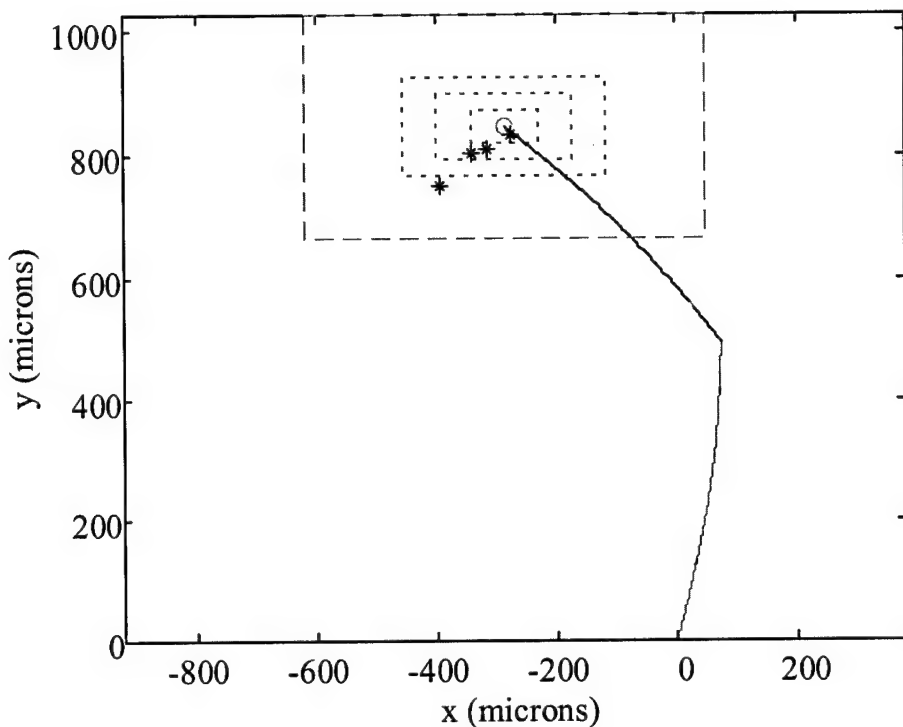
Figure D-6: 45/135 8 mil variant.

## D.2 8 Mil Warp Test Structures



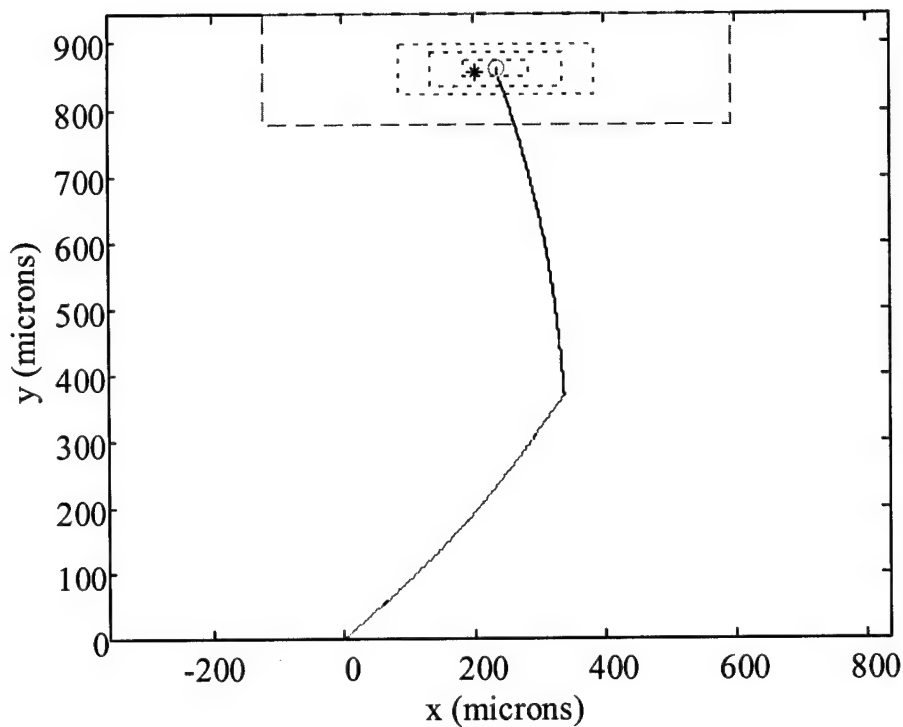
Variable ( $x_i$ )	$df^x/dx_i$	$df^y/dx_i$	$tol_i$	$nominal_i$	impact $f_i^x$	impact $f_i^y$
$L_1$ ( $\mu\text{m}$ )	-6.5492E-02	7.0645E-01	2.00	500.00	1.3098E-01	1.4129E+00
$L_2$ ( $\mu\text{m}$ )	-1.0251E+00	5.8588E-02	2.00	500.00	2.0503E+00	1.1718E-01
stress <sub>poly</sub> (Pa)	-4.6839E-08	-7.9675E-08	2820000.00	-7900000.00	1.3209E-01	2.2468E-01
stress <sub>gold</sub> (Pa)	-5.9114E-07	-1.0155E-06	21000000.00	103500000.00	1.2414E+01	2.1326E+01
R <sub>sol/poly</sub> p1pd1 ( $\mu\text{m}$ )	1.8436E-03	1.4896E-03	1000.00	6000.00	1.8436E+00	1.4896E+00
R <sub>sol/poly</sub> p1pd2 ( $\mu\text{m}$ )	5.7456E-04	1.6865E-03	1000.00	6000.00	5.7456E-01	1.6865E+00
R <sub>sol/poly</sub> p12pd1 ( $\mu\text{m}$ )	2.9382E-04	1.5010E-03	1000.00	6000.00	2.9382E-01	1.5010E+00
$h_{1x}$ ( $\mu\text{m}$ )	1.0000E+00	0.0000E+00	0.50	0.00	5.0000E-01	0.0000E+00
$h_{1y}$ ( $\mu\text{m}$ )	0.0000E+00	1.0000E+00	0.50	0.00	0.0000E+00	5.0000E-01
$h_{2x}$ ( $\mu\text{m}$ )	6.2515E-02	9.9805E-01	0.50	0.00	3.1258E-02	4.9902E-01
$h_{2y}$ ( $\mu\text{m}$ )	-9.9805E-01	6.2508E-02	0.50	0.00	4.9902E-01	3.1254E-02
$D_1$ ( $\mu\text{m}$ )	4.0876E+00	2.8431E+00	25.95	214.75	1.0607E+02	7.3779E+01
$D_2$ ( $\mu\text{m}$ )	6.9976E-01	3.3704E+00	25.95	214.75	1.8159E+01	8.7462E+01
$I_1$ ( $\mu\text{m}$ )	-6.0435E+00	-4.1548E+00	6.00	131.6	3.6261E+01	2.4929E+01
$I_2$ ( $\mu\text{m}$ )	-9.0498E-01	-4.7835E+00	6.00	131.6	5.4299E+00	2.8701E+01
$w_1$ ( $\mu\text{m}$ )	-7.6925E-01	-5.3505E-01	6.00	131.6	4.6155E+00	3.2103E+00
$w_2$ ( $\mu\text{m}$ )	-1.3169E-01	-6.3428E-01	6.00	131.6	7.9013E-01	3.8057E+00
Temperature (°C)	9.5574E-01	1.6419E+00	6.00	27.00	5.7345E+00	9.8513E+00
T0	T_WC	T_S3	T_S2	T_S1		
-414.36	195.55	114.66	76.44	38.22		
595.74	260.55	123.00	82.00	41.00		

Figure D-7: 90/90 8 mil warp variant.



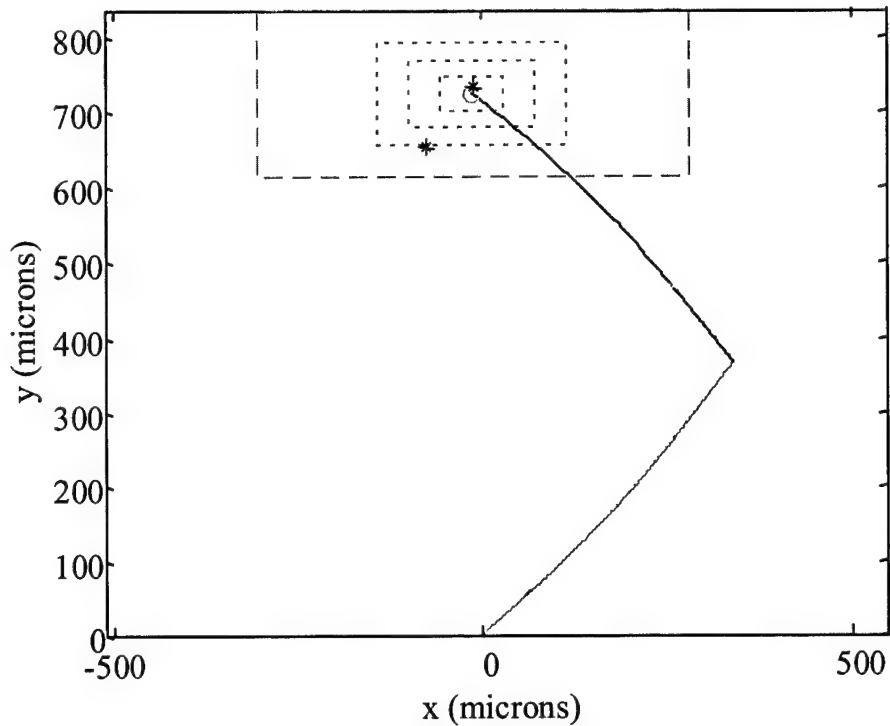
Variable ( $x_i$ )	$df^x/dx_i$	$df^y/dx_i$	$tol_i$	$nominal_i$	impact $f^x_i$	impact $f^y_i$
$L_1$ ( $\mu\text{m}$ )	-2.1932E-01	7.9445E-01	2.00	500.00	4.3864E-01	1.5889E+00
$L_2$ ( $\mu\text{m}$ )	-8.3953E-01	6.0449E-01	2.00	500.00	1.6791E+00	1.2090E+00
stress <sub>poly</sub> (Pa)	-8.8534E-08	-6.0351E-08	2820000.00	-7900000.00	2.4967E-01	1.7019E-01
stress <sub>gold</sub> (Pa)	-1.3604E-06	-8.7133E-07	21000000.00	103500000.00	2.8568E+01	1.8298E+01
R <sub>sol/poly</sub> p1pd1 ( $\mu\text{m}$ )	2.7145E-03	1.0403E-03	1000.00	6000.00	2.7145E+00	1.0403E+00
R <sub>sol/poly</sub> p1pd2 ( $\mu\text{m}$ )	8.1303E-04	7.4391E-04	1000.00	6000.00	8.1303E-01	7.4391E-01
R <sub>sol/poly</sub> p1pd1 ( $\mu\text{m}$ )	6.7424E-04	6.9954E-04	1000.00	6000.00	6.7424E-01	6.9954E-01
$h_{1x}$ ( $\mu\text{m}$ )	1.0000E+00	0.0000E+00	0.50	0.00	5.0000E-01	0.0000E+00
$h_{1y}$ ( $\mu\text{m}$ )	0.0000E+00	1.0000E+00	0.50	0.00	0.0000E+00	5.0000E-01
$h_{2x}$ ( $\mu\text{m}$ )	3.9799E-02	9.9921E-01	0.50	0.00	1.9899E-02	4.9960E-01
$h_{2y}$ ( $\mu\text{m}$ )	-9.9921E-01	3.9810E-02	0.50	0.00	4.9960E-01	1.9905E-02
D <sub>1</sub> ( $\mu\text{m}$ )	5.8093E+00	1.9548E+00	25.95	214.75	1.5075E+02	5.0728E+01
D <sub>2</sub> ( $\mu\text{m}$ )	1.7612E+00	1.7963E+00	25.95	214.75	4.5704E+01	4.6614E+01
I <sub>1</sub> ( $\mu\text{m}$ )	-8.5652E+00	-2.8623E+00	6.00	131-6	5.1391E+01	1.7174E+01
I <sub>2</sub> ( $\mu\text{m}$ )	-3.9803E+00	-4.1615E+00	5.00	70+5	1.9902E+01	2.0808E+01
w <sub>1</sub> ( $\mu\text{m}$ )	-1.0933E+00	-3.6788E-01	6.00	131-6	6.5595E+00	2.2073E+00
w <sub>2</sub> ( $\mu\text{m}$ )	-6.0143E-01	-6.1341E-01	18.00	70+18	1.0826E+01	1.1041E+01
Temperature (°C)	2.1995E+00	1.4087E+00	6.00	27.00	1.3197E+01	8.4524E+00
T <sub>0</sub>	T_WC	T_S3	T_S2	T_S1		
-284.90	334.52	170.36	113.57	56.79		
846.65	181.81	77.56	51.70	25.85		

Figure D-8: 90/135 8 mil warp variant.



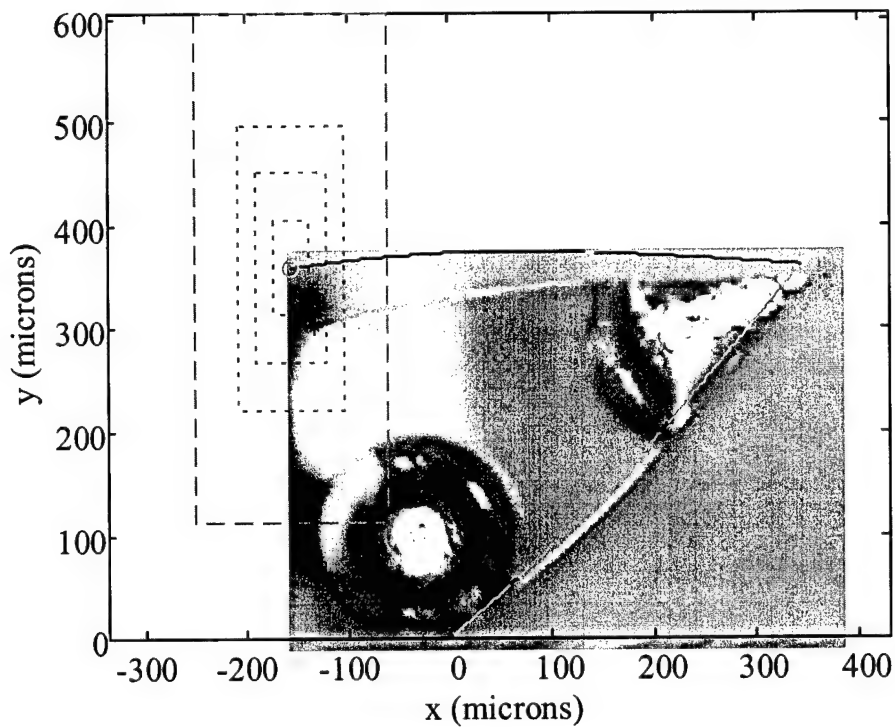
Variable ( $x_i$ )	$df^x/dx_i$	$df^y/dx_i$	$tol_i$	$nominal_i$	impact $f^x_i$	impact $f^y_i$
$L_1$ ( $\mu\text{m}$ )	2.6651E-01	7.8773E-01	2.00	500.00	5.3302E-01	1.5755E+00
$L_2$ ( $\mu\text{m}$ )	-3.6200E-01	9.6911E-01	2.00	500.00	7.2400E-01	1.9382E+00
stress <sub>poly</sub> (Pa)	-1.0927E-07	1.3269E-09	2820000.00	-7900000.00	3.0813E-01	3.7420E-03
stress <sub>gold</sub> (Pa)	-1.8269E-06	9.1632E-08	21000000.00	103500000.00	3.8365E+01	1.9243E+00
$R_{\text{sol/poly}}$ p1pd1 ( $\mu\text{m}$ )	1.7360E-03	-4.2614E-04	1000.00	6000.00	1.7360E+00	4.2614E-01
$R_{\text{sol/poly}}$ p1pd2 ( $\mu\text{m}$ )	1.0893E-03	1.6661E-04	1000.00	6000.00	1.0893E+00	1.6661E-01
$R_{\text{sol/poly}}$ p1pd3 ( $\mu\text{m}$ )	9.4930E-04	2.0686E-04	1000.00	6000.00	9.4930E-01	2.0686E-01
$h_{1x}$ ( $\mu\text{m}$ )	1.0000E+00	0.0000E+00	0.50	0.00	5.0000E-01	0.0000E+00
$h_{1y}$ ( $\mu\text{m}$ )	0.0000E+00	1.0000E+00	0.50	0.00	0.0000E+00	5.0000E-01
$h_{2x}$ ( $\mu\text{m}$ )	5.8840E-01	8.0857E-01	0.50	0.00	2.9420E-01	4.0429E-01
$h_{2y}$ ( $\mu\text{m}$ )	-8.0858E-01	5.8839E-01	0.50	0.00	4.0429E-01	2.9420E-01
$D_1$ ( $\mu\text{m}$ )	4.3071E+00	-1.1796E+00	25.95	214.75	1.1177E+02	3.0611E+01
$D_2$ ( $\mu\text{m}$ )	2.4625E+00	5.1457E-01	25.95	214.75	6.3901E+01	1.3353E+01
$I_1$ ( $\mu\text{m}$ )	-1.0260E+01	2.8107E+00	5.00	70+5	5.1302E+01	1.4053E+01
$I_2$ ( $\mu\text{m}$ )	-5.6291E+00	-1.2530E+00	5.00	70+5	2.8146E+01	6.2652E+00
$w_1$ ( $\mu\text{m}$ )	-1.4708E+00	4.0282E-01	18.00	70+18	2.6475E+01	7.2508E+00
$w_2$ ( $\mu\text{m}$ )	-8.4090E-01	-1.7572E-01	18.00	70+18	1.5136E+01	3.1629E+00
Temperature (°C)	2.9537E+00	-1.4815E-01	6.00	27.00	1.7722E+01	8.8889E-01
T0	T_WC	T_S3	T_S2	T_S1		
235.84	359.38	150.76	100.50	50.25		
861.10	83.03	37.77	25.18	12.59		

**Figure D-9:** 135/135 8 mil warp variant.



Variable ( $x_i$ )	$df^x/dx_i$	$df^y/dx_i$	$tol_i$	$nominal_i$	$impact \hat{r}^x_i$	$impact \hat{r}^y_i$
$L_1$ ( $\mu\text{m}$ )	3.4365E-01	6.2958E-01	2.00	500.00	6.8730E-01	1.2592E+00
$L_2$ ( $\mu\text{m}$ )	-8.1989E-01	6.1815E-01	2.00	500.00	1.6398E+00	1.2363E+00
$\text{stress}_{\text{poly}}$ (Pa)	-8.5313E-08	-3.7941E-08	2820000.00	-7900000.00	2.4058E-01	1.0699E-01
$\text{stress}_{\text{gold}}$ (Pa)	-1.2363E-06	-5.3152E-07	21000000.00	103500000.00	2.5961E+01	1.1162E+01
$R_{\text{sol/poly}} \text{ p1pd1}$ ( $\mu\text{m}$ )	1.4507E-03	8.9138E-05	1000.00	6000.00	1.4507E+00	8.9138E-02
$R_{\text{sol/poly}} \text{ p1pd2}$ ( $\mu\text{m}$ )	1.4146E-03	1.0833E-03	1000.00	6000.00	1.4146E+00	1.0833E+00
$R_{\text{sol/poly}} \text{ p1pd2}$ ( $\mu\text{m}$ )	1.0781E-03	1.0849E-03	1000.00	6000.00	1.0781E+00	1.0849E+00
$h_{1x}$ ( $\mu\text{m}$ )	1.0000E+00	0.0000E+00	0.50	0.00	5.0000E-01	0.0000E+00
$h_{1y}$ ( $\mu\text{m}$ )	0.0000E+00	1.0000E+00	0.50	0.00	0.0000E+00	5.0000E-01
$h_{2x}$ ( $\mu\text{m}$ )	6.0637E-01	7.9520E-01	0.50	0.00	3.0319E-01	3.9760E-01
$h_{2y}$ ( $\mu\text{m}$ )	-7.9519E-01	6.0637E-01	0.50	0.00	3.9759E-01	3.0318E-01
$D_1$ ( $\mu\text{m}$ )	3.6220E+00	5.7715E-02	25.95	214.75	9.3991E+01	1.4977E+00
$D_2$ ( $\mu\text{m}$ )	2.4540E+00	2.4139E+00	25.95	214.75	6.3682E+01	6.2641E+01
$l_1$ ( $\mu\text{m}$ )	-8.6275E+00	-1.1951E-01	5.00	70+5	4.3137E+01	5.9754E-01
$l_2$ ( $\mu\text{m}$ )	-3.4153E+00	-3.4808E+00	6.00	131-6	2.0492E+01	2.0885E+01
$w_1$ ( $\mu\text{m}$ )	-1.2369E+00	-1.9709E-02	18.00	70+18	2.2263E+01	3.5476E-01
$w_2$ ( $\mu\text{m}$ )	-4.6183E-01	-4.5428E-01	6.00	131-6	2.7710E+00	2.7257E+00
Temperature (°C)	1.9987E+00	8.5935E-01	6.00	27.00	1.1992E+01	5.1561E+00
T0	T_WC	T_S3	T_S2	T_S1		
-11.54	292.02	128.47	85.65	42.82		
724.12	111.09	67.29	44.86	22.43		

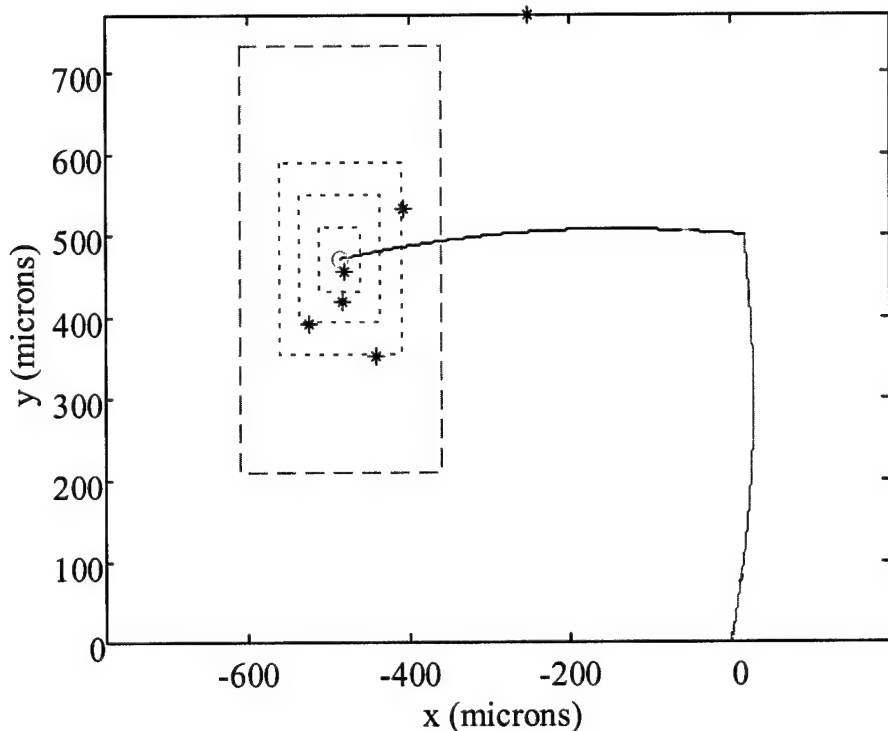
Figure D-10: 135/90 8 mil warp variant.



Variable ( $x_i$ )	$df^x/dx_i$	$df^y/dx_i$	$tol_i$	$nominal_i$	$impact f^x_i$	$impact f^y_i$
$L_1$ ( $\mu\text{m}$ )	5.6356E-01	5.3093E-01	2.00	500.00	1.1271E+00	1.0619E+00
$L_2$ ( $\mu\text{m}$ )	-1.0067E+00	-1.4270E-01	2.00	500.00	2.0134E+00	2.8541E-01
stress <sub>poly</sub> (Pa)	-2.7426E-08	-5.4157E-08	2820000.00	-7900000.00	7.7341E-02	1.5272E-01
stress <sub>gold</sub> (Pa)	-2.8266E-07	-6.0234E-07	21000000.00	103500000.00	5.9358E+00	1.2649E+01
R <sub>sol/poly</sub> p1pd1 ( $\mu\text{m}$ )	6.9136E-04	3.8983E-04	1000.00	6000.00	6.9136E-01	3.8983E-01
R <sub>sol/poly</sub> p1pd2 ( $\mu\text{m}$ )	4.2227E-04	2.4244E-03	1000.00	6000.00	4.2227E-01	2.4244E+00
R <sub>sol/poly</sub> p2pd1 ( $\mu\text{m}$ )	-3.5313E-05	2.2514E-03	1000.00	6000.00	3.5313E-02	2.2514E+00
$h_{1x}$ ( $\mu\text{m}$ )	1.0000E+00	0.0000E+00	0.50	0.00	5.0000E-01	0.0000E+00
$h_{1y}$ ( $\mu\text{m}$ )	0.0000E+00	1.0000E+00	0.50	0.00	0.0000E+00	5.0000E-01
$h_{2x}$ ( $\mu\text{m}$ )	6.3393E-01	7.7340E-01	0.50	0.00	3.1696E-01	3.8670E-01
$h_{2y}$ ( $\mu\text{m}$ )	-7.7339E-01	6.3393E-01	0.50	0.00	3.8670E-01	3.1697E-01
D <sub>1</sub> ( $\mu\text{m}$ )	1.7986E+00	7.7975E-01	25.95	214.75	4.6673E+01	2.0234E+01
D <sub>2</sub> ( $\mu\text{m}$ )	-2.0700E-02	4.6581E+00	25.95	214.75	5.3716E-01	1.2088E+02
I <sub>1</sub> ( $\mu\text{m}$ )	-4.2962E+00	-1.8230E+00	5.00	70+5	2.1481E+01	9.1151E+00
I <sub>2</sub> ( $\mu\text{m}$ )	9.9196E-02	-4.0494E+00	15.00	217-15	1.4879E+00	6.0741E+01
w <sub>1</sub> ( $\mu\text{m}$ )	-6.1419E-01	-2.6627E-01	18.00	70+18	1.1055E+01	4.7929E+00
w <sub>2</sub> ( $\mu\text{m}$ )	2.6011E-03	-5.8532E-01	7.00	217-7	1.8207E-02	4.0973E+00
Temperature (°C)	4.5699E-01	9.7385E-01	6.00	27.00	2.7419E+00	5.8431E+00
T <sub>0</sub>	T_WC	T_S3	T_S2	T_S1		
-155.89	95.51	53.05	35.37	17.68		
359.58	246.14	138.00	92.00	46.00		

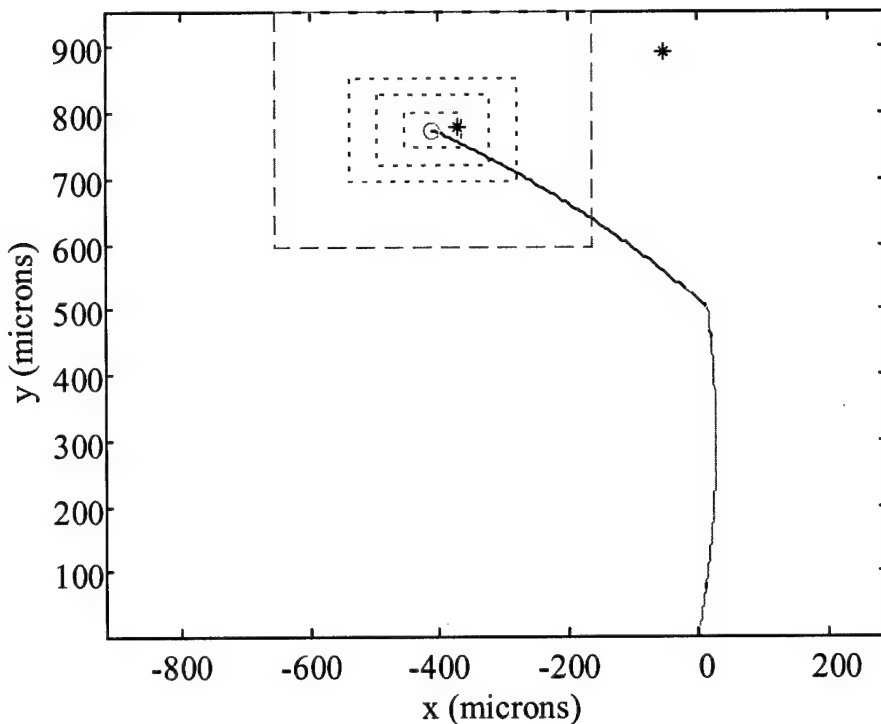
Figure D-11: 135/45 8 mil warp variant.

### D.3 4 Mil Warp Test Structures



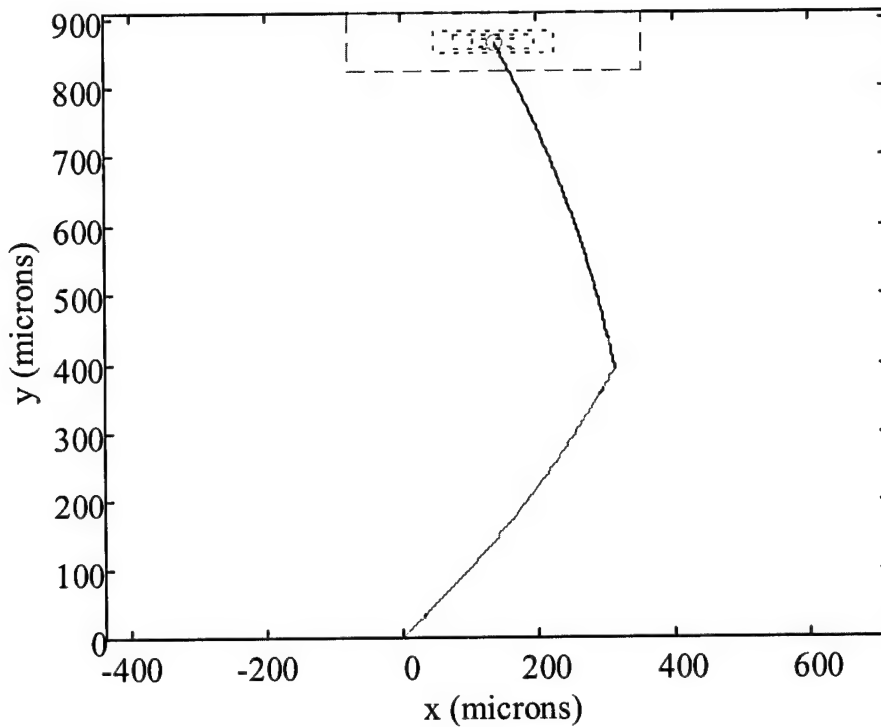
Variable ( $x_i$ )	$df^x/dx_i$	$df^y/dx_i$	$tol_i$	$nominal_i$	$impact f_i^x$	$impact f_i^y$
$L_1$ ( $\mu m$ )	-1.0678E-01	7.1026E-01	2.00	500.00	2.1357E-01	1.4205E+00
$L_2$ ( $\mu m$ )	-1.0128E+00	-2.1580E-01	2.00	500.00	2.0255E+00	4.3160E-01
$stress_{poly}$ (Pa)	-2.4931E-08	-8.8261E-08	2820000.00	-7900000.00	7.0306E-02	2.4889E-01
$stress_{gold}$ (Pa)	-4.7651E-07	-1.5106E-06	21000000.00	103500000.00	1.0007E+01	3.1723E+01
$R_{sol/poly}$ p1pd1 ( $\mu m$ )	8.2980E-04	9.4174E-04	1000.00	6000.00	8.2980E-01	9.4174E-01
$R_{sol/poly}$ p1pd2 ( $\mu m$ )	1.1216E-05	9.6746E-04	1000.00	6000.00	1.1216E-02	9.6746E-01
$R_{sol/poly}$ p1pd1 ( $\mu m$ )	-5.9551E-05	8.9787E-04	1000.00	6000.00	5.9551E-02	8.9787E-01
$h_{1x}$ ( $\mu m$ )	1.0000E+00	0.0000E+00	0.50	0.00	5.0000E-01	0.0000E+00
$h_{1y}$ ( $\mu m$ )	0.0000E+00	1.0000E+00	0.50	0.00	0.0000E+00	5.0000E-01
$h_{2x}$ ( $\mu m$ )	-8.3801E-02	9.9648E-01	0.50	0.00	4.1901E-02	4.9824E-01
$h_{2y}$ ( $\mu m$ )	-9.9647E-01	-8.3817E-02	0.50	0.00	4.9824E-01	4.1908E-02
$D_1$ ( $\mu m$ )	6.3822E+00	6.5797E+00	11.41	111.45	7.2821E+01	7.5075E+01
$D_2$ ( $\mu m$ )	-3.9600E-01	6.7998E+00	11.41	111.45	4.5184E+00	7.7586E+01
$I_1$ ( $\mu m$ )	-8.9965E+00	-9.2608E+00	2.00	69.00	1.7993E+01	1.8522E+01
$I_2$ ( $\mu m$ )	6.1658E-01	-9.3746E+00	2.00	69.00	1.2332E+00	1.8749E+01
$w_1$ ( $\mu m$ )	-1.1344E+00	-1.1695E+00	8.00	69.00	9.0750E+00	9.3559E+00
$w_2$ ( $\mu m$ )	7.0386E-02	-1.2086E+00	8.00	69.00	5.6309E-01	9.6688E+00
Temperature ( $^{\circ}C$ )	7.7042E-01	2.4423E+00	6.00	27.00	4.6225E+00	1.4654E+01
T0	T WC	T S3	T S2	T S1		
-486.02	125.06	76.52	51.01	25.51		
471.43	261.24	117.27	78.18	39.09		

Figure D-12: 90/90 4 mil warp variant.



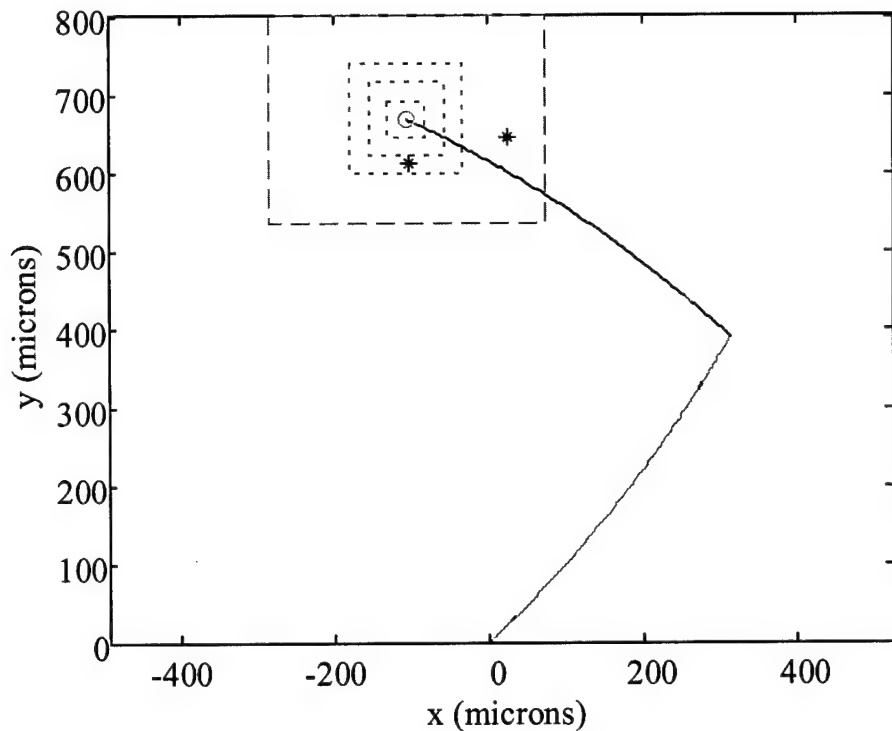
Variable ( $x_i$ )	$\frac{dr^x}{dx_i}$	$\frac{dr^y}{dx_i}$	$tol_i$	$nominal_i$	impact $r^x_i$	impact $r^y_i$
$L_1$ ( $\mu\text{m}$ )	-2.8997E-01	7.6426E-01	2.00	500.00	5.7993E-01	1.5285E+00
$L_2$ ( $\mu\text{m}$ )	-9.5141E-01	4.2334E-01	2.00	500.00	1.9028E+00	8.4668E-01
$stress_{poly}$ (Pa)	-7.7325E-08	-7.6467E-08	2820000.00	-7900000.00	2.1806E-01	2.1564E-01
$stress_{gold}$ (Pa)	-1.5257E-06	-1.3610E-06	21000000.00	103500000.00	3.2039E+01	2.8582E+01
$R_{sol/poly}$ p1pd1 ( $\mu\text{m}$ )	1.4099E-03	7.9435E-04	1000.00	6000.00	1.4099E+00	7.9435E-01
$R_{sol/poly}$ p1pd2 ( $\mu\text{m}$ )	2.8239E-04	4.1404E-04	1000.00	6000.00	2.8239E-01	4.1404E-01
$R_{sol/poly}$ p1pd1 ( $\mu\text{m}$ )	2.5433E-04	3.9970E-04	1000.00	6000.00	2.5433E-01	3.9970E-01
$h_{1x}$ ( $\mu\text{m}$ )	1.0000E+00	0.0000E+00	0.50	0.00	5.0000E-01	0.0000E+00
$h_{1y}$ ( $\mu\text{m}$ )	0.0000E+00	1.0000E+00	0.50	0.00	0.0000E+00	5.0000E-01
$h_{2x}$ ( $\mu\text{m}$ )	-9.8701E-02	9.9511E-01	0.50	0.00	4.9351E-02	4.9755E-01
$h_{2y}$ ( $\mu\text{m}$ )	-9.9512E-01	-9.8709E-02	0.50	0.00	4.9756E-01	4.9355E-02
$D_1$ ( $\mu\text{m}$ )	1.0480E+01	5.5385E+00	11.41	111.45	1.1958E+02	6.3194E+01
$D_2$ ( $\mu\text{m}$ )	1.5490E+00	2.4098E+00	11.41	111.45	1.7674E+01	2.7495E+01
$I_1$ ( $\mu\text{m}$ )	-1.4755E+01	-7.8052E+00	2.00	69.00	2.9510E+01	1.5610E+01
$I_2$ ( $\mu\text{m}$ )	-4.0080E+00	-6.3731E+00	2.00	33+tol	8.0160E+00	1.2746E+01
$w_1$ ( $\mu\text{m}$ )	-1.8628E+00	-9.8441E-01	8.00	69.00	1.4902E+01	7.8753E+00
$w_2$ ( $\mu\text{m}$ )	-5.6725E-01	-8.8246E-01	6.00	33+tol	3.4035E+00	5.2947E+00
Temperature ( $^{\circ}\text{C}$ )	2.4667E+00	2.2005E+00	6.00	27.00	1.4800E+01	1.3203E+01
T0	T WC	T S3	T S2	T S1		
-409.10	245.58	130.48	86.99	43.49		
774.14	179.22	78.99	52.66	26.33		

Figure D-13: 90/135 4 mil warp variant.



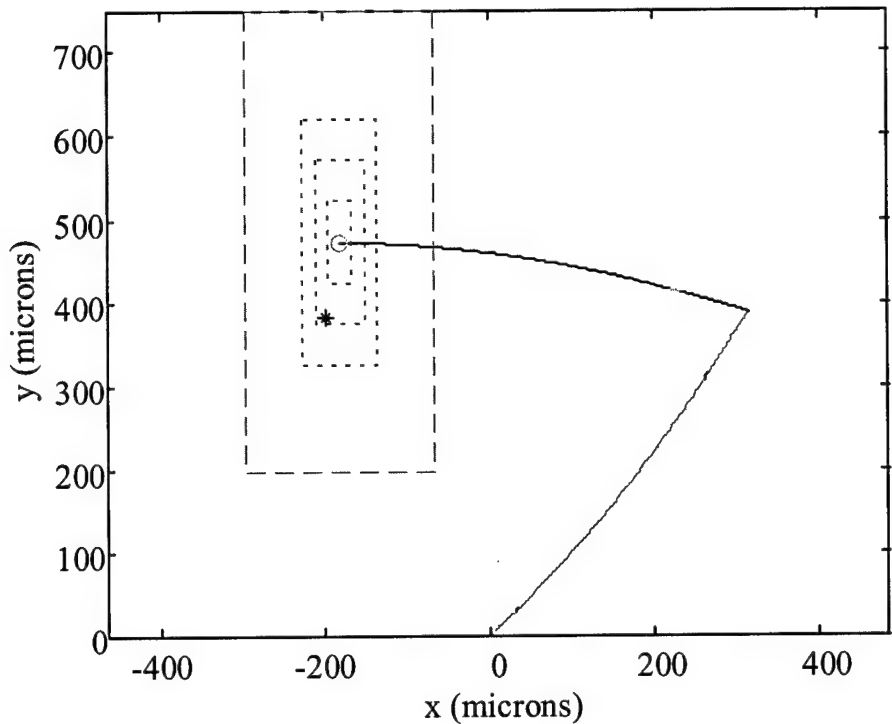
Variable ( $x_i$ )	$df^k/dx_i$	$df^l/dx_i$	tol <sub>i</sub>	nominal <sub>i</sub>	impact $f^k_i$	impact $f^l_i$
L <sub>1</sub> (μm)	2.3213E-01	7.9088E-01	2.00	500.00	4.6425E-01	1.5818E+00
L <sub>2</sub> (μm)	-5.0720E-01	9.0948E-01	2.00	500.00	1.0144E+00	1.8190E+00
stress <sub>poly</sub> (Pa)	-1.0927E-07	-1.3274E-08	2820000.00	-7900000.00	3.0815E-01	3.7433E-02
stress <sub>gold</sub> (Pa)	-2.1775E-06	-1.3534E-07	21000000.00	103500000.00	4.5729E+01	2.8421E+00
R <sub>sol/poly</sub> pl1pd1 (μm)	8.2609E-04	-1.1884E-04	1000.00	6000.00	8.2609E-01	1.1884E-01
R <sub>sol/poly</sub> pl1pd2 (μm)	4.7432E-04	1.6183E-04	1000.00	6000.00	4.7432E-01	1.6183E-01
R <sub>sol/poly</sub> pl2pd1 (μm)	4.4328E-04	1.6720E-04	1000.00	6000.00	4.4328E-01	1.6720E-01
h <sub>1x</sub> (μm)	1.0000E+00	0.0000E+00	0.50	0.00	5.0000E-01	0.0000E+00
h <sub>1y</sub> (μm)	0.0000E+00	1.0000E+00	0.50	0.00	0.0000E+00	5.0000E-01
h <sub>2x</sub> (μm)	5.1805E-01	8.5536E-01	0.50	0.00	2.5902E-01	4.2768E-01
h <sub>2y</sub> (μm)	-8.5535E-01	5.1804E-01	0.50	0.00	4.2768E-01	2.5902E-01
D <sub>1</sub> (μm)	4.9142E+00	-7.8490E-01	11.41	111.45	5.6071E+01	8.9557E+00
D <sub>2</sub> (μm)	2.6850E+00	9.9861E-01	11.41	111.45	3.0636E+01	1.1394E+01
I <sub>1</sub> (μm)	-1.3296E+01	2.1019E+00	2.00	33+tol	2.6592E+01	4.2037E+00
I <sub>2</sub> (μm)	-7.0357E+00	-2.6997E+00	2.00	33+tol	1.4071E+01	5.3994E+00
w <sub>1</sub> (μm)	-1.7996E+00	2.8743E-01	6.00	33+tol	1.0797E+01	1.7246E+00
w <sub>2</sub> (μm)	-9.8325E-01	-3.6569E-01	6.00	33+tol	5.8995E+00	2.1941E+00
Temperature (°C)	3.5206E+00	2.1881E-01	6.00	27.00	2.1124E+01	1.3129E+00
T <sub>0</sub>	T_WC	T_S3	T_S2	T_S1		
138.18	215.61	87.62	58.41	29.21		
865.10	43.09	16.75	11.17	5.58		

**Figure D-14:** 135/135 4 mil warp variant. (No Data)



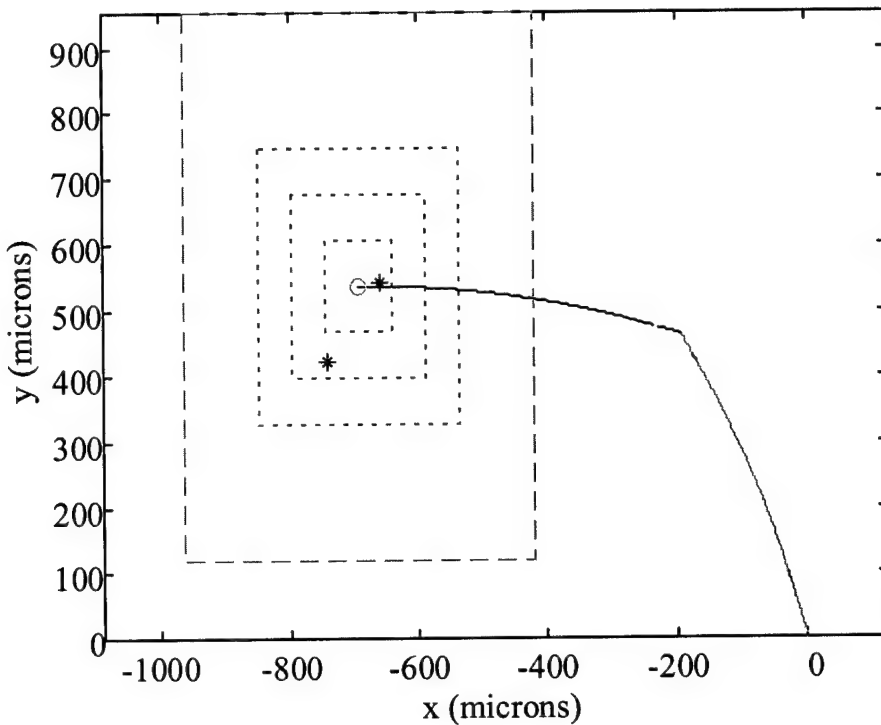
Variable ( $x_i$ )	$df^x/dx_i$	$df^y/dx_i$	tol <sub>i</sub>	nominal <sub>i</sub>	impact $f^x_i$	impact $f^y_i$
$L_1$ ( $\mu\text{m}$ )	3.4488E-01	6.3861E-01	2.00	500.00	6.8976E-01	1.2772E+00
$L_2$ ( $\mu\text{m}$ )	-9.3981E-01	4.3476E-01	2.00	500.00	1.8796E+00	8.6952E-01
stress <sub>poly</sub> (Pa)	-7.4405E-08	-5.4160E-08	2820000.00	-7900000.00	2.0982E-01	1.5273E-01
stress <sub>gold</sub> (Pa)	-1.3964E-06	-9.3218E-07	21000000.00	103500000.00	2.9325E+01	1.9576E+01
R <sub>sol/poly</sub> pl1pd1 ( $\mu\text{m}$ )	6.3529E-04	1.1768E-04	1000.00	6000.00	6.3529E-01	1.1768E-01
R <sub>sol/poly</sub> pl1pd2 ( $\mu\text{m}$ )	5.8924E-04	7.6741E-04	1000.00	6000.00	5.8924E-01	7.6741E-01
R <sub>sol/poly</sub> pl2pd1 ( $\mu\text{m}$ )	4.9088E-04	7.5416E-04	1000.00	6000.00	4.9088E-01	7.5416E-01
$h_{1x}$ ( $\mu\text{m}$ )	1.0000E+00	0.0000E+00	0.50	0.00	5.0000E-01	0.0000E+00
$h_{1y}$ ( $\mu\text{m}$ )	0.0000E+00	1.0000E+00	0.50	0.00	0.0000E+00	5.0000E-01
$h_{2x}$ ( $\mu\text{m}$ )	5.3061E-01	8.4761E-01	0.50	0.00	2.6530E-01	4.2381E-01
$h_{2y}$ ( $\mu\text{m}$ )	-8.4762E-01	5.3061E-01	0.50	0.00	4.2381E-01	2.6530E-01
D <sub>1</sub> ( $\mu\text{m}$ )	3.7993E+00	5.9708E-01	11.41	111.45	4.3350E+01	6.8127E+00
D <sub>2</sub> ( $\mu\text{m}$ )	3.7615E+00	5.6785E+00	11.41	111.45	4.2919E+01	6.4791E+01
I <sub>1</sub> ( $\mu\text{m}$ )	-1.0281E+01	-1.6232E+00	2.00	33+tol	2.0562E+01	3.2464E+00
I <sub>2</sub> ( $\mu\text{m}$ )	-5.1337E+00	-7.8773E+00	2.00	69.00	1.0267E+01	1.5755E+01
w <sub>1</sub> ( $\mu\text{m}$ )	-1.3913E+00	-2.1865E-01	6.00	33+tol	8.3478E+00	1.3119E+00
w <sub>2</sub> ( $\mu\text{m}$ )	-6.6858E-01	-1.0093E+00	8.00	69.00	5.3486E+00	8.0744E+00
Temperature (°C)	2.2577E+00	1.5071E+00	6.00	27.00	1.3546E+01	9.0427E+00
T <sub>0</sub>	T <sub>WC</sub>	T <sub>S3</sub>		T <sub>S2</sub>	T <sub>S1</sub>	
-105.11	179.33	73.45		48.97	24.48	
668.84	133.72	70.97		47.31	23.66	

**Figure D-15:** 135/90 4 mil warp variant.



Variable ( $x_i$ )	$d\hat{r}^k/dx_i$	$d\hat{r}^k/dx_i$	$tol_i$	$nominal_i$	impact $\hat{r}_i^k$	impact $\hat{r}_i^k$
$L_1$ ( $\mu m$ )	4.6087E-01	5.8912E-01	2.00	500.00	9.2173E-01	1.1782E+00
$L_2$ ( $\mu m$ )	-1.0323E+00	1.6628E-02	2.00	500.00	2.0646E+00	3.3257E-02
stress <sub>poly</sub> (Pa)	-4.0797E-08	-6.5491E-08	2820000.00	-7900000.00	1.1505E-01	1.8468E-01
stress <sub>gold</sub> (Pa)	-7.4254E-07	-1.1210E-06	21000000.00	103500000.00	1.5593E+01	2.3540E+01
R <sub>sol/poly</sub> p1pd1 ( $\mu m$ )	4.4547E-04	1.9131E-04	1000.00	6000.00	4.4547E-01	1.9131E-01
R <sub>sol/poly</sub> p1pd2 ( $\mu m$ )	2.9562E-04	1.1509E-03	1000.00	6000.00	2.9562E-01	1.1509E+00
R <sub>sol/poly</sub> p12pd1 ( $\mu m$ )	1.7603E-04	1.1096E-03	1000.00	6000.00	1.7603E-01	1.1096E+00
$h_{1x}$ ( $\mu m$ )	1.0000E+00	0.0000E+00	0.50	0.00	5.0000E-01	0.0000E+00
$h_{1y}$ ( $\mu m$ )	0.0000E+00	1.0000E+00	0.50	0.00	0.0000E+00	5.0000E-01
$h_{2x}$ ( $\mu m$ )	5.3765E-01	8.4317E-01	0.50	0.00	2.6883E-01	4.2158E-01
$h_{2y}$ ( $\mu m$ )	-8.4318E-01	5.3765E-01	0.50	0.00	4.2159E-01	2.6883E-01
$D_1$ ( $\mu m$ )	2.6902E+00	1.0273E+00	11.41	111.45	3.0696E+01	1.1721E+01
$D_2$ ( $\mu m$ )	1.6581E+00	9.8452E+00	11.41	111.45	1.8919E+01	1.1233E+02
$I_1$ ( $\mu m$ )	-7.2854E+00	-2.7806E+00	2.00	33+tol	1.4571E+01	5.5612E+00
$I_2$ ( $\mu m$ )	-1.7668E+00	-1.0856E+01	8.00	96-tol	1.4134E+01	8.6847E+01
$w_1$ ( $\mu m$ )	-9.8516E-01	-3.7618E-01	6.00	33+tol	5.9110E+00	2.2571E+00
$w_2$ ( $\mu m$ )	-2.2514E-01	-1.3368E+00	13.00	96-tol	2.9268E+00	1.7379E+01
Temperature ( $^{\circ}C$ )	1.2005E+00	1.8124E+00	6.00	27.00	7.2032E+00	1.0874E+01
T0	T WC	T S3	T S2	T S1		
-180.84	115.15	45.34	30.23	15.11		
473.60	275.52	145.97	97.31	48.66		

Figure D-16: 135/45 4 mil warp variant.



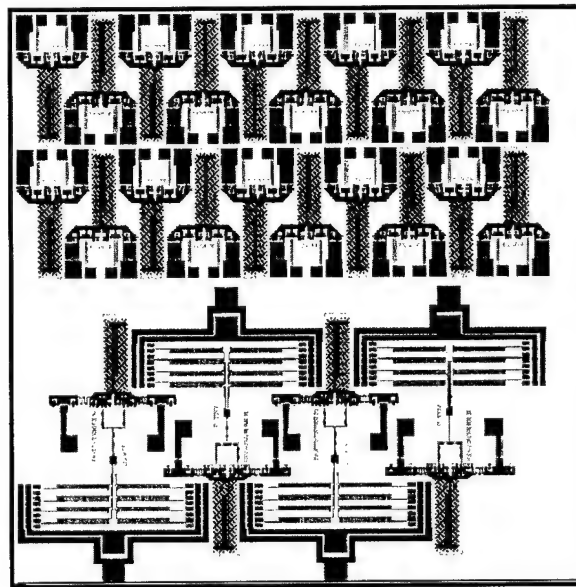
Variable ( $x_i$ )	$df^x/dx_i$	$df^y/dx_i$	$tol_i$	$nominal_i$	impact $f^x_i$	impact $f^y_i$
$L_1$ ( $\mu\text{m}$ )	-5.7724E-01	5.7294E-01	2.00	500.00	1.1545	1.1459
$L_2$ ( $\mu\text{m}$ )	-1.0413E+00	-5.1805E-03	2.00	500.00	2.0827	0.0104
$\text{stress}_{\text{poly}}$ (Pa)	-3.7729E-08	-1.0108E-07	2820000.00	-7900000.00	0.1064	0.2851
$\text{stress}_{\text{gold}}$ (Pa)	-7.6952E-07	-1.7982E-06	21000000.00	103500000.00	16.1600	37.7626
$R_{\text{sol/poly}} p1pd1$ ( $\mu\text{m}$ )	1.1925E-03	1.6538E-03	1000.00	6000.00	1.1925	1.6538
$R_{\text{sol/poly}} p1pd2$ ( $\mu\text{m}$ )	8.7227E-05	4.9352E-04	1000.00	6000.00	0.0872	0.4935
$R_{\text{sol/poly}} p12pd1$ ( $\mu\text{m}$ )	6.7542E-05	4.6892E-04	1000.00	6000.00	0.0675	0.4689
$h_{1x}$ ( $\mu\text{m}$ )	1.0000E+00	0.0000E+00	0.50	0.00	0.5000	0.0000
$h_{1y}$ ( $\mu\text{m}$ )	0.0000E+00	1.0000E+00	0.50	0.00	0.0000	0.5000
$h_{2x}$ ( $\mu\text{m}$ )	-4.9904E-01	8.6658E-01	0.50	0.00	0.2495	0.4333
$h_{2y}$ ( $\mu\text{m}$ )	-8.6657E-01	-4.9905E-01	0.50	0.00	0.4333	0.2495
$D_1$ ( $\mu\text{m}$ )	1.0664E+01	1.3740E+01	11.41	111.45	121.6793	156.7748
$D_2$ ( $\mu\text{m}$ )	4.2151E-01	2.8335E+00	11.41	111.45	4.8094	32.3304
$I_1$ ( $\mu\text{m}$ )	-1.1932E+01	-1.5370E+01	8.00	96-tol	95.4555	122.9585
$I_2$ ( $\mu\text{m}$ )	-1.0352E+00	-7.4528E+00	2.00	33+tol	2.0703	14.9056
$w_1$ ( $\mu\text{m}$ )	-1.4481E+00	-1.8657E+00	13.00	96-tol	18.8247	24.2542
$w_2$ ( $\mu\text{m}$ )	-1.5436E-01	-1.0376E+00	6.00	33+tol	0.9261	6.2258
Temperature ( $^{\circ}\text{C}$ )	1.2441E+00	2.9073E+00	6.00	27.00	7.4649	17.4439
T0	T_WC	T_S3	T_S2	T_S1		
-691.66	273.23	156.90	104.60	52.30		
536.82	417.85	208.12	138.75	69.37		

Figure D-17: 45/135 4 mil warp variant.

## Appendix E CAD Design Summaries

This appendix contains captured images of the computer-aided drawings (CAD) of the MEMS designs that I submitted for fabrication during this research. The designs are specified by Cronos specified MUMPs fabrication run number, die size, and a brief description including a brief statement of modifications from a previous design, if applicable.

### E.1 MUMPs 27



**Figure E-1:** MUMPs 27; 2 mm × 2 mm; microrobot leg array for thermally evaporated indium solder self-assembly.

## E.2 MUMPs 29

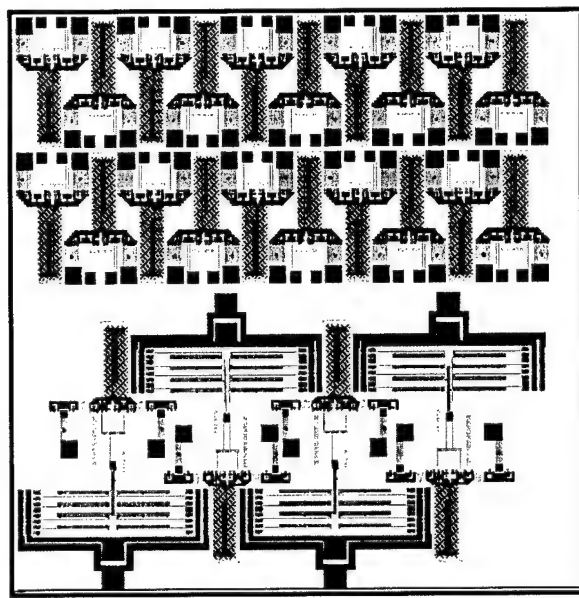


**Figure E-2:** MUMPs 29 Die 1; 2 mm × 2 mm; microrobot leg array for thermally evaporated indium solder self-assembly, more compliant locking tabs, and metallization only on the solder pads.

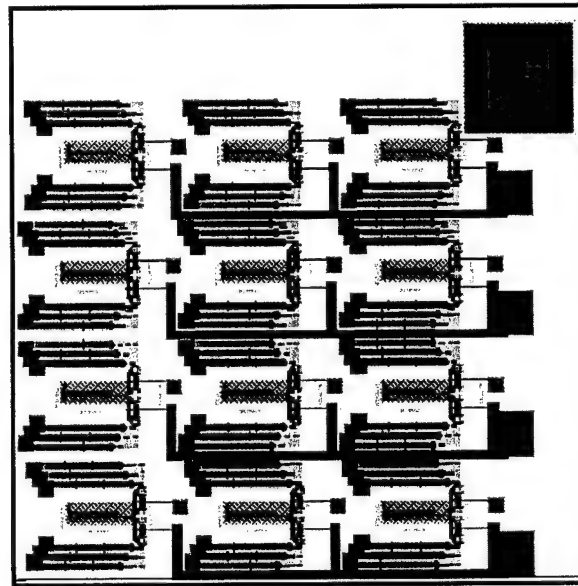


**Figure E-3:** MUMPs 29 Die 2; 2 mm × 2 mm; microrobot leg array for gold on polysilicon bilayer self-assembly.

### E.3 MUMPs 32

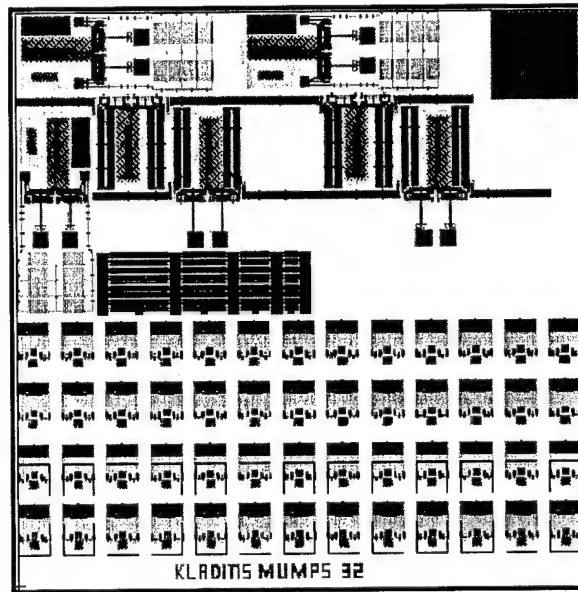


**Figure E-4:** MUMPs 32 Die 1; 2 mm × 2 mm; microrobot leg array for gold on polysilicon bilayer and scratch drive self-assembly, corrugated gold on polysilicon thermally actuated bilayer cantilevers, and array of simple plates for thermally evaporated indium solder self-assembly.

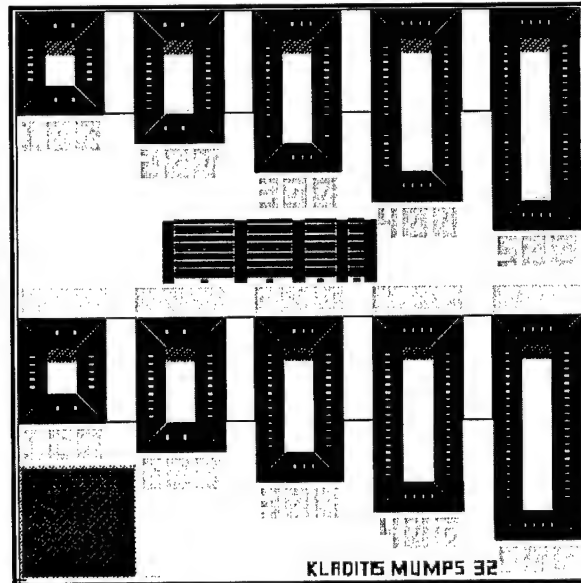


**Figure E-5:** MUMPs 32 Die 2; 2 mm × 2 mm; polysilicon and PSG casts for electrostatically actuated SiCN cantilevers and corrugated gold on polysilicon thermally actuated bilayer cantilevers.

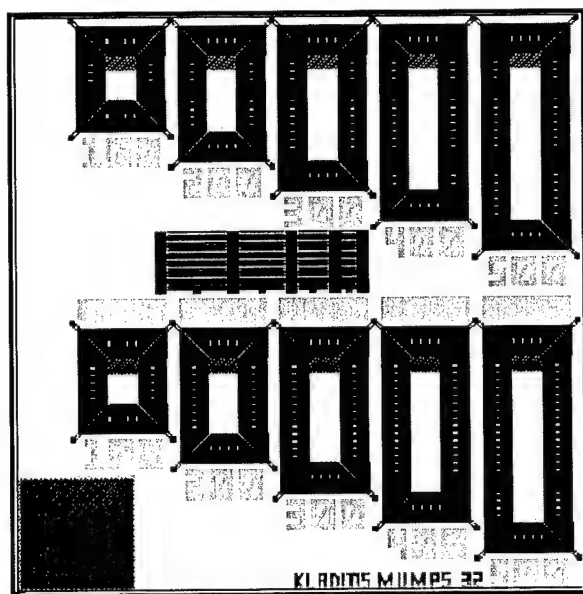


**Figure E-6:** MUMPs 32 Die 3; 2 mm × 2 mm; polysilicon and PSG casts for electrostatically actuated SiCN cantilevers and corrugated gold on polysilicon thermally actuated bilayer cantilevers. The polysilicon cast has breakaway tethers.

#### E.4 MUMPs 33

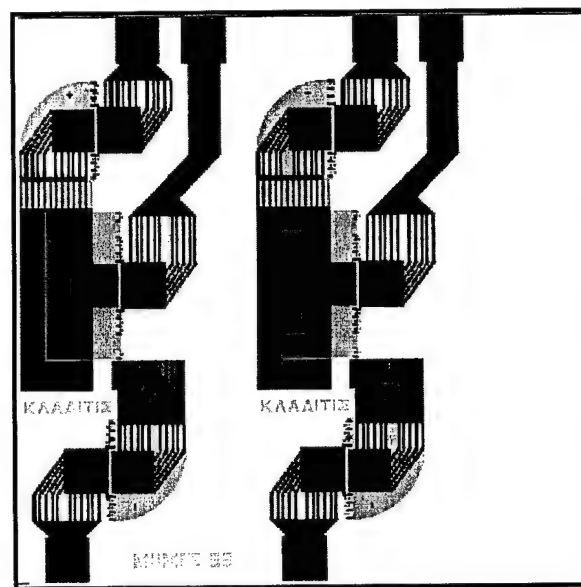


**Figure E-7:** MUMPs 33 Die 1; 2 mm × 2 mm; normally open electrostatically actuated switches for 8 mil solder self-assembly.

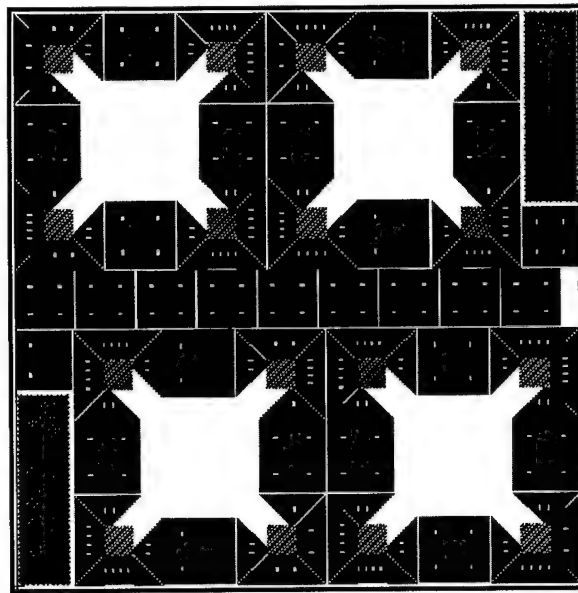


**Figure E-8:** MUMPs 33 Die 2; 2 mm × 2 mm; polysilicon and PSG casts for electrostatically actuated SiCN supported membranes.

### E.5 MUMPs 34

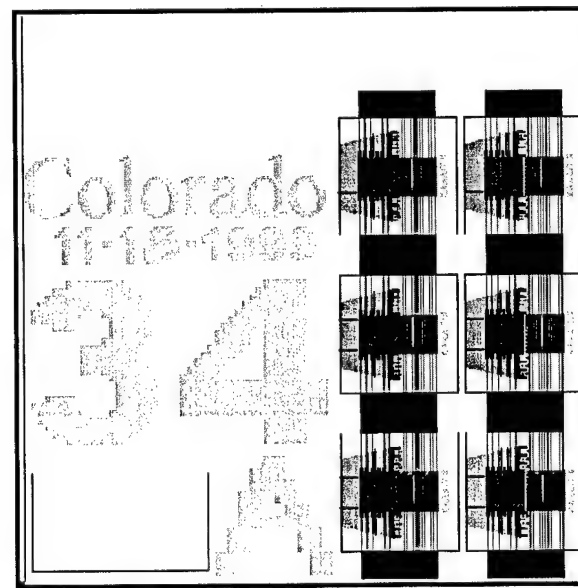


**Figure E-9:** MUMPs 34 Die 1; 2 mm × 2 mm; point heaters.

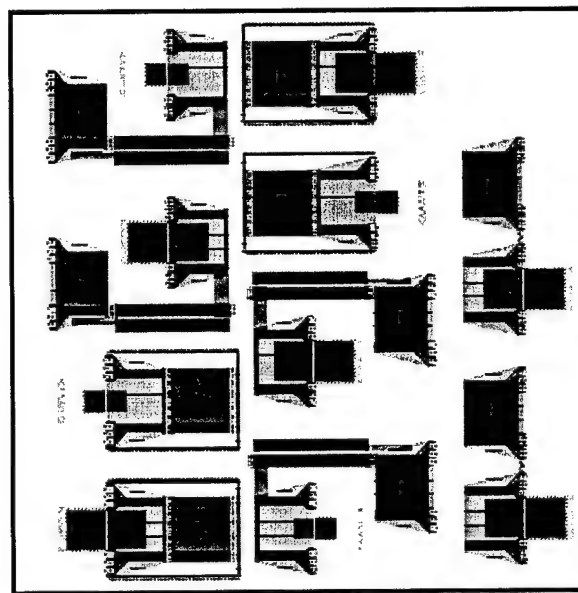


**Figure E-10:** MUMPs 34 Die 2; 2 mm × 2 mm; push-up, pull-up, and tandem linkage demonstrations for 8 mil solder self-assembly.

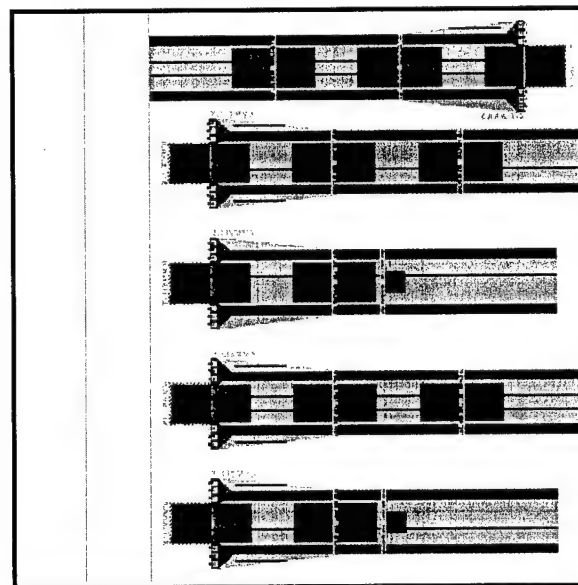


**Figure E-11:** MUMPs 34 Die 3; 2 mm × 2 mm; fiber optic cable grippers.

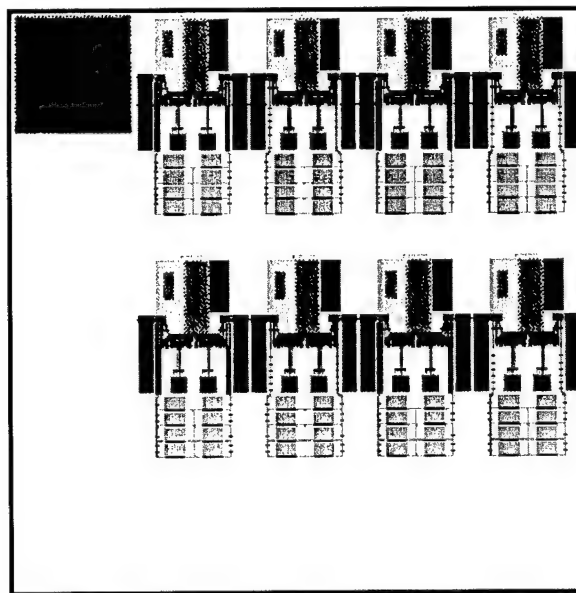


**Figure E-12:** MUMPs 34 Die 4; 2 mm × 2 mm; microrobot leg array for scratch drive self-assembly.

## E.6 MUMPs 35

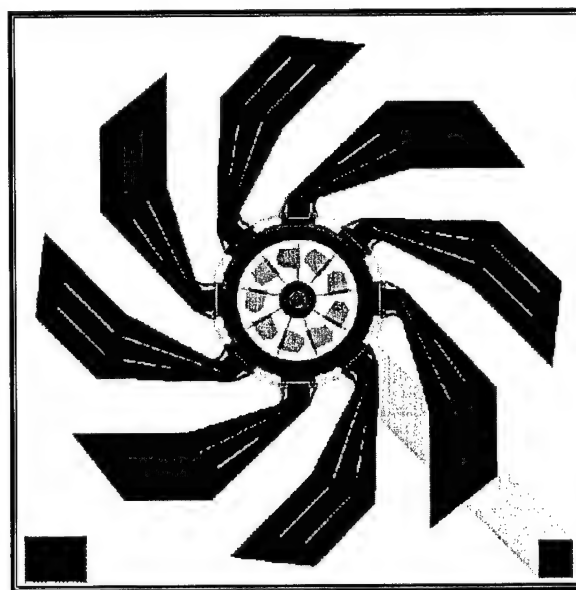


**Figure E-13:** MUMPs 35 Die 1; 2 mm × 2 mm; solder self-assembled micro axial flow fan. Solder pad and hinge area design – Kladitis. Rotary scratch drive motor and wing design – Linderman.

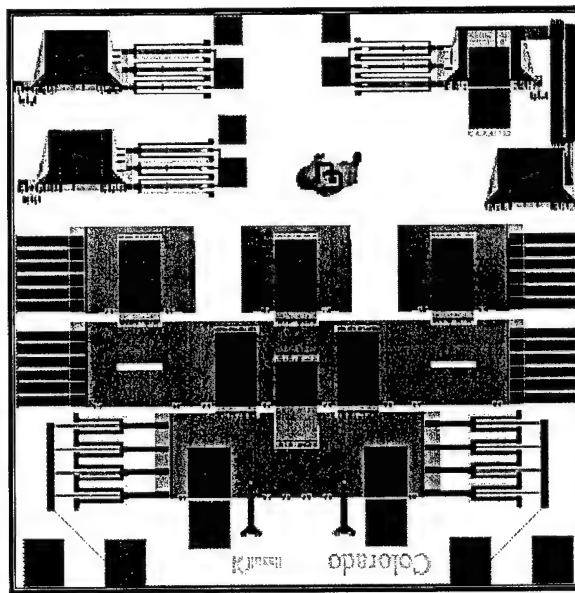


**Figure E-14:** MUMPs 35 Die 2; 2 mm × 2 mm; simple mirrors for vertically deflecting electro-thermal actuator assembly – top half. Bottom half belongs to Kevin Harsh.

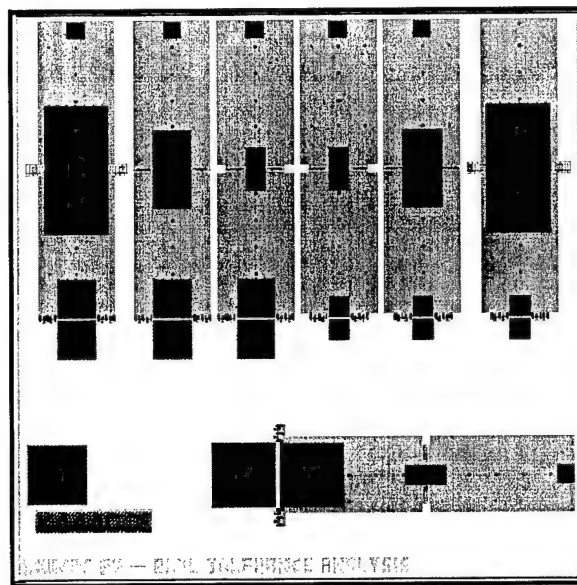


**Figure E-15:** MUMPs 35 Die 3; 2 mm × 2 mm; 8 mil two-solder-joint test structure.

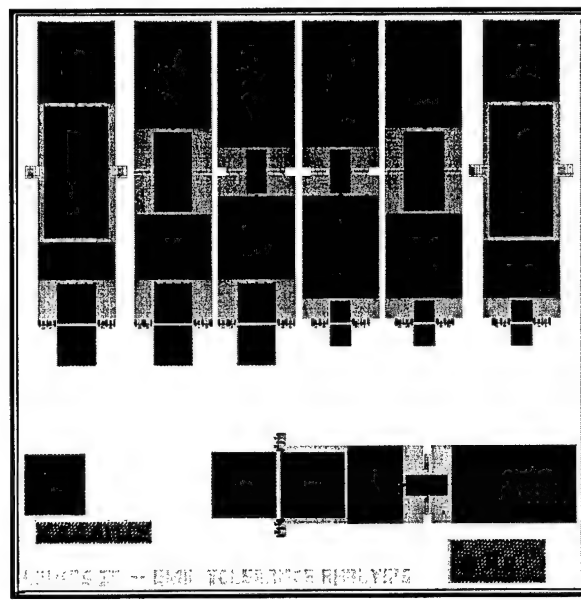


**Figure E-16:** MUMPs 35 Die 4; 2 mm × 2 mm; 8 mil warp two-solder-joint test structure.

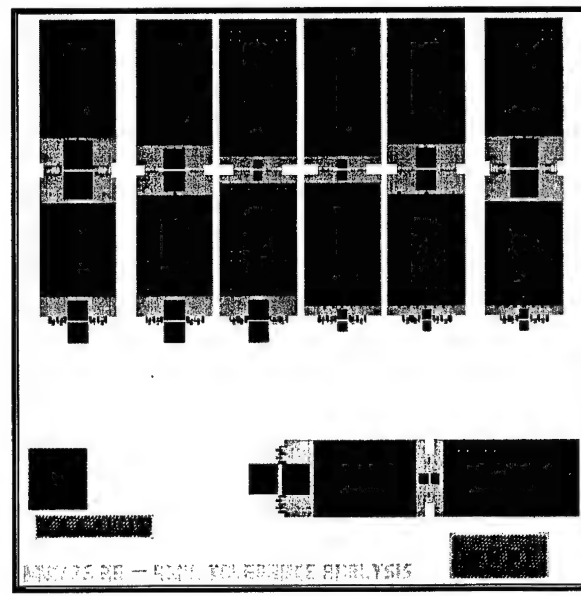


**Figure E-17:** MUMPs 35 Die 5; 2 mm × 2 mm; 4 mil warp two-solder-joint test structure.

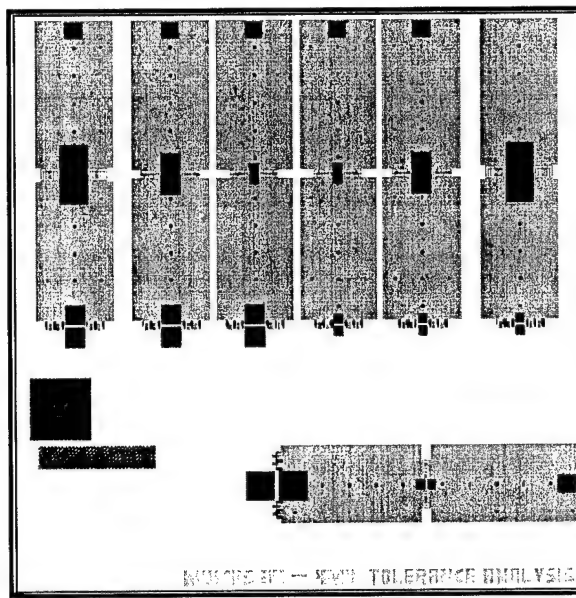


**Figure E-18:** MUMPs 35 Die 6; 2 mm × 2 mm; 4 mil two-solder-joint test structure.

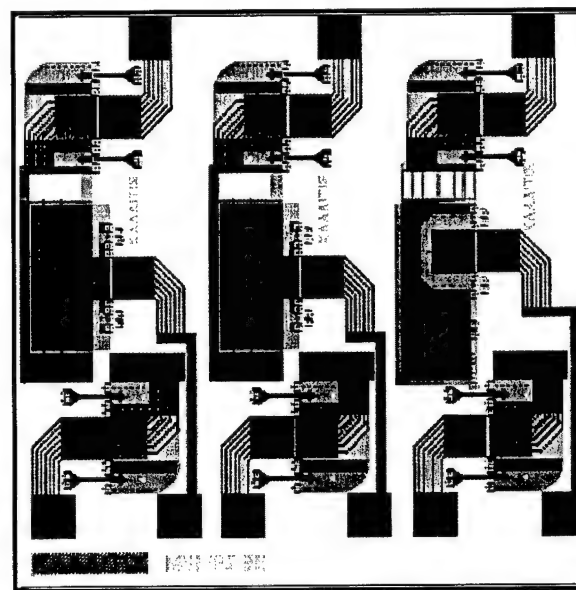


**Figure E-19:** MUMPs 35 Die 7; 2 mm × 2 mm; normally open and normally closed electrostatically actuated switches for 8 mil solder self-assembly.

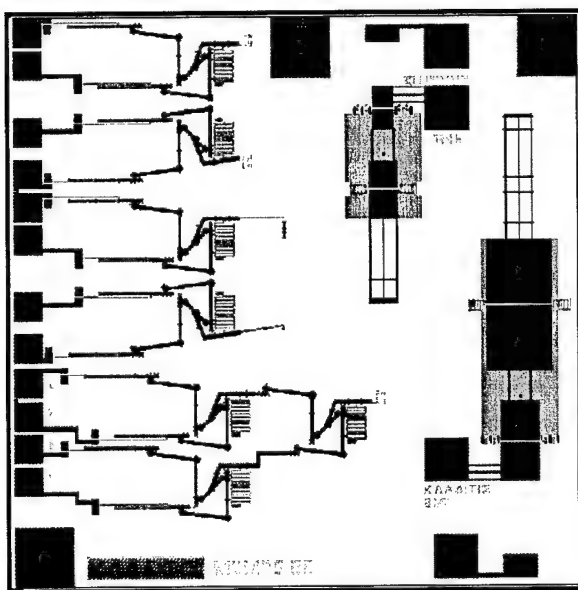


**Figure E-20:** MUMPs 35 Die 8; 2 mm × 2 mm; mechanical NAND gates, NOR gates, XOR circuit, and 4 mil and 8 mil solder self-assembled thermostats.

## E.7 MUMPs 36

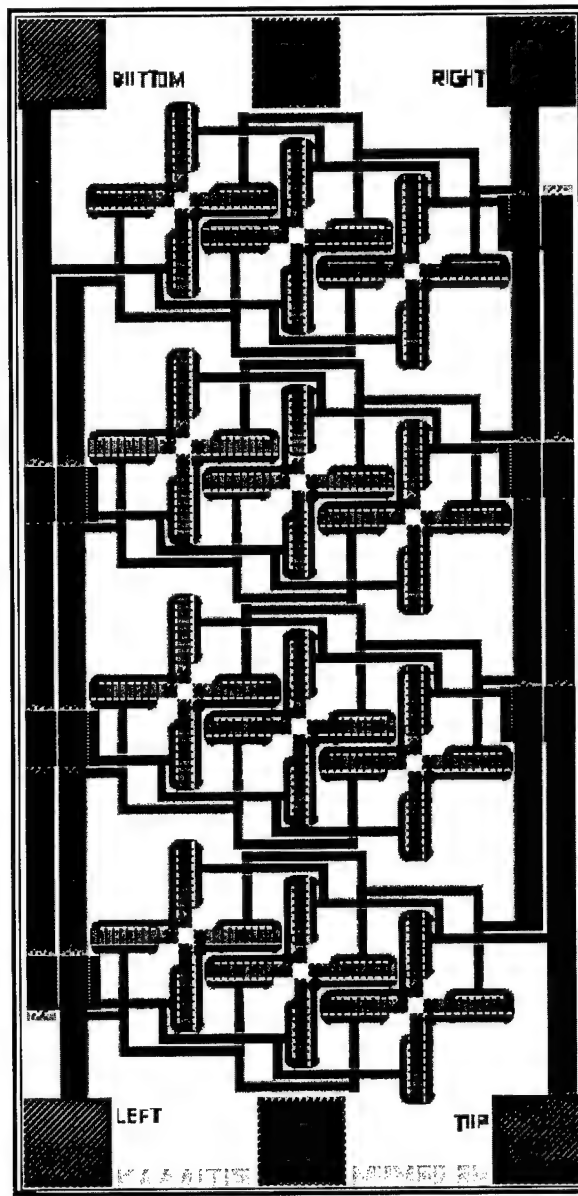


**Figure E-21:** MUMPs 36 Die 1; 4 mm × 2 mm; 2-D micro conveyer with gold on polysilicon thermally actuated bilayer cantilevers as conveyer arms.

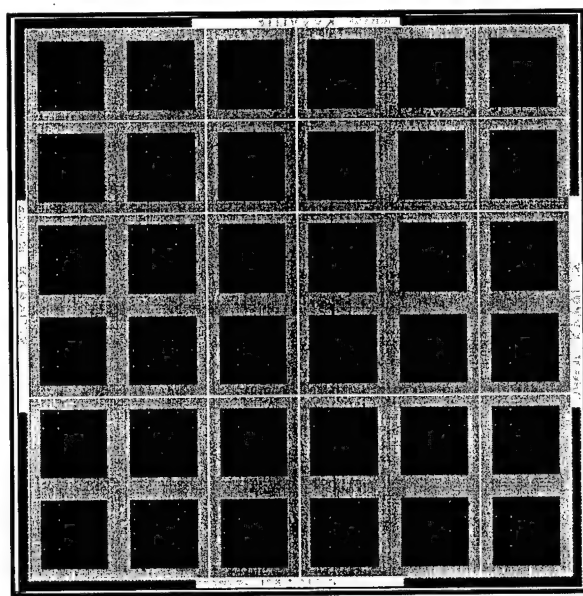


**Figure E-22:** MUMPs 36 Die 2; 2 mm × 2 mm; jumping robot powered by gold on polysilicon bifurcating plates.

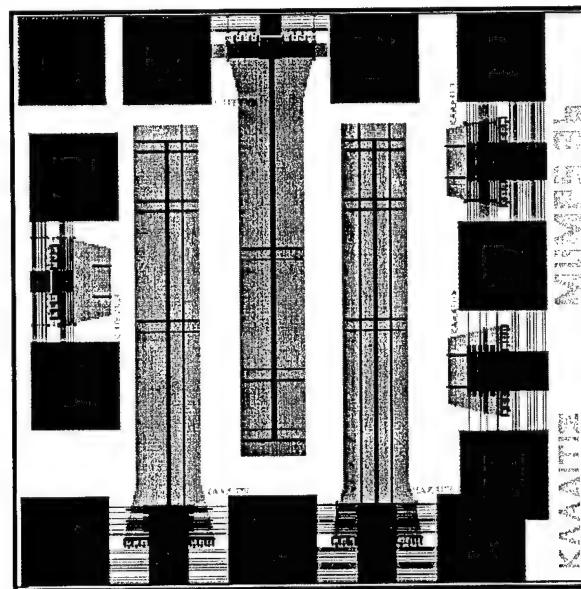


**Figure E-23:** MUMPs 36 Die 3; 2 mm × 2 mm; point heaters with power optimized heaters and larger attached structure.

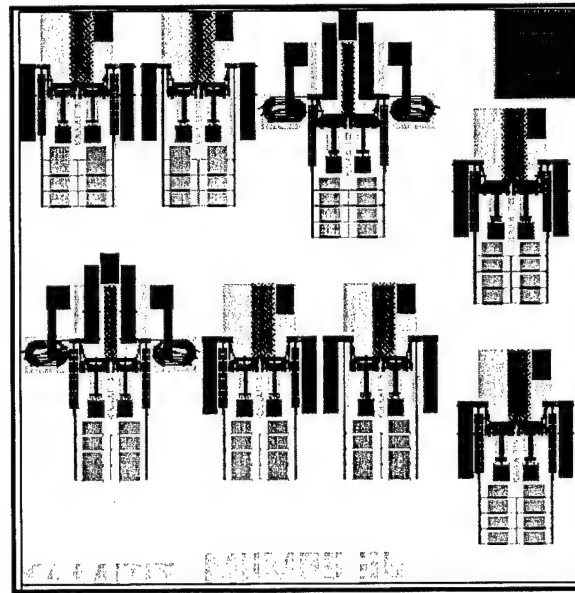


**Figure E-24:** MUMPs 36 Die 4; 2 mm × 2 mm; array of microrobot legs for chain and stiff beam tethered scratch drive actuator self-assembly. Bushings stuck to nitride.

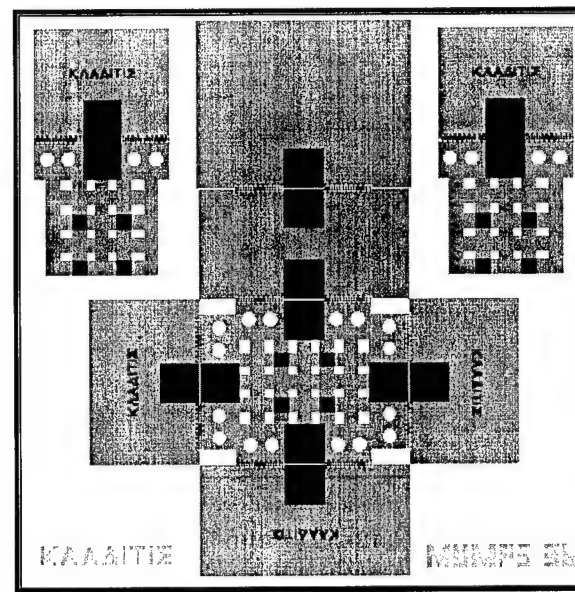


**Figure E-25:** MUMPs 36 Die 5; 2 mm × 2 mm; 8 mil solder self-assembling box and simple plates where solder self-assembly is performed on the back side after flip chipping this chip to another substrate.

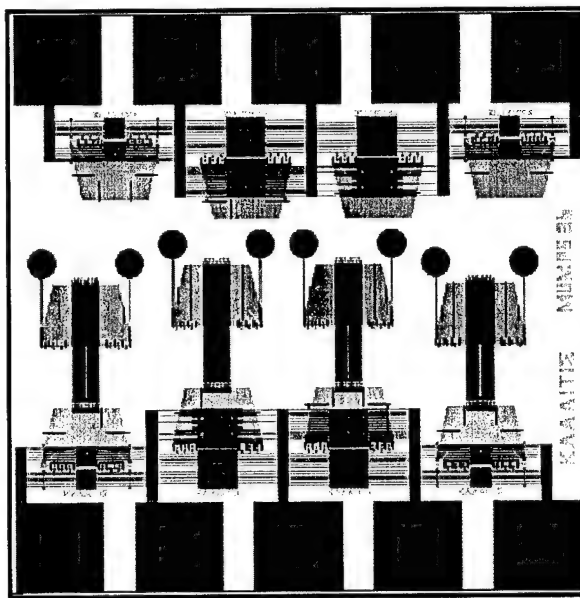


**Figure E-26:** MUMPs 36 Die 6; 2 mm × 2 mm; point heaters with power optimized heaters and larger linkage attached structures.

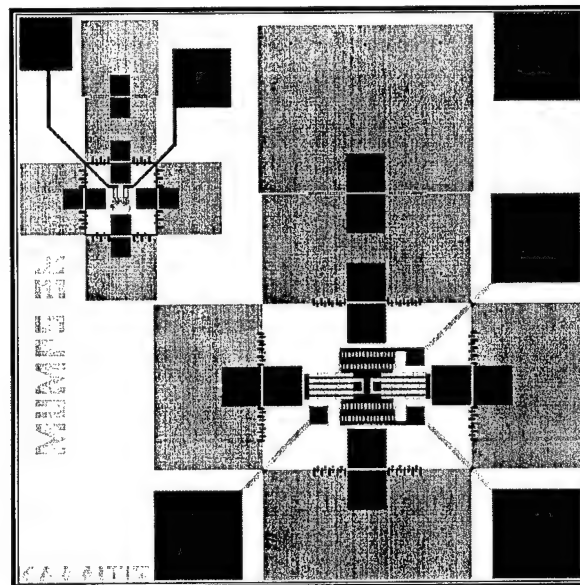


**Figure E-27:** MUMPs 36 Die 7; 2 mm × 2 mm; μpackages.

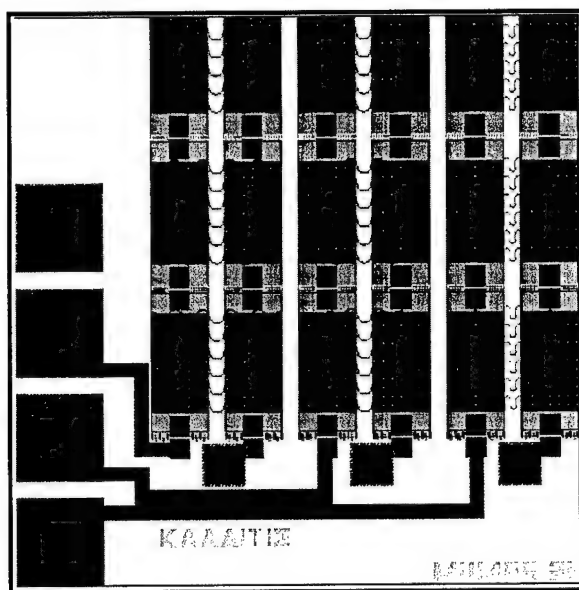


**Figure E-28:** MUMPs 36 Die 8; 2 mm × 2 mm; 4 mil solder self-assembled electro-thermally actuated gold on polysilicon bilayer grippers.

## E.8 MUMPs 38

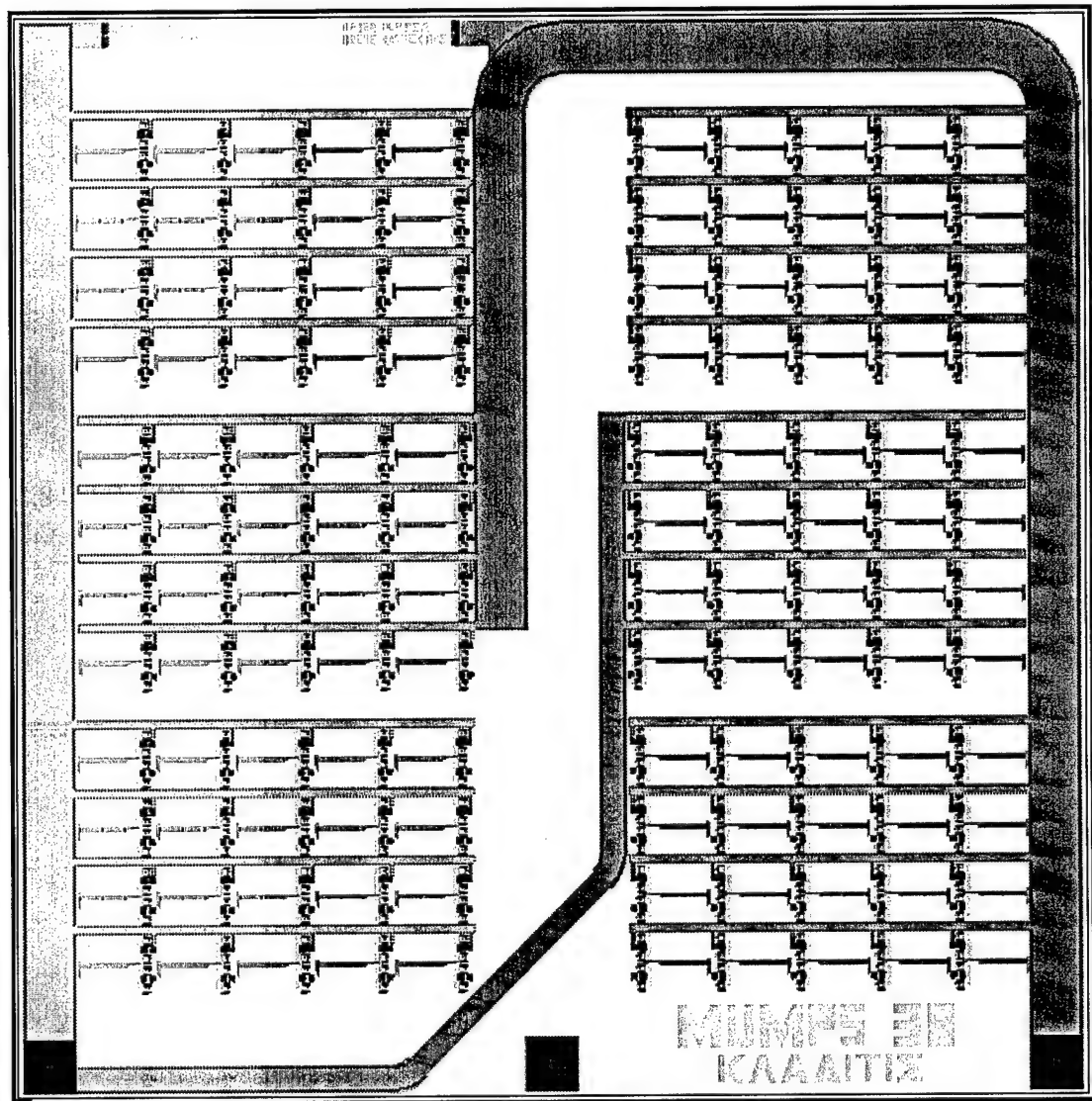


**Figure E-29:** MUMPs 38 Die 1; 4 mm × 4 mm; solder self-assembled microrobot where the solder is deposited on the leg solder pads using mask-less electroplated solder. In the unreleased state, the whole robot is covered in PSG except for the solder pads and bond pads.

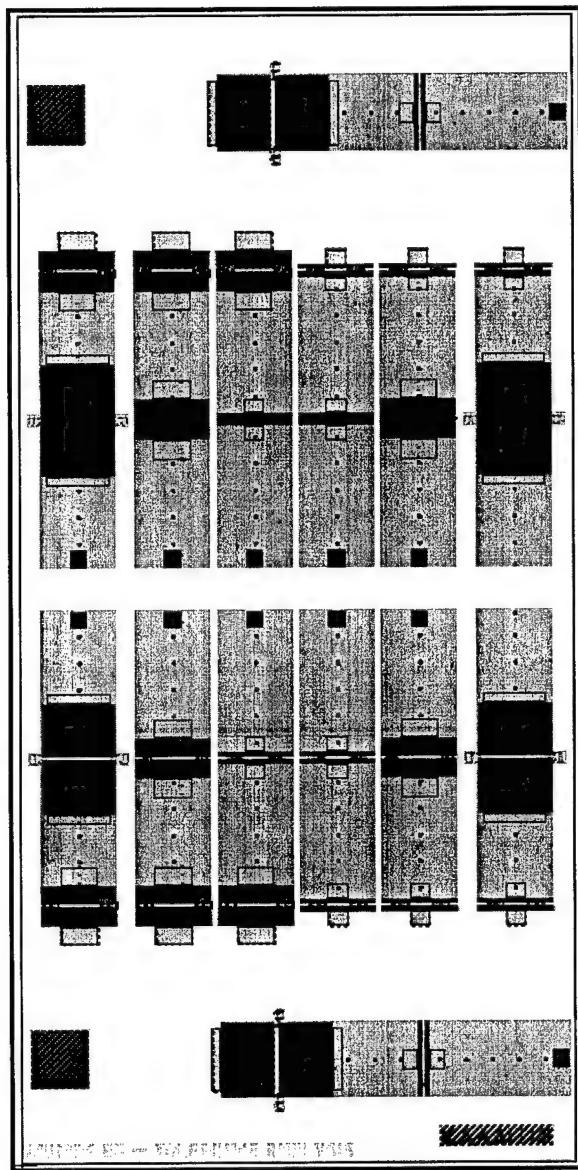


**Figure E-30:** MUMPs 38 Die 2; 4 mm × 2 mm; 8 mil two-solder-joint test structure with solder pads that span the whole width of the plate structures.

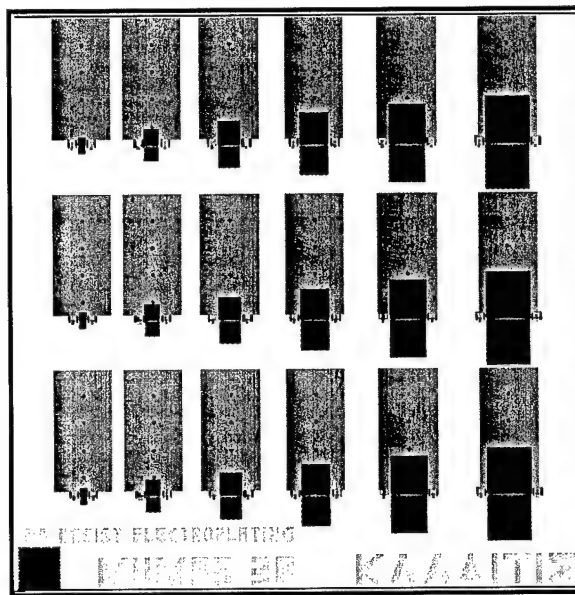


**Figure E-31:** MUMPs 38 Die 3; 2 mm × 2 mm; solder self-assembled simple plates where the solder is deposited on the solder pads using mask-less electroplated solder. In the unreleased state, the whole die is covered in PSG except for the solder pads and bond pads.

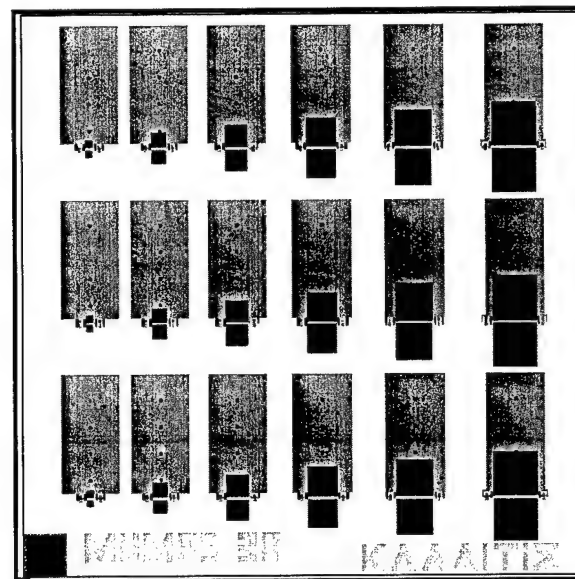


**Figure E-32:** MUMPs 38 Die 4; 2 mm × 2 mm; solder self-assembled simple plates where the solder is deposited on the solder pads using electroplated solder. Unlike the previous version, these solder pads are not connected to the substrate.

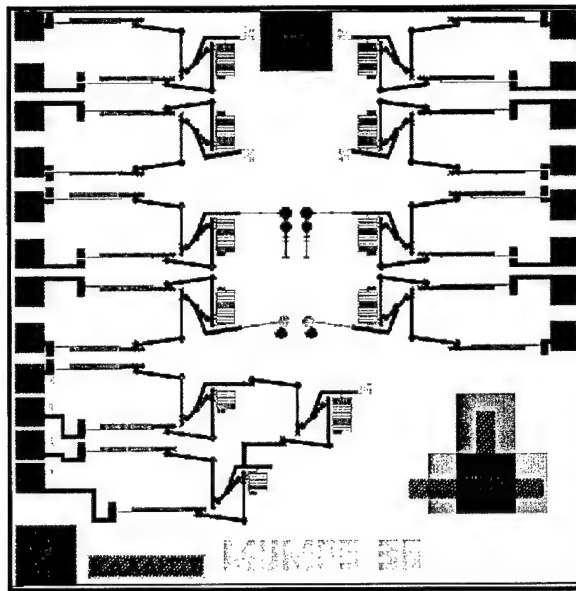


**Figure E-33:** MUMPs 38 Die 5; 2 mm × 2 mm; mechanical NAND gates, NOR gates, and XOR circuit where the gate spring compliance is varied by number of coils.

### E.9 MUMPs 39

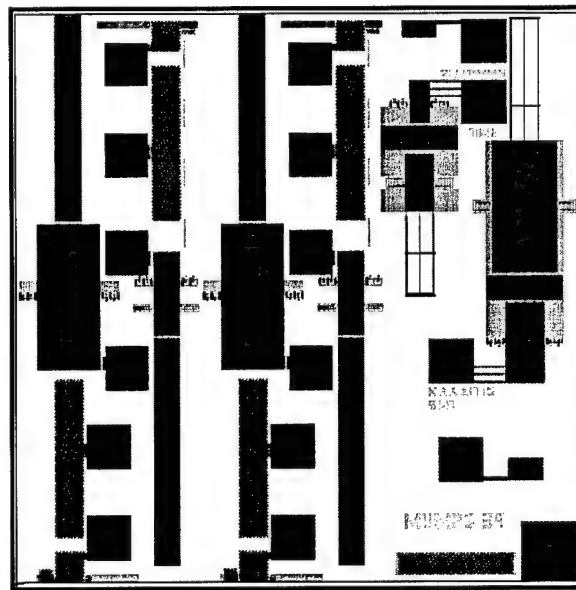


**Figure E-34:** MUMPs 39 Die 1; 2 mm × 2 mm; 8 and 4 mil solder self-assembled thermostats.

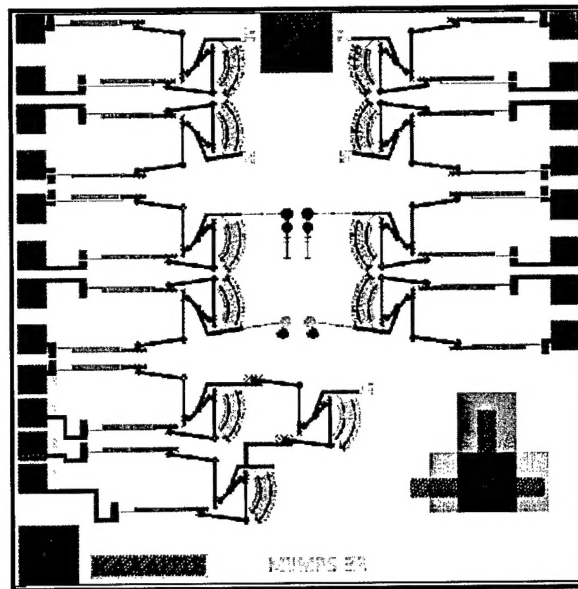


**Figure E-35:** MUMPs 39 Die 2; 2 mm × 2 mm; mechanical NAND gates, NOR gates, and XOR circuit where the gate spring compliance is varied by polysilicon layer.

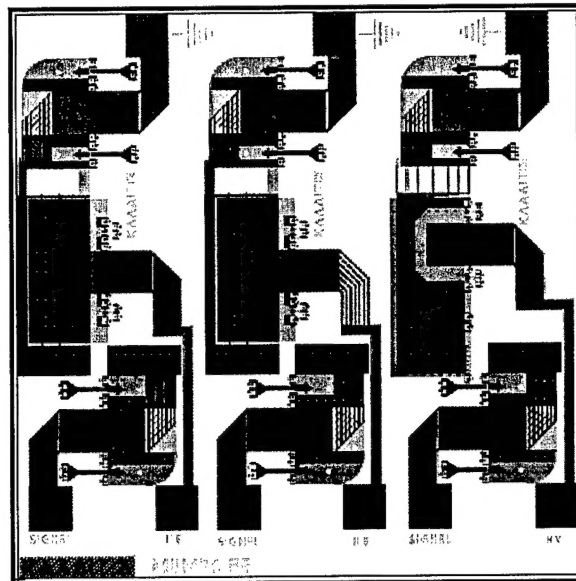


**Figure E-36:** MUMPs 39 Die 3; 2 mm × 2 mm; normally open and normally closed electrostatically actuated switches, for 8 mil solder self-assembly, with improved mechanical stops and modified wiring.

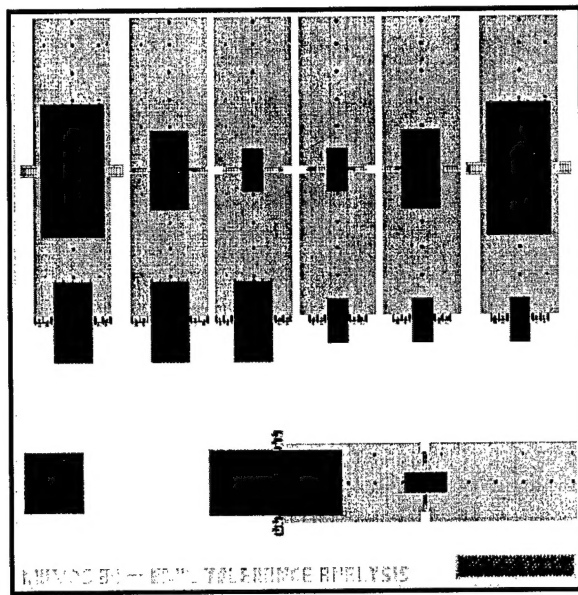


**Figure E-37:** MUMPs 39 Die 4; 2 mm × 2 mm; 8 mil two-solder-joint test structure.

#### E.10 MUMPs 40

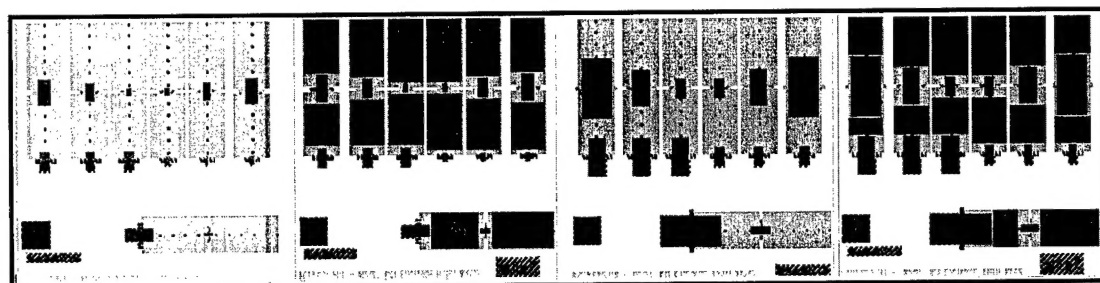


**Figure E-38:** MUMPs 40 Dice 1-4; 2 mm × 2 mm; 4 mil and 8 mil warp/non warped two-solder-joint test structures.

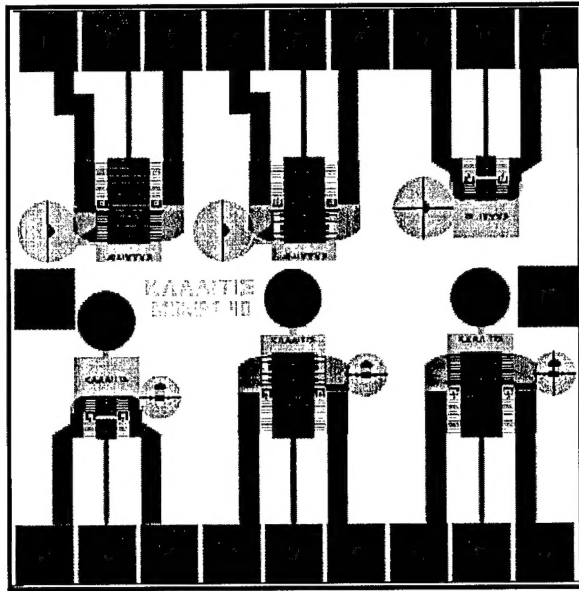


**Figure E-39:** MUMPs 40 Die 5; 2 mm × 2 mm; point heaters with inductive angular position sensors and circular mirrors.

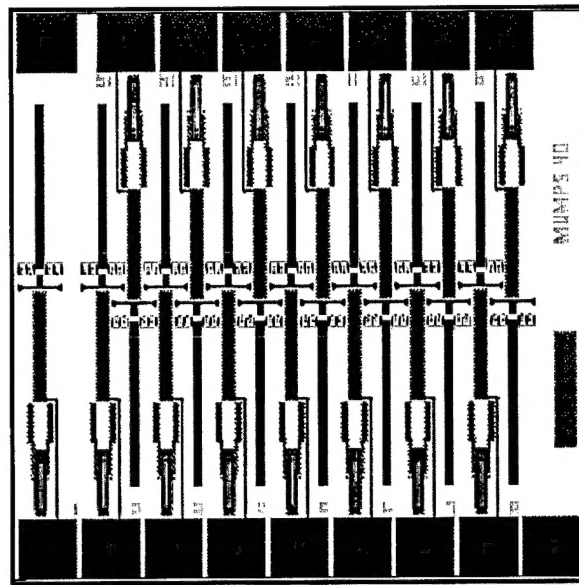


**Figure E-40:** MUMPs 40 Die 6; 2 mm × 2 mm; array of bifurcating beams with ratcheted pre-tensioner.

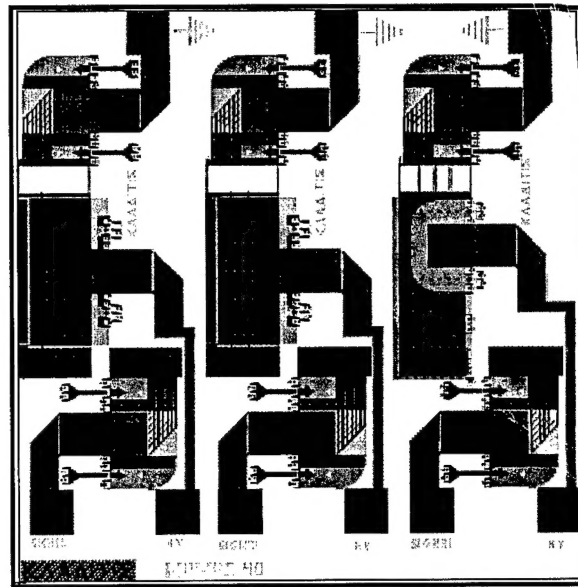


**Figure E-41:** MUMPs 40 Die 7; 2 mm × 2 mm; normally open and normally closed electrostatically actuated switches, for 8 mil solder self-assembly, with less stiff flexures.

### E.11 MUMPs 42

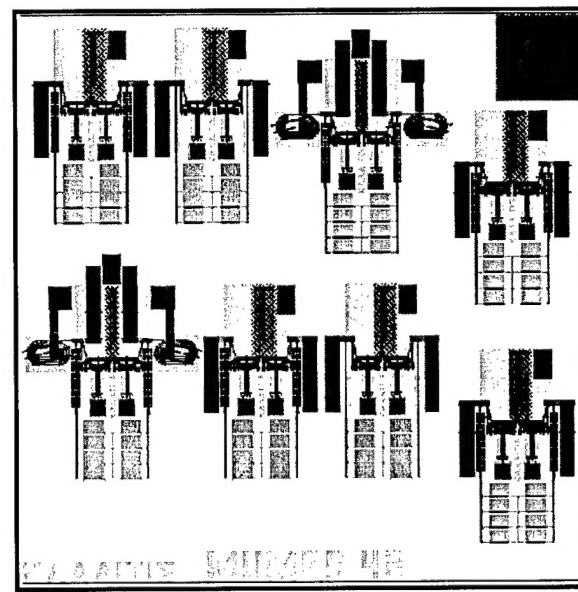


**Figure E-42:** MUMPs 42 Die 1; 2 mm × 2 mm; array of microrobot legs for chain and stiff beam tethered scratch drive actuator self-assembly. Bushings not stuck to nitride.